Electrocatalysts in Nanotubes

Abdullah Kurtoglu

Thesis submitted to the University of Nottingham for the degree of Doctor of Philosophy

[April 2018]

Abstract

In the context of limited availability of fossil fuels and the impact of the current fossil-based energy utilisation, the synthetic development of novel electrocatalysts materials for applications in environmentally friendly energy conversion have been extensively investigated. This thesis is focused on the development of new hybrid metal-carbon nanostructures as efficient electrocatalyst materials for hydrogen fuel cell applications with enhanced performance and/or durability. The nanoscale confinement and graphitic step–edge stabilization of precious metal nanoparticle based electrocatalysts with in hollow graphitized carbon nanofibers were performed. These metal-carbon nanostructures were then investigated using high resolution transmission electron microscopy (HRTEM) for their structures, and by electrochemical method in order to determine their electrocatalytic performance and durability in the redox reaction of oxygen and hydrogen.

Properties of supported metal nanoparticles are significantly influenced by the nature of the carbon surface. Careful design of platinum-based electrocatalyst involving confinement of pre-formed platinum nanoparticles (PtNP) into the internal cavities of hollow shortened graphitized carbon nanofibers (S-GNF) are an excellent approach for creating highly durable nanoreactors (PtNP@S-GNF) towards oxygen reduction reaction. Systematic structural-electrochemical correlations of PtNP on carbon black and on the surface, and inside GNF possessing two qualitatively different surfaces (external continuous graphitic layers and internal stepped layers of grapheme) demonstrate the importance of metal-carbon interactions. Once PtNP@S-GNF nanoreactor is assembled, surfactant molecules, which are necessary to control the PtNP size during their formation in solution, are effectively removed by heating, while PtNP remain immobilised within the S-GNF cavity due to stabilising effects of the graphitic step-edges that inhibit ripening and coalescence of the nanoparticles allowing the retention of their electrocatalytic properties. Catalyst confinement in PtNP@S-GNF creates a nanoscale environment in which at potentials relevant to fuel cell cathodes, the reduction of O_2 proceeds exclusively via a four-electron pathway, and in contrast to commercial Pt/C or PtNP deposited on GNF surface, the specific activity and the electrochemical active surface area remain largely unchanged after durability test. This heralds a new methodology for construction of hybrid electrocatalyst nanomaterial, PtNP@S-GNF where metal NPs are confined and simultaneously electrically connected to the electrode after 50,000 cycles retaining 80% of their activity which can enable the sustainable use of platinum for fuel cell applications.

The oxygen reduction reaction (ORR) and oxygen evolution reaction (OER) catalytic performances of bifunctional electrocatalyst, Mn_4O_3NP supported on graphitised nanofiber (Mn_3O_4/GNF) and encapsulated into shortened GNF (Mn_3O_4@S-GNF) were carried out. We observed that Mn_3O_4NP on exterior surface of GNF exhibited lower activity than that on interior surface of S-GNF which was explained by arguing that a higher surface of interaction of Mn_3O_4NP with the step-edge inside GNF than with the convex surface of the outside of GNF, hence a better connectivity of catalytic centers in Mn_3O_4@S-GNF leading to a higher $E_{1/2}$ potential as compared to Mn_3O_4/GNF. We also noticed that both GNF and S-GNF show better durability behaviour than rest of carbon nanostructures because of stronger graphitic atomic structure.

The PdS_2NP supported on carbon nanostructures were investigated for HER/HOR as a bifunctional electrocatalyst and it was tested in the same test-bed of GNF and S-GNF just as in the case of platinum nanoparticle electrocatalyst. Electrochemical durability test on the catalytic performance of PdS_2@S-GNF(PR24) shows that Pd nanoparticles remain immobilised on S-GNF surface. Which indicate that Pd has the possibility of replacing more expensive platinum as potential electrocatalyst for the use in fuel cell and water splitting devices.

These surprising nanoscale confinement properties of metal nanoparticle based hybrid nanostructure will open up a new strategy for their use in fuel cell for redox reaction platform. We also believe that the electrocatalysis in carbon nanoreactors can be extended to other processes of high technological value.

Publications

1) M. del Carmen Gimenez-Lopez*, A. Kurtoglu, D. A. Walsh, A. N. Khlobystov*, "Extremely Stable Platinum-Amorphous Carbon Electrocatalyst within Hollow Graphitized Carbon Nanofibers for the Oxygen Reduction Reaction", *Advanced Materials*, **2016**, *28*, 9103-9108.

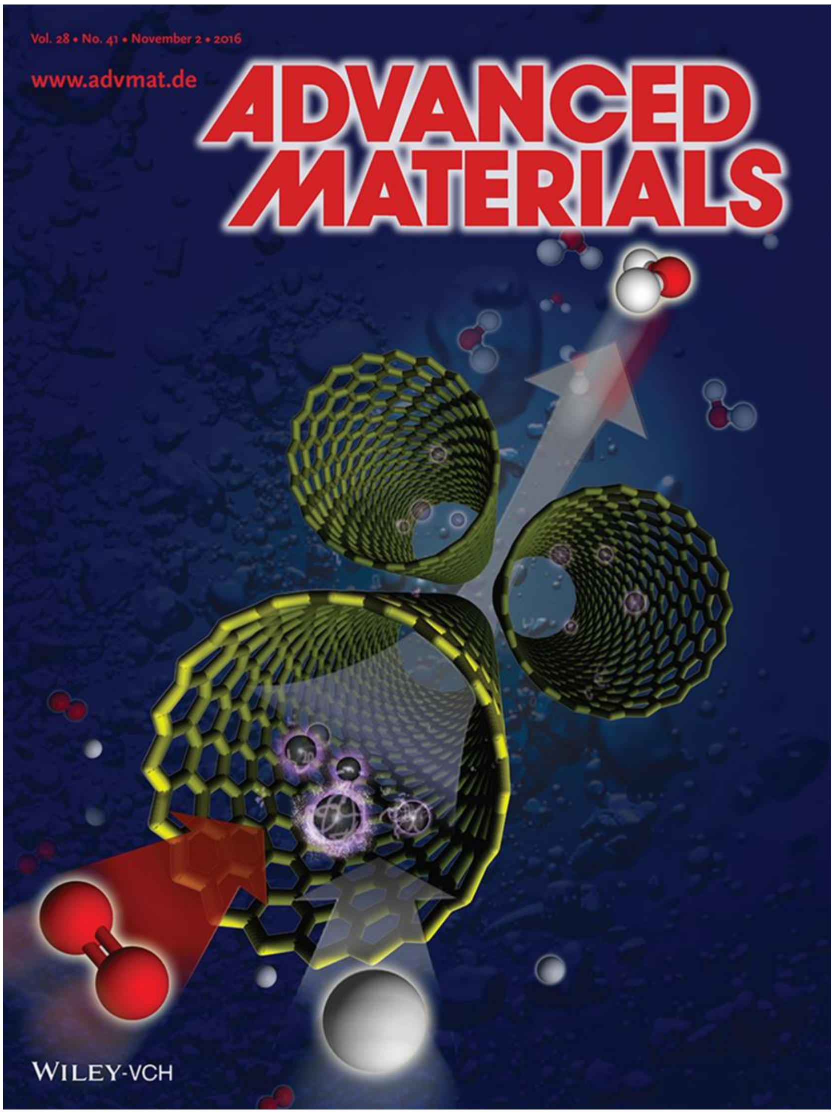

Our design suggestion cover was accepted to publish for inside back cover.

2) A. Kurtoglu, D. A. Walsh, A. N. Khlobystov*, M. del Carmen Gimenez-Lopez*, "Platinum Nanoparticles on Carbon Surfaces and Encapsulated in Hollow Graphitised Nanofibers: Designing Highly Durable Electrocatalytic Nanoreactors for the Oxygen Reduction Reaction", *manuscript in preparation*.

Acknowledgments

First and foremost, I would like to express my sincere gratitude to my supervisor **Prof. Andrei Khlobystov** for the invaluable guidance and continuous support throughout my PhD studies and for sharing his immense knowledge in the field with patience, enthusiasm and motivation. I could not have imagined having a better advisor and mentor to do and learn science. Thank you for your encouragement and suggestion and for giving me an opportunity to work you.

Secondly, my sincere thanks go to **Dr. Maria C. Gimènèz-Lòpez**, who I would turn to when my supervisor was away or engaged in another project. She was always happy to assist and share her practical knowledge and experimental know-how on the project. Besides being a supervisor, she has been a wonderful friend whose company was always a fun. Without her precious support, it would not be possible to conduct this research.

I also would like to express my thanks to **Dr. Darren Walsh** for the valuable support and guidance on anything and everything related to electrochemistry. I must mention the help I received from **Carlos Herreros Lucas** in carrying out imaging and XRD experiment on the Mn_3O_4/CN and PdS_2/CN nanostructures and providing these materials. Thanks go **Dr. Thomas Chamberlain** for his support in teaching and supplying some of the nanotube-guest samples, ie SWNT hybrid materials that were used in the project. I thank **Mehtap Aygun** for her help in thermal analysis and electrochemistry analysis for Mn_3O_4/CN work, and **Glen Murray** for running electrochemistry experiments, imaging of my samples and for proof reading my thesis. I also thank **Abdul Baten abi** for some proofreading.

I am very grateful for the friendship and help that I received from the Nottingham Nanocarbon, Gimenez and Waslh Electrochemistry group members, in particular, MSc project student working with me **Adam Dennington**. I thank **Dr. Graham Rance** for always making time

for my questions and his kind help. I am grateful to **Rhys Lodge** for imaging some samples. Also, I would like to express my sincere gratitude to all the technical staff, particularly **Mark Guyler** for providing a safe and happy working environment, and friendly atmosphere at numerous social events. The technical staff in Advanced Materials Group were very helpful. Special thanks go to **Prof. Paul Brown** and **Dr. Nigel Neate** for their constant help and expertise using a range of techniques, in particular, XRD and DSC measurements.

I would also like to express my deepest gratitude and profound love to **my parents, Hacıbek & Saynur,** and **sisters** for supporting and encouraging me throughout all my life and studies. I finish with my small family, where the most basic source of my life energy resides. A huge thank goes to my two daughters, **Nalan** and **Canan**, for the cuddles, laughter, the occasional push to keep me going, and for their patience while their dad was studying on this thesis instead of spending time with them. To my other half, **Nilay**, for her support, encouragement, and patience throughout all my studies. Her tolerance of my occasional stress during the writing process, and of course for her unwavering love that is the bedrock upon which the past five years of my life have been built. Their support has been unconditional all these years; they have cherished with me every great moment and supported me whenever I needed it. I could not do this without them.

List of acronyms, abbreviations and symbols

Acronym, abbreviation or symbol	Definition
PEMFC	Proton exchange membrane fuel cell
GC	Glassy carbon
RDE	Rotating disk electrode
RRDE	Rotating-ring disk electrode
RHE	Reversible hydrogen electrode
@	[...] encapsulated within [...]
/	[...] deposited on [...]
A	Electrode area
AD	Arc discharge
ad	Adsorbed
Ageo	Geometric Electrode surface area
I–V	Current-potential
OOH*	Adsorbed superhydroxyl species
OH*	Adsorbed hydroxyl species
O*	Adsorbed oxygenated species
E^0	Standard electrode potential
DFT	Density functional theory
AgNP	Silver nanoparticle(s)
AuNP	Gold nanoparticle(s)
CN	Hollow carbon nanostructures
CNF	Carbon nanofibers
CNT	Carbon nanotube
Co	Concentration
CV	Cyclic voltammetry
D0	Diffusion coefficient of solvent
$E_{1/2}$	Half wave potential
Ea	Activation energy
ECSA	Electrochemical surface area
EDX	Energy-dispersive X-ray
F	Faraday constant
GCE	Glassy carbon electrode
GMWNT	Graphitised multi-walled carbon nanotubes
GNF	Graphitised carbon nanofiber
HER	Hydrogen evolution reaction
HOR	Hydrogen oxidation reaction

HRTEM	High resolution transmission electron microscope
IR	Infra-red
IR	Current x resistance
LSV	Linear sweep voltammetry
Mn_3O_4NP	Manganese oxide nanoparticles
MWNT	Multi-walled carbon nanotube(s)
n	Number of electrons transferred
NP	Nanoparticle
NT	Nanotube
OER	Oxygen evolution reaction
ORR	Oxygen reduction reaction
PdNP	Palladium nanoparticle(s)
PdS2	Palladium sulphate nanoparticles
PTFE	Poly(tetrafluoroethylene)
Q	Charge
R	Gas constant
SWNT	Single-walled carbon nanotube(s)
T	Temperature
TEM	Transmission electron microscopy
TGA	Thermogravimetric analysis
v	Scan rate
RuPtNP	Ruthenium-Platinum nanoparticles
BF-TEM	Bright field-transmission electron microscopy
CNF-H	Carbon nanofibers- herringbone
CNF-P	Carbon nanofibers- nanoplatelet
CNF-tH	Carbon nanofibers- tube herringbone
CNF-tP	Carbon nanofibers-tube nanoplatelet
FeCuNP	Iron cupper nanoparticle(s)
H_{ad}	Adsorbed hydrogen
Hupd	Hydrogen under potential deposition
Ik	Mass-transport free kinetic current
Id	Diffusion-limiting current
PtNP	Platinum nanoparticle(s)
URFC	Unitized regenerative fuel cell
V	Voltage

Contents

Chapter 1. Electrocatalysts in Carbon nanotubes

1.1. Energy-related electrochemical process

One of the biggest challenges facing the world today is the increasing global demand for affordable and secure energy, while at the same time tackling climate change. In this context, electrochemistry as a fundamental science that researches the conversion between energy stored in chemical bonds and electricity will play a significant role in facing these energy challenges.

Electrochemical systems, such as fuel cells, presents some of the most environmentally friendly and efficient technologies for energy conversion and storage. These technologies are based on chemical reactions at the interface, permitting a high thermodynamic efficiency in the energy conversion.[1] For an electrochemical fuel cell system, the theoretical efficiency is much higher than a conventional heat engine limited by Carnot efficiency at low temperature (**Figure 1-1a**).[2] In an electrochemical process, the energy conversion is a clean and direct way with small impact to the environment, avoiding the climate change and pollution problems raised by fossil fuel burning.[3] However, the electrochemical energy conversion in these ways is often restricted by high activation barriers that need an extra energy to overcome. An overpotential or a faradaic efficiency is the extent of this barrier: a low faradaic efficiency or a high overpotential will lead to excess of energy to heat.[4]

Electrocatalysts are considered a key component for efficient electrochemical conversions, as they are used to modify the electrode in order to lower the activation energy (E_a) and increase the conversion rate in the chemical process **Figure 1-2b**). In energy conversion for large-scale applications, electrocatalysts should be low-cost, durable, sustainable and energy efficient.

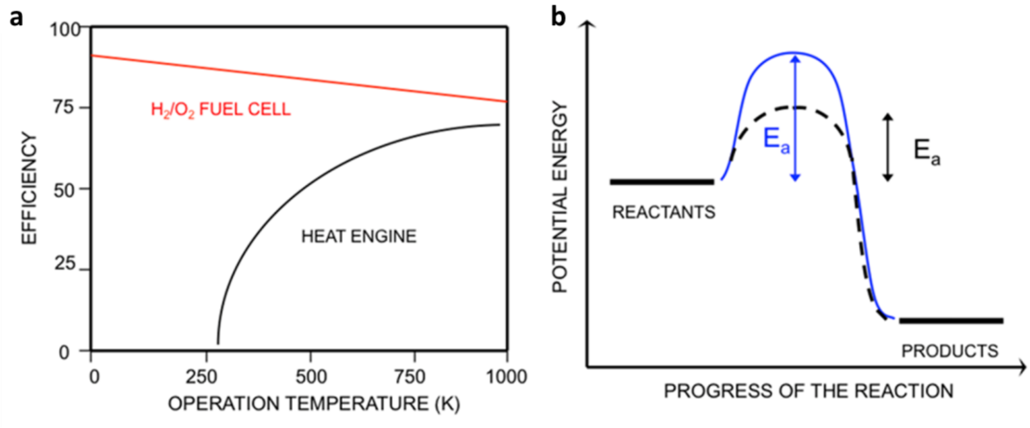

Figure 1-1. (**a**) Comparison of energy conversion efficiency in a heat engine and H_2–O_2 electrochemical fuel.[2] (**b**) Potential energy along a reaction coordinates for a typical exothermic uncatalysed (blue line) and catalysed (dashed line) process.

However, most of the existing electrocatalysts do not meet one or more of the mentioned requirements. Because of their high performance and stability,[5] precious metal-based materials play an important role in our society for essential energy-based electrochemical conversions including hydrogen oxidation reactions (HOR) and hydrogen evolution reactions (HER), oxygen evolution reactions (OER) and oxygen reduction reactions (ORR) among others.

1.2. Oxygen Reduction Reaction (ORR) in fuel cells

Oxygen reduction reaction (ORR) is the cathode reaction for a range of energy applications including fuel cells,[6-15] redox flow batteries[16-20] and charging process of rechargeable metal-air batteries.[21-31] The thermodynamic equilibrium potential for the ORR is 1.23 V versus the reversible hydrogen electrode (RHE), but even on Pt group metals which are the most active catalyst materials, significant current is only observed at potentials below 0.9 V.[10] In a typical fuel-cell device, the fuel (hydrogen typically) is oxidised at the anode, whereas oxygen is chosen to take the electrons released from the fuel at the cathode, thus converting the chemical energy in the fuel into electrical energy (**Figure 1-2**). General, between the fuel oxidation reactions, electrons go outside the cell to provide electricity and protons travel from the anode to the cathode inside through the membrane to perform the charge flow in the circuit.[32]

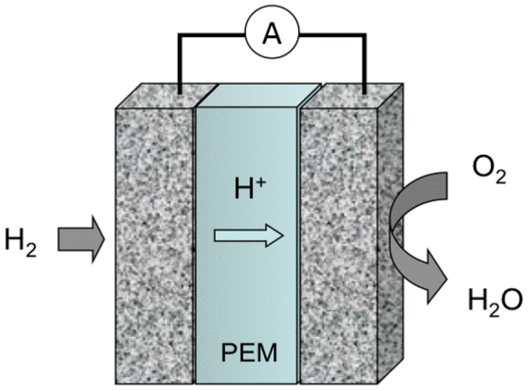

Figure 1-2. A typical proton exchange membrane (PEM) fuel cell with H_2 as fuel.[33]

1.2.1. Electrochemical evaluation of the ORR

In all electrocatalytic process that generally occurs at fluid/solid interfaces, the catalytic reaction occurs after the reactants go through the fluid layer surrounding the catalyst particles. Then, the reactants are adsorbed on the catalysts surface and the electron transfer occurs resulting in some chemical bonds being broken and new bonds forming to make the products that are finally desorbed from the surface (**Figure 1-3**). When the reactant interacts too weakly with the catalyst surface, the adsorption cannot take place and the reaction does not proceed. On the contrary, if the interaction is too strong, the desorption process cannot occur and the catalyst surface is blocked by products. Thus, an optimum catalytic activity is expected when the binding energy of the reactant molecules is either not too strong or too weak.[34, 35]

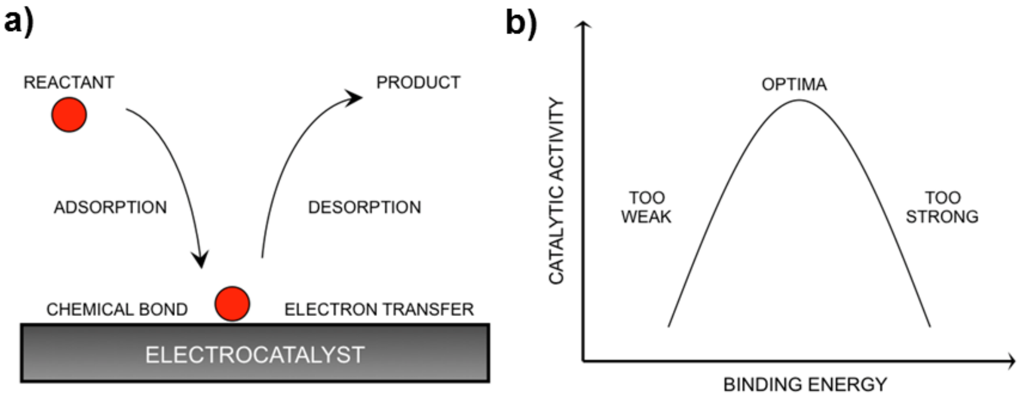

Figure 1-3. (**a**) Schematic diagram of an electrocatalytic process occurring at the electrode/electrolyte interface. (**b**) A typical Volcano plot for an electrocatalytic process.[36]

The ORR involves a multi-electron transfer process in which O_2 is converted into H_2O or OH^-, depending on the solution used in the electrochemical studies. Because of the strength of the O=O bond, and the fact that four coupled electron and proton transfers are required, the ORR is kinetically very slow.[36] A detailed understanding of the metal-catalysed electrochemical reduction of oxygen to H_2O will help to target the development of new electrocatalyst approaches. In acidic solution, O_2 can be reduced in a $4e^-$ process and be converted into H_2O: $O_2 + 4H^+ + 4e^- \rightarrow 2H_2O$ ($E^0 = 1.229$ V). O_2 may also undergo a partial $2e^-$ reduction to form hydrogen peroxide, H_2O_2 (**Equation 1-1**), followed by another $2e^-$ reduction to convert H_2O_2 into water (**Equation 1-2**).[37]

$$O_2 + 2H^+ + 2e^- \longrightarrow H_2O_2 \quad E° = 0.70\ \text{V}$$ **Equation 1-1**

$$H_2O_2 + 2H^+ + 2e^- \longrightarrow 2H_2O \quad E° = 1.76\ \text{V}$$ **Equation 1-2**

In alkaline solution, O_2 can be reduced by a $4e^-$ process to form hydroxide, OH^-: $O_2 + 2H_2O + 4e^- \rightarrow 4OH^-$ ($E^0 = 0.401$ V), or by $2e^-$ processes to form HO_2^- (**Equation 1-3**) and then HO^- (**Equation 1-4**).[38]

$O_2 + H_2O + 2e^- \rightarrow HO_2^- + OH^-$ $E° = -0.065$ V **Equation 1-3**

$HO_2^- + H_2O + 2e^- \rightarrow 3OH^-$ $E° = 0.867$ V **Equation 1-4**

In the alkaline and acid solutions, ORR on a Pt surface typically goes through the $4e^-$ pathway; but on a Pt surface, the true nature of the ORR mechanism is complex and not well understood. Oxygen may be converted into different intermediates, such as hydroxyl (OH), superhydroxyl (OOH) and oxygenated (O), and species under standard conditions (E^0 is referenced to the standard hydrogen electrode (Pt, a_{H+}=1, P_{H2}=1 bar, 298 K). Currently density functional theory (DFT) calculations[35] display that at high oxygen coverage, the ORR inclines to go to an associative mechanism, in which superhydroxyl species are first formed and then O–O bond is broken, whereas at low oxygen coverage, the ORR goes a dissociative mechanism in which the O–O bond is broken before a hydroxyl species are formed.

It is believed that in the ORR rate-limiting step is the first electron transfer step, $Pt(O_2)_{ads} + e- \rightarrow Pt(O_2^-)_{ads}$, with oxygen adsorption onto a surface primarily covered by impurities (hydroxyls) rather than reactive intermediates. This key assumption suggests that any electrocatalyst modification done to the atomic or electronic structure of the surface that delays hydroxyls adsorbing and blocking O_2 adsorption sites will have a positive impact in the specific activity. Thus, different approaches have been used to shift average energy of the *d*-electrons (the d-band centre with respect to the Fermi level) of the metal catalyst, which is believed to affect the adsorption coverage of the hydroxyl species that interfere with the ORR including, (i) modification of the electrocatalysts particle size and shape, (ii) use of different supports such as a variety of different types of carbon/nano-carbon and metal oxides, (iii) creating over layer systems such as nanostructured thin films or alloys and (iv) core-shell structures.

Electrochemically evolution of the ORR process, the catalyst is generally mixed in a mixture of solvents and deposited on a glassy carbon (GC) rotating-ring disk electrode (RRDE) as illustrated in **Figure 1-4**.[6] The Pt loading is carefully controlled to ensure a thin layer of catalyst deposition on the RRDE electrode surface. When the layer is too thick, both the uncertainty in qualifying catalytic activities[39] and the mass-transport loss[6] increase.

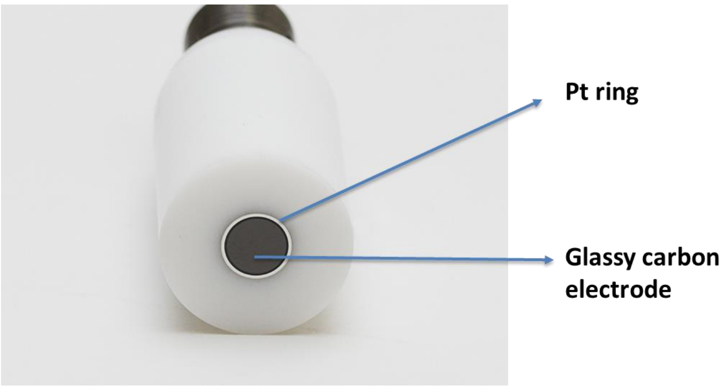

Figure 1-4. A typical rotating Pt ring-disk glassy carbon electrode (RRDE) from Pine Instruments, the ring surrounds the glassy carbon electrode.

The electrochemical properties of the electrocatalyst in acidic solution are first evaluated by cyclic voltammetry to obtain a cyclic voltammogram (CV) (**Figure 1-5a**) and to calculate the electrochemically active surface area (ECSA) of the catalyst. In a cathodic scanning process, H^+ is first reduced to H_2 adsorbed on the catalyst surface, and the associated region under the current density-potential curve is referred to as the H_2 adsorption area. The adsorbed H_2 is oxidized, which generates H^+, and the associated region covered by the curve is referred to as the H_2 desorption area. The H_2 desorption region, surrounded by the curve (**Figure 1-5a**) and the potential scanning baseline, is integrated to get the ECSA.[40] ORR activities are measured in an oxygen saturated acid or alkaline solution with the RDE rotating at a certain speed and a potential scan of 1.05-0 V vs reversible hydrogen electrode (RHE) at rates of 5-20 mV/s. From the ORR polarisation curves, half-wave potentials ($E_{1/2}$) of electrocatalysts can be calculated and used to qualitatively determine the catalyst activity: generally, the higher the potential, the better the ORR activity. The kinetic current at 0.85 V (vs. RHE) is found out from the polarisation curve according to the *Koutecky*-Levich *equation:*[11] $1/J = 1/J_k + 1/J_d$; where J is the current density found experimentally, J_k is the mass-transport free kinetic current density and J_d is the diffusion-limited current density, as shown in the **Figure 1-5b**. The specific activity of a catalyst can be calculated by normalising the J_k with its ECSA. From the same experimental data, one can also calculate the mass activity of the catalyst by normalising the J_k with the catalyst loading.

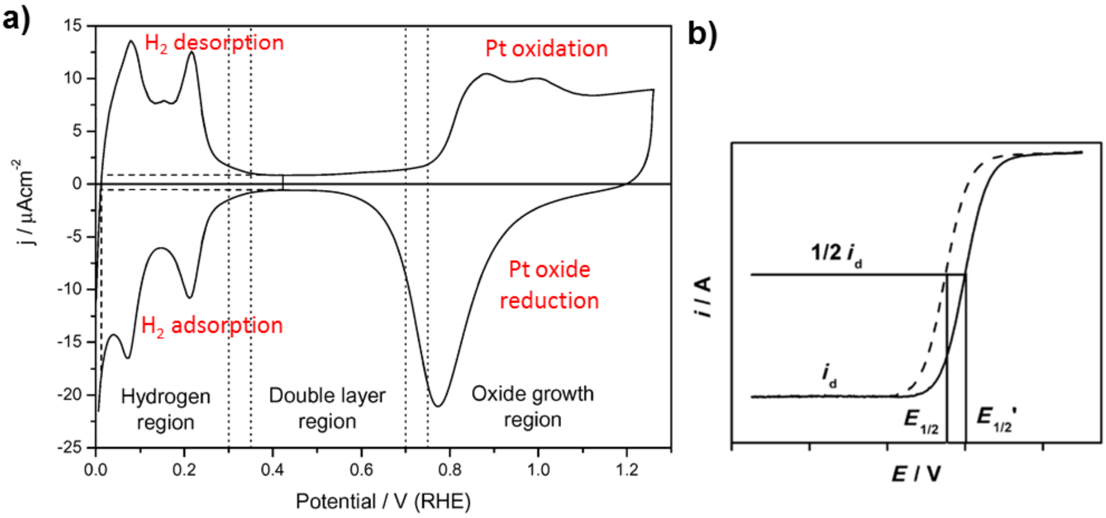

Figure 1-5. (**a**) A cyclic voltammogram of a polycrystalline Pt electrode in N_2-saturated 0.5 M H_2SO_4 at a sweep rate of 50 mV/s, [41] (**b**) Typical ORR polarization curves of two catalysts.[42]

In fuel cell, the direct 4-electron pathway of the ORR is highly favoured. The 2-electron reduction pathway is typically used in industry for H_2O_2 production, whereas the 1-electron reduction pathway ($O_2 + e^- \rightarrow O_2^-$; $O_2^- + e^- \rightarrow O_2^{2-}$) is of importance in the investigation of the ORR mechanism. An understanding of the ORR mechanism can be found by plotting the overpotential *vs.* log(J_k) or fitting the polarisation curve, as the transfer coefficient, the number of electrons transferred in the rate-determining step (rds), and the exchange current density (J_0) can be calculated. To deduce the ORR mechanism, the rotating ring-disk electrode

(RRDE) is generally used, as the intermediate species produced on the disk electrode where the ORR occurs can be easily detected on the ring.

Catalyst durability (lifetime experiments) is assess by cycling the potentials over 0.6–1.1 V (vs. RHE) in an acid solution. The ECSA change of the catalyst and the shift of the ORR polarisation curve before and after this durability experiments are compared to determine the durability of the catalyst. The smaller the ECSA change and the shift of the ORR polarisation curve, the better the durability.[43]

1.2.2. Mass transport

Mass transport is the transfer of species in bulk solution and arises because of differences in chemical or electrical potential between two different places (**Figure 1-6**). The reactant species must be transferred from the bulk solution to the electrode surface for a reaction to take place. There are three forms of mass transport for the arrival of a reactant species to the electrode surface:

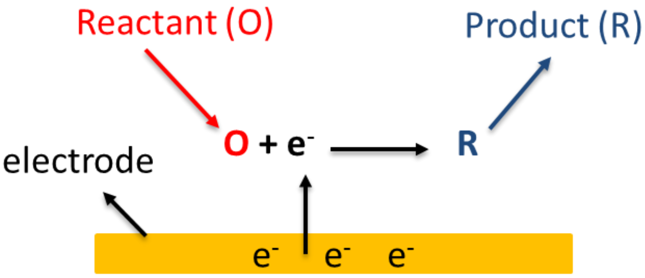

Figure 1-6. Schematic illustration of mass trasport of species in solution.

- **Migration** – the transfer of charged species across an electric potential difference.
- **Diffusion** – the transfer of a reactant species due to a gradient of chemical potential, such as a concentration difference.

- **Convection** –the natural transfer of species because of forced convection such as mechanical stirring, or density gradients.

1.2.2.1. Diffusion

The natural movement of both neutral and charged species in solution is described diffusion that is not influenced by the existence of an electric field (**Figure 1-7**). The rate of diffusion is entirely dependent of the presence of a concentration gradient, as illustrated by Pick's laws (**Equation 1-5**) of diffusion:

$$J_{d,O}(x,t) = -D_O \frac{\partial C_O\ (x,t)}{\partial x}$$ **Equation 1-5**

where $J_{d;o}$ is the diffusional flux of species O, dCo/dx is the concentration gradient in the x-direction and D_O is the diffusion coefficient.

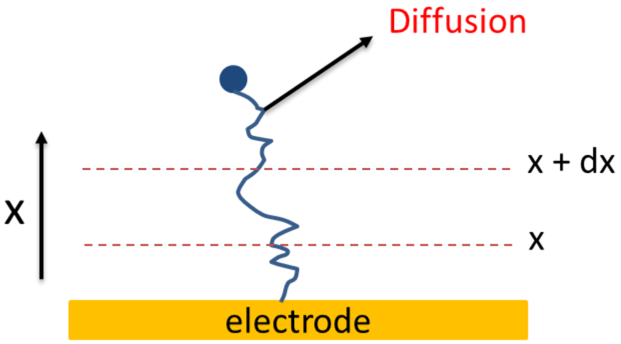

Figure 1-7. Schematic illustration of diffusion process of species in solution.

The variation of the concentration of a substance as a function of time is of more interest to the electrochemist, and is obtained using Pick's second law (**Equation 1-6**).

$$\left(\frac{\partial C_O\ (x,t)}{\partial t}\right) = D_O \left(\frac{\partial^2 C_O\ (x,t)}{\partial x^2}\right)$$ **Equation 1-6**

- Microelectrode

A microelectrode is that they are smaller than the scale of the diffusion layer developed in readily achievable experiments.[44] Diffusion can occur in two dimensions (**Figure 1-8**) on disc microelectrodes which are routinely used in electrochemical experiments and theoretical treatment. Therefore, microelectrodes are a suitable mechanistic tool for the investigation of the homogeneous kinetics of the chemical reaction between species in solution or the heterogeneous electron transfer at the electrode.

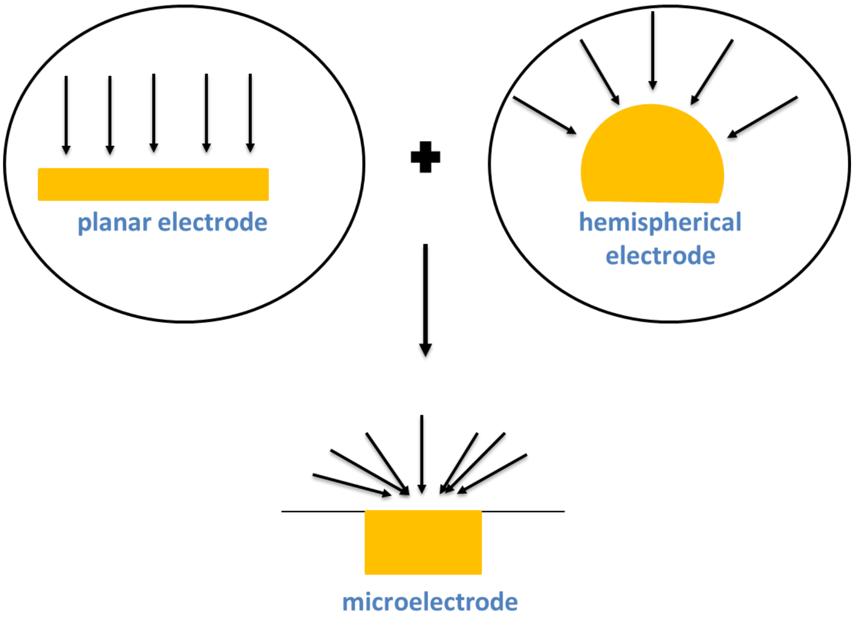

Figure 1-8. Schematic displaying the uniform diffusion at planar and hemispherical electrodes in comparison to the non-uniform accessibility of the disc microelectrode.

- Rotating disk electrodes (RDEs)

The rotating disc electrode (RDE) contains of electrode material that has been fixed in a shaft of protecting material such as Teflon or epoxy resin. The RDEs attract to researchers to use in electrochemistry by the fact that the mathematical models covering hydrodynamic and convective-diffusion calculations are well known for the steady state. The velocity profile of a fluid acting near a rotating disc drawn in **Figure 1-9**.[45]

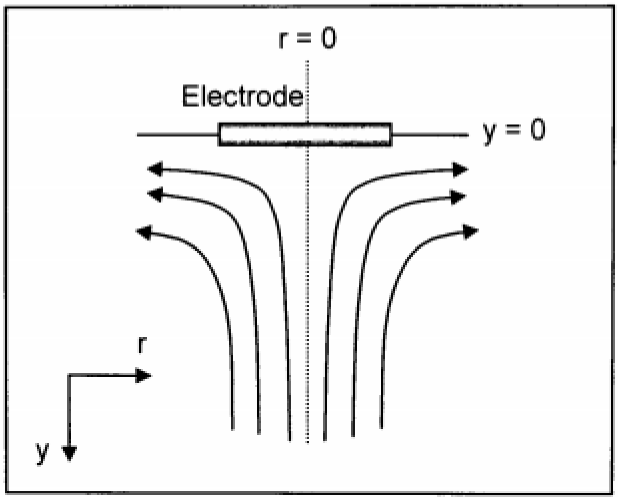

Figure 1-9. Flow velocities at a rotating disc electrode.[45]

After application of the above velocity profile to the convective-diffusion equations, we obtain a general solution for the transport limited current as a function of electrode rotation speed. This is known as the Levich equation, shown below:

$J_d = 0.620nFD_o^{2/3}v^{-1/6}C_o\omega^{1/2}$ **Equation 1-7**

1.2.3. Cyclic Voltammetry

Cyclic voltammetry (CV) is one of most common electro-analytical method. The CV measurement contains the application of a potential to the working electrode, which changes with time, according to a triangular potential waveform as shown in **Figure 1-10**. The plot of I vs. E is known as a voltammogram.

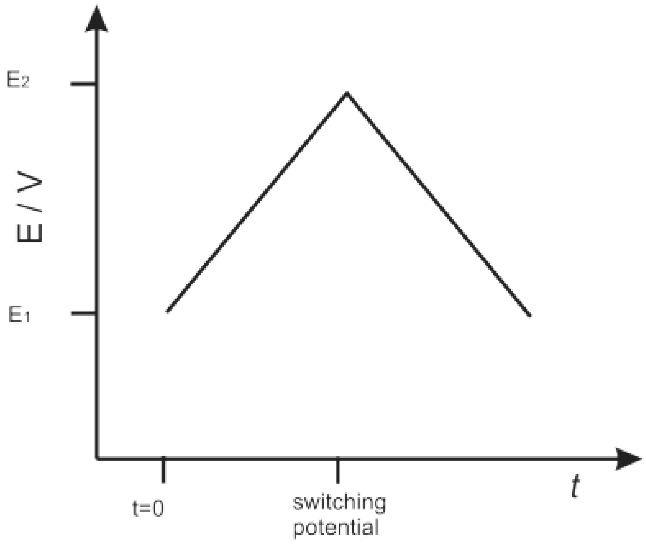

Figure 1-10. A triangular cyclic voltammetric waveform.[44]

Typical cyclic voltammogram on planar electrode are showed in **Figure 1-11**. The three voltammograms shown correspond to'reversible', 'quasi-reversible' and 'irreversible' electron transfer processes with the same potential.

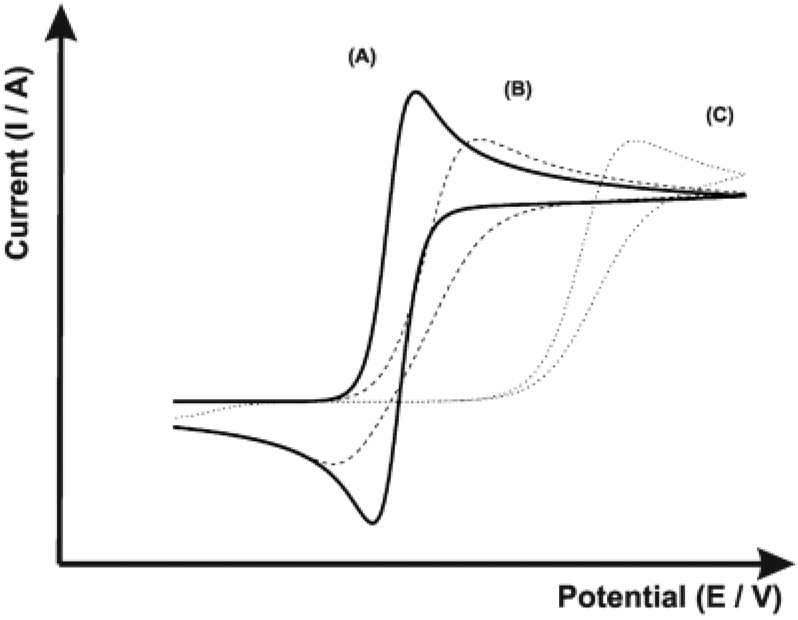

Figure 1-11. Examples of reversible (**a**), quasi – reversible (**b**) and irreversible (**c**) cyclic voltammetry.[44]

A maximum current (peak) is detected because of the balance between electron transfer and diffusion. The peak current, i_p, at 298 K can be calculated using the Randles-Sevcik equation:

$$i_p = (2.69x10^5)n^{\frac{3}{2}} AD^{\frac{1}{2}}v^{\frac{1}{2}}c_{bulk}$$ **Equation 1-8**

The voltammogram of microelectrodes is sigmoidal shape as shown in **Figure 1-12** and reaches a steady-state current (i_{ss}) which is described a limiting current, in contrast to macroelectrodes.

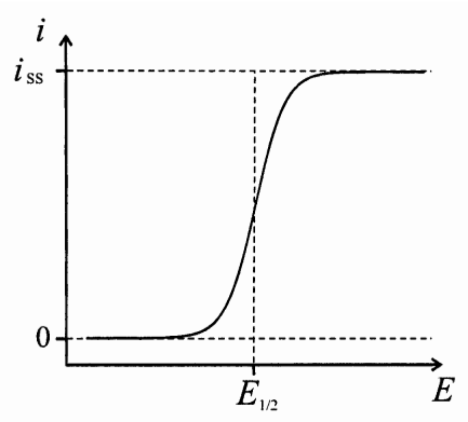

Figure 1-12. Steady-state voltammetry at a microdisk electrode.[44]

1.2.4. Tafel Analysis and Butler-Volmer Kinetics

The kinetic current density or current density in absence of mass transport effect, J_k, is a function of the exchange current density, J_0, this relationship can be calculated by the Butler-Volmer equation as:

$$J_k = J_0\left(\exp\left(\frac{-\alpha cF}{RT}\eta\right) - \exp\left(\frac{\alpha cF}{RT}\eta\right)\right)$$ **Equation 1-9**

Where J_k is the overall current density, J_0 is the exchange current density (in Am^{-2}) η is the overpotential, and α is the transfer coefficient. The relationship between the overall current density, J, and the currents with and without mass transport effects is calculated by the well-known Koutecky-Levich equation (**Equation 1-10**). Koutecky-Levich equation can be solved for the kinetic current and expressed as:

$$J_k = \frac{J_d \, x \, J}{J_d - J}$$ **Equation 1-10**

Substituting **Equation 1-11** in the Butler-Volmer equation:

$$\frac{J_d \, x \, J}{J_d - J} = J_0 \left(\exp\left(\frac{-\alpha cF}{RT}\eta\right) - \exp\left(\frac{\alpha cF}{RT}\eta\right) \right)$$ **Equation 1-11**

For large negative overpotentials the second term, *exp(αaFη/RT)*, becomes negligible and **Equation 1-12** becomes the Tafel form:

$$\frac{J_d \, x \, J}{J_d - J} = J_0 \left(\exp\left(\frac{-\alpha cF}{RT}\eta\right) \right)$$ **Equation 1-12**

Rearranging **Equation 1-13**:

$$\eta = \frac{RT}{\alpha F} ln J_0 - \frac{RT}{\alpha F} ln \left(\frac{J_d \, x \, J}{J_d - J} \right)$$ **Equation 1-13**

The relationship between overpotential and current densities at high overpotentials when the system is not mass transfer affected is given by Tafel as:

$$\eta = \mathrm{a} + \mathrm{b}\,log\left(\frac{J_d\,x\,J}{J_d - J}\right)$$ **Equation 1-14**

Plots of $log\,J$ vs η are known as Tafel plots, they are useful tools to evaluate kinetic parameters. Tafel plots generate a linear region of slope b. From b the transfer coefficient, α, can be calculated. When the linear region is extrapolated to zero overpotential $log\,J_0$ is obtained. Data points for Tafel analysis of the kinetically controlled region were taken from the near-steady-state voltammograms, with linear sweep voltammetries at scan rate 1 mV s^{-1}. To determine Tafel data parameters $log\,(J_d x J/J_d - J)$ vs η data were plotted.

1.3. The reverse reaction of ORR: Oxygen evolution reaction (OER)

OER is an electrochemical reaction to produce O_2 by electrochemical oxidation of H_2O, which is solar fuel synthesis,[46-51] a half reaction of water splitting,[52-54] and is also taken place in the charging process of rechargeable metal-air batteries.[29, 31]

For both ORR and OER, developing efficient bifunctional catalysts is extremely challenging but necessary, particularly for unitized regenerative fuel cells (URFC),[55-61] a promising energy storage device that works as a fuel cell and in reverse as a water electrolyser producing H_2 and O_2 to feed the fuel cell.

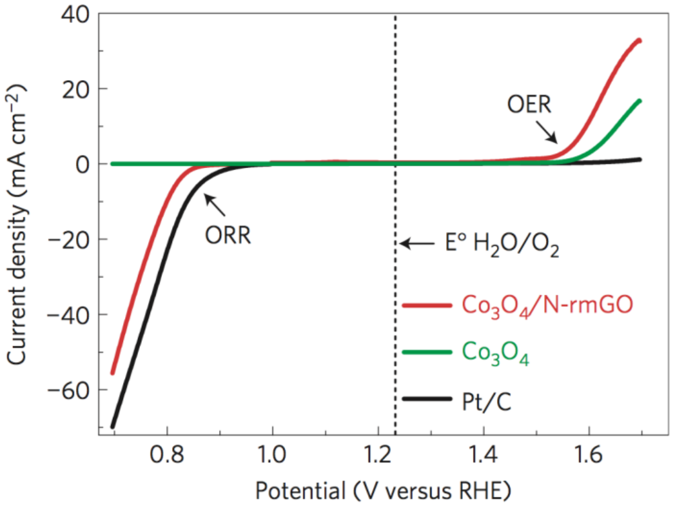

Figure 1-13. The ORR and OER polarisation curves of Co_3O_4/NrmGO hybrid, Co_3O_4 nanocrystals and Pt/C catalysts in O_2-saturated 0.1M KOH.[43]

OER or water oxidation is also very slow as a multistep proton-coupled electron transfer is involved in the process. Currently, the most active OER catalysts are RuO_2 and IrO_2, [62-72] but they suffer due to their scarcity and the high cost of precious metals. Thus, many efforts have been taken to develop lower cost alternatives based on first-row transition metal oxides.[73] Recently, it has been reported that a hybrid material containing of Co_3O_4 nanocrystals grown on reduced graphene oxide (NrmGO)[43] acts a bifunctional catalyst for both ORR and OER with high activity (**Figure 1-13**) with similar activities on manganese oxide[56] and spinel CoMnO[74] catalysts.

The most generally accepted mechanisms of OER (**Equation 1-15-17**) on different electrodes surface in alkaline media involve steps below,

$OH^-_{ads} \rightleftarrows OH_{ads} + e^-$ **Equation 1-15**

$OH^- + OH_{ads} \rightleftarrows O_{ads} + H_2O + e^-$ **Equation 1-16**

$O_{ads} + O_{ads} \rightleftarrows O_2$ **Equation 1-17** where the electron-transfer taking place is rate determining step.[75-77]

We would like also to extend this methodology to hybrid bifunctional non-precious metal catalysts for ORR and OER. Inspired by nature catalyst for OER,[78] we focused our attention on manganese oxide particles that are very stable, inexpensive and abundant materials. For both reactions, the development of a bifunctional catalyst, which could be particularly useful for energy storage applications, is a significant challenge in the field. For instance, the catalyst could be employed in a URFC which is an energy storage device that can employ intermittent renewable energy like wind or solar. This type of fuel cell in the electrolysis mode splits water into H_2 and O_2 and in the fuel cell mode consumes H_2 to produce electricity.[57, 58] For both the fuel cell reaction and the water electrolysis, no existing catalyst material runs close the equilibrium potential for either the ORR or the OER. Therefore, the efficiency of the full conversion cycle, from electricity to hydrogen and back to electricity in an URFC, will be increased with enhanced bifunctional catalysts.[79] Furthermore, the best OER electrocatalysts are RuO_2 and IrO_2,[59-61, 69] but they are not as active for the ORR as Pt.[80] The best electrocatalysts for the ORR is Pt,[21] but Pt has only limited activity for the OER.

The photosynthetic oxygen evolving complex (OEC) in nature catalysed the OER with a cubane-like $CaMn_4O_x$ active site.[78] Consequently, manganese (Mn) oxide surface,[60, 61, 78, 81] have already confirmed activity for the OER, are highly interesting materials for bifunctional catalysis.

1.4. Hydrogen evolution reaction (HER) / Hydrogen oxidation reaction (HOR)

Hydrogen is often considered as a future energy carrier in the transition of our reliance from the current hydrocarbon economy to a hydrocarbon-renewable hybrid economy.[82] The hydrogen evolution reaction (HER) is the cathodic reaction in electrolysers used to harvest hydrogen and the hydrogen oxidation reaction (HOR) is the anodic reaction on the anode used to consume hydrogen as a fuel in fuel cells. On platinum electrodes both reactions are illustrated as of extremely fast kinetics[83] and almost perfect reversibility.

The HER/HOR in acid solution on Pt*(hkl)* proceeds via a combination of the following elementary reaction steps: the dissociative adsorption of molecular hydrogen without electron transfer (**Equation 1-18**) or with simultaneous electron transfer (**Equation 1-19**) and followed by the discharge of adsorbed hydrogen (H_{ads}) (**Equation 1-20**).[84-87]

Tafel: $2H_{ads} \rightleftarrows H_2$ **Equation 1-18**

Heyrovsky: $H_{ads} + H^+ + e^- \rightleftarrows H_2$ **Equation 1-19**

Volmer: $H^+ + e^- \rightleftarrows H_{ads}$ **Equation 1-20**

The possible HER/HOR mechanisms based on these three elementary reactions are thus the Tafel–Volmer (**Equation 1-18, 20**) or the Heyrovsky-Volmer (**Equation 1-19, 20**) reaction sequence. It is hypothesized that one of the reactions in each of the two reaction sequences are rate-determining steps for the simplest kinetic HER/ HOR mechanism.

In particular, the HER on different metals in alkaline and acidic media is one of the most studied reactions in the field.[85, 88-92]. The HER as a form water splitting has attracted much attention in recent years[50, 82, 93] due to the fact that hydrogen is a promising candidate as an energy carrier for future fuel cells, and the HER can supply hydrogen of high purity. However, large amount of electrical energy is needed to perform these electrochemical processes because of the hydrogen overpotential. An effective electrocatalyst for the electrochemical HER should decrease the overpotential to minimize the electrical energy consumption, and hence increase the efficiency of this significant electrochemical process. Various materials have been studied to make the durable and efficient cathodic catalysts to reduce the overpotential of the HER. [94-104]

The most effective HER electrocatalysts are Pt-group metals.[105-107] However, development of a highly active and more abundant material for HER electrocatalysis still remains a challenge in this field. Palladium is less expensive than platinum, also shows interesting electrocatalytic properties for various oxidation and reduction electrode processes. In this respect, active platinum-group metals catalysts should be used to lower the overpotential to enhance efficiency of catalyst materials.[91, 101, 107] Pt is very expensive and low abundance in the world.[108] Pt and Pd have very similar properties and the cost of palladium is lower than platinum. Therefore, Pd could be a good alternative for Pt as the catalyst in this field. Many studies have been performed to improving the activity of Pd by surface modification and alloying.[95, 97-100, 104, 109]

1.5. Carbon nanostructures as support for electrocatalyst nanoparticle

Catalytic activity of the electrocatalyst can be maximised using a carbon support that contributes to increase the dispersion and utilisation of the active catalyst. The stability of the catalyst can be further enhanced by increasing the interactions between the catalyst and the support to form strongly coupled hybrid materials. Carbon support also provides paths for the flow of electrons in the electrocatalytic system, which is very important for non-precious metal-based electrocatalysts, especially for those with low electrical conductivity.

Conventional Pt electrocatalysts are generally formed and supported on conductive with high surface area amorphous carbon.[110] However, this amorphous carbon support does not have long-range order in the graphitic lattice and may be poorly connected with the NP catalyst, thus leading to high electron transfer resistance and undesired increase in ORR overpotential. As a result, electrocatalyst NP tend to sinter/aggregate causing ORR activity degradation.[15, 111] Moreover, this carbon support suffers from corrosion that aggravates the NP sintering /aggregation issues and further decreases the durability of the catalyst.[112]

Recently, graphene (G) has been widely studied as an alternative support to improve NP catalyst durability and activity owing to its high durability, high conductivity, high surface area and strong interaction only with NP.[113] PtNP-G catalysts were synthesised by chemical reduction of the Pt precursor onto the graphene surface.[114] ORR studies in these composites show that G as a support is able to enhance both Pt stability and activity. A solution-phase self-assembly method was also used to deposit monodispersed preformed Pt alloy NP on graphene after mixing both components under sonication.[115] Undoubtedly, this approach offers significant number of advantages, as NP-G interaction can be better tuned for ORR, taking into account that the surfactant can be easily removed by acid treatment. By using preformed NP in the solution-phase self-assembly method, the composition, size and morphology of the NP supported on graphene can be easily controlled, and thus, the NP activity. On the other hand, as the preformed NP are surrounded by long carbon-chain surfactant molecules, van der Waals forces are responsible for the NP-G formation yielding to composites with uniformly dispersed NP on graphene.

Carbon nanotubes (CNT) as electrocatalyst supports also show exceptional nanoparticles catalyst activity. Power densities higher than the Pt/Vulcan XC 72R-based electrode (435 $mWcm^{-2}$) for the same Pt loadings have been reported for some PtNP-CNT composites.[116] One the major advantages of using these tubular structures as a support material is their electrochemical stability. Nevertheless, CNT have relatively small specific surface area and weak interactions with the supported metal NP that restrict the catalytic activity. The impregnation technique is widely used to form nanoparticles on the surface of CNTs. Taking into account that CNTs are chemically relatively inert, activating their surfaces is an essential precondition for coupling nanoparticles to them. Chemical treatments are used to generate acid groups on CNTs. In a typical process, CNT are functionalised by refluxing in a mixture of nitric and sulphuric acid. This creates defects and chemical groups (e.g. -OH, -COOH) on the surface of the nanotubes with which the Pt catalyst precursor (H_2PtCl_6 or K_2PtCl_4) interacts yielding composites with well dispersed Pt nanoparticle after in-situ reduction (**Figure 1-14**).[117, 118]

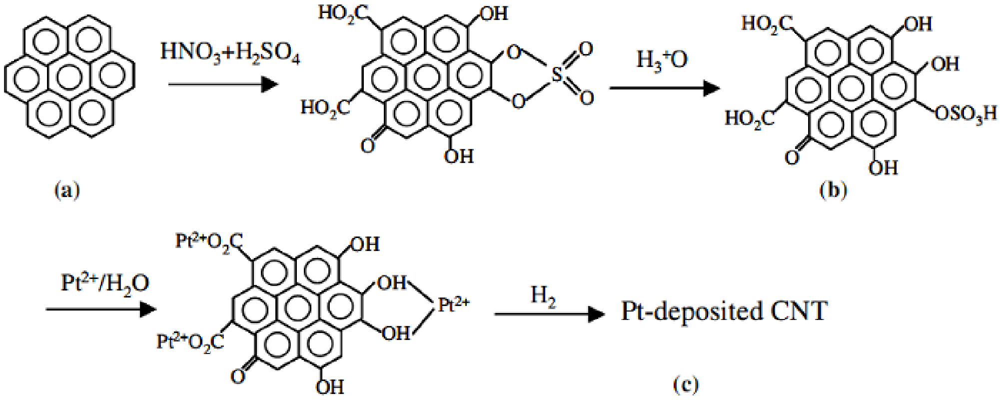

Figure 1-14. Scheme of the mechanism for Pt deposition via the oxidation of CNT.[118]

The in-situ reduction of Pt precursors using the polyol process, in which an ethylene glycol solution is heated to harvest the colloidal particles, has been also applied to decorate CNT with 2-6 nm PtNP (**Figure 1-15**). [116] Interestingly, high-electrocatalytic activity for ORR of these composites with relatively low-Pt-loadings has been reported.[119]

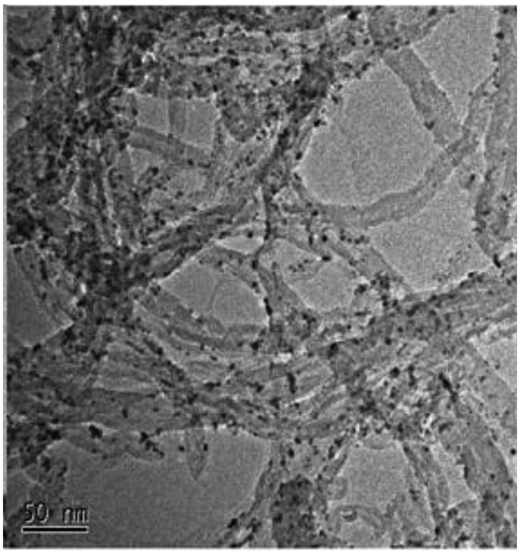

Figure 1-15. HRTEM images of PtNP supported on carbon nanotubes after in-situ reduction.[116]

Carbon nanofibres (CNF) are cylindrical nanostructures with graphene layers arranged as cups, stacked, plates or cones (**Figure 1-16**)[120]. They own chemical and electronic properties similar to CNT. However, CNF possess larger diameters than CNT, up to a couple of hundred nanometres.[121] Interestingly, this type of carbon nanostructures offers the possibility to access both outer and inner carbon surfaces for effective metal deposition and distribution and owing to their low transport resistance.

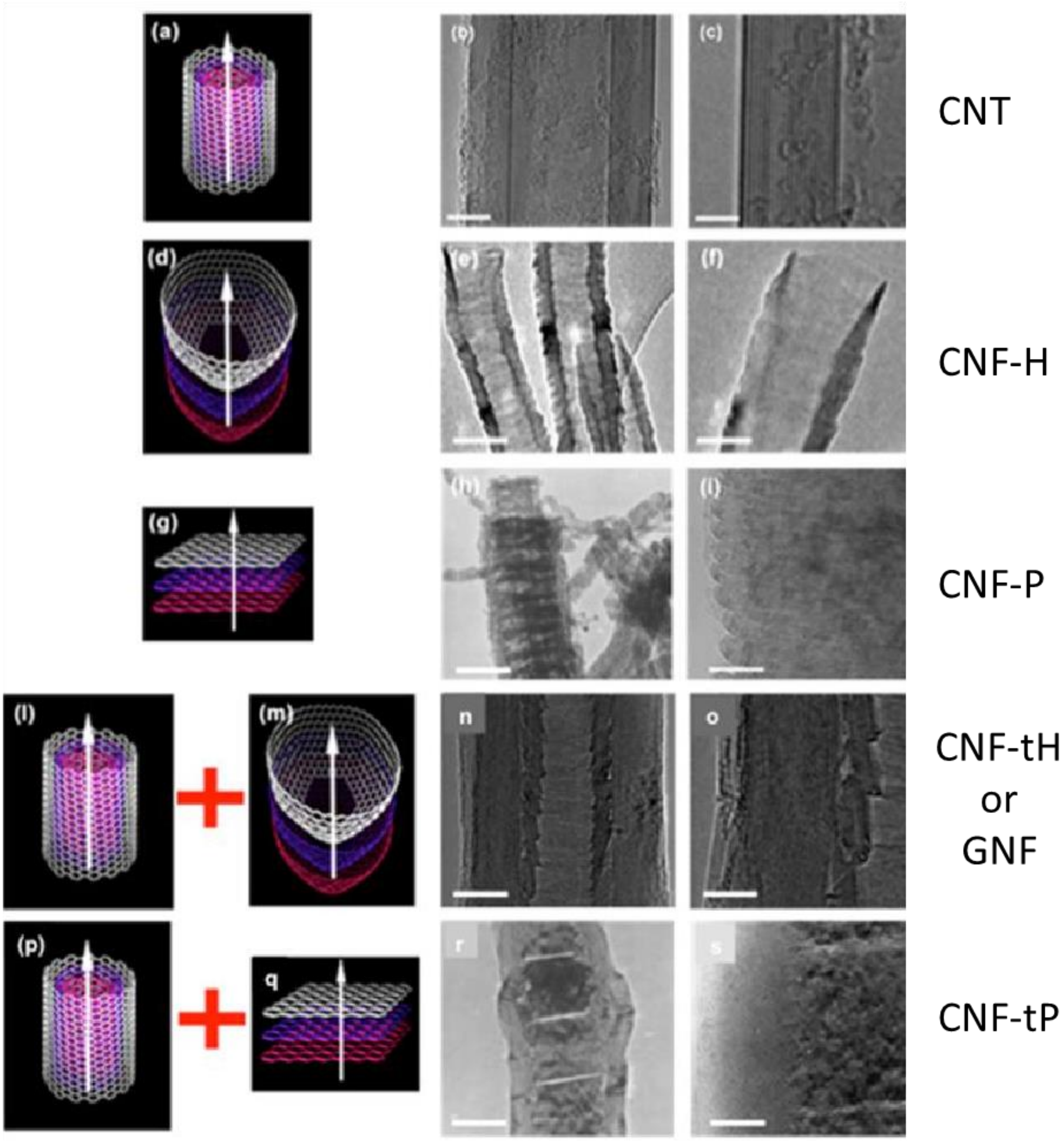

Figure 1-16. Schematic representations and related bright-field transmission electron microscopy (BF-TEM) images of hollow carbon nanostructures. Multi-walled carbon nanotubes (MWNT) (**b, c**), herringbone or cup stacked nanofibers (CNF-H) (**e, f**), stacked nanoplatelet nanofibers (CNF-P) (**h, i**). Nanofibres combined with concentric tube exterior structure and herringbone or cup stacked interior structure (CNF-tH or graphitised carbon nanofiber (GNF)) (**n, o**). Combined nanofibres with concentric tube exterior structure and stacked nanoplatelet interior structure (CNF-tP) (**r, s**). Scale bars are 5 nm (**c, i, o, s**), 10 nm (**b, o**), 50 nm (**f**) and 100 nm (**e, h**).[120]

As a consequence, CNF exhibit high effective surface areas and mesoporous properties. Since Rodriguez et al. reported the use of CNF as a catalyst support for FeCuNP,[122] CNF have been extensively researched as fuel cell supports. 2-4 nm Pt nanoparticles supported on stacked-cup CNF were prepared using the polyol method [116]. An enhancement in the ORR activity of

400% has been observed for PtNP deposited on tubular type CNF compared to commercial Vulcan carbon black.[123] It is believed that this huge enhancement in performance is due to the fact that PtNP adopt particular crystallographic orientations when dispersed in CNF. Recently, using an in-situ reduction of a Pt precursor Singh et al. have demonstrated a highly efficient approach for the excellent deposition and effective distribution of ca. 2 nm PtNP on both sides of carbon nanofibres (**Figure 1-17**).[124]

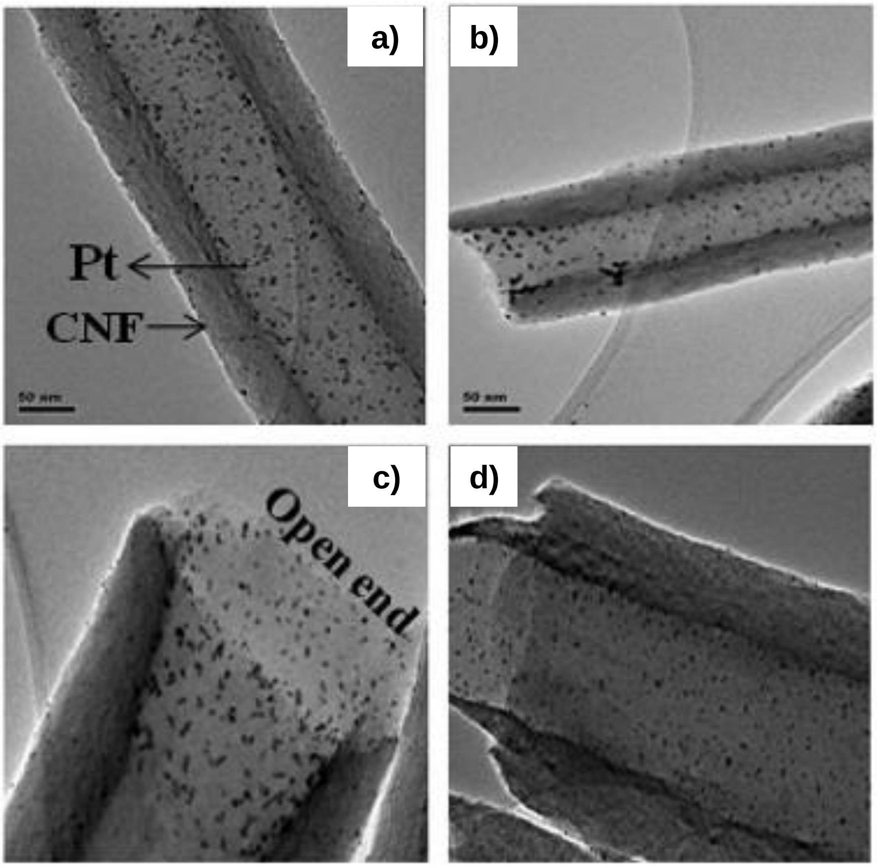

Figure 1-17. HRTEM is illustrating nanoparticle distribution, decoration, open ends of CNF for Pt/fCNF (images **a-d**, scale bar 50 nm).[124]

In this study, acid pre-treated CNF are employed to increase the NP dispersion and enhance their stability. For effective inside CNF decoration, the authors used a mixture of ethylene glycol and water to tune the surface tension and polarity of the media. One of the first examples of preformed NP encapsulated in CNF using impregnation methods was reported by Serp et. al. In this case, CNF exteriors were functionalised to guide NP interaction (**Figure 1-18**). An important drawback of this approach was that PtRuNP confined in the functionalised CNF underwent Ostwald ripening and consequently agglomeration at room temperature thus significantly reducing their surface area.[125]

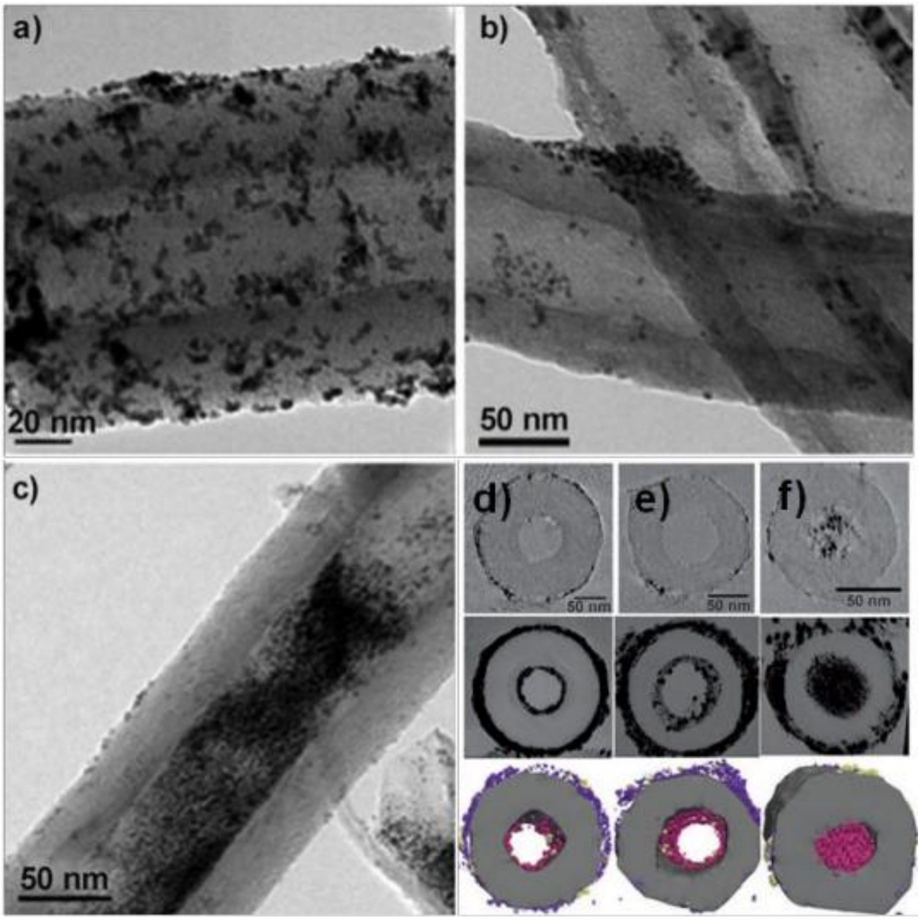

Figure 1-18. BF-TEM images of RuPtNP and CNFs. PtNP deposited on CNF-H (**a**). PtNP deposited and encapsulated on / into CNF-P (**b**). PtNP encapsulated into CNF-tH (**c**) and the isosurface of PtNP-CNF-tH (**d-f**).[125]

1.6. Aim and objectives

The constraint due to both the scarcity and high cost of the precious metals are factors that cannot be ignored. Although lower costs materials have been extensively investigated as electrocatalysts for fuel cell applications, most of them still underperform with respect to platinum-based materials that show high activities and stabilities.[3] Thus, strategies to develop new hybrid materials and/or improve the electrocatalytic activity and durability of existing materials are highly needed.

The aim is to reduce costs by reducing cathode loadings to <0.1 mg Pt/cm^2 without loss of performance or durability. Current US Department of Energy (DOE) 2017 target for electrocatalyst aims for to reduce total Pt content (anode + cathode) to a loading of 0.125 mg/cm^2 on membrane exchange assemblies able to produce rated stack power densities of 8.0 kW/g. Durability is also one of the main issues in fuel cells, as the cathode reaching potentials above the onset of oxidation of carbon in contact with platinum shows serious degradation. The electrocatalyst is subjected to coalescence, poisoning and dissolution under these conditions, thus decreasing both the catalytic efficiency and the active catalyst surface area, which leads to an undesired increase in overpotentials.[21] Current Pt electrocatalysts providing high fuel cell performance is far less than the 5000 hours set as the year 2017 target by the US Department of Energy (DoE).[21]

So far, some of the countermeasures being developed to overcome durability problems in fuel cells are the use of more stable graphitised carbon materials, using catalyst supports that will not electrochemically corrode, and adding oxygen evolution catalysts to the mix to clamp the potentials at the start of water oxidation. In this context, graphitised hollow CNF as support materials have the potential to improve the lifetime of the Pt-based catalyst owing to their corrugated internal and external surfaces. In this work, we will focus our studies in CNF with corrugated interior only, which may provide a mechanism for controlling position of NP and their growth properties in combination with confinement effects. We anticipate that the internal surface of cylindrical CNF with more exposed edge graphene step edges along the surface can be effectively exploited as potential sites for chemical/physical interactions with metal nanoparticles. These anchoring points will contribute to enhance the durability and chemical stability of the catalyst to resist corrosion as well as to mitigate Ostwald ripening and leaching Pt during fuel cell processes. In principle, no functionalization of the carbon support is required to afford intimate interactions with support enhancing NP dispersitivity, which will preserve CNF electrical conductivity required for electrocatalysis.

The insertion of nanoparticles into one-dimensional hollow tubular carbon nanostructures(CN) has been achieved mainly through the capillary filling of a molten metal salt followed by pyrolysis of the encapsulated material.[126] or the sublimation of a metal precursor.[127] The main disadvantage of these approaches is a lack of control over the morphology, size and composition of the NP formed inside hollow CN, which as we know can have very significant implications for Pt-based electrocatalyst. Previous studies in my group show that it is possible to not only encapsulate preformed NP with specific composition, size, and shape but also to take advantage of the corrugated interiors of CNF for controlling the assembly of these nanoparticles, and therefore, their properties.[128, 129] However, none of the previous works dealing with the insertion of preformed NP into hollow tubular carbon nanostructures study energy-related electrochemical conversions in these types of composites. We firmly believe that these hybrid metal-carbon nanostructures may present new opportunities for the development of ORR/OER and HOR/HER electrocatalysts meeting the requirements of durability, activity and low cost for large-scale electrochemical applications.

The main aim of this study is to develop new hybrid metal-carbon nanostructures as efficient electrocatalyst materials for hydrogen fuel cell and water splitting applications with enhance performance and/or durability.

The key objective of this study is to prove whether the corrugated interiors of CNF can serve as anchoring points to stabilise the electrocatalytic PtNP to avoid ripening and aggregation.

To test our hypothesis, we selected graphitised carbon nanofibres (average external diameter for PR24-GNF is 96 ± 32 nm and for PR19-GNF is 115 ± 37 nm)[130] that possess graphene layers which produce long herringbone stacks of truncated graphitic cones at an angle (**Figure 1-16m-o**). The stacked-cone structure of the GNF is obvious, with the projection of their sidewalls in TEM clearly showing graphitic planes oriented at an angle of ~ 30 degree relative to the main GNF (**Figure 1-19**). Very faint lines, spaced at ~ 13 - 15 nm, detected to intersect with the internal surface of these nanofibres coincide with the edges of the graphitic cones. Each line seems to be formed by a stack of few rolled-up sheets of graphene creating a step-edge of 3.3±0.2 nm in height (**Figure 1-19**), which could play a role in the nanoparticle assembly.

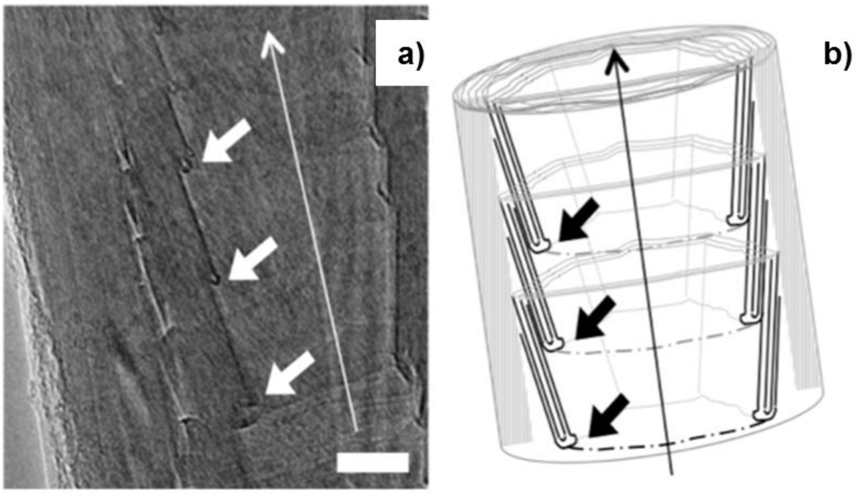

Figure 1-19. TEM images of host GNF (**a**) showing its internal structure and (**b**) schematic representation of the herringbone GNF, scale bar is 10 nm. The long arrows indicate the main growth axes of the nanofibre. The short arrows point to the internal step-edges of the GNF.[131]

Preformed PtNP with sizes commensurate with the height of the step-edge will be synthesised for the encapsulation into GNF by solution-phase self-assembled techniques leading to PtNP@GNF (PtNP encapsulated into GNF) with most of the NP within the internal cavity of the GNF. By shortening GNF, we are hoping to reduce transport resistance of NP into GNF cavity and facilitate oxygen diffusion during ORR. Electrocatalytic performance of

PtNP@GNF with long and short GNF will be evaluated. To understand confinement effects on the electrochemical activity of these composites, PtNP will be deposited outside and inside GNF. Moreover, the effect of oxidative functionalisation of the GNF on the electrochemical response of the composite material will be examined. To further understand step-edge and nanoparticles interactions and their effects on the electrocatalytic performance, PtNP@GNF composites will be prepared using in-situ reduction methods: (**i**) chemical reduction of a Pt complex after impregnation in GNF and (**ii**) sublimation of a metal precursor into GNF followed by pyrolysis of the encapsulated material. The electrocatalytic performance and durability tests (by continuously applying linear potential sweeps up to 50,000 cycles) in the ORR of the prepared hybrid nanostructures will be analysed in detail using different electrochemical techniques. Parameters such as specific activity, mass activity and electrochemical surface area (ECSA) will be carefully evaluated. Structures of PtNP@GNF will be determined using transmission electron microscopy, and correlated with their electrocatalytic properties.

In addition, we will study the electrocatalytic performance of a bifunctional electrocatalyst including (**i**) preformed and (**ii**) in-situ synthesised Mn_3O_4NP encapsulated into GNF (Mn_3O_4NP@GNF) and compare its performance towards ORR and OER with Mn_3O_4NP supported on surface of different carbon nanostructures such as GNF, graphene, CNT, amorphous carbon (carbon black). It is proposed to use the stabilizing effects of GNF corrugated interiors composed of rolled-up graphene sheets (nanocones) (**Figure 1-19**) to improve durability of Mn_3O_4NP which are known to be highly labile in conditions.[132] As the key objective of this study, the electrocatalytic activity for the ORR and the OER of new hybrid electrocatalysts will be evaluated and compared with Pt/C for the ORR and Ir/C commercial electrocatalyst for OER. To understand confinement effects on the electrochemical activity of these electrocatalysts, Mn_3O_4NP are deposited external and internal GNF. Further objective is to prove whether the corrugated interiors of GNF can serve as anchoring points to stabilise the Mn_3O_4 NP to avoid ripening and aggregation. Therefore, durability of the Mn_3O_4NP@GNF electrocatalysts will be assessed in a durability test by continuously applying linear potential sweeps up to 5000 cycles.

Finally, we will study the PdS_2-CN hybrid nanostructures as active electrocatalyst for HER in the electrolysis reaction and also HOR in the fuel cell anode reaction. The PdS_2-CN nanostructures will be tested for HER/HOR as a bifunctional electrocatalyst. In addition, our hypothesis that GNF step-edges play an important role in stabilising catalytic centres may give an opportunity to improve the electrocatalyst durability in HER using the same principles as described above for the ORR and OER. One of objective of this study is to investigate properties of PdS_2NP@GNF and to evaluate the effects of nanoscale confinement by comparing catalytic activity of it with PdS_2NP on amorphous carbon and graphene. Another objective of this work is to assess durability of the PdS_2NP@GNF electrocatalysts in an accelerated durability test by continuously applying linear potential sweeps up to 5000 cycles. Commercial Pd/C and Pt/C will be utilized as benchmark electrocatalysts.

Chapter 2. Hybrid platinum nanoparticles-graphitised nanofiber as electrocatalyst materials for ORR

2.1. Introduction

Fuel-cell technology is a very promising alternative for clean and renewable source of energy.[133-137] However, the instability of precious platinum nanoparticles (PtNP), frequently used as electrocatalyst in polymer electrolyte fuel cells, due to migration and agglomeration of nanoparticles during fuel cell operations is currently a significant drawback for the widespread commercialisation of this technology. There is an urgent demand for developing new Pt-based electrocatalyst materials combining high activity with superior durability to retain their structure and properties in the harsh electrochemical conditions.

The conventional state-of-the-art electrocatalysts typically consist of PtNP (diameters of 2–5 nm) on conductive carbon supports with high surface area, such as carbon black (C), especially Vulcan XC-72R.[11] However, this kind of carbon support is thermochemically unstable and suffers from corrosion caused by electrochemical oxidation under fuel cell operating conditions.[136] As a result, catalyst nanoparticles tend to aggregate and sinter, which in turn leads to a decrease of the electrochemical surface area and activity of the electrocatalysts, affecting the catalyst durability and reliability.[138, 139] More stable graphitised carbon materials such as graphene and carbon nanotubes have been proposed to overcome the durability problems.[140-142] Although an improved catalytic activity has been reported for these electrocatalyst materials, there are still outstanding problems related to the poor catalyst dispersion on the carbon nanotubes surface and the restacking of graphene limiting the mass transport of reactants and products.[143]

Graphitised hollow carbon nanofibres (GNF) are an ideal low cost alternative for electrocatalayst mass production for low temperature fuel cells, as they exhibit a good resistance to electronic and electrochemical oxidations similar to carbon nanotubes.[120, 123, 144, 145] However, these one-dimensional nanostructures have larger diameters, up to two of hundred nanometers, offering the possibility to access both inner and outer carbon surface for effective deposition of PtNP while also enabling low mass transport resistance to fuels and products in the fuel cell electrodes.[146-149] Unlike multi-walled carbon nanotubes that consist of a set of concentric nanotubes with smooth surface, GNF exhibit corrugated interior surfaces defined by internal stacked-nanocone structures, with a typical step-edge comprising rolled-up several graphene sheets being *ca.* 3 nm high (**Figure 2-1**).

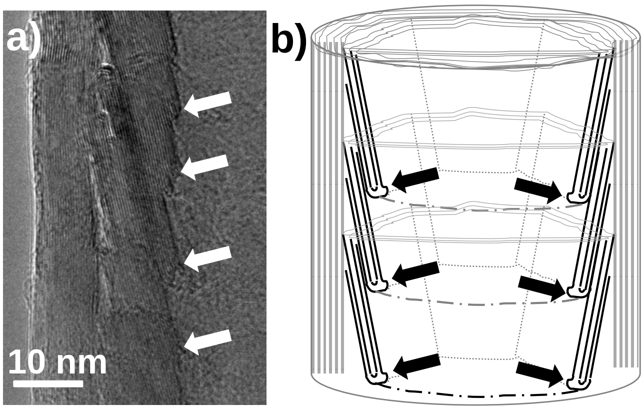

Figure 2-1. (**a**) HRTEM image (**b**) schematic representation of the herringbone GNF step-edges.

Recent studies in our group have shown that the GNF corrugated surfaces can provide a mechanism for controlling position of NP and their growth.[129, 131, 150] For example, very small metal NP (*ca.* 2 nm) adsorbed on the atomically smooth graphitic surfaces of the GNF exterior grow to *ca.* 13 nm and beyond, whilst the same metal NP adsorbed on the interior surfaces of GNF grow to the same maximum size of *ca.* 6 nm, regardless of the stimulus for their growth, which is explained by the GNF interior step-edges imposing significant barriers for the migration of the metal nanoparticles, thus precluding their growth by coalescence mechanisms. Moreover, the size of the growing metal NP at GNF internal step-edges may also be influenced by electrostatic interactions arising from charge transfer between the adsorbed NP and the nanocone graphene stacks.[151] The different external and internal surface morphologies of GNF provide a unique environment for studying the effect of the electrostatic interactions and structural factors on the electrocatalyst performance.

In previous studies,[129, 131, 146-152] the exposed graphene edges along the axis of non-graphitised carbon nanofibers have been utilised for the stabilisation of the catalyst nanoparticles, however it is known that the carbon corrosion is initiated readily at such defect sites due to the high concentration of dangling bonds. In contrast, we propose to harness the stabilising effects of GNF corrugated interiors composed of rolled-up graphene sheets (nanocones), that have no dangling bonds, to improve the electrochemical durability of PtNP in the oxygen reduction reaction (ORR) that takes place at the fuel cell cathode in which PtNP are known to be highly labile.

2.2. Aim, objectives and scope of experiments

The main aim of this chapter is to develop new highly stable hybrid metal-carbon nanostructures as efficient electrocatalyst materials for hydrogen fuel cell applications. We propose to use the stabilising effects of GNF corrugated interiors composed of rolled-up graphene sheets (nanocones) to improve durability of PtNP which are known to be highly labile during the oxygen reduction reaction (ORR) at the fuel cell cathode.

The key objective of this chapter is to prove whether the corrugated interiors of GNF can serve as anchoring points to stabilise the electrocatalytic PtNP to avoid ripening and aggregation. Preformed PtNP with sizes commensurate with the height of the step-edge is synthesised for the encapsulation into GNF by solution-phase self-assembled techniques leading to PtNP@GNF with most of the NP within the internal cavity of the GNF. By shortening GNF (S-GNF), we are hoping to reduce transport resistance of NP into GNF cavity and facilitate oxygen diffusion during ORR. Electrocatalytic performance of PtNP into long (PtNP@GNF) and short nanofibers (PtNP@S-GNF) is evaluated. To understand confinement effects on the electrochemical activity of these composites, PtNP are deposited external and internal GNF. Moreover, the effect of oxidative functionalisation of the GNF on the electrochemical response of the composite material is examined.

In this study, we demonstrate that the insertion of pre-formed PtNP into the internal cavities of GNF (PtNP@GNF), using solution-phase assembly techniques followed by heat treatment to improve the PtNP-GNF contact by removing the surfactant molecules from surface of nanoparticles, is a highly effective and facile approach for creating a highly durable ORR electrocatalyst which retains activity up to 50,000 cycles, thus outperforming commercial Pt electrocatalyst (Pt/C) and other known electroctalysts based on PtNP. The insertion of PtNP within GNF ensures that at potentials relevant to fuel cell cathodes, reduction of O_2 proceeds exclusively *via* a four-electron pathway. In order to understand physicochemical reasons for the enhanced durability of PtNP@GNF, the catalyst was compared with PtNP adsorbed on surface of GNF (PtNP/GNF) and with platinum deposited into GNF cavity in a form of Pt-compounds (Pt@GNF) rather than pre-formed PtNP. To evaluate the role of the carbon support, further comparative study was carried out for pre-formed PtNP deposited on carbon black (Vulcan XC-72R). In all cases, PtNP@GNF has shown to perform better than the control samples. Detailed transmission electron microscopy (TEM) imaging reveals anchoring of PtNP to the GNF step-edges, which enables control of nanoparticle size, distribution and prevents nanoparticle coalescence and ripening during the electrochemical reactions as the key mechanism underpinning the remarkable durability of the electrocatalyst.

2.3. Experimental Section

2.3.1. Chemicals

1-octadecene (90%), oleylamine (>70%), oleic acid (90%), platinum (II) acetylacetonate, hexachloroplatinic acid ($H_2PtCl_6.6H_2O$), ethylene glycol, nitric acid, isopropyl alcohol, hexane, Nafion® (5% solution in a mixture of lower aliphatic alcohols and water) were used as received from Sigma Aldrich. Graphitised nanofibers (GNF) were supplied by Pyrograf® Products Inc. and the Pt/C commercial catlayst (20 wt%, HiSPECTM 3000) was supplied by Johson Matthey. Ultra-pure water purified with Millipore Advantage A10 water equipment (resistivity 18.2 MΩ•cm at 25 ˚C) was used in all experiments.

2.3.2. Synthesis of preformed nanoparticles

2.3.2.1. Synthesis of oleylamine and oleic acid-stabilized preformed PtNP

PtNP were synthesised from platinum (II) acetylacetonate using the method previously reported by Wang C.et al.[153]. The synthesis was performed using standard air free techniques and commercially available reagents: 1-octadecene (90%), oleylamine (>70%), oleic acid (90%), and iron pentacarbonyl ($Fe(CO)_5$) and platinum (II) acetylacetonate.

Under a nitrogen flow, $Pt(acac)_2$ (50mg) was mixed with of 1-octadecene (2.5 mL) (ODE), oleic acid (1 mL) and oleylamine (0.25mL). The formed solution was slowly heated to 120°C over 20 min. After 30 min of heating at 120°C, under a blanket of nitrogen, one drop (0.01 ~ 0.03 ml) of $Fe(CO)_5$ solution (prepared by mixing $Fe(CO)_5$ (0.1 mL) with ODE (1 mL)) was added to this solution. The temperature was increased up to 200 °C (heat rate = 3-5°C/min) and left at this temperature for 30 min. The solution was cooled down to room temperature then isopropanol (80 mL) was added and the product was separated by centrifugation (8000 rpm for 30 min). The final product (~ 25 mg) was dispersed in 5 ml of hexane for further use. High resolution transmission electron microscope (HRTEM) (average particle size (APS) / nm: 3 ± 0.6), Energy dispersive X-ray (EDX), X-ray diffractometry (APS/nm: 3.1) and thermogravimetric analysis (TGA), and cyclic voltammetry (CV) measurement were performed for this PtNP.

2.3.2.2. Synthesis of alkylthiol-stabilised AgNP

Dodecanethiol (0.1 mL) was added drop wise to a solution of silver nitrate (153 mg) in ethanol (30 mL) and the mixture was stirred vigorously for 10 min. A saturated solution of sodium borohydride (2.5 g) in ethanol (60 mL) was then added and the mixture stirred vigorously for 2 hr at room temperature. The product was precipitated from solution by the further addition of ethanol (300 mL) before storing at -20˚C for 24 hr. The precipitate was then filtered using a 0.45 μm pore size polytetrafluoroethylene (PTFE) membrane filter and washed with ethanol (200 mL) and acetone (200mL) before final drying under vacuum to yield a black solid (~150 mg of AgNP). HRTEM (average particle size (APS) / nm: 9.8 ± 1.2) and XRD analysis were performed for this AgNP.

2.3.3. The preparation of hollow carbon nanostructures

2.3.3.1. Preparation of shortened graphitised nanofibers (S-GNF) via ball milling

50 mg of GNF as received with a length of 10-100 μm were mechanically ground in an ambient atmosphere using a Retsch MM 400 ball mill instrument, containing a steel ball with a diameter of 10 mm. The rolling speed of the milling machine is fixed at 10 Hz for 3 hours to obtain the desired S-GNF (average length: 0.2-20 μm) (**Figure 2-6**).

2.3.3.2. Preparation of shortened graphitised nanofibers (S-GNF) via oxidative cutting with AgNP

The former approach involves first the acid treatment of GNF (25 mg) by refluxing for 24 hours at 110 ˚C in concentrated nitric acid to yield Ox-GNF (20 mg), then followed by the decoration of Ox-GNF (20mg) with AgNP (20 mg), and finally, the oxidative cutting of the Ox-GNF at 440 ˚C in air until have a weight loss of 50% was obtained using deposited AgNP as catalyst.

2.3.3.3. Preparation of oxidized shortened nanofibres (Ox-S-GNF)

Ox-S-GNF (50mg) were obtained by refluxing the produced S-GNF at 110 ˚C in 60 ml concentrated nitric acid for 24 hours. Water was added to the mixture after cooling down the reaction, and then filtered through PTFE membrane (pore size 0.45 µm). The obtained Ox-S-GNF (40mg) were washed with distilled water to remove the excess of acid until reaching a neutral pH and dried in the oven at 125 ˚C for 90 min and stored in a desiccator.

2.3.3.4. Preparation of shortened and open arc discharge (AD) multi-walled carbon nanotubes (S-MWNT) with ball milling

100 mg of AD-MWNT (MER Corporation) as received with a length of 1-5 µm were mechanically ground in an ambient atmosphere using a Retsch MM-400 ball mill instrument, containing a steel ball with a diameter of 10 mm. The rolling speed of the milling machine is fixed at 10 Hz for 3 hours to obtain the desired S-MWNT (0.03-1 µm length).

2.3.3.5. Preparation of opened end of SWNT via heating in air

In order to open the ends of the SWNT, which are initially sealed by fullerene like end cap, the nanotubes (50 mg) were placed in a ceramic crucible then were heated in air for 30 minutes at 370 ^{0}C in a tube furnace until a weight loss of 20% was observed[154]. The product (~40 mg) was then placed in a glass vial to use.

2.3.3.6. Preparing hybrid materials obtained using the preformed PtNP with ex-situ approach

- Preparation of PtNP@S-GNF hybrid material via insertion of PtNP into S-GNF

10 mg of freshly heated S-GNFs in air at 450 ˚C during 20 min were added under argon into a hexane suspension of PtNP obtained from platinum (II) acetylacetonate using a modified method previously reported in the literature by Wang C. et al.[155] with a 1:1 (PtNP:S-GNF) mass ratio. After stirring the mixture for 3 hours, the hexane was gradually removed to concentrate the solution and finally dried. A small amount of hexane was then added to re-dissolve any non-encapsulated PtNP, and the mixture was stirred again for 3 hours and dried. The process was repeated for three times to ensure that the majority of PtNP were transport inside S-GNF. The mixture was then sonicated in hexane (sonic probe diameter 3 mm, 20 kHz) for 30 min to removed non-encapsulated PtNP, filtered through a PTFE membrane (pore size 0.45 µm) and washed with hexane, methanol and finally acetone to yield a black solid product (~8 mg). HRTEM, EDX (**Figure A- 1**), and thermogravimetric analysis (TGA) (**Figure A- 2**), and cyclic voltammetry (CV) (**Figure 2-15**) measurement were performed for this material.

- The removal of non-encapsulated nanoparticles

Our previous study,[129] it was found that non-encapsulated nanoparticles could be removed successfully from the external surface of GNF by an ultrasound treatment. Therefore, PtNP@S-GNF (10 mg) composite material was sonicated in hexane (sonic probe diameter 3 mm, 20 kHz) for 30 min to remove non-encapsulated PtNP.

- Preparation of PtNP/GNF, PtNP/S-GNF, PtNP/Ox-S-GNF and PtNP/C Hybrid Materials

2 mg PtNP was mixed with the selected carbon support GNF (8 mg), S-GNF (8 mg), Ox-GNF (8 mg) or carbon black (Vulcan XC-72R) (8mg) in 50 ml of hexane and gently sonicated in a sonic bath for 30 min. The mixture was filtered through a PTFE membrane (pore size 0.45 µm), washed with hexane, methanol and finally acetone to yield the desired black solid product (PtNP/GNF, PtNP/S-GNF, PtNP/Ox-S-GNF or PtNP/C).

- Remove surfactant of PtNP

We tested a thermal procedure for the removal of the surfactant molecules from the encapsulated PtNP by heating PtNP@S-GNF (10mg) in air at 175 ˚C for 5 h, which enables the removal of the organic surfactant as confirmed by TGA.

2.3.3.7. Preparing hybrid materials obtained using the in-situ reduction of PtNP

- Preparation of Pt_1@S-GNF hybrid material

Freshly dried 10 mg of Ox-S-GNF were added to a solution of potassium hexachloro-platinic acid ($H_2PtCl_6.6\ H_2O$) (1.4 mg) in water (5 ml) and stirred for 3 hours under argon. The mixture was dried to ensure all solvent was removed, and then water was added to re-dissolve any potassium hexachloro-platinic acid outside Ox-S-GNF. The mixture was stirred again and then the process was repeated three times during the experiment in order to ensure a capillarity filling of Ox-S-GNF then the product material was filtered through PTFE membrane. 8 mg of this black solid were suspended by sonication for 10 minutes in 25 ml ethylene glycol:water (85:15 ratio) and the pH adjusted to 13 with a NaOH solution. The solution was then heated under continuous stirring in an oil bath at 120 ˚C to reduce Pt and the obtained material (~5.6 mg) was filtered through a PTFE membrane.

- Preparation of Pt_1/C hybrid material

For synthesis Pt_1/C hybrid material, similarly 10 mg of carbon black were suspended by sonication for 10 minutes in 25 ml ethylene glycol:water (85:15 ratio) and then were added to a solution of potassium hexachloro-platinic acid ($H_2PtCl_6.6\ H_2O$) (1.4 mg) in water and the pH adjusted to 13 with a NaOH solution. The solution was then heated under continuous stirring in an oil bath at 120 ˚C to reduce Pt and the obtained material (~ 8.5 mg) was filtered through a PTFE membrane.

2.3.3.8. Preparing hybrid materials obtained the in-situ formation by decomposition of a volatile complex

- Preparation of Pt_2@S-GNF, Pt_2@MWNT and Pt_2@SWNT Hybrid Material

Pt(II)(acac)$_2$ readily sublimes at elevated temperature and can therefore be inserted into SWNT, S-MWNT and S-GNF from the gas phase. Molecules of the platinum complex can diffuse into the carbon support through their termini.

- Preparation of Pt_2@S-GNF hybrid material

5 mg of S-GNF and 1 mg of $Pt(acac)_2$ were introduced within a pyrex reaction tube in which a high vacuum was then applied using a turbo pump, and the sample was then sealed and heated for 3 days at 150 ˚C. The formation of crystals on the top of the pyrex tube during the heating process confirms that platinum containing molecules had entered the gas phase.

During heating crystals were observed to have condensed on the top of the pyrex tube which was taken as confirmation that the platinum containing molecules had entered the gas phase. Periodically the reaction tube was turned over in the oven to mix the SWNT and the crystallized molecules and this process was repeated several times over the 3 days experiment. The mixture was stirred and then the THF removed three times during 3 days in order to ensure that the majority of the molecules were transported inside of the NT. Finally, all of the Pt materials from outside of the MWNT, THF was removed to give dry samples.

- Preparation Pt_2@MWNT hybrid material

AD-MWNT were shortened and opened by ball milling at 10Hz for 3 hours, then the MWNT heated in air for 30 minutes at 800˚C to open end of MWNT. Freshly opened and shortened MWNT was introduced within a pyrex reaction tube and along with a two-fold excess of the platinum metal complex by weight and both materials were mixed together. High vacuum was then applied using a turbo pump and the sample was sealed and then heated for 3 days at 150^0C. Upon heating under reduced pressure, the platinum molecules enter the gas phase and diffuse into the MWNT through their open ends. The mixture was stirred and then the THF removed three times during 3 days in order to ensure that the majority of the molecules were transported inside of the NT. Finally, all of the Pt materials from outside of the MWNT, THF was removed to give dry samples.

- Preparation of Pt_2@SWNT hybrid material

In order to open the ends of the SWNTs, which are initially sealed by fullerene like end cap, the nanotubes were heated in air for 30 minutes at 370 ^{0}C in a tube furnace until a weight loss of 20% was observed[154]. Freshly opened and shortened SWNT was introduced within a pyrex reaction tube and along with a two-fold excess of the platinum metal complex by weight and both materials were mixed together. High vacuum was then applied using a turbo pump and the sample was sealed and then heated for 3 days at 150 ^{0}C. Upon heating under reduced pressure, the platinum molecules enter the gas phase and diffuse into the SWNT through their open ends. The mixture was stirred and then the THF removed three times during 3 days in order to ensure that the majority of the molecules were transported inside of the NT. Finally, all of the Pt materials from outside of the SWNT, THF was removed to give dry samples.

2.3.4. Material Characterisation

XRD patterns were obtained on a Bruker AXS D8-Advanced diffractometer with Cu Kα radiation (λ=1.5418 Å). Samples for TEM analysis were prepared dispersing the material either in hexane or HPLC grade iso-propanol by ultasonication, and then drop casting the solution onto lacey carbon film coated copper grid. The samples were dried under nitrogen gas flow for 3 minutes to remove any residual solvent. HRTEM image was obtained on a JEOL 2010F TEM using accelerating voltage of 200 kV and 100 kV. EDX analysis is the standard method for the local identification of elements within a sample in a scanning electron microscope (SEM) or TEM. In this study, EDX analysis was performed using Oxford Link Isis package on a JEOL2100F TEM operated at 200 kV and 100kV. This provided quantitative elemental compositions for the individual nanoparticles and the electrocatalysis hybrid materials.

TGA measures the amount and rate of change in the weight of a material as a function of the temperature or time in a controlled atmosphere. Measurements are used primarily to determine the composition of materials and to predict their thermal stability at temperature up to 1000 ºC. The technique can characterise materials that exhibit weight loss or gain loss due to decomposition, oxidation, or dehydration TGA analyses were performed in a TA/TGA Q500 instrument over the range 25 - 1000 ºC in air and nitrogen, at a scan rate of 5 ºC min^{-1}.

2.3.5. Electrochemical Measurements

The three-electrode cell used for cyclic voltammetry (CV) measurements and rotating disk electrode (RDE) measurement, and the four-electrode cell used for rotating ring disk electrode (RRDE) measurement. In the study of the oxygen reduction reaction, the cathodic reaction must be the rate determining reaction. At the counter electrode (the anode) water was oxidized to oxygen and protons. The area of the counter electrode was larger than that of the cathode to ensure that the anode reaction was not limiting.

The electrochemical experiments were performed on an electrochemical work station CH instruments Inc. 700D and Autolab potentiostat PGSTAT204 using a glassy carbon electrode (GCE) as working electrode in a commercial (Pine Instruments) GCE disk electrode, a Ag/AgCl (IJ Cambria Scientific Ltd.) and a HydroFlex reversible hydrogen electrode (RHE) electrodes as reference electrodes, respectively. The GCE was cleaned with 0.05μm principal particle size alumina powder solution (Agar Scientific Ltd.) on a polishing paper to remove any impurity which may affect electrochemical measurements. The investigated samples were dropped onto the GCE as ink with an optimised constant metal loading of 100 $\mu g/cm^2$ and then dried in air.[156, 157] The potential was cycled at fast scan rates (500 or 200 mV/s) for up to 100 cycles before readings were taken in order to remove any impurities and unwanted species from the surface of the platinum electrodes. Impedance measurements, the cell resistance was measured immediately after OER and ORR measurements taking the ac impedance spectra from 32 to 0.1 kHz and a voltage perturbation of 10 mV. The real part of the resistance at 1 kHz was taken as the cell resistance and was used to obtain the IR-free potential of the working electrode.

The cyclic voltammetry is used to distinguish catalytic activity of fuel cell by measuring a real active surface area via determining current-voltage curve. The electrochemically active surface area of the electrocatalysts was determined by the cyclic voltammetry. Cyclic voltammetry measurements were performed in nitrogen saturated 0.1 M $HClO_4$ at scan rates of 50 mV/s between 0.05 V and 1.05 V.

For the rotating disk electrode (RDE) measurements[158] for ORR the working electrode was scanned cathodically at a rate of 5 mVs^{-1} with varying rotating speed from 400 rpm to 2000 rpm. Koutecký–Levich plots (J_k^{-1}vs. $\omega^{-1/2}$) were analysed at various electrode potentials and the slopes of their best linear fit lines were used to calculate the number of electrons transfer on the basis of the Koutecký-Levich equation:

$$1/J= 1/J_d + 1/J_k \qquad \textbf{Equation 2-1}$$

where J_d is given by Levich Equation:

$$J_d = 0.620nFD_o^{2/3} v^{-1/6} C_o \omega^{1/2} \qquad \textbf{Equation 2-2}$$

where j is the measured current density, J_k and J_d are the kinetic- and diffusion limiting current densities, ω is the angular velocity, n is transferred electron number, F is the Faraday constant,

C_o is the bulk concentration of O_2, v is the kinematic viscosity of the electrolyte, and k is the electron-transfer rate constant. For the Tafel plot, the kinetic current was calculated from the mass-transport correction of RDE by:

$J_k = (J \text{ x } J_d) / (J_d - J)$ **Equation 2-3**

The number of electrons transferred, n, can be quantified from the disc (I_{disc})and ring currents (I_{ring}) using this equation:

$$n = \frac{4I_{disc}}{I_{disc} + (I_{ring}/N)}$$ **Equation 2-4**

The specific activity of a catalyst was determined by normalising the i_k with its real surface area (A_{real}) and the mass activity of the catalyst was obtained by normalising the i_k with the catalyst loading.

For the ORR experiments, the Pt ring electrode as second working electrode was potentiostated at 1.2 V versus the reversible hydrogen electrode (RHE) where the detection of peroxide is diffusion limited. Electrochemical durability tests were carried out by continuously applying linear potential sweeps with a scan rate of 100 mV/s from 0.6 to 1.1 V vs RHE, which caused surface oxidation/reduction cycles of Pt.[159] For comparison, a Pt/C catalyst with the same Pt loading as that in the electrocatalysts were subjected to the same potential cycling conditions. ECSA values in m^2/g_{Pt} were calculated from the electrochemical surface area of platinum (A_{ec}), the platinum loading (W) and the geometric surface area of the electrode (A_{geo}) using the following expression: ECSA (m^2/g_{Pt}) = A_{ec} (m^2)/ (W (g_{Pt}/ m^2) $*$ $\square_{geo}$ (m^2)). The electrochemical surface area of platinum (A_{ec}) was in turn calculated by dividing the total charge of the hydrogen desorption (QH_{des}) in µC by a known value for the amount of charge transferred during desorption of a monolayer of hydrogen from Pt (210 μC/m^2). The hydrogen desorption peak in the cyclic voltammogram is integrated to obtain the QH_{des} value.

Impedance measurements, the cell resistance was measured immediately after RDE measurements using Autolab potentiostat PGSTAT204 taking the ac impedance spectra from 32 to 0.1 kHz and a voltage perturbation of 10 mV. The real part of the resistance at 1 kHz was taken as the cell resistance and was used to obtain the IR-free potential of the working electrode.

2.4. Results and Discussion

2.4.1. Study of the composite materials for ORR obtained using the preformed PtNP encapsulation into GNF with ex-situ approach

2.4.1.1. Synthesis of preformed PtNP and structural characterisation

PtNP have been synthesised using a well-established protocol based on the reduction of platinum (II) acetylacetonate (Pt(acac)$_2$) at elevated temperatures (200 °C) in presence of surfactant molecules, which allows us to define precisely the size and shape of nanoparticles before encapsulation or deposition in GNF. High-resolution transmission electron microscopy (HRTEM) imaging of the synthesised PtNP showed polyhedral nanoparticles uniformly dispersed on the carbon film of the TEM grid with an average diameter of 3.0 ± 0.6 nm (**Figure 2-2**). As a face centred cubic (fcc) structure, PtNP adopts a polyhedral shape with low-index planes (111) and (100) as facets that lower the overall surface energy making the nanoparticle thermodynamically stable, and both planes are clearly observed in HRTEM (**Figure 2-2**). X-ray diffraction (XRD) pattern is consistent with metallic Pt (**Figure 2-3)**, exhibiting characteristic features of an fcc structure such as a strong 2θ peak at around 40° corresponding to the (111) planes. Using Scherrer equation for the full width at the half maximum of this diffraction peak, the average nanoparticles diameter in the sample is calculated to be ~3.1 nm, which is in agreement with the average diameter observed by HRTEM.

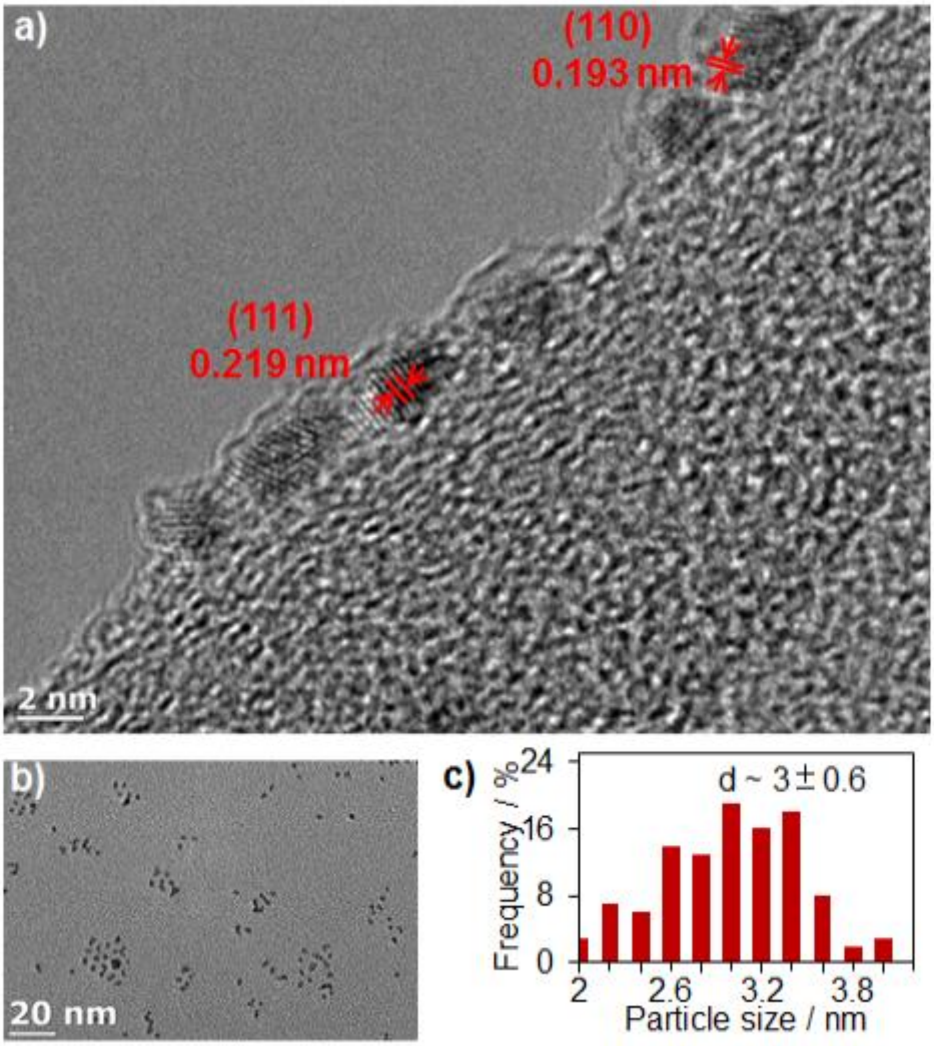

Figure 2-2. **(a-b)** HRTEM images of PtNP dispersed on the carbon film and **(c)** the particle size distribution with average size of the preformed PtNP.

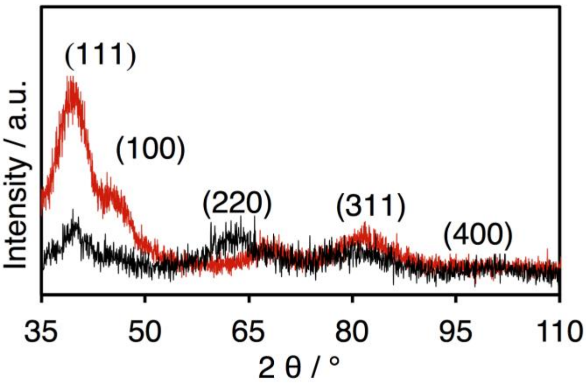

Figure 2-3. XRD diffraction pattern for the obtained PtNP before (black) and after (red) heat treatment in air at 175 ˚C for 2 h.

2.4.1.2. Shortening of graphitised carbon nanofibers (GNF)

To study the effect of the graphitised carbon nanofibers (GNF) on the electrochemical behaviour of the composite materials, GNF were shortened before the encapsulation of the preformed PtNP. In contrast to carbon nanotubes, GNF has open-ends, which is very advantageous for encapsulating PtNP. Shortening GNF can help (i) to avoid transport resistance along the internal cavities of the GNF during NP encapsulation, (ii) to reduce mass transport problems associated with the O_2 diffusion into the GNF during ORR experiments and (iii) with the water transport from GNF internal cavity to out in fuel cells. Both shortening of the nanofibers will facilitate the dispersion of the composite PtNP-GNF materials, and therefore, the quality of the film on the electrode surface for the electrochemical measurements. Two different approaches were used to prepare short GNF (S-GNF): (i) by oxidative cutting with silver nanoparticles (AgNP) and (ii) by ball milling.

- Shortening GNF via oxidative cutting with AgNP

The former approach involves first the acid treatment of GNF by refluxing for 24 hours at 110 ˚C in concentrated nitric acid to yield Ox-GNF, then followed by the decoration of Ox-GNF with AgNP (**Figure A- 5, 4**), and finally, the oxidative cutting of the Ox-GNF at 440 ˚C in air until have a weight loss of 50% was obtained using deposited AgNP as catalyst (**Figure 2-4**).

As a result of the oxidative cutting, some GNFs were shortened average length from 10-100 μm to 2-50 μm (**Figure 2-5**). However most of GNF are more than 10μm in length and a significant number of defects can be clearly observed in HRTEM not only on surface of GNF but also in the internal structure and step edges of the GNF (**Figure 2-5d-f**). In summary, these results show that shortened GNF with this method are not convenient to use as support carbon materials for encapsulation of pre-formed PtNP.

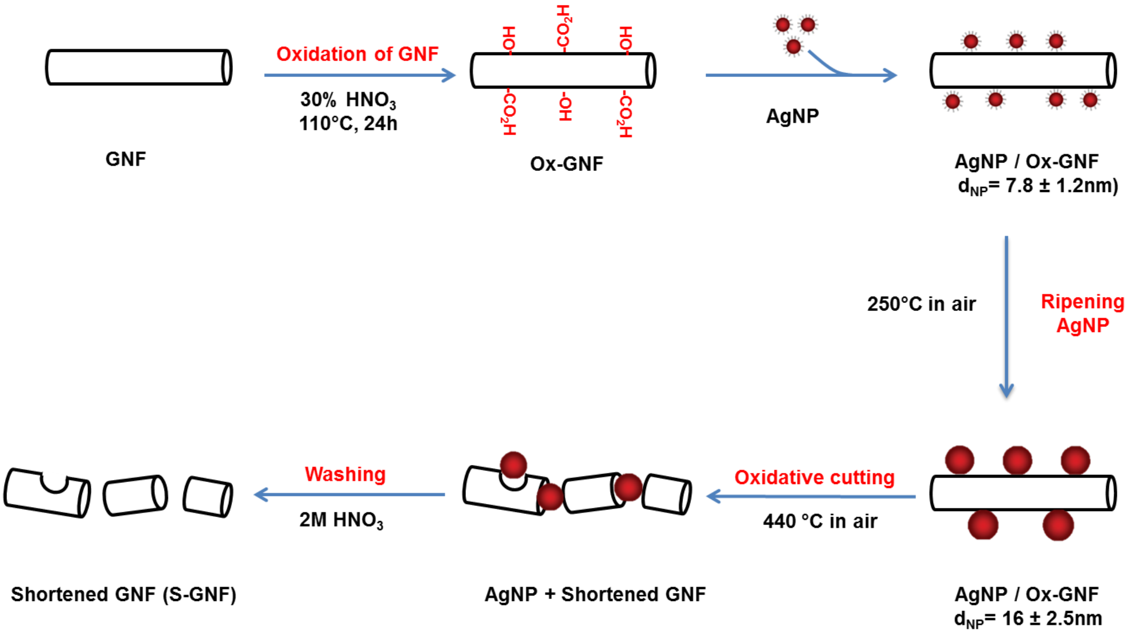

Figure 2-4. Schematic diagram for the oxidative cutting process of GNF with Ag NP.

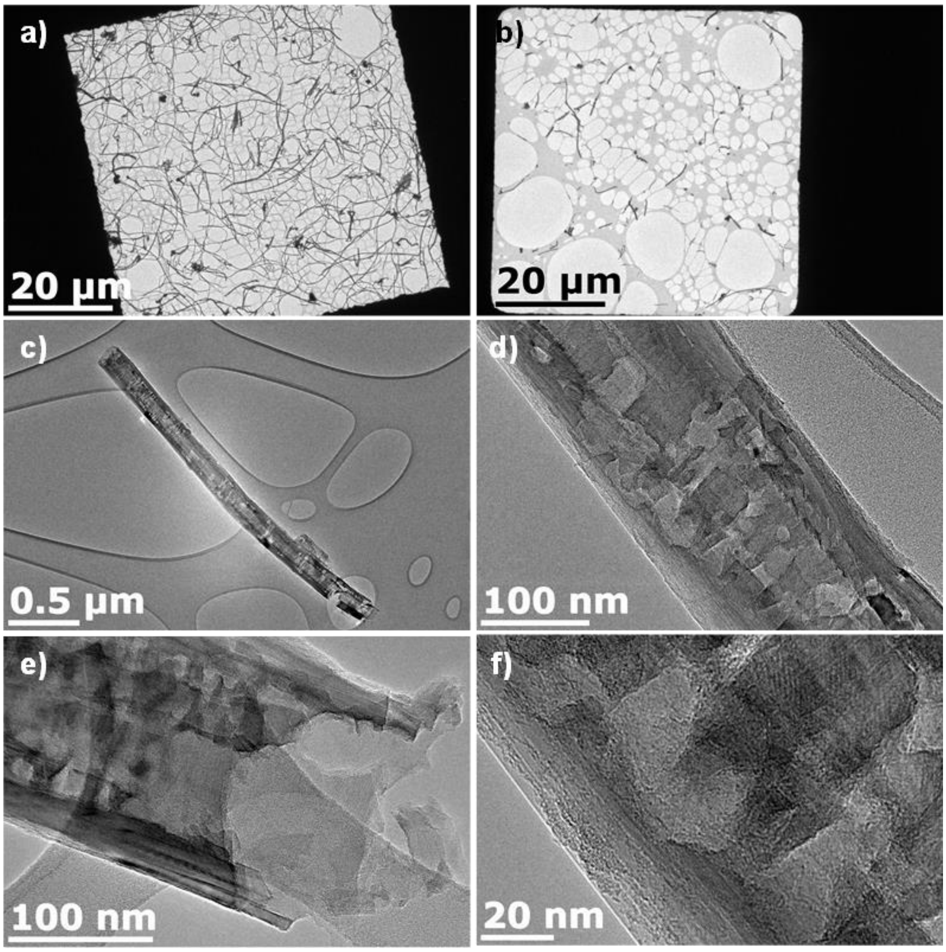

Figure 2-5. HRTEM images of GNF (**a**) before and (**b-f**) after oxidative cutting with AgNP.

- Shortening GNF via ball milling

The later approach is simply a mechanical process that allows the tuning of the length of the carbon nanofibers by adjusting the duration of the ball milling process. This process can easily reduce the GNF average length from 10-100 nm to 0.2-20 μm leading to shortened GNF (S-GNF) with an intact internal structure (**Figure 2-6**), in contrast with that observed for the oxidative cutting approach. Therefore, shortened GNF obtained with this method (S-GNF) will be used for the encapsulation experiments later on.

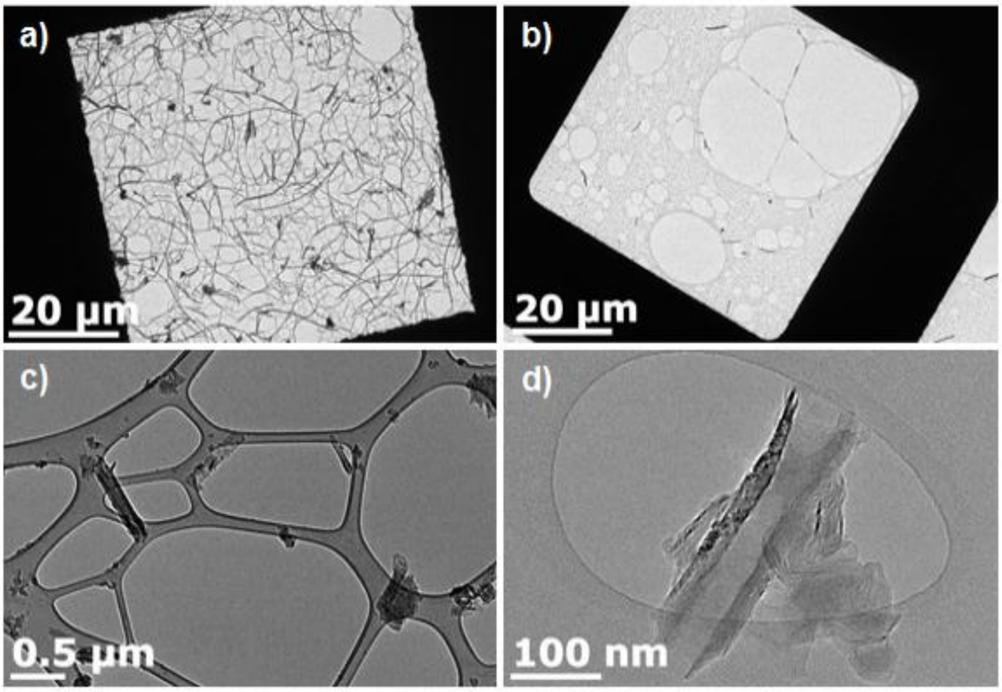

Figure 2-6. HRTEM images of GNF (**a**) before and (**b-d**) after ball milling.

2.4.1.3. Synthesis of PtNP@S-GNF hybrid electrocatalyst

Surface of PtNP prepared by this method is stabilised by hydrophobic surfactants, and therefore the nanoparticles are soluble in hexane – a solvent with a low surface tension that can easily penetrate into internal cavities of hollow graphitised nanofibers and wet their hydrophobic internal cavities, and thus deliver the pre-formed PtNP into the interior. To enhance mass transport of solvent, reactants and products during ORR, the pristine graphitised nanofibers (GNF) with a 10-100 nm length were shortened by mechanical milling to 0.2-20 nm length (S-GNF) prior PtNP insertion (**Figure 2-6**). Dry S-GNF immersed in a solution of PtNP in hexane (using an optimised 1:1 weight ratio) under ultrasound agitation to promote the diffusion of nanoparticles into the internal cavities are able to uptake PtNP from solution. The resulting hybrid material was carefully washed with hexane to eliminate any PtNP absorbed on the external surface of S-GNF. Thermogravimetric analysis (TGA) indicates that PtNP@S-GNF contains only about 10 % of Pt by weight (**Figure A- 2**). TEM analysis performed on the resultant hybrid material (**Figure 2-7a)** clearly indicate that nanoparticles were successfully inserted in S-GNF.

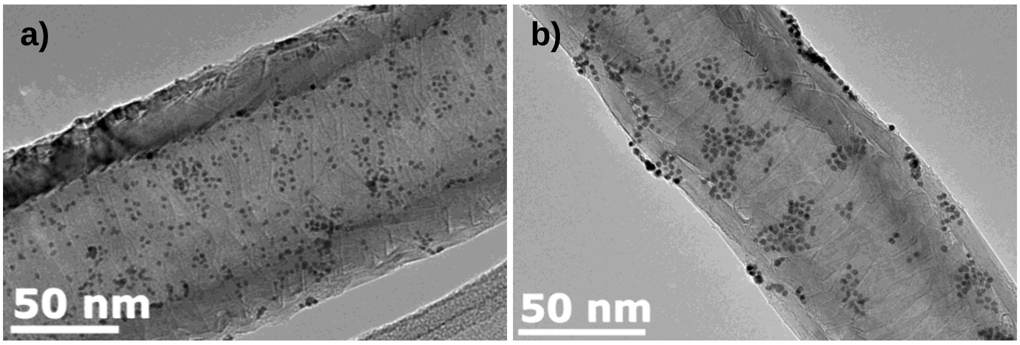

Figure 2-7. HRTEM images and schematic diagrams of 3.0 ± 0.6 nm pre-formed PtNP (**a**) inside (PtNP@S-GNF) and (**b**) outside nanofibers (PtNP/S-GNF) before heating.

Our recent studies[129, 150, 151] have shown that van der Waals forces play crucial role in interactions of metal nanoparticles with carbon nanotubes and nanofibers and their effectiveness is related to the contact surface between NP and GNF. When a nanoparticle is positioned on the smooth graphitic external surface of a GNF, the area of surface contact is minimal, but if the nanoparticle is residing at a graphitic step-edge, the surface of interaction increases significantly. Critically, if the nanoparticle is of a size equal with the size of the step-edge (*ca.* 3 nm), the surface area of contact is at a maximum, thus leading to stabilisation of

NP at the step-edge.[129] Since the pre-formed PtNP in this study before encapsulation in GNF have the average diameter of 3.0 ± 0.6 nm, they match well the size of graphitic step-edges in GNF, which ensures effective encapsulation, and formation of PtNP@S-GNF. Conversely, any nanoparticles bigger than the step-edge size would have a lower energy gain from adsorption at the internal corrugations of GNF as compared with flat areas of the exterior graphitic surface, due to a poorer geometric fit with the step-edges.[151]

In order to ascertain the confinement effects of the GNF nanocontainers on the electrochemical properties of PtNP, the same nanoparticles were deposited on the external surface of both shortened nanofibers (PtNP/S-GNF) and shortened nanofibers treated with nitric acid to oxidise their surfaces (PtNP@Ox-S-GNF) (**Figure 2-8**). In addition, same pre-formed PtNP were deposited on carbon black (PtNP/C) (**Figure 2-9c**) were used alongside with and commercial Pt/C (**Figure 2-11**) as reference materials for PtNP/S-GNF and PtNP@S-GNF.

To maximise the active surface area of platinum catalyst, and therefore its ORR activity it is important to remove any molecules adsorbed on PtNP prior to the ORR experiments. We tested a thermal procedure for the removal of the surfactant molecules from the encapsulated PtNP by heating PtNP@S-GNF in air at 175 ˚C for 5 h, which enables the removal of the organic surfactant as confirmed by TGA (**Figure A- 2**). Our previous studies[129, 150] showed that whereas gold nanoparticles deposited on the exteriors of GNF undergo Ostwald ripening increasing significantly in size when heated, the NP positioned at the step-edges inside the GNF grow to a much lesser extent and retain a specific size distribution dictated by the graphitic step-edge that imposes a barrier for particle migration, which is essential for ORR catalysis. HRTEM imaging confirms that PtNP obey the same principle, as after heating in air at 175 ˚C for 5 h PtNP increase in size only to 5.3 ± 0.4 nm and remain inside GNF (**Figure 2-9a**). The thermally activated growth of PtNP is clearly limited by the step-edges hindering PtNP migration and coalescence, which in principle may provide a highly effective electrocatalyst large active surface area.

2.4.1.4. Synthesis of PtNP/S-GNF, PtNP/Ox-S-GNF and PtNP/C Hybrid Materials

In order to ascertain the confinement effects of the GNF nanocontainer on the electrochemical properties of PtNP, the nanoparticles were deposited on the external surface of both shortened nanofibers (PtNP/S-GNF) and shortened nanofibres treated with nitric acid to oxidise their surfaces (PtNP/Ox-S-GNF) (**Figure 2-8**). In addition, PtNP deposited on carbon black (PtNP/C) (**Figure 2-9c**) and commercial Pt/C (**Figure 2-11**) were used as reference materials to evaluate the effects of graphitic surfaces of GNF on the properties of PtNP.

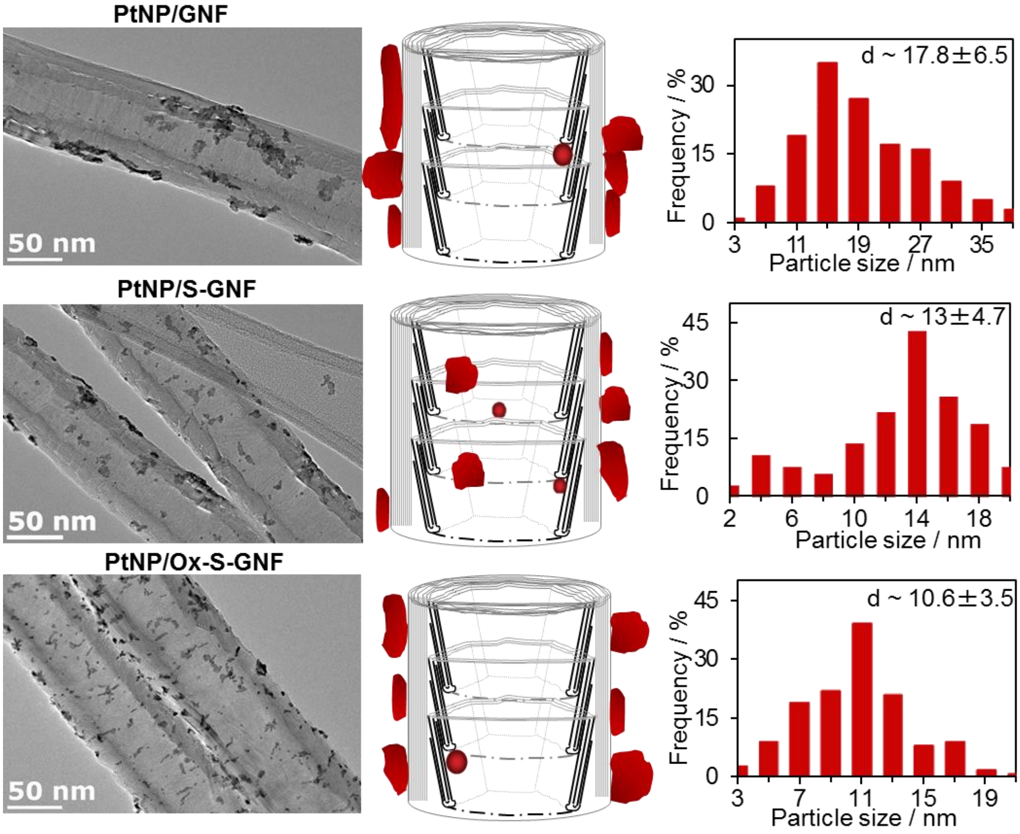

Figure 2-8. HRTEM images after heat treatment at 175 °C in ait for 5 hour, schematic diagrams, particle size distributions and average sizes of PtNP outside pristine nanofibers (PtNP/GNF), short nanofibers (PtNP/S-GNF) and oxidised short nanofibers (PtNP/Ox-S-GNF).

In contrast, in PtNP/S-GNF, where nanoparticles are largely located on the smooth external surfaces of nanofibers, a similar heat treatment leads to the increase in size from 3.0 ± 0.6 nm to > 13 nm (**Figure 2-9b**, **10).** It is interesting that the introduction of surface defects on GNF either by mechanical milling (S-GNF) or chemical oxidation (Ox-S-GNF) has a noticeable influence on the final size of PtNP during the thermal treatment with the trend PtNP/GNF > PtNP/S-GNF > PtNP/Ox-S-GNF confirming that greater concentration of surface defects suppresses the ripening and coalescence of nanoparticles (**Figure 2-8**). Although the introduction of carboxylic groups on the external surface of S-GNF (PtNP@Ox-S-GNF) slows down the NP growth (10.6 ± 3.5 nm), the size reached after heating is far larger than the one observed for PtNP trapped at the step-edges within S-GNF (5.3 ± 0.4 nm), highlighting the importance of our methodology. Surprisingly, under the same conditions PtNP deposited on carbon black exhibited only a small increase in size (3.6 ± 0.8 nm) that is close in size to nanoparticles in commercial Pt/C (**Figure 2-11**). This indicates very strong interactions between platinum and carbon black surface (**Figure 2-9c**) due to the high degree of functionalisation of carbon black surface with oxygen-containing groups (*i.e.* carboxylic, quinonic, lactonic, phenolic and others groups),[151] which effectively inhibit PtNP migration and coalescence to even greater extent than the graphitic step-edges of S-GNF. However, the high degree of functionalisation and the significant disorder of carbon black may have a detrimental effect on the catalytic performance of nanoparticles because of a potentially high electron transfer resistance and undesired increase in ORR overpotential, and greater tendency to corrosion [120, 123, 139, 143-145] than S-GNF.

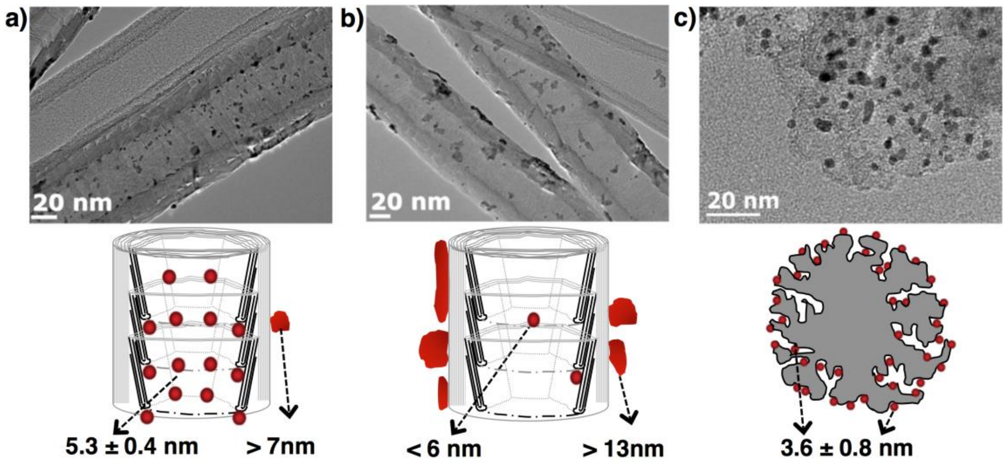

Figure 2-9. HRTEM images and schematic diagrams illustrating the PtNPs inside nanofibers (PtNP@S-GNF) (**a**), outside nanofibers (PtNP/S-GNF) (**b**) and deposited on carbon black (Vulcan XC-72R) (PtNP/C) (**c**).

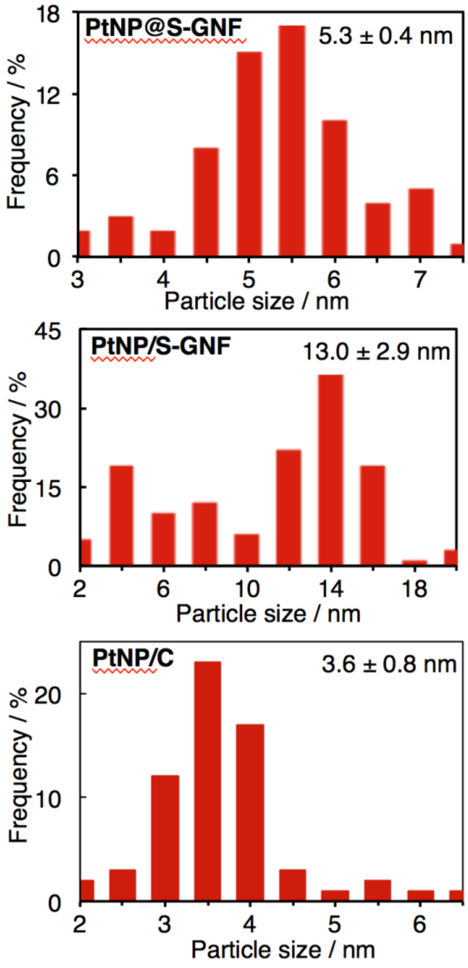

Figure 2-10. Particle size distribution and average sizes for PtNP inside S-GNF (PtNP@S-GNF), outside (PtNP/S-GNF) and supported on carbon black (PtNP/C) after heating in air at 175 ˚C for 2 h.

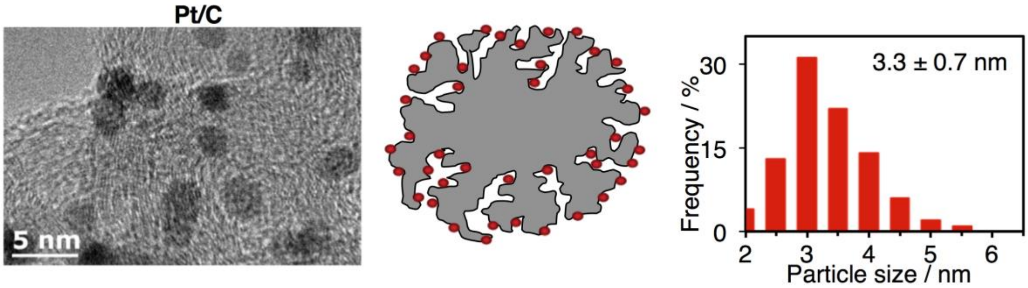

Figure 2-11. HRTEM images, schematic diagrams, particle size distributions and average size of PtNP for the standard commercial electrocatalyst Pt/C (Johnson Matthey 20 wt%, HiSPECTM3000).

2.4.1.5. Electrochemical analysis

- Electrochemically Active Surface Area (ECSA)

Cyclic voltammetry (CV) was applied to characterise the basic electrochemical properties of the prepared electrocatalyst materials in a nitrogen saturated acidic solution (0.1M $HClO_4$). CV measurements demonstrated significantly increase in the electrochemically active surface area (ECSA) after the removal of surfactant molecules from PtNP by heating at 175 ^{o}C for 5 h in air, without affecting the oxidation state of platinum. This can be clearly observed for PtNP inside pristine nanofibers (PtNP@GNF) where a H_{upd} peak emerged after the removal of surfactant (**Figure 2-12**) yielding an ECSA value of 15.4 m^2/g that is far from the theoretical value calculated from the NP size obtained from TEM. However, a higher increase in ECSA (44 m^2/g) after heating that is closer to the theoretical value (49 m^2/g) expected for *ca.* 5.3 nm PtNP was achieved when shortened carbon nanofibers were used (PtNP@S-GNF) (**Figure 2-13**), due to both a lower resistance for mass transport through shorter GNF and a better quality electrochemical films that can be prepared from PtNP@S-GNF (**Figure 2-14**). Hence, all further electrochemical measurements were carried out for electrocatalysts prepared from S-GNF that were subjected to heating at 175 ^{o}C for 5 h prior to electrochemical characterisation.

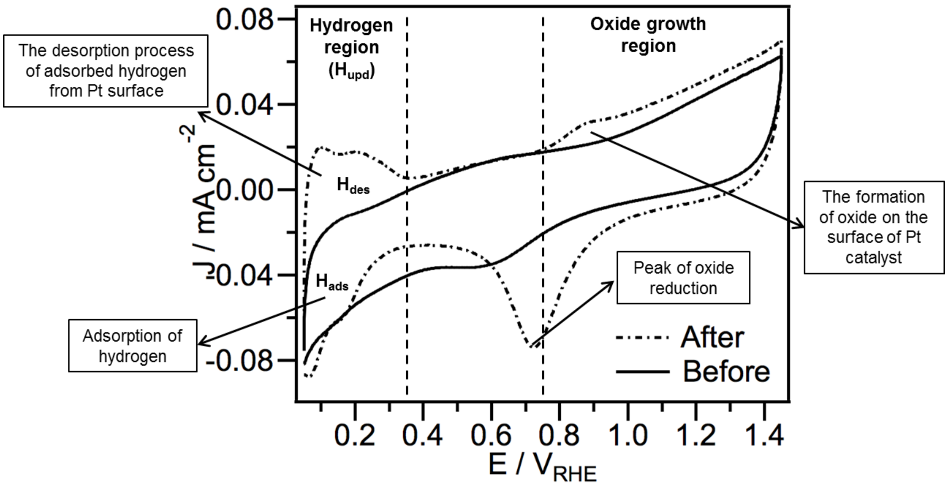

Figure 2-12. Voltammograms of PtNP@GNF before and after heating at 175 °C for 5h. H_{des}: hydrogen desorption, H_{ads}: hydrogen adsorption and H_{upd}: hydrogen underpotential deposited.

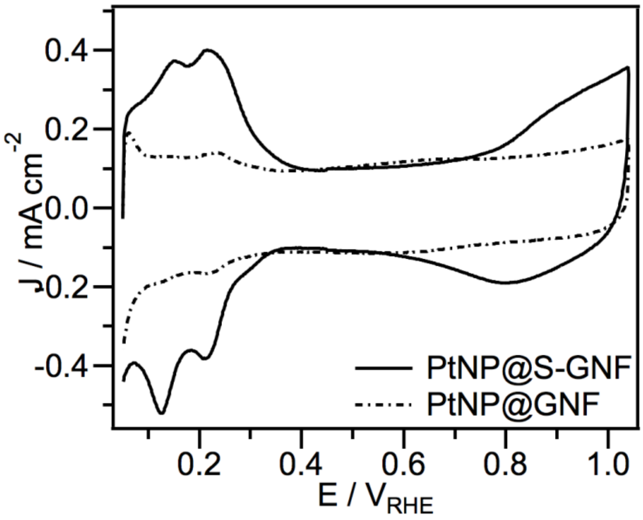

Figure 2-13. Voltammograms of PtNP encapsulated in short (solid line) and long (dash line) GNF.

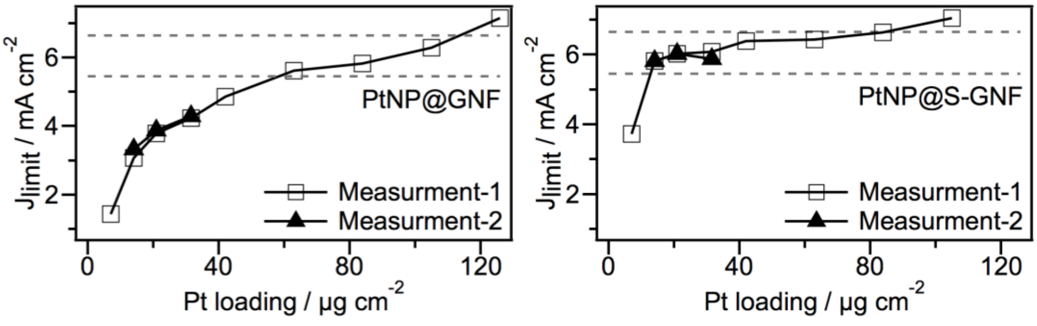

Figure 2-14. Limiting current versus Pt loading for PtNP@S-GNF and PtNP@GNF. Theoretical J_{limit} ±10% is shown between two-dash lines.

Three electrocatalyst materials (PtNP@S-GNF, PtNP/S-GNF, PtNP/C) were selected for a comparative study with Pt/C commercial catalyst to investigate the effects of nanoscale confinement on electrochemical properties and ascertain the difference between graphitic and amorphous carbon supports. In contrast to PtNP/S-GNF, PtNP@S-GNF and PtNP/C showed the same typical hydrogen desorption and adsorption features in the potential region between 0.05 and 0.30 V and the onset of the oxide formation in the anodic sweep similar the commercial catalyst (Pt/C) (**Figure 2-15**). The ECSA values decrease in the following order: Pt/C ~ PtNP/C > PtNP@S-GNF > PtNP/S-GNF is noticed, which correlates well with the increase of the NP size (measured by TEM), after the removal of surfactant, (**Table 2-1**) dictated by the nature of carbon surface as discussed in previous section. While the nanoparticles appear to be most durable on carbon black when heat-treated in the gas phase, this does not guarantee similarly high durability under fuel cell conditions in solution. Surface defects and oxygen-containing groups on the carbon supports can slow down the ripening and coalescence of nanoparticles as in the case of PtNP/Ox-S-GNF (*ca.* 10.6 nm compared to *ca.* 13.0 nm for NP supported on less defective S-GNF), but does not directly translate to the electrochemical behaviour, as the ECSA of PtNP/Ox-S-GNF (28 ± 5 m^2/g) is almost half of the value measured for the PtNP@S-GNF with the same Pt loading (44 ± 6 m^2/g).

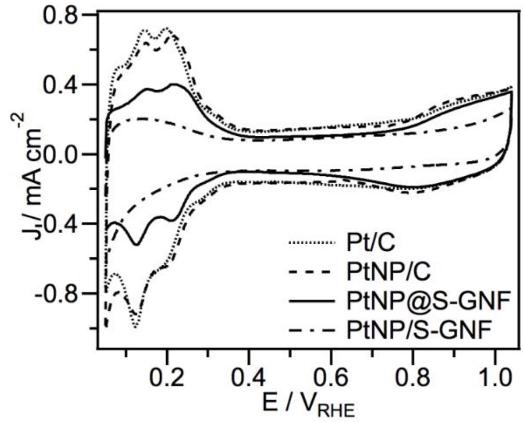

Figure 2-15. Voltammograms of the standard supported Pt commercial catalyst (Pt/C), PtNP deposited on carbon (PtNP/C), PtNP inside nanofibers (PtNP@S-GNF), and PtNP inside and outside nanofibers (PtNP/S-GNF) with the same Pt loading (14 μg/cm^2) in nitrogen saturated 0.1 M $HClO_4$ at room temperature; current densities (*J*) normalized to the geometric electrode area.

Table 2-1. Summary of electrochemical parameters for PtNP@S-GNF and PtNP/S-GNF, PtNP/C and Pt/C before and after 5000 cycles durability test.

	ECSA (m^2/g)	**Theoretical surface area of NP**	**Average NP size (nm)**	**Half-wave potential at 1600 rpm (V)**	**Specific activity at 0.85 V (mA/cm^2)**	**Mass Activity at 0.85 V (A/mg)**	**Tafel slope @ RT lcd/hcd (mV/dec)**
PtNP@S-GNF	44 ± 6	53 ± 4	5.3 ± 0.4	0.785	0.36	0.195	84/124
PtNP@S-GNF after	43 ± 5	42 ± 4	5.8 ± 0.5	0.783	0.35	0.190	84/136
PtNP/S-GNF	12 ± 2	22 ± 6	13.0 ± 2.9	0.595	0.07	0.01	145/167
PtNP/S-GNF after	4 ± 1	17± 3	16.0 ± 4.3	0.572	0.20	0.008	156/174
PtNP/C	72 ± 10	78 ± 14	3.6 ± 0.8	0.825	0.358	0.261	74/150
PtNP/C after	48 ± 6	54 ± 8	5.2 ± 0.9	0.786	0.272	0.133	65/134
Pt/C	74 ± 12	85 ± 15	3.3 ±0.7	0.840	0.544	0.396	95/136
Pt/C after	56 ± 8	60 ± 9	4.7 ± 0.8	0.813	0.312	0.182	75/131

- Oxygen Reduction Reaction (ORR) Activity

Polarisation curves for the ORR obtained for the three key electrocatalyst materials synthesised in this study (PtNP@S-GNF, PtNP/S-GNF, PtNP/C) and Pt/C on a rotating ring disk electrode in O_2-saturated 0.1 M $HClO_4$ solution at 1600 rpm are shown in **Figure 2-16**. The potential corresponding to one-half of the diffusion current (half-wave potential, $E_{1/2}$) can be used to qualitatively determine the catalyst activity: the higher the potential, the better the ORR activity.[158]

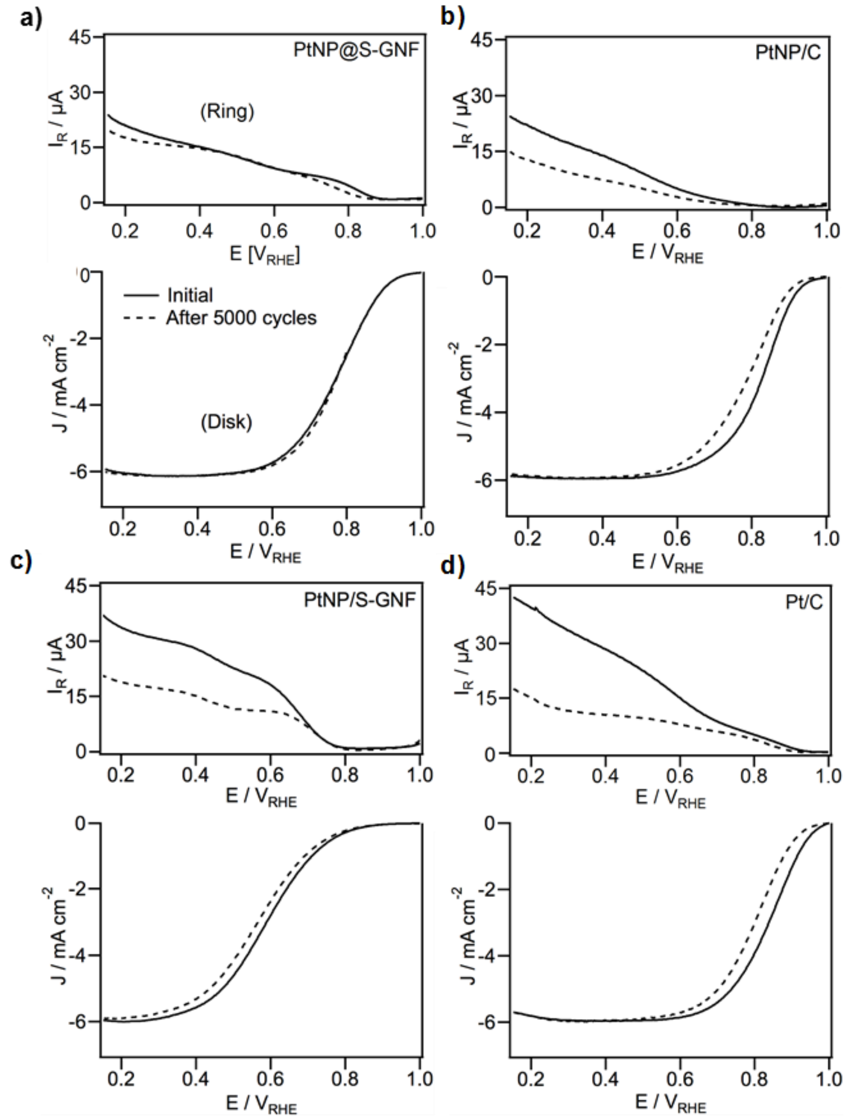

Figure 2-16. Ring and disk currents obtained during the ORR in the anodic sweep before (solid line) and after (dash line) 5000 cycles on (**a**) PtNP@S-GNF, (**c**) PtNP/S-GNF, (**b**) PtNP/C, and (**d**) Pt/C at room temperature at scan rate of 5 mV/s; current densities (*J*) normalized to the geometric electrode area.

The $E_{1/2}$ for PtNP/C (0.825 V) is similar to the one found for the commercial catalyst (0.840 V), while the $E_{1/2}$ for PtNP@S-GNF is marginally lower (0.785 V) and PtNP/S-GNF significantly lower (0.595 V). This indicates that activity of PtNP is only slightly reduced by the confinement in nanocontainers, which is remarkable considering the high aspect ratio of GNF. More surprisingly, PtNP on surface of GNF exhibit the lowest activity among the materials, which is unexpected since NP in PtNP/S-GNF should be more accessible for O_2

than in PtNP@S-GNF. This can be explained by a higher surface of interaction of PtNP with the step-edge inside GNF than with the convex surface of the outside of GNF, hence a better connectivity of catalytic centres in PtNP@S-GNF leading to a higher $E_{1/2}$ potential as compared to PtNP/S-GNF.

A Tafel analysis of the rotating ring-disk electrode (RRDE) data (E *vs.* log(J_k)) for the selected electrocatalyst and the commercial catalyst is shown in **Figure 2-18**. The specific activity was determined by normalising the J_k to the calculated ECSA values, while the catalyst mass activity was obtained by normalising to the catalyst loading on the electrode (14 µg/cm^2). The specific activities of the selected catalysts follow the trend: Pt/C > PtNP@S-GNF ≈ PtNP/C >> PtNP/S-GNF (**Table 2-1**), with the specific activity of the commercial Pt/C electrocatalyst only slightly exceeding that of PtNP@S-GNF. This observation suggests that when differences in surface areas are accounted for, the activity of PtNP@S-GNF is comparable to the commercial electrocatalyst. It is significant that the specific activities obtained for the electrocatalysts (Pt_1@S-GNF and Pt_2@S-GNF) where PtNP were prepared *in situ* in GNF are lower than that for PtNP@S-GNF, indicating that the approach involving the encapsulation of pre-formed nanoparticles with well-determined size and shape allows PtNP to be positioned more effectively at the step-edges, and therefore providing stronger interaction with GNF nanocontainers. This finding is in agreement with the previous studies of AuNP durability in GNF performed by TEM structural characterisation,[129, 131, 150, 151] but the effect of step-edge stabilisation on functional properties of nanoparticles (e.g. catalytic and electrochemical activities) have been demonstrated for the first time in the present study. Nanoparticles deposited on surface of nanofibers in PtNP/S-GNF showed by far the lowest specific activity due to the extensive PtNP ripening and coalescence on the GNF external surface (**Table 2-1 and Figure 2-18**). Although the introduction of defects on the external S-GNF surface inhibits the NP ripening and improves the ECSA value, the specific activity found for PtNP/Ox-S-

GNF (0.01 mA/cm^2) is still the lower in comparison to PtNP@S-GNF (0.36 mA/cm^2) which indicates the defects introduced during the oxidative treatment may have detrimental impact on electron transfer processes between PtNP and GNF (**Figure 2-8**).

- Mechanism and Kinetics of the ORR

RRDE measurements can shed light on the mechanism of oxygen reduction reaction as the H_2O_2 produced during the ORR occurring on the disk electrode can be detected on the ring. Following a potential region in the polarisation curves where the ORR is under mixed kinetic-diffusion region, diffusion limiting currents were noted in the potential window between 0.1 V to about 0.6 V for all the studied electrocatalyst materials, except PtNP/Ox-S-GNF (**Figure 2-16**). The amount of ring current produced above 0.6 V appears to be negligible compared to the disk currents, indicating that for PtNP@S-GNF and PtNP/C the ORR proceeds with insignificant production of hydrogen peroxide (H_2O_2). A small decrease in the disk currents below 0.2 V accompanying a simultaneous increase in the ring currents for PtNP@S-GNF, PtNP/C and Pt/C can be detected in the H_{upd} region. A similar increase of peroxide production in the H_{upd} region has been previously reported for Pt single-crystal electrodes where the adsorbed hydrogen hinders the O-O bond cleavage leading to the peroxide formation as a result.[160]

The electron transfers number (*n*) was calculated to be *ca.* 4.0 for PtNP@S-GNF and PtNP/C, and *ca.* 3.3 for PtNP/S-GNF at 0.6-0.8 V from the slopes of Koutecký-Levich plots (**Figure 2-17**), indicating that at potentials relevant to fuel cell cathodes reduction of O_2 proceeds exclusively *via* a four-electron pathway ($O_2 + 4H^+ + 4e^- \rightarrow 2H_2O$) similar to the Pt/C commercial catalyst measured under the same conditions, which is in sharp contrast to PtNP/S-GNF. As expected, H_2O_2 formation becomes apparent only at potentials below 0.6 V and increases significantly in the hydrogen desorption region (<0.3 V).

In the kinetic region within the potential range between 0.9 V and 0.7 V two Tafel slopes can be observed for PtNP@S-GNF and PtNP/S-GNF (**Figure 2-18**). The low Tafel slope represents a region where the ORR occurs on oxide–covered Pt, and for the high Tafel slope the ORR proceeds on metallic Pt surface (**Figure 2-12**). As we are primarily evaluating changes in Tafel slope associated with catalyst confinement, it is worth noting that values of the slopes corresponding to ORR on metallic Pt surface are affected by the blocking and/or electronic effects of adsorbed species.[161]

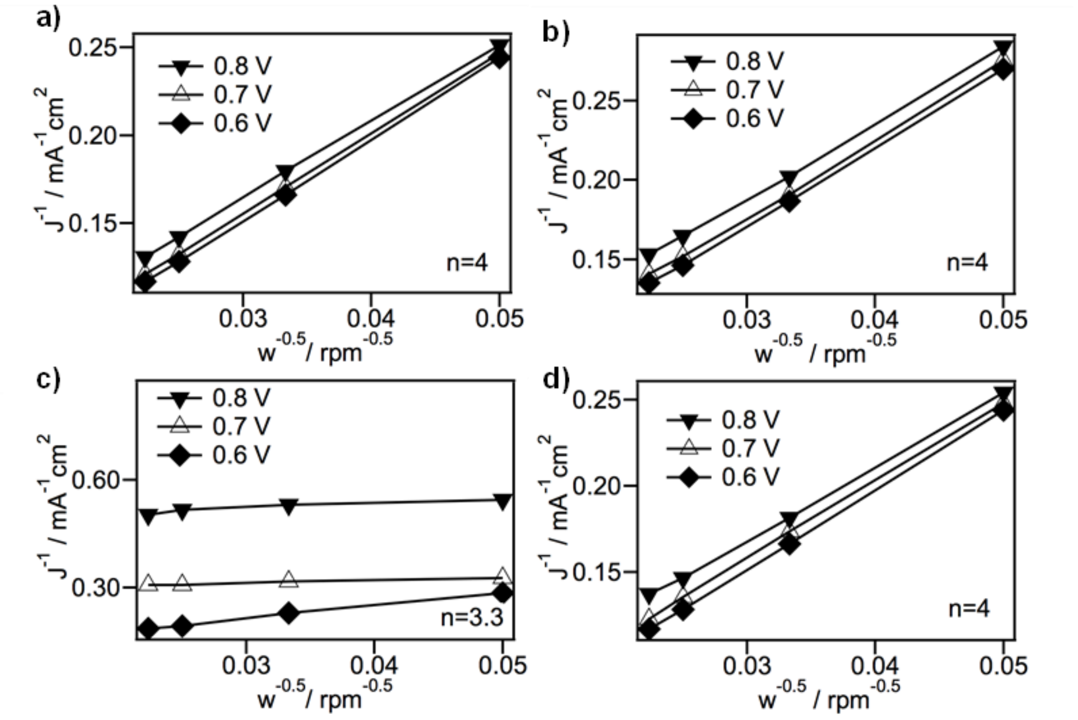

Figure 2-17. Koutecky-Levich plots of J^{-1} (current density) *versus* $\omega^{-0.5}$ (rotating speed) at various potentials extracted from the data I-V curves, current densities (J) normalized to the geometric electrode area for PtNP@S-GNF (**a**), PtNP/C (**b**), PtNP/S-GNF (**c**) and Pt/C (**d**).

Interestingly, at high current (low potential) the slope found for PtNP@S-GNF (124 mV/dec) is lower than the value found for PtNP/S-GNF and Pt/C (**Figure 2-18 and Table 2-1**) and only slightly higher than the pure kinetic value of 120 mV/dec,[156, 157] thus indicating possible effects of the corrugated internal surface of GNF on the rate-determining step of the reaction, which appears to be controlled entirely by the first electron transfer, based on the observed slope for PtNP@S-GNF (**Figure 2-18**).

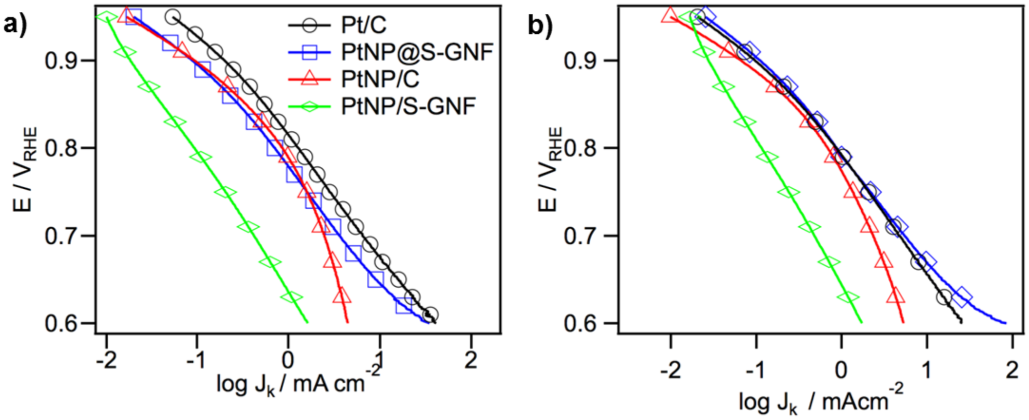

Figure 2-18. Tafel plots for the ORR normalised to the real surface area at room temperature, anodic sweep 5 mV/s, 1600 rpm on PtNP@S-GNF, PtNP/S-GNF, PtNP/C and Pt/C. (**a**) before and (**b**) after 5000 cycles.

2.4.1.6. Durability test

Durability studies of the selected electrocatalyst were performed in a durability test by continuously applying linear potential sweeps from 0.6-1.1 V, which causes surface oxidation/reduction cycles of platinum. For comparison, a Pt/C commercial catalyst with the same Pt loading as that in PtNP@S-GNF and PtNP/C was subjected to the same potential conditions, and after 5000 cycles, the changes in the Pt surface area and the electrocatalytic activity towards the ORR were carefully determined (**Table 2-1**, **Figure 2-16, 19**). Interestingly, after cycling the initial specific activity of PtNP@S-GNF (0.35 mA/cm^2) became slightly higher than the specific activity of Pt/C commercial catalyst (0.312 mA/cm^2), while the specific activity of PtNP/C decreased (0.272 mA/cm^2). This clearly indicates that the durability of PtNP encapsulated in S-GNF (PtNP@S-GNF) is better than that of the commercial catalyst and PtNP/C control sample, and therefore, overall performance PtNP@S-GNF is superior to other electrocatalysts (**Figure 2-19**). TEM imaging electrocatalysts after the cycling provides explanation of the observed performance as no significant change in particle size or morphology was found for PtNP@S-GNF (average increase of size c.a. 0.5 nm after 5000 cycles) in contrast with that observed for the electrocatalyst materials obtained by *in situ* methods (average increase of size c.a. 5.3 nm after 5000 cycles for Pt_1@S-GNF) (**Figure 2-37 and Table 2-4**). Because the cross section of GNF is polygonal (not circular) the surface area of contact between the PtNP and GNF in PtNP@S-GNF is further maximized when the PtNP are located at the apexes of the graphitic facets of step-edges (**Figure 2-1**), which leads to an improvement in the van der Waals interactions between the PtNP and the CN that immobilise the nanoparticles, thus preventing their migration and growth above 6 nm in diameter during electrochemical reactions. This is in agreement with the marginal change in the specific and mass activity observed for PtNP/S-GNF (**Table 2-1 and Figure A- 3**). A significant change in particle size and morphology was also found for PtNP/C and the commercial catalyst Pt/C from 3.6 ± 0.8 nm to 5.2 ± 0.9 nm and from 3.3 ± 0.7 nm to 4.7 ± 0.8 nm, respectively, after 5000 cycles, as shown by the TEM (**Figure 2-19 and Table 2-1**). Moreover, the ECSA values obtained for PtNP/C and Pt/C correlate well with the increased nanoparticle size and hence decreased electroactive surface area of platinum. The lack of durability of PtNP on carbon black may be related to the absence of long-range order in in this support material leading to electrochemical corrosion that aggravated the PtNP sintering and led to a reduced the durability of PtNP/C and Pt/C. For PtNP@S-GNF, measured as the currents of O_2 reduction obtained before and after 5000 potential cycles shows only a 2 mV degradation in half-wave potential of ORR polarisation curves over the cycling period (**Figure 2-16**). Futhermore, no significant change in the polarisation curves of H_2O_2 oxidation was found for this electrocatalyst. This provides further evidence of the stabilising effect of step-edges in GNF cavity and benefits of PtNP confinement within the nanocontainers. In contrast, Pt/C and PtNP/C both showed the degradation in ORR half-wave potential of 27 mV and 39 mV, respectively (**Figure 2-16**).

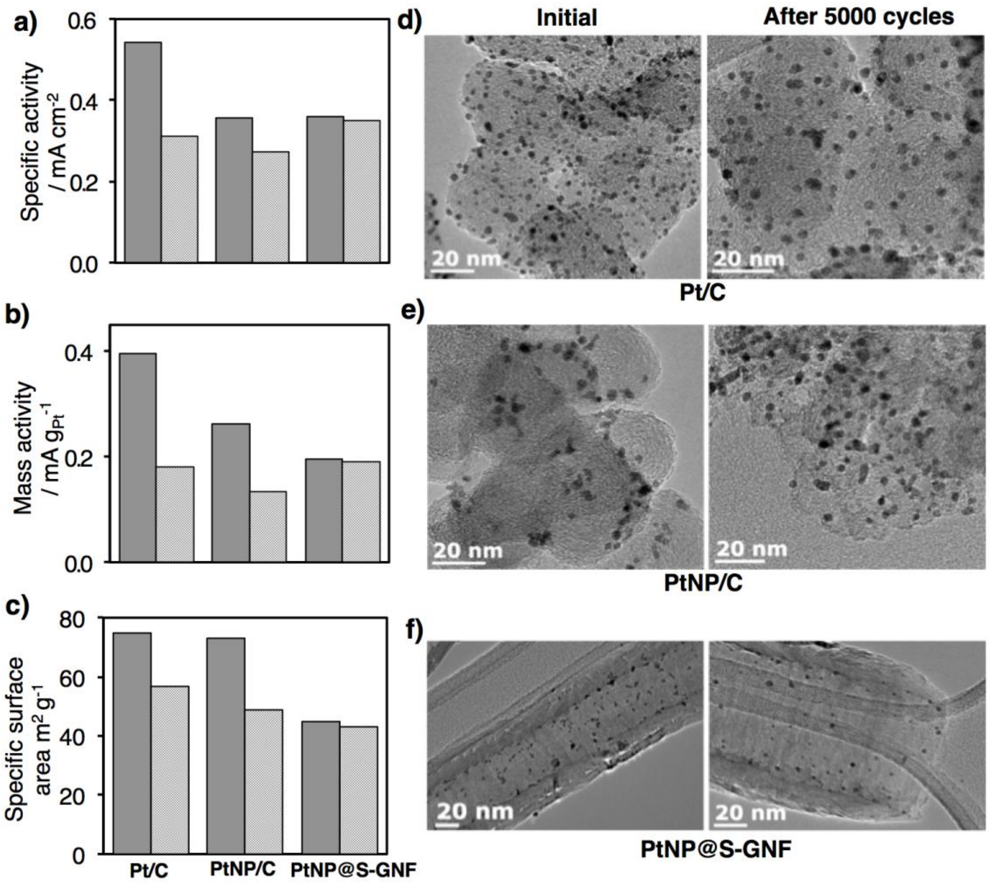

Figure 2-19. Durability characterization of the Pt/C, PtNP@S-GNF and PtNP/C by cycling 5000 times the potential between 0.6 and 1.1 V (vs RHE) in an oxygen saturated 0.1 M $HClO_4$ electrolyte at room temperature with a sweep rate of 100 mV/s. (**a**-**c**) Summary of the specific activity, mass activity and specific surface area (mass transfer corrected (**d**-**f**) HRTEM images of the catalysts before and after potential cycling.

In this respect, one of the issues accociated with carbon black is related to poorer connectivity with the catalyst NP due to structural disorder and corrosion under electrochemical conditions, thus leading may not cause only to the lack of durability of PtNP, but also to a higher electron transfer resistance and undesired increase in ORR overpotential as compared to the graphitic GNF.

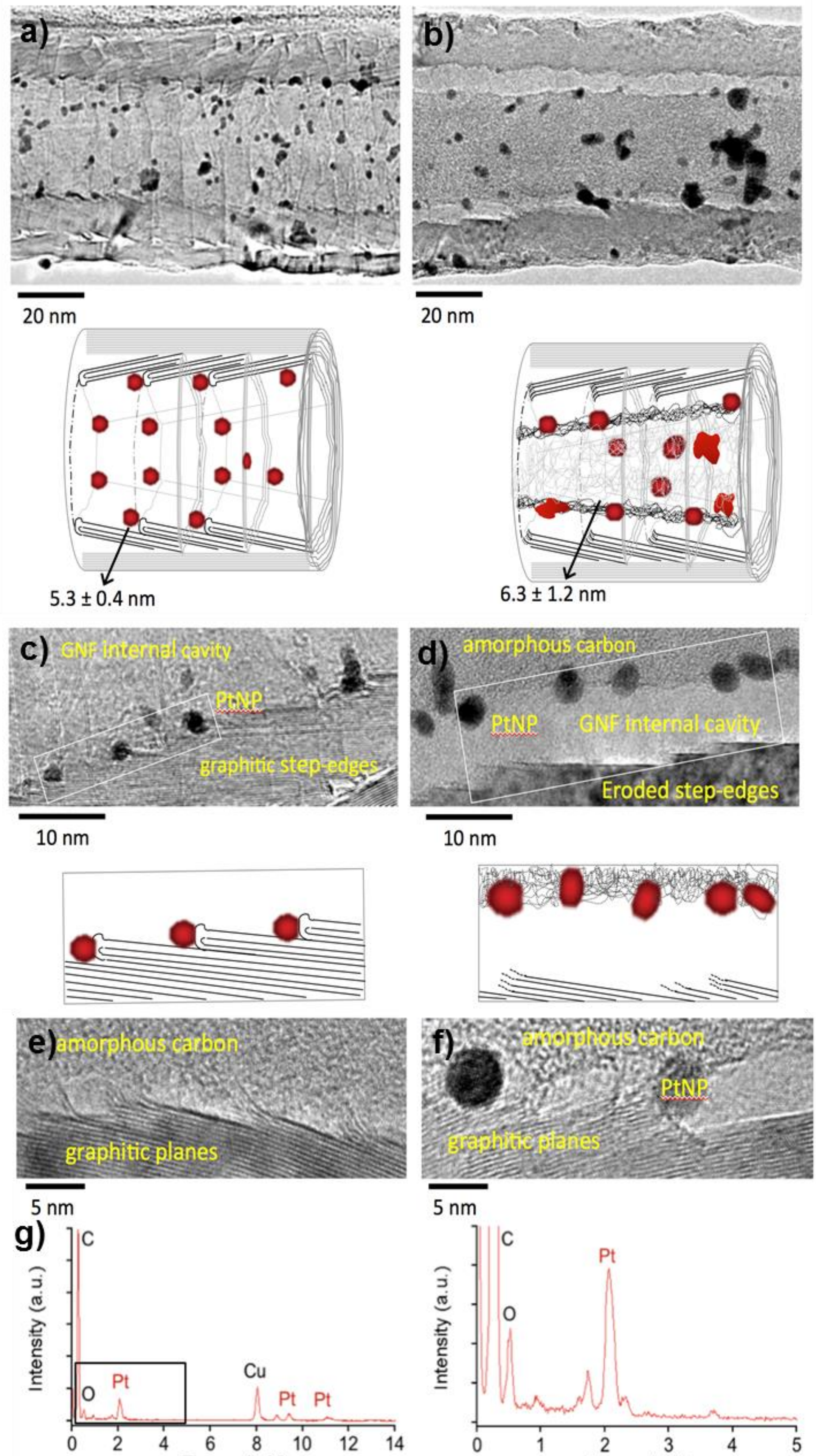
a)
b)
20 nm
20 nm
5.3 ± 0.4 nm
6.3 ± 1.2 nm
c)
GNF internal cavity
PtNP
graphitic step-edges
10 nm
d)
amorphous carbon
PtNP
GNF internal cavity
Eroded step-edges
10 nm
e)
amorphous carbon
graphitic planes
5 nm
f)
amorphous carbon
PtNP
graphitic planes
5 nm
g)
C
O
Pt
Cu
Pt
Pt
Intensity (a.u.)
0
2
4
6
8
10
12
14
Energy (keV)
C
Pt
O
Intensity (a.u.)
0
1
2
3
4
5
Energy (keV)

Figure 2-20. HRTEM images of PtNP@S-GNF before oxygen reduction reaction (A) with PtNP positioned predominantly at the graphitic step-edges (C) and the internal cavity of GNF completely clear (step-edges running across the GNF are clearly visible as transverse lines in the micrograph). After exposure of PtNP@S-GNF to 50,000 potential cycles in ORR, internal cavity of GNF becomes filled with amorphous carbon (B) located in the middle of the GNF, with all PtNP adhered to the amorphous carbon (D). Graphitic step-edges appear to be ‘unravelling’ during the ORR giving rise to amorphous carbon, as clearly indicated by individual graphitic layers of GNF observed half-way through amorphisiation (E). PtNP after 50,000 potential cycles remain inside GNF adhered to amorphous carbon (D) or sandwiched between the amorphous carbon and GNF wall (F). In either case, a 5-10 nm gap formed between the inner wall of GNF and the layer amorphous carbon allowing efficient access of reactants to catalytic centres PtNP during ORR. Energy dispersive X-ray analysis confirms that composition of PtNP@S-GNF remains virtually unchanged after 50,000 cycles, and local-probe EDX analysis shows c.a. 1.5 atomic % of oxygen incorporated in the amorphous carbon structure (G).

The electrochemical performance of the PtNP@S-GNF was studied at room temperature in a nitrogen-saturated 0.1M $HClO_4$ by cyclic voltammetry (CV), and compared with that of a commercial platinum on carbon black (Pt/C, nanoparticle diameter: 3.3 ± 0.7 nm) (**Figure 2-11**) with the same Pt loading (14 μg/cm^2 loading) under exactly the same conditions. Electrocatalyst durability studies involving 50,000 cycles were performed in a durability test by continuously applying linear potential sweeps from 0.6-1.1 V, which caused surface oxidation/reduction cycles of platinum. Changes in the electrochemically active Pt surface area and the electrocatalytic activity towards the ORR were carefully determined every 10,000 cycles (**Figure 2-21a**). Polarisation curves for the ORR obtained for both electrocatalyst on a rotating disk electrode in O_2-saturated 0.1 M $HClO_4$ solution at 1600 rpm were also investigated every 10,000 cycles (**Figure 2-21b**).

The PtNP@S-GNF and the commercial catalyst (Pt/C) showed similar hydrogen desorption and adsorption features in the potential region between 0.05 and 0.30 V, and the onset of the oxide formation in the anodic sweep. However, the initial electrochemical surface area (ECSA) for the PtNP@S-GNF is lower than for the commercial Pt/C due to a smaller initial NP size in the latter material (measured by TEM, **Figure 2-9a, c**). The half-wave potential ($E_{1/2}$) for PtNP@S-GNF (0.785 V) is marginally lower than the one found for the commercial catalyst (0.840 V), suggesting that, in principle, the activity of our electrocatalyst material is slightly lower than the commercial Pt/C. This is also in agreement with the difference in specific activity at 0.85 V observed for the commercial Pt/C electrocatalyst (0.544 mA/cm^2) and PtNP@S-GNF (0.360 mA/cm^2) that was determine by normalising the kinetic limiting current density (J_k) to the calculated ECSA values. A Tafel analysis of the rotating ring-disk electrode (RRDE) data (E vs. log(J_k)) for PtNP@S-GNF and the commercial catalyst after 5,000 potential cycles is shown in **Figure A-13**.

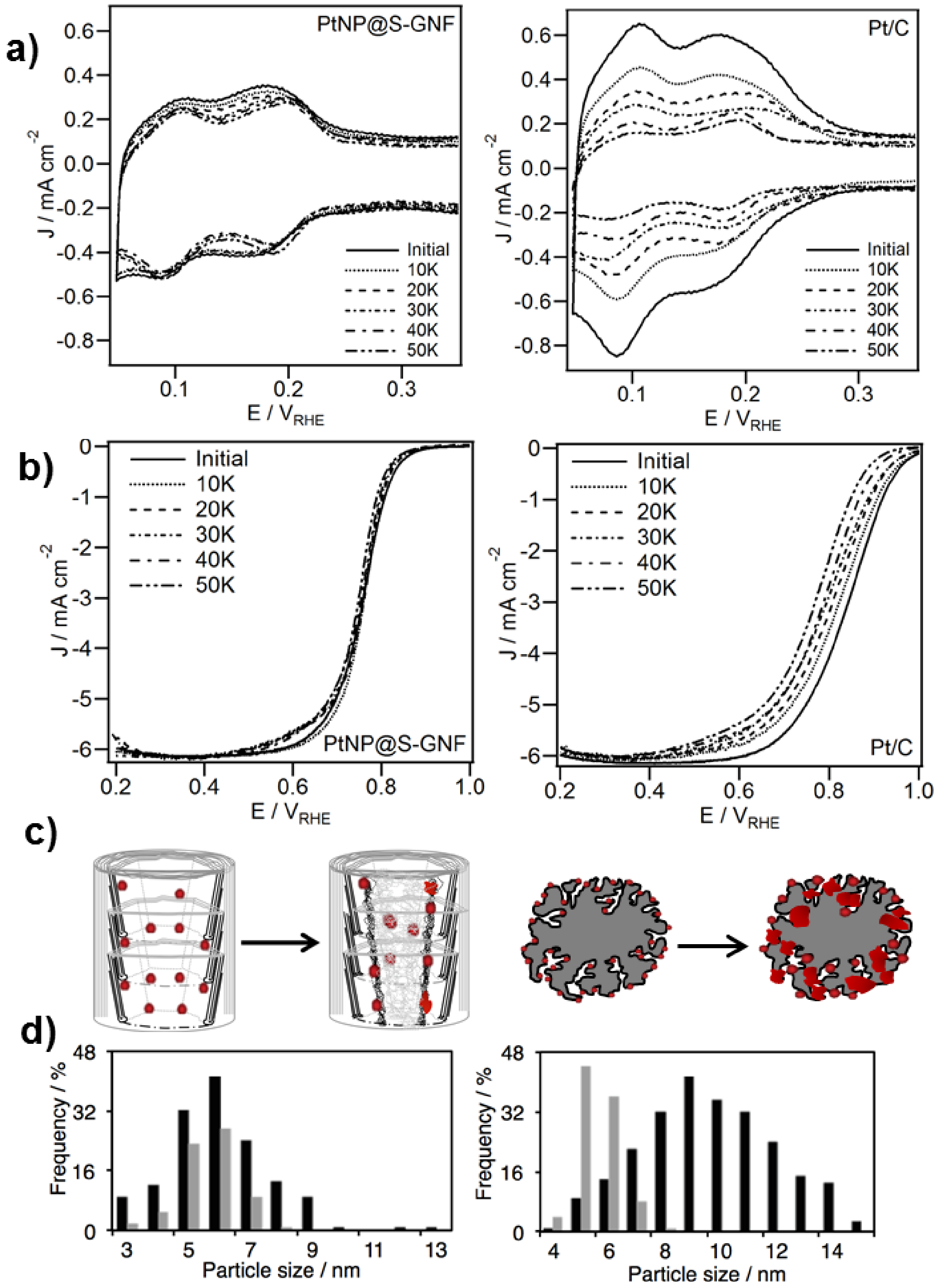

Figure 2-21. Comparison of the PtNP@S-GNF and Pt/C electrocatalysts over 50,000 potential cycles in oxygen reduction reaction using voltammograms (**a**) and ORR polarisation curves (**b**), showing superior durability of PtNP@S-GNF. Schematic diagrams (**c**) and nanoparticle size distribution before (grey data bars) and after (black data bars) 50,000 cycles of ORR (**d**), demonstrating a higher durability of catalytic nanoparticles to ripening in PtNP@S-GNF than in Pt/C which explains the significantly higher electrocatalytic durability of PtNP@S-GNF.

While the overall initial performance of Pt on carbon black appears to be better than for PtNP inside GNF, only after the first 5,000 cycles the specific activity of PtNP@S-GNF became slightly higher (0.35 mA/cm^2) than the specific activity of Pt/C commercial catalyst (0.312 mA/cm^2) under same conditions (**Figure 2-22a** and **Table 2-1**). This clearly indicates that the durability of catalytic centres in PtNP@S-GNF is significantly enhanced as compared to the commercial catalyst. Furthermore, TEM analysis of both electrocatalysts after 5,000 cycles provides explanation for the observed performance as no significant changes in particle size was found for PtNP@S-GNF (an average increase of size *c.a.* 0.5 nm) which contrasts to the commercial electrocatalyst Pt/C showing an average increase of PtNP size *c.a.* 1.4 nm (from 3.3 nm to 4.7 nm) (**Table 2-1**). Internal graphitic step-edges of GNF combined with the polygonal cross-section of GNF channels ensure that the surface area of contact between the PtNP and GNF in PtNP@S-GNF is maximized when the PtNP are located at the apexes of the graphitic facets of step-edges, which leads to an improvement in the van der Waals interactions between the PtNP and the CN that immobilise the nanoparticles, thus preventing their migration and growth beyond 6 nm during electrochemical cycling. In contrast, the ECSA values obtained for Pt/C correlate well with the continuouly increasing nanoparticle size in this electrocatalyst during ORR and hence electroactive surface area of platinum that gradually decreases with a growing number of the potential cycles (**Figure 2-22b** and **Table 2-1**). The lack of durability of PtNP on carbon black may be related to the absence of long-range order in in this support material leading to electrochemical corrosion that aggravates the Pt nanoparticle sintering and leads to a reduced durability of Pt/C. The degradation in half-wave potential of ORR polarisation curves over the first 5,000 cyles for PtNP@S-GNF of only 2 mV, that is in sharp contrast with that observed for the Pt/C (27 mV), provides further evidence of the stabilising effects of step-edges in GNF cavity and PtNP confinement within the GNF (**Figure 2-21b** and **Table 2-1**). The poorer electrical connectivity of carbon black with the Pt may give rise to a higher electron transfer resistance and undesired increase in ORR overpotential as compared to the graphitic GNF.

The superior durability of PtNP@S-GNF becomes particularly striking over 50,000 cycles of ORR (**Figure 2-22a-b** and **Table 2-2**). While the initial specific activity of the commercial electrocatalyst Pt/C is better than the activity of our PtNP@S-GNF for an identical (total) Pt loading, beyond 10,000 cycles, the activity of Pt/C decreases dramatically due to a quick drop of the active surface area, with a loss of 71 % of the initial activity after 50,000 cycles (**Figure 2-22a**). Remarkably, under the same conditions the specific activity of PtNP@S-GNF material decreased only by 12% after 50,000 cycles showing a significantly more stable activity than that of Pt/C. It is worth noting that no significant change in the polarisation curves of ORR was found for PtNP@S-GNF after durability tests (**Figure 2-21b**) confirming that the ORR mechanim remains unaltered throughout these extensive measurements.

Table 2-2. Summary of electrochemical parameters for PtNP@S-GNF and Pt/C before and after 50,000 potential cycles.

	ECSA (m^2/g)	**Theoretical surface area of NP (m^2/g)**	**Average NP size (nm)**	**Half-wave potential at 1600 rpm (V)**	**Specific activity at 0.85 V (mA/cm^2)**	**Mass Activity at 0.85 V (A/mg)**	**Tafel slope @ RT lcd/hcd (mV/dec)**
PtNP@S-GNF	44 ± 6	53 ± 4	5.3 ± 0.4	0.785	0.360	0.195	84/124
PtNP@S-GNF after	41 ± 5	42 ± 4	6.2 ± 0.5	0.776	0.318	0.181	86/138
Pt/C	74 ± 12	85 ± 15	3.3 ±0.7	0.840	0.544	0.396	95/136
Pt/C after	26 ± 3	60 ± 9	9.6 ± 2.5	0.792	0.159	0.096	105/145

Detailed high resolution TEM imaging of the PtNP@S-GNF after 50,000 cycles revealed an unexpected transformation taking place inside GNF (**Figure 2-20b, 20d, 23, 24**). The rolled-up graphitic structure of internal step-edges in GNF become 'unzipped' (**Figure 2-20e**) during the oxygen reduction reaction forming a layer of amorphous carbon lining the inner surface of hollow GNF (**Figure 2-20d**). EDX analysis does not show any significant amount of oxygen in the amorphous material inside GNF, but it is apparent that PtNP adhere to the amorphous carbon presumably due to dangling bonds on the disordered carbon surface providing excellent anchoring sites for the catalytic centres (**Figure 2-20g**).

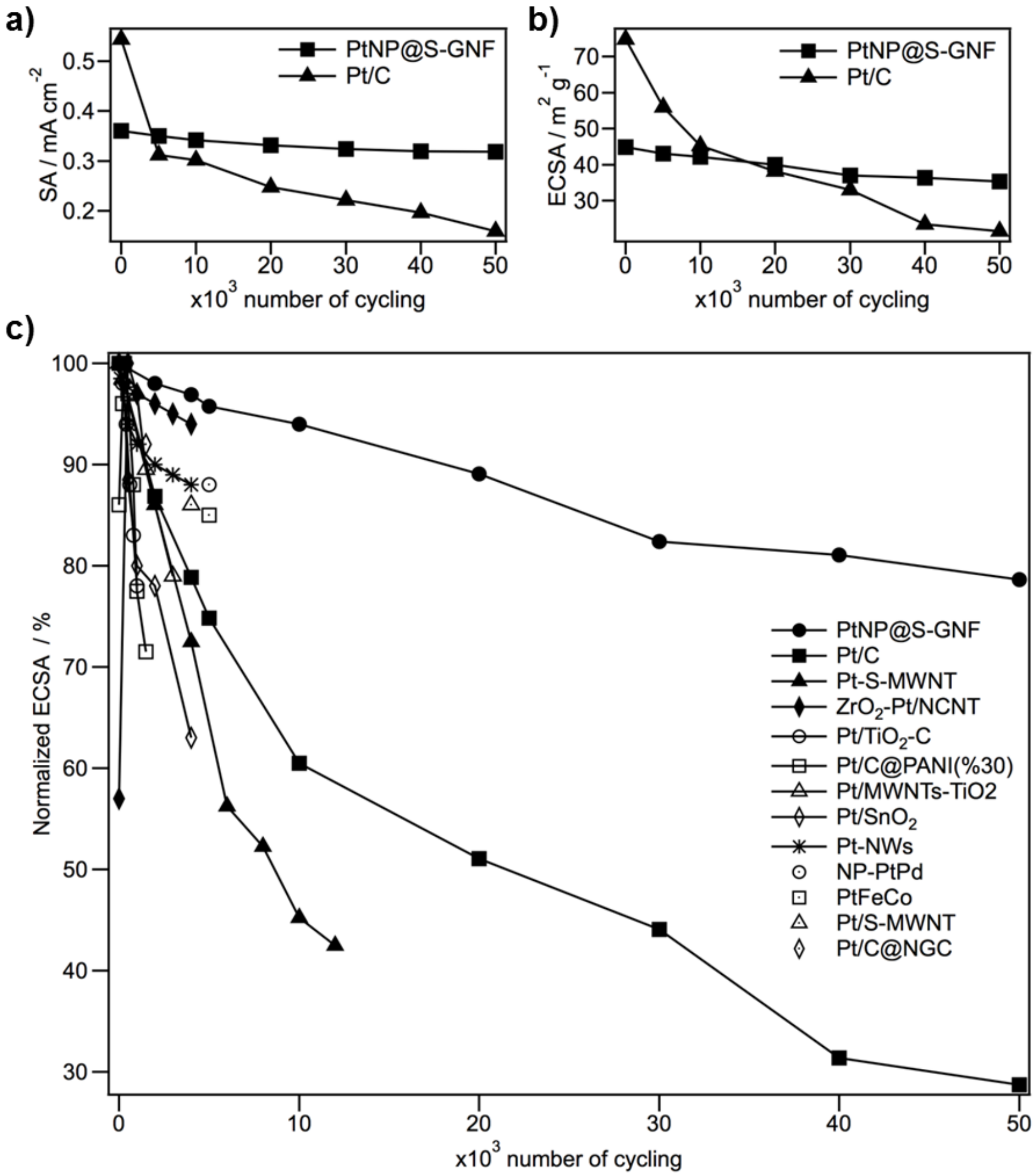

Figure 2-22. Comparison of PtNP@S-GNF and Pt/C over 50,000 potential cycles for (**a**) the electrochemical active surface area (ECSA) and (**b**) the specific activity (SA) at 0.85V vs. RHE. (**c**) Comparison of changes of ECSA (%) for PtNP@S-GNF, Pt/C and Pt electrocatalysts reported in the literature (**Pt-S-MWCNT**[162], **ZrO_2–Pt/NCNT**[163], **Pt/TiO_2-C**[164], **Pt/C@PANI(30%)**[165], **Pt/MWNTs-TiO_2**[166], **Pt/SnO_2**[167], **Pt-NWs**[168], **NP-PtPd**[169], **PtFeCo**[170], **Pt/S-MWNT**[171], **Pt/C@NGC**[172]) emphasising the overall excellent performance of PtNP@S-GNF (black cicrles) with respect to the state-of-the-art electrocatalysts.

While remaining confined within highly electrically conducting GNF and simultaneously being stabilised by the electrochemically generated amorphous carbon, remarkably, PtNP remain accessible to the reactants of ORR due to a gap of *c.a.* 10 nm between the layer of amorphous carbon and the GNF inner wall (**Figure 2-20d, 23, 24**), thus maintaining their high catalytic activity and exceptional durability even after 50,000 cycles due to the nanoscale confinement.

TEM images for PtNP@S-GNF after 50,000 cycles showed only a small change in PtNP size from 5.3 ± 0.4 nm to 6.2 ± 0.5 nm, unlike the significant increase in size for the commercial Pt/C from 3.4 ±1.2 nm to 9.6 ± 2.5 nm found under the same conditions (**Figure 2-21c, d**). Comparison of the optical diffractograms of the encapsulated PtNP before and after 50,000 cycles in TEM indicates no changes on the (110) lattice plane (*d*-spacing value of 0.193 nm) (**Figure A- 8**) confirmign that PtNP remain metallic state throughout the potential cycling.

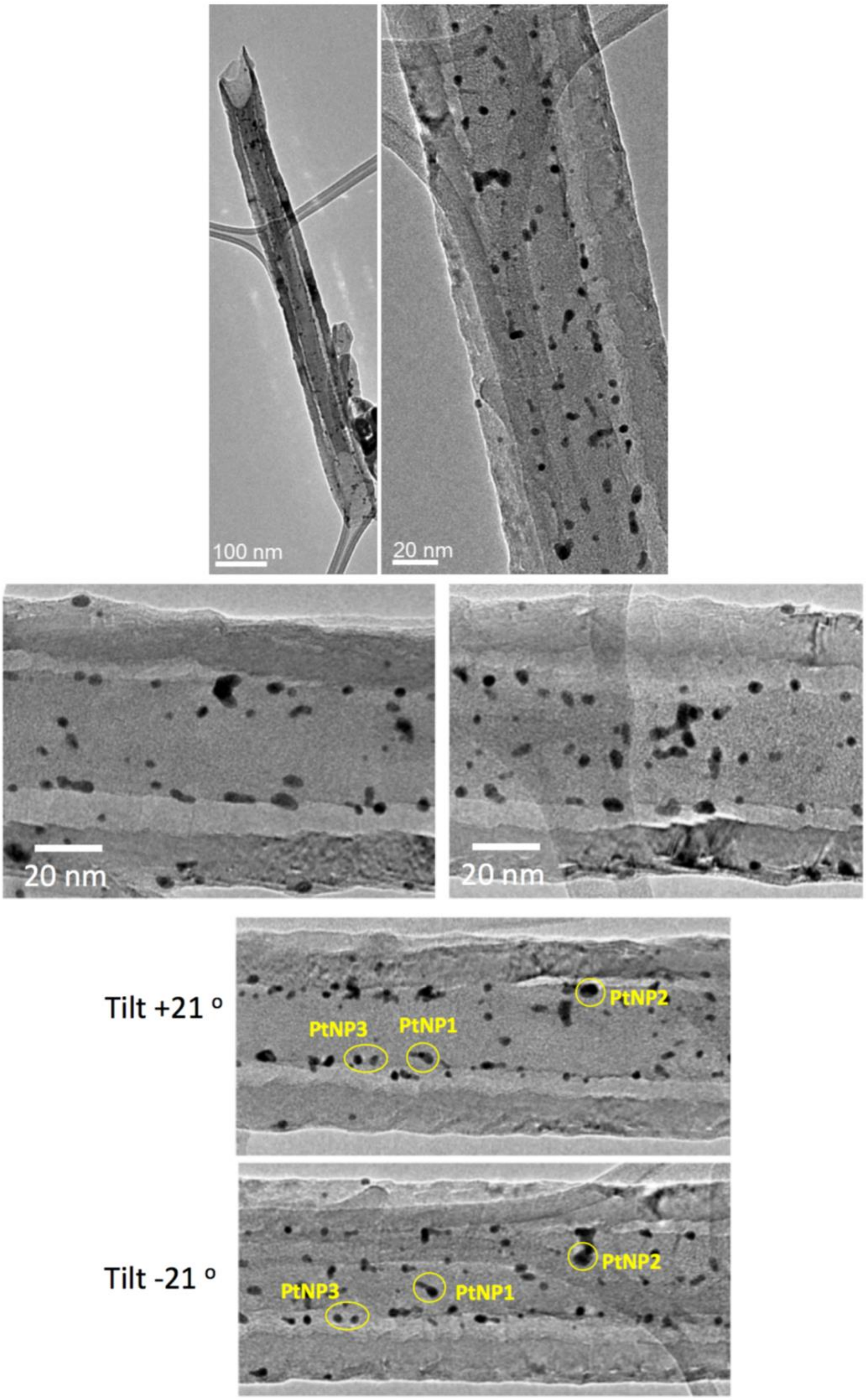

Figure 2-23. HRTEM images of the PtNP@S-GNF after 50,000 potential cycling. When tilted around GNF axis the PtNPs change their positions (as illustrated for three examples highlighted in circles) but remain inside GNF and adhered primarily on the layer of amorphous carbon rather than the GNF inner wall.

A detailed comparison of the ECSA changes in potential cycling experiments for PtNP@S-GNF with other state-of-the-art Pt electroctalysts reported in the literature**[162-172]** (including the commercial Pt/C as a benchmark) (**Figure 2-22c** and **Table A- 1)** further highligths the excellent long-term durability of PtNP within GNF retaining much of their activity over the 50,000 potential cycles thus outperforming all known electrocatalyst materials for ORR. The observed degradation in the half-wave potential of ORR polarisation curves for PtNP@S-GNF of only 9 mV after 50,000 potential cycles is an exceptional behaviour as shown by other studies.[159] These surprising and remarkable properties of PtNP@S-GNF open up a new strategy for harnessing the nanoscale confinement in sustainable use of platinum in electrocatalysis and other technological applications that require stabilisation of metal nanoparticles under harsh conditions. We believe that the reported synthetic strategy can be extended to other precious metals to inhibit their coalescence and thus to preserve their functional properties during potential cycling. Also the electrocatalysis in carbon nanoreactors can be extended to other processes of high technological value, such as methanol oxidation or hydrogen evolution reaction among others.

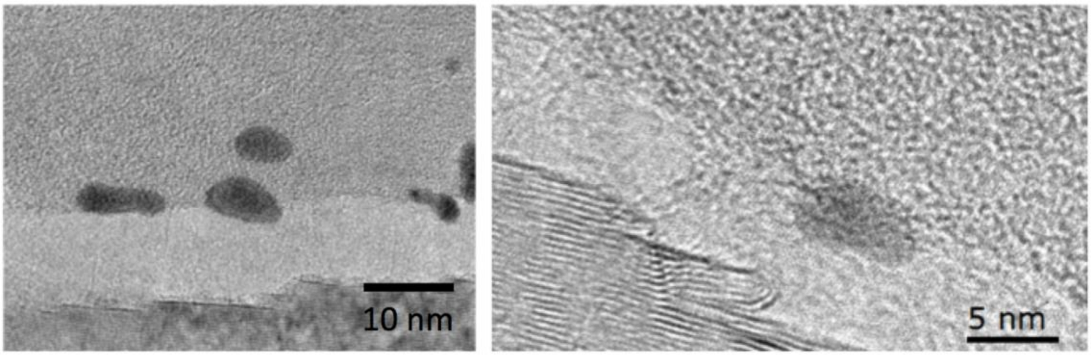

Figure 2-24. High-magnification HRTEM images of PtNP in PtNP@S-GNF after 50,000 potential cycling.

2.4.2. Study of the Pt-GNF materials for ORR obtained using the in-situ reduction of PtNP

2.4.2.1. Synthesis of Pt_1@S-GNF

It is important to note that the vast majority of previous studies on electrocatalytic metal-carbon hybrid materials were reported for PtNP formed from molecular precursors directly on the carbon support. To compare performance of nanoparticles pre-formed then inserted in GNF with the more widely spread nanoparticles formed *in situ* on carbon,[146, 151] S-GNF were impregnated with a $H_2PtCl_6 \cdot 6H_2O$ solution followed by reduction of the platinum compound to Pt metal inside GNF. The selected methods[173] involves the chemical impregnation of a platinum salt ($H_2PtCl_6 \cdot 6H_2O$) solution into the S-GNF cavity followed by in-situ reduction. The acid treated shortened carbon nanofibers by refluxing for 24 hours at 120 ˚C in concentrated nitric and sulphuric acids were used for the insertion of the Pt salt into S-GNF. This acid treatment increases the hydrophilicity of the nanofibers, so this may enhance capillarity filling of S-GNF to insertion of the Pt salt.

Freshly dried of Ox-S-GNF were added to a solution of potassium hexachloro-platinic acid ($H_2PtCl_6.6\ H_2O$) in water in order to ensure a capillarity filling of the Pt salt into the acid treated of S-GNF. The composite material was thoroughly washed to remove platinum salt adsorbed on the external surface of the GNF before the in-situ reduction leading to Pt_1@S-GNF material. The chemical impregnation of a platinum salt ($H_2PtCl_6 \cdot 6H_2O$) was performed into the acid treated S-GNF cavity using a mixture of ethylene glycol and water (85:15) at 120 °C (**Figure 2-25**).

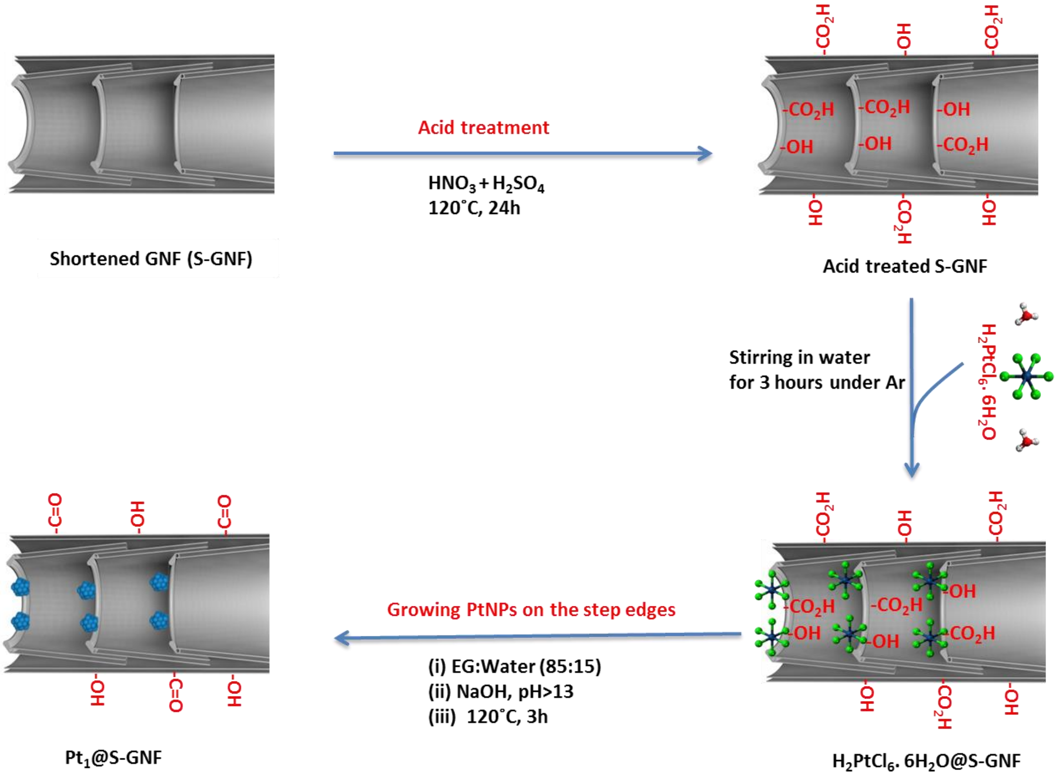

Figure 2-25. Schematic diagram of the methodology employed to prepare Pt_1@S-GNF composites.

A sample containing PtNP which chemically impregnated on carbon black (Pt_1/C) was prepared under same conditions as a control sample for comparison with Pt_1@S-GNF

2.4.2.2. Structural characterisation

HRTEM images for Pt_1@S-GNF (**Figure 2-26**) show the successful formation of PtNP in GNF using the *in situ* reduction but reveal two different sets of nanoparticles: the smaller nanoparticles reside at the step-edges in GNF (diameter *c.a.* 3 - 6 nm), and the larger nanoparticles are randomly distributed (diameter > 6 nm). This method appears to have less effective control over the size of encapsulated NP compared to the pre-formed PtNP where size distribution is strictly defined before encapsulation in GNF.

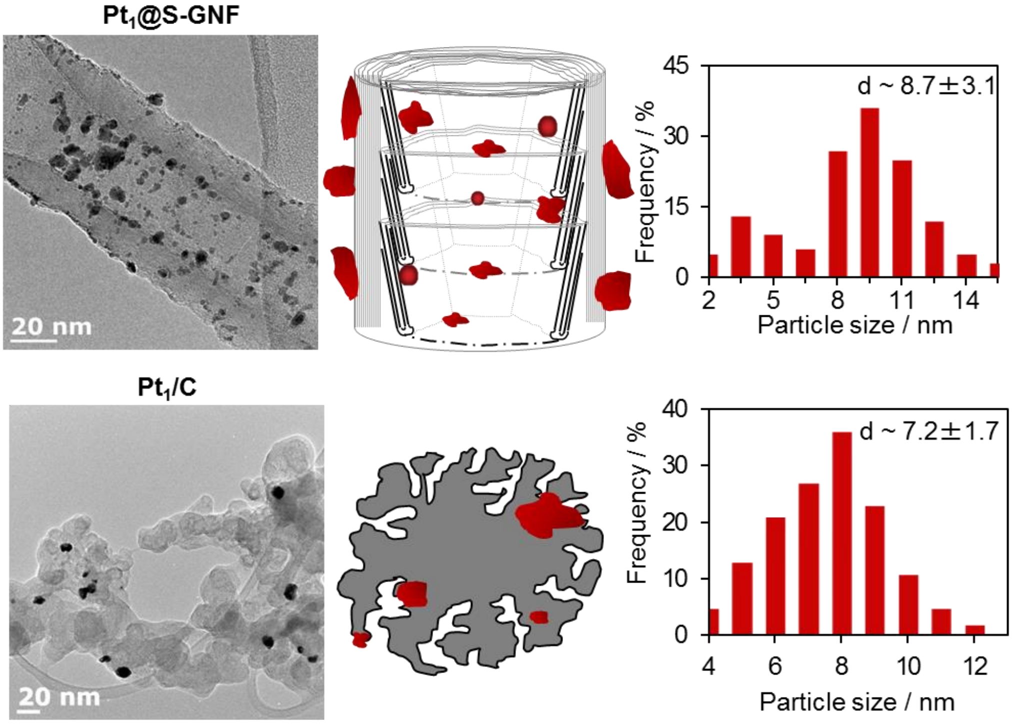

Figure 2-26. HRTEM images, schematic diagrams, particle size distributions and average sizes of PtNP for Pt_1@S-GNF and Pt_1/C.

HRTEM analysis performed on Pt_1/C show the formation of c.a. 7.2±1.7 nm PtNP on carbon black (**Figure 2-26**). In contrast to S-GNF, just one set of size distribution is observed when carbon black is used as a support.

2.4.2.3. Electrochemical properties towards ORR

Pt_1@S-GNF and Pt_1/C were first evaluated electrochemically by CV between 0.05 and 1.05V (vs RHE) at room temperature in a nitrogen purged $HClO_4$ electrolyte. The shape of the hydrogen desorption (H_{des}) region for Pt_1@S-GNF and Pt_1/C is very similar to that observed for the Pt/C electrocatalyst and also shows the same typical H-adsorption (H_{ads}) and desorption (H_{des}) features in the potential window between 50 and 300 mV (**Figure 2-27**). Because of its smallest particle size, Pt/C has the highest specific surface area compared to Pt_1@S-GNF and

Pt_1/C. The obtained ESCA for Pt_1@S-GNF and Pt_1/C seems to be in perfect agreement with the theoretical surface area of PtNP values in materials obtained from TEM (**Table 2-3**).

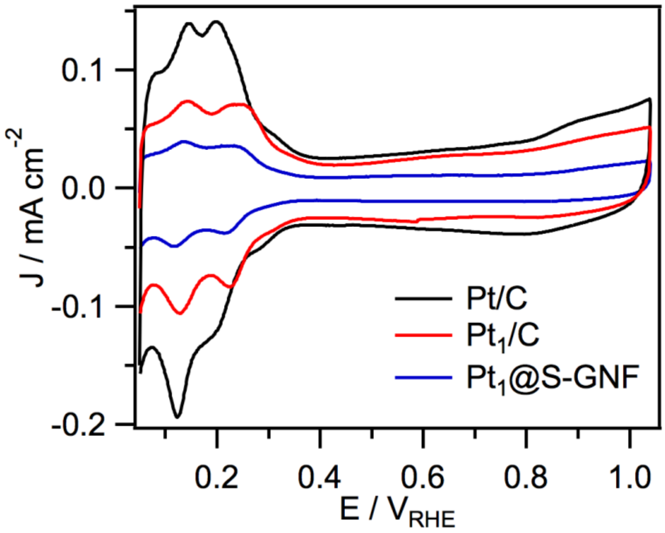

Figure 2-27. Voltammograms of the standard supported Pt commercial catalyst, Pt_1@S-GNF and Pt_1/C in nitrogen saturated 0.1 M $HClO_4$ at room temperature; current densities were normalised to the geometric electrode area.

Ring-disk measurements for Pt_1@S-GNF and Pt_1/C in O_2 saturated 0.1 M $HClO_4$ at room temperature are shown in **Figure 2-28** and compared with the Pt/C standard EC. Following a potential window where the ORR is under mixed kinetic-diffusion region, the diffusion limiting currents were noted in the potential window between 0.1 to about 0.6 V for Pt_1@S-GNF and Pt_1/C. The ring currents amount to insignificant fractions of the disk currents in the potential window above 0.6 V for all Pt_1@S-GNF and Pt_1/C, which indicates that the ORR proceeds with insignificant production of hydrogen peroxide (H_2O_2) in solution throughout the potential window for the ORR. It shows that at potentials relevant to fuel cell cathodes, reduction of O_2 proceeds for Pt_1@S-GNF and PtNP@S-GNF exclusively via a complete four-electron step. H_2O_2 formation becomes apparent only at potentials negative of 0.6 V and increases significantly in the H_{des} region (<0.3V). Closer inspection shows that the appearance of ring currents follows quantitatively the decrease in disk currents from its diffusion limited value as expected for a change in the ORR pathway from a four to a two-electron pathway (**Figure 2-29**).[160] Similar results were demonstrated for Pt single-crystal electrodes and the full discussion of the change in the ORR pathway in this potential window is described in the literature.[36, 174] Presumably the same reaction mechanism applies to these supported preformed PtNP in our experiment. The initial peroxide yield formed appears to be lower for Pt/C than that for Pt_1@S-GNF and Pt_1/C.

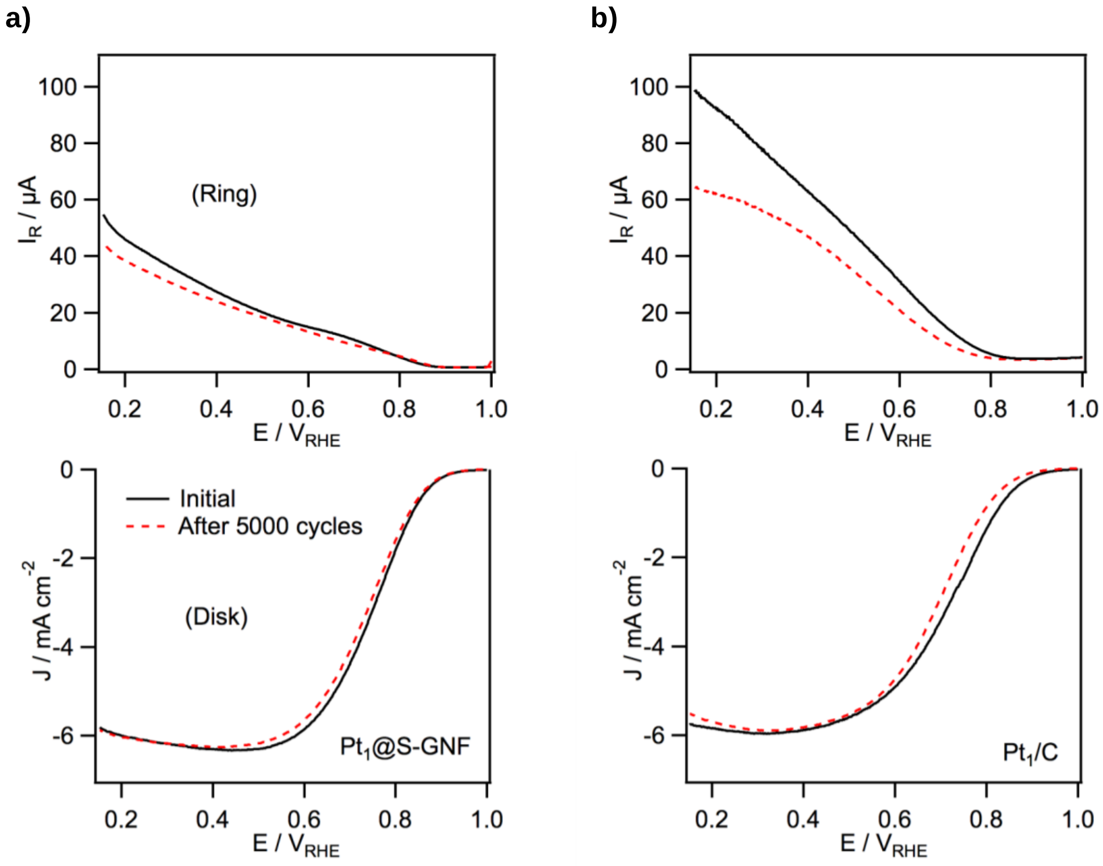

Figure 2-28. Ring and disk currents obtained during the ORR in the anodic sweep before (solid line) and after (dash line) 5000 cycles on (**a**) Pt_1@S-GNF and (**b**) Pt_1/C at room temperature at scan rate of 5 mV/s; current densities (*J*) normalized to the geometric electrode area.

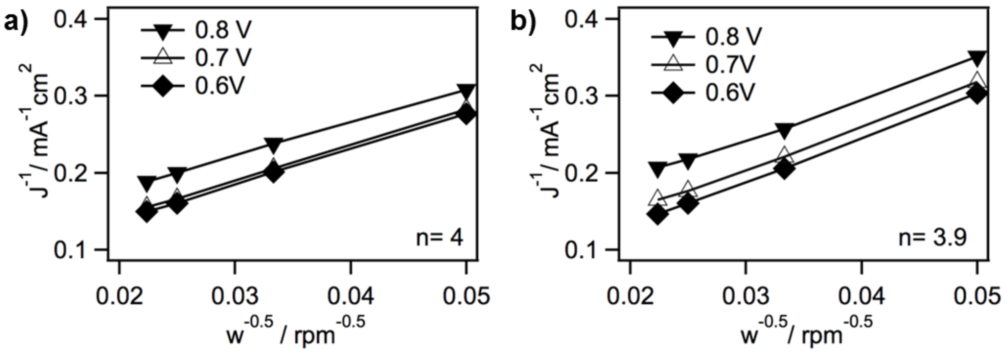

Figure 2-29. Koutecký-Levich plots of J^{-1} (current density) versus $\omega^{-0.5}$ (rotating speed) at various potentials extracted from the data I-V curves, current densities (J) normalized to the geometric electrode area for Pt_1@S-GNF (**a**), Pt_1/C (**b**).

Figure 2-30 compares the Tafel plots for the mass transport corrected specific current densities at a rotation rate of 1600 rpm for Pt_1@S-GNF, Pt_1/C and Pt/C before (**Figure 2-30a**) and after durability test (**Figure 2-30b**). The performance of the studied electrocatalysts before durability test follows this trend Pt/C > Pt_1@S-GNF > Pt_1/C. After cycling the potential 5000 times, the activity of Pt_1@S-GNF seems to get closer to activity of the commercial Pt/C.

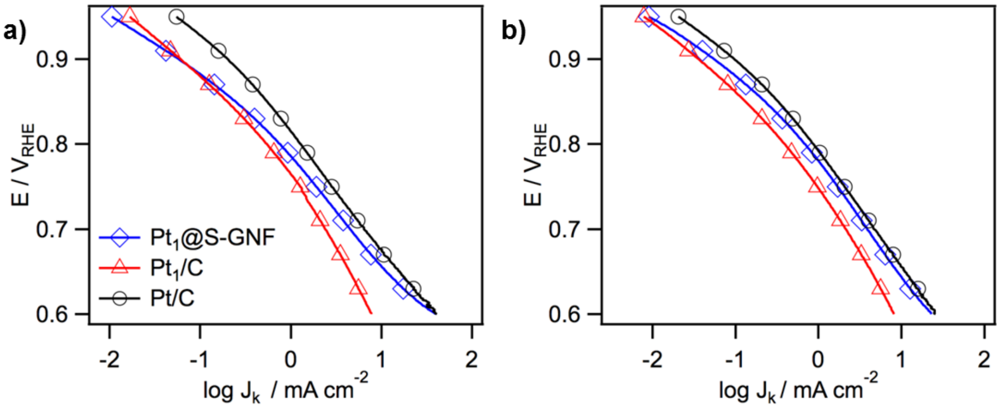

Figure 2-30. Tafel plots for the ORR normalised to the real surface area at room temperature, anodic sweep 5 mV/s, 1600 rpm on Pt_1@S-GNF, Pt_1/C and Pt/C. (**a**) before and (**b**) after 5000 cycles.

2.4.2.4. Durability test

Durability studies of the selected electrocatalyst were pre formed in a durability test by continuously applying linear potential sweeps from 0.6-1.1V, which causes surface oxidation/reduction cycles of platinum. For comparison, a Pt/C commercial catalyst with the same Pt loading as that in Pt_1@S-GNF was subjected to the same potential conditions, and after 5000 cycles, the changes in the Pt surface area and the electrocatalytic activity towards the ORR were carefully determined (**Table 2-3, Figure 2-28**).

The catalytic activity of Pt_1@S-GNF, measured as the currents of O_2 reduction obtained before and after potential cycling shows only a 5 mV degradation in half-wave potential over the cycling period. In contrast, the corresponding change observed for Pt/C is 27 mV and 24 mV for Pt_1/C (**Table 2-3**). This clearly evidence the stabilising effect of step edges and confiniment on the underlying Pt. **Table 2-3** summarises some electrochemical parameters and **Figure 2-31** shows durability characterization of the Pt1@S-GNF, Pt1/C and Pt/C obtained before and after durability test.

Table 2-3. Summary of electrochemical parameters for Pt_1@S-GNF, Pt_1/C and Pt/C before and after 5000 cycles durability tests.

	ECSA (m^2/g)	**Theoretical surface area of NP (m^2/g)**	**Average NP Size (nm)**	**Half-wave potential at 1600 rpm (V)**	**Specific activity at 0.85 V (mA/cm^2)**	**Mass Activity at 0.85 V (mA/cm^2)**	**Tafel slope @ RT (mV/dec) lcd/hcd**
Pt_1@S-GNF	24±4	32±8	8.7±3.1	0.753	0.24	0.06	72/121
Pt_1@S-GNF after	18±2	20±4	14 ±3.4	0.748	0.19	0.041	90/143
Pt_1/C	40±5	39±8	7.2±1.7	0.717	0.19	0.044	96/149
Pt_1/C after	29±4	31±7	8.8±2.1	0.693	0.13	0.025	84/138
Pt/C	74±12	85±15	3.3±0.7	0.840	0.544	0.396	95/136
Pt/C after	56±8	60±9	4.7±0.8	0.813	0.312	0.182	75/131

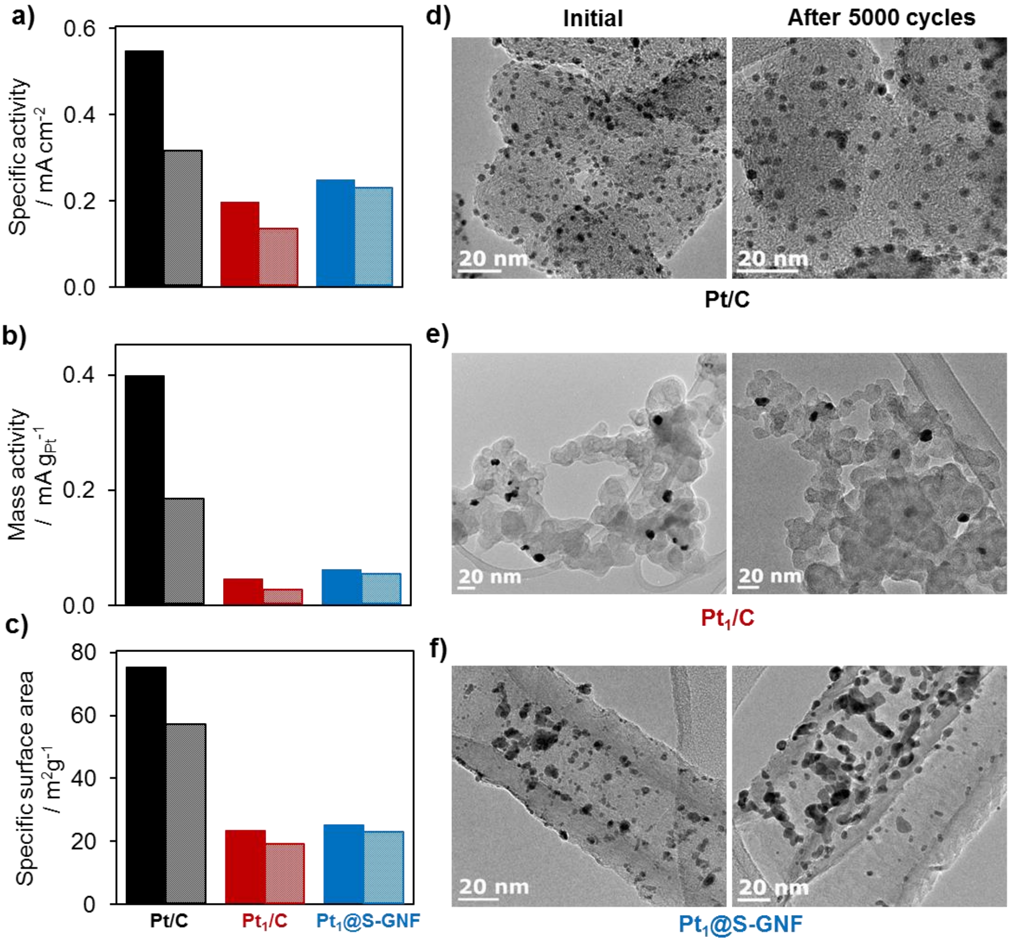

Figure 2-31. Durability characterization of the Pt_1@S-GNF, Pt_1/C and Pt/C, by cycling 5000 times the potential between 0.6 and 1.1 V (vs RHE) in an oxygen saturated 0.1 M $HClO_4$ electrolyte at RT with a sweep rate of 100 mV/s: (**a-c**) summary of the specific activity, mass activity and specific surface area (**d-f**) HRTEM characterization of the catalysts before and after the potential cycling.

2.4.3. Study of the Pt-GNF materials for ORR obtained the in-situ formation by decomposition of a volatile complex

2.4.3.1. Synthesis of P_2@S-GNF

Another common *in situ* method involving decomposition of a volatile complex $Pt(acac)_2$ at 400 °C inside S-GNF leads to the formation of PtNP adsorbed randomly on the external and internal surface of GNF (Pt_2@S-GNF) (**Figure 2-32**).

2.4.3.2. *Structural characterisation*

I*n situ* method involving decomposition of the volatile complex inside S-GNF leads to the formation of PtNP did not attached to the step-edges, with a broad size distribution (6.0 ± 1.6 nm), which again is inferior to the sample obtained from pre-formed PtNP. However, TGA analysis for Pt_2@S-GNF showed much lower loading that the one obtained from the impregnation $H_2PtCl_6 \cdot 6H_2O$ solution followed by thermal reduction Pt_1S-GNF (**Figure A- 4**).

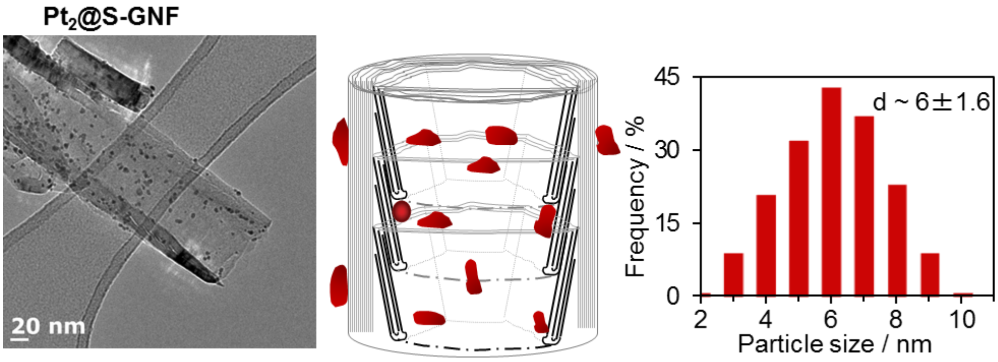

Figure 2-32. HRTEM images, schematic diagrams, particle size distributions and average sizes of PtNP for Pt_2@S-GNF.

High-resolution TEM measurements performed for Pt_2@SWNT and Pt_2@S-MWNT (**Figure 2-33**) showed that meanwhile SWNT was successfully filled with $Pt(acac)_2$ molecules in the gas phase, MWNT ends remain close after ball milling hindering their filling. Thus, acid treatment is required prior ball milling to effectively open the MWNT ends.

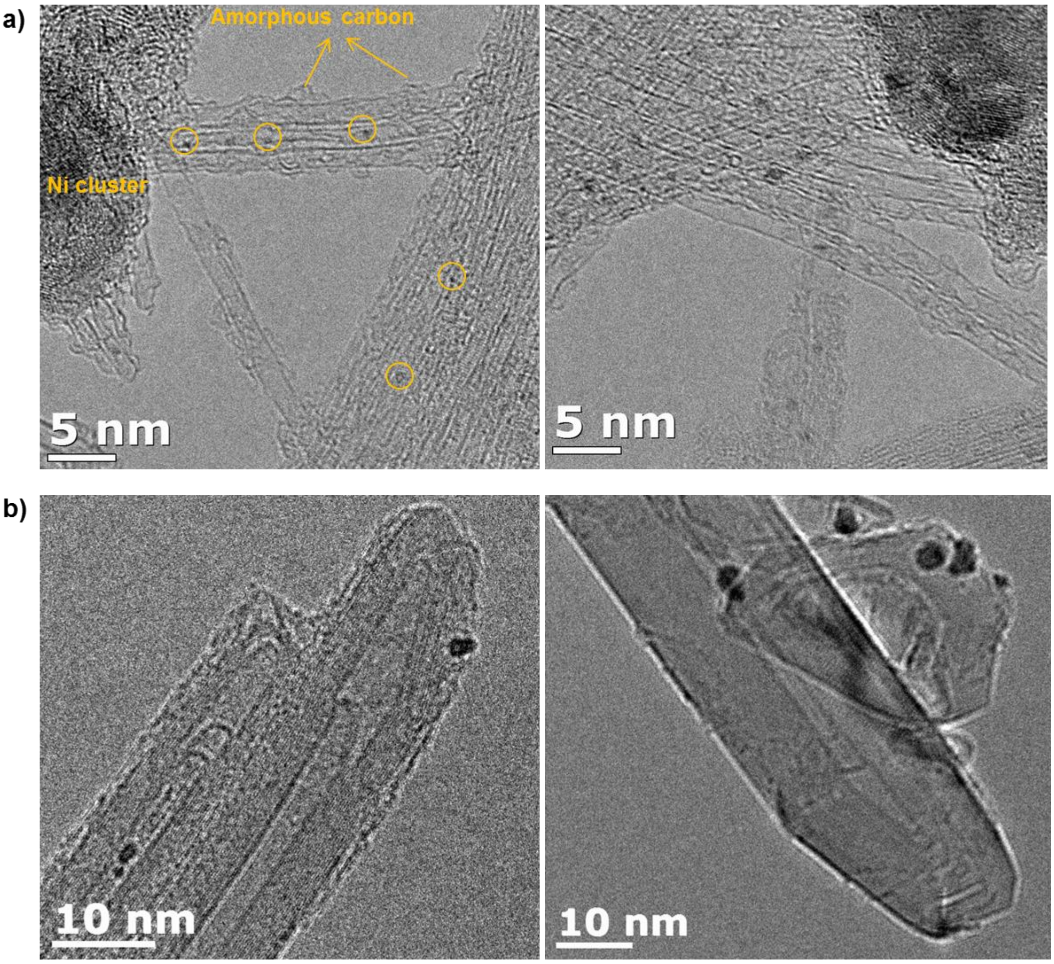

Figure 2-33. HRTEM images of (**a**) Pt_2@SWNT that yellow circles represent PtNP in SWNT and (**b**) Pt_2@S-MWNT.

2.4.3.3. Electrochemical properties towards ORR

Pt_2@SWNT, Pt_2@S-MWNT and Pt_2@S-GNF were evaluated electrochemically by CV between 0.05 and 1V (vs RHE) at room temperature in a nitrogen purged $HClO_4$ electrolyte (**Figure 2-34**). The shape of the hydrogen desorption (H_{des}) region for Pt_2@S-MWNT and Pt_2@S-GNF is very similar to that observed for the Pt/C electrocatalyst and also demonstrates the same typical H-adsorption and desorption features in the potential window between 50 and 300 mV (**Figure 2-34**). However, the behaviour of Pt_2@SWNT seems to be quite different with respect to the one observed for the other electrocatalyts. We believe that the capacitance effect of the carbon coated nickel particles (30%) used during the production of the SWNT play an important role on the electrochemical properties. Moreover, the obtained ESCA for Pt_2@SWNT seems to be in disagreement with the theoretical atom surface area value obtained from TEM (**Table 2-4**). Therefore, the CV results for Pt_2@SWNT should be carefully considered.

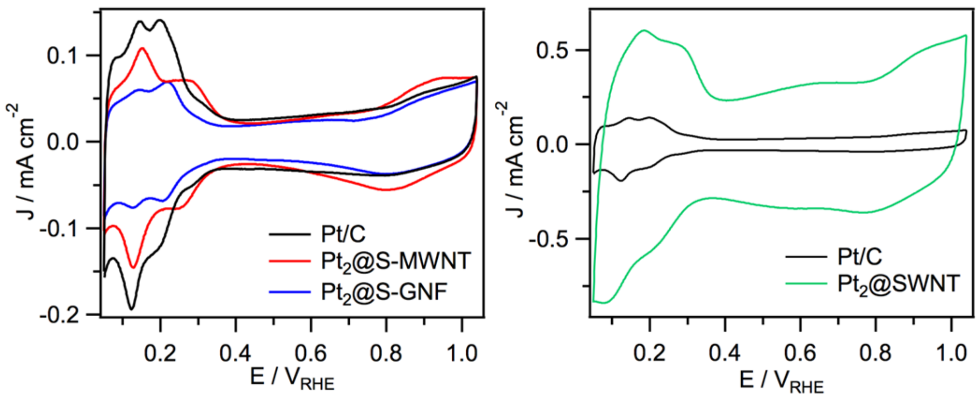

Figure 2-34. Voltammograms of Pt_2@SWNT, Pt_2@S-MWNT, Pt_2@S-GNF and Pt/C in nitrogen saturated 0.1 M $HClO_4$ at room temperature; current densities were normalised to the geometric electrode area.

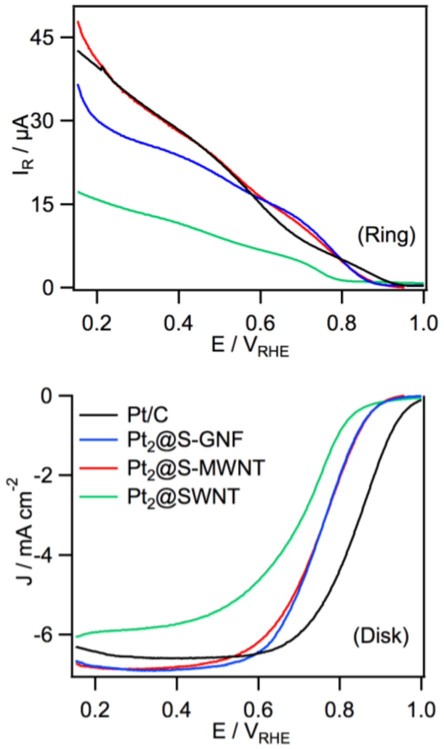

Figure 2-35. Disk and ring currents obtained during the ORR in the anodic sweep on Pt$_2$@SWNT, Pt$_2$@S-MWNT, Pt$_2$@S-GNF and Pt/C at room temperature at scan rate of 5 mV/s.

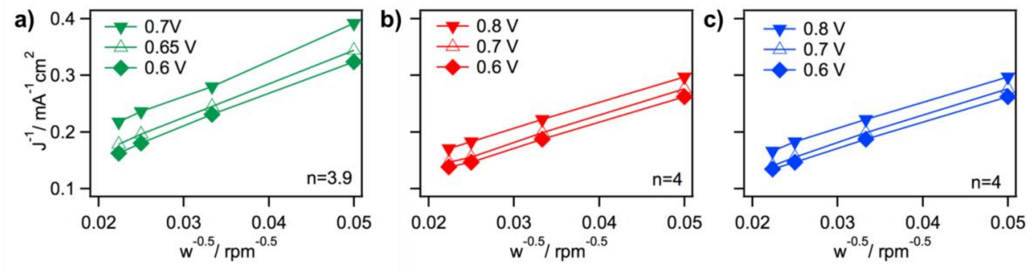

Figure 2-36. Koutecky-Levich plots for (**a**) Pt$_2$@SWNT, (**b**) Pt$_2$@S-MWNT and (**c**) Pt$_2$@S-GNF at various potentials extracted from the data I-V curves (current densities normalized to the geometric electrode area)**.**

Figure 2-35 show a sample set of ring-disk measurements for Pt$_2$@SWNT, Pt$_2$@S-MWNT and Pt$_2$@S-GNF in O_2 saturated 0.1M $HClO_4$ at room temperature and the respective Koutecký-Levich plots (**Figure 2-36**). The ORR in the studied electrocatalysts seems to take place through the same reaction mechanism that the rest of electrocatalysts analysed in this report. From this curve is easy to see that Pt$_2$@SWNT display a different behaviour to the rest of electrocatalyts hybrid materials.

In the kinetic region within the potential range between 0.9 V and 0.7 V two Tafel slopes can be observed for Pt_2@SWNT, Pt_2@S-MWNT and Pt_2@S-GNF (**Figure 2-35**). The low Tafel slope represents a region where the ORR occurring on oxide–covered Pt and for the high Tafel slope the ORR proceeds on metallic Pt surface (**Figure 2-12**). It should be noted that the measured cell resistance has been corrected only with IR losses, as we are primarily interested in highlighting changes in Tafel slope with catalyst confinement. Interestingly, at high current (low potential) the slope found for Pt_2@S-GNF (135 mV/dec) is higher than the value found for Pt_2@S-MWNT and Pt/C (**Figure 2-37** and **Table 2-4**) and also slightly higher than the pure kinetic value of 120 mV/dec showing that the diffusion limiting losses inside nanocontainers are less important than expected. In contrast, the slope at high current for Pt_2@S-GNF is much lower than the value found for Pt_2@SWNT (212 mV/dec), thus the mass diffusion problems of O_2 into SWNT during the ORR are expected for containers with very narrow diameters

It is clearly observed that the performance of the studied electrocatalysts follows this trend Pt/C > Pt_2@S-GNF > Pt_2@S-MWNT > Pt_2@SWNT for an identical (total) metal loading (**Figure 2-38).** Interestingly, both Pt_2@S-GNF and Pt_2@S-MWNT show same mass activity, however for Pt_2@S-GNF the specific activity is much higher (**Table 2-4**). The specific surface area value observed for Pt_2@SWNT is not well understood as mass diffusion problems of O_2 into SWNT during the ORR are expected for containers with very narrow diameters (**Figure 2-38**).

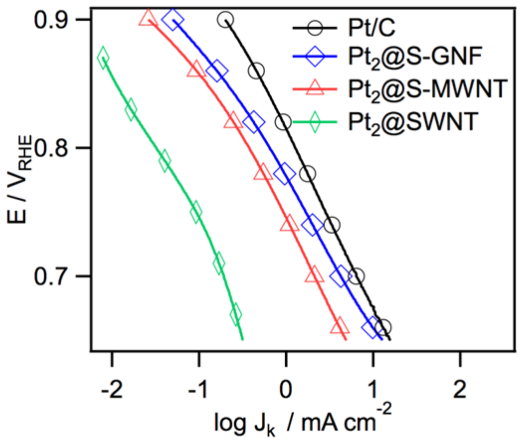

Figure 2-37. Tafel plots for the ORR at room temperature, anodic sweep 5 mV/s, 1600 rpm on standard Pt/C, Pt$_2$@SWNT, Pt$_2$@S-MWNT and Pt$_2$@S-GNF catalysts.

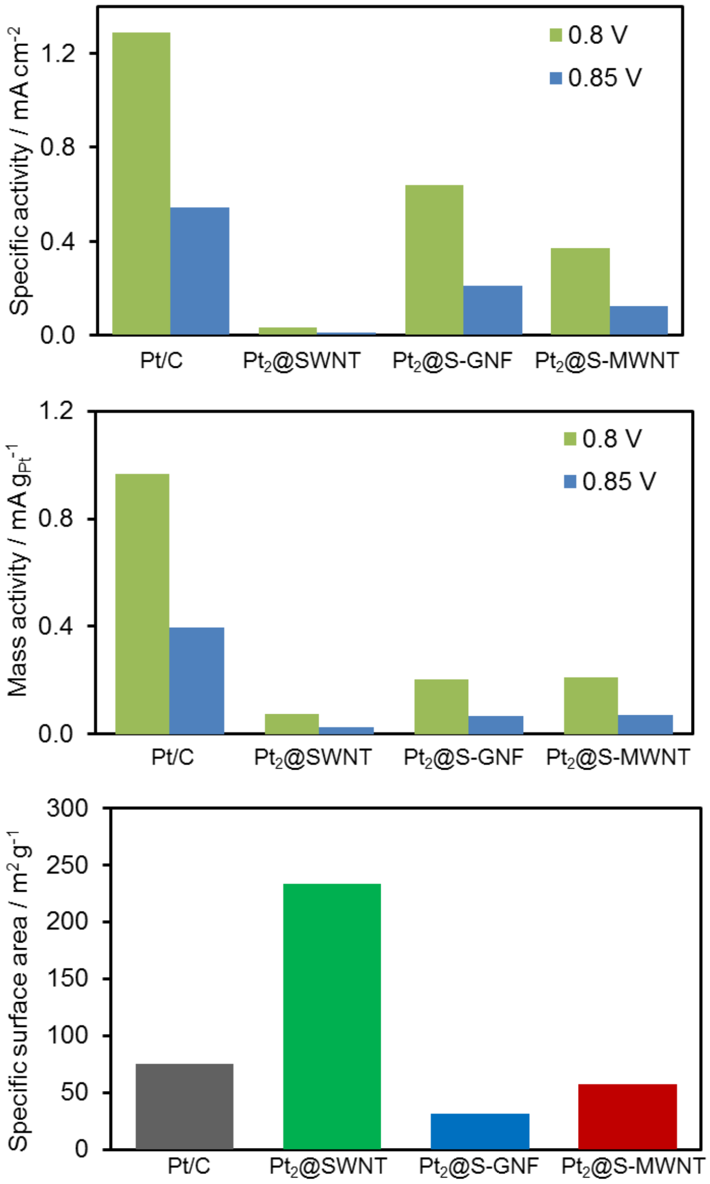

Figure 2-38. Summary of specific surface area, the specific activity, mass activity, and specific surface area.

It is significant that the specific activities obtained for the electrocatalysts (Pt_1@S-GNF and Pt_2@S-GNF) where PtNP were prepared *in situ* in GNF are lower than that for PtNP@S-GNF, indicating that the approach involving the encapsulation of pre-formed nanoparticles with well-determined size and shape allows PtNP to be positioned more effectively at the step-edges, and therefore providing stronger interaction with GNF nanocontainers.

Table 2-4. Summary of electrochemical parameters for Pt_2@SWNT, Pt_2@S-MWNT, Pt_2@S-GNF and Pt/C.

	ECSA (m^2/g)	**Theoretical surface area of NP (m^2/g)**	**Average NP size (nm)**	**Half-wave potential at 1600 rpm (V)**	**Specific activity at 0.85 V (mA/cm^2)**	**Mass Activity at 0.85 V (mA/cm^2)**	**Tafel slope @ RT (mV/dec) lcd/hcd**
Pt_2@SWNT	233±4	350±40	0.8±0.1	0.707	0.011	0.026	105/212
Pt_2@S-MWNT	57±7	62±7	4.5±0.6	0.756	0.12	0.066	85/120
Pt_2@S-GNF	31±3	47±10	6±1.6	0.756	0.21	0.07	80/135
Pt_2@S-GNF after	18±2	28±5	10±2.4	0.702	0.15	0.03	90/150
Pt/C	74±12	85±15	3.3±0.7	0.840	0.544	0.396	95/136
Pt/C after	56 ± 8	60 ± 9	4.7 ± 0.8	0.813	0.312	0.182	75/131

2.4.3.4. Durability test

Durability studies of the selected electrocatalyst were pre formed in a durability test by continuously applying linear potential sweeps from 0.6-1.1V, which causes surface oxidation/reduction cycles of platinum. For comparison, a Pt/C commercial catalyst with the same Pt loading as that in Pt_2@S-GNF was subjected to the same potential conditions, and after 5000 cycles, the changes in the Pt surface area and the electrocatalytic activity towards the ORR were carefully determined (**Table 2-4**, **Figure 2-39**). After cycling the specific activity of Pt_2@S-GNF (from 0.21 to 0.15 mA/cm^2) slightly decrease than the specific activity of Pt/C commercial catalyst (from 0.544 to 0.312 mA/cm^2). This clearly indicates that the durability of Pt_2@S-GNF is better than the commercial catalyst despite the specific activity of Pt_2@S-GNF is lower than the Pt/C (**Figure 2-39**).

A significant change in particle size or morphology was found for Pt_2@S-GNF after cycling that is in contrast with that observed for the electrocatalyst materials obtained by *pre-formed nanoparticle* approach. As it is shown by the TEM, the average size of the PtNP change by c.a. 4 nm. The surface area of contact between the PtNP and S-GNF in Pt_2@S-GNF is maximized when the PtNP are located at the apexes of the graphitic facets of step-edges, which leads to an improvement in the van der Waals interactions between the PtNP and the CN. However, HRTEM shown that PtNP are located randomly internal and external surface of GNF. Therefore, this is not favourable interaction, occurring at the step-edges, immobilises the nanoparticles, thus not preventing their migration and growth above 6 nm in diameter during electrochemical reactions. This is in agreement with the marginal change in the specific and mass activity observed for Pt_2@S-GNF (**Table 2-4**).

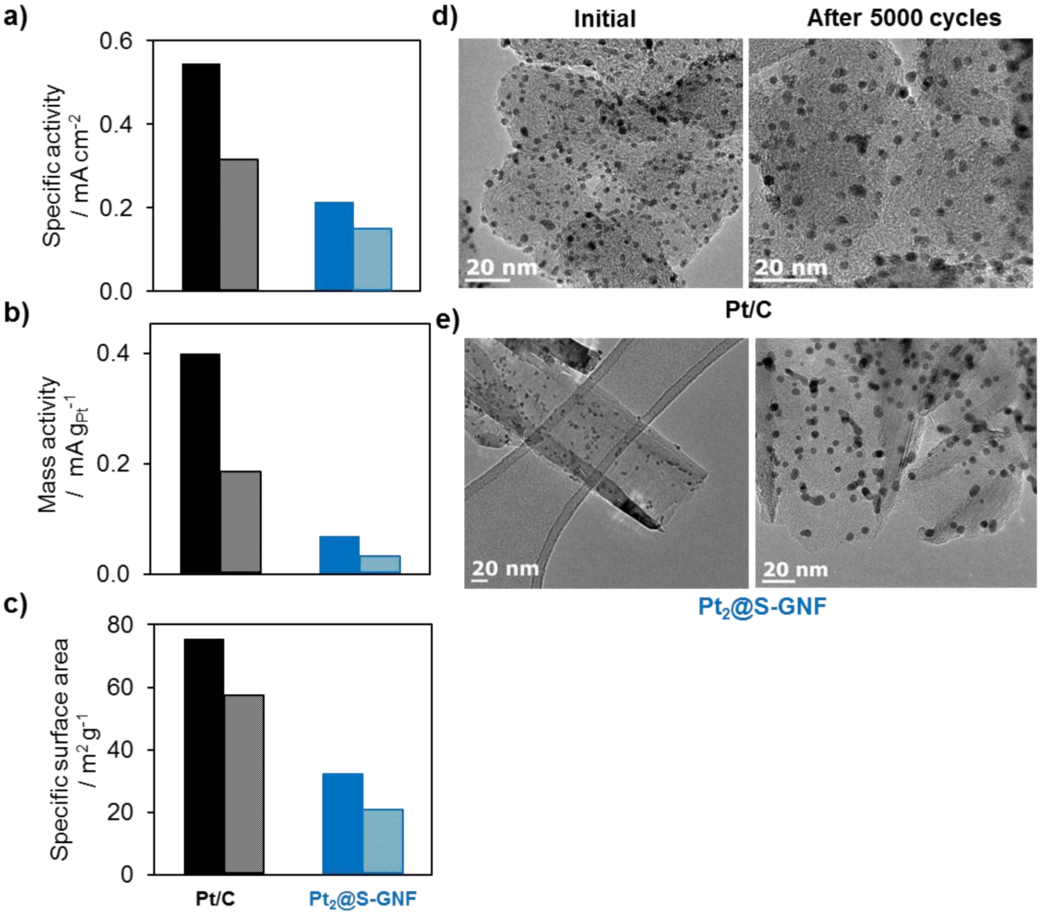

Figure 2-39. Durability characterization of the Pt/C and Pt_2@S-GNF by cycling 5000 times the potential between 0.6 and 1.1 V (vs RHE) in an oxygen saturated 0.1 M $HClO_4$ electrolyte at room temperature with a sweep rate of 100 mV/s. (**a**-**c**) Summary of the specific activity, mass activity and specific surface area (mass transfer corrected (**d**-**e**) HRTEM images of the catalysts before and after potential cycling.

Similarly, an important change in particle size and morphology was found for the commercial catalyst Pt/C from 3.3 ± 0.7 nm to 4.7 ± 0.8 nm, respectively, as shown by the TEM (**Figure**

2-39 and **Table 2-4**). Moreover, the ECSA values obtained for Pt/C are in agrement with significant changes in PtNP size. This may indicate that carbon black as a support material not having long-range order in the graphitic lattice suffered from electrochemical corrosion that aggravated the PtNP sintering and further reduced the durability of Pt/C.

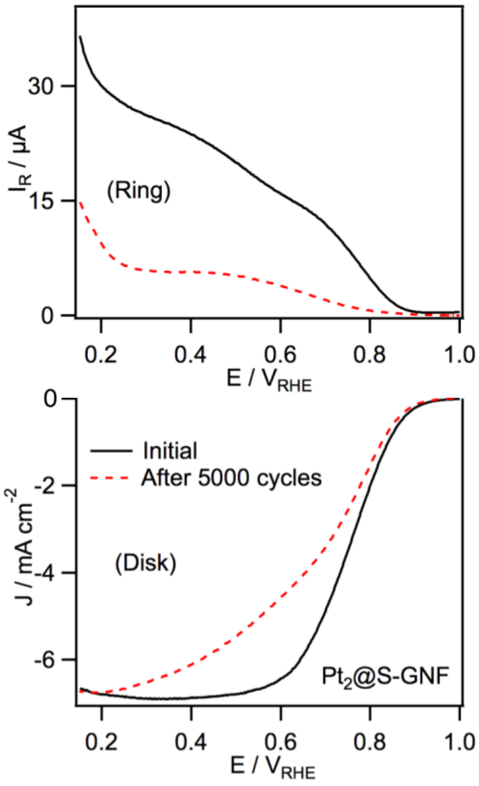

Figure 2-40. Ring and disk currents obtained during the ORR in the anodic sweep before (solid line) and after (dash line) 5000 cycles on Pt_2@S-GNF at room temperature at scan rate of 5 mV/s; current densities (*J*) normalized to the geometric electrode area.

For Pt_2@S-GNF, measured as the currents of O_2 reduction obtained before and after potential cycling shows a 54 mV degradation in half-wave potential of ORR polarization curves over the cycling period (**Figure 2-40**). Futhermore, a significant change in the polarization curves of H_2O_2 oxidation was found for this electrocatalyst. This provides evidence of unstabilise PtNP while locating randomly internal and external surface of S-GNF. In the same way, Pt/C showed the degradation in half-wave potential of 27 mV, respectively (**Figure 2-16**). Carbon black as support materials may be poorly connected with the catalyst NP due to corrosion suffered in the durability experiment, thus leading to high electron transfer resistance and undesired increase in ORR overpotential. It is worth noting that preformed PtNP encapsulated into S-GNF (PtNP@S-GNF) is the only material that is able to maintain constant size of PtNP and ECSA area after potential cycling, **(Table 2-1)** which demonstrates the importance of catalyst confinement in the nanocontainer.

Figure 2-41 compares the Tafel plots within the potential range between 0.9 V and 0.7 V for the mass transport corrected specific current densities at a rotation rate of 1600 rpm for Pt_2@S-GNF and Pt/C before and after durability test.

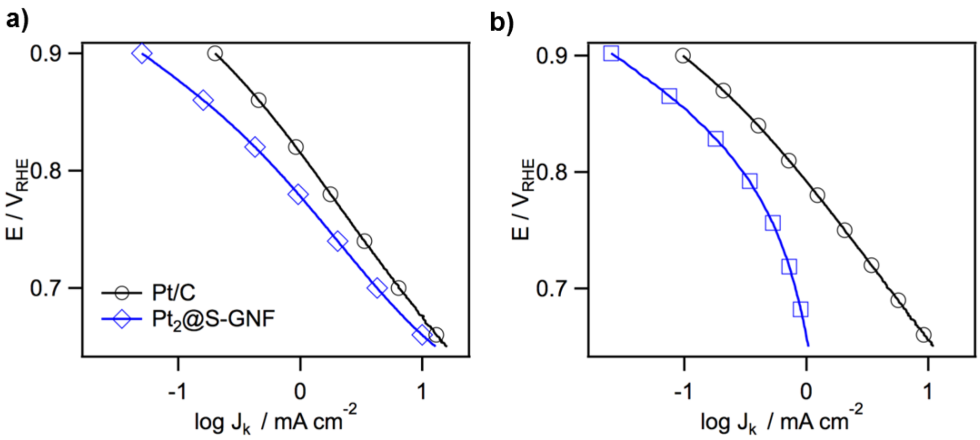

Figure 2-41. Tafel plots for the ORR normalised to the real surface area at room temperature, anodic sweep 5 mV/s, 1600 rpm on Pt_2@S-GNF Pt/C. (**a**) before and (**b**) after 5000 cycles.

2.4.4. Comparing three study of electrocatalytic performance using different insertion methods

The electrocatalytic performance for ORR of the hybrid PtNP in S-GNF electrocatalyst materials obtained using three different insertion methods (**1**-Ex-situ insertion of preformed PtNP, **2**-In-situ chemical reduction of PtNP, **3**- In-situ thermal decomposition of a volatile Pt complexes) can be easily compare by analysing their respective Tafel plots (**Figure 2-42**). PtNP@S-GNF by far has the highest catalytic activity compared to Pt_1@S-GNF and Pt_2@S-

GNF that show similar behaviours, which is in agreement with what is observed in **Table 2-4**. A comparison of the specific activities of PtNP@S-GNF, Pt_1@S-GNF and Pt_2@S-GNF electrocatalysts at 0.85 V (vs. RHE) is given in **Table 2-4**. The specific activity of PtNP@S-GNF reaches 0.36 mA/cm^2, which is higher than that of Pt_1@S-GNF (0.244 mA/cm^2) and Pt_2@S-GNF (0.21 mA/cm^2). Therefore, the method involving the encapsulation of preformed PtNP into S-GNF seems to be better approach compared other two in-situ methods for preparing PtNP in S-GNF electrocatalyst materials.

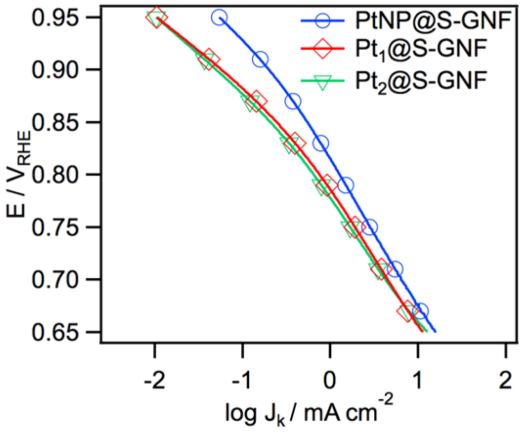

Figure 2-42. Tafel plots for the ORR at room temperature, anodic sweep 5 mV/s, 1600 rpm on PtNP@S-GNF, Pt_1@S-GNF and Pt_2@S-GNF

This may indicate that the ex-situ encapsulated performed PtNP interacts stronger with the step-edges than the in-situ formed PtNP that contribute to improve the interaction and charge trasnfer between PtNP and GNF. Furthermore, this ex-situ method provides a better control over the size, shape and most important atomic structure of PtNP than chemical impregnation followed by reduction or thermal decomposition of a volatile complex. This could contribute to improve interaction between Pt atoms and O_2 during ORR, and caused enhancement of ORR activity.

2.5. Conclusion

We developed a method of assembly electrocatalytically active hybrid nanomaterials where pre-formed platinum nanoparticles are inserted into hollow graphitised nanofibers. The nanofibers play a dual role: a nanoscale container confining and controlling the environment around nanoparticles, and a highly electrically conducting support effectively connecting the catalytically active nanoparticles to the electrode. We discovered that PtNP interact much stronger with the graphitic step-edges of the GNF cavity than the smooth exterior of GNF or carbon black support. While the graphic step-edge improves the electric contact between PtNP and electrode, and substantially enhances durability of PtNP during the electrocatalytic cycle, the GNF cavity creates conditions highly beneficial for oxygen reduction reaction on PtNP. As a result, the electrocatalytic nanoreactors PtNP@S-GNF, where nanofibers are shortened to improve the mass transport during the reaction, have been demonstrated to possess initial ECSA comparable to best Pt/carbon electrocatalysts reported to date, and outstanding durability retaining much of their activity over the long-term (50,000 potential cycles) thus outperforming all known electrocatalysis for oxygen reduction reaction. The remarkable and unexpected properties of Pt nanoparticles within carbon nanocontainers open new avenues for improving durability of electrochemical devices and enhancing sustainable use of Pt and other elements with critically low abundance to ensure future technological progress.

Chapter 3. Bifunctional manganese oxide-carbon nanostructure (Mn_3O_4-CN) electrocatalyst for ORR/OER

3.1. Introduction

The performance of oxygen reduction reaction (ORR) and oxygen evolution reaction (OER) is hindered by its slow kinetics and consequent demand of a high overpotential to drive these electrochemical reactions.[175] In addition, although Pt-based catalysts are the best ORR catalysts, they are not effective for OER, due to the production of Pt oxides on the catalyst surface at high overpotentials, hindering their catalytic ability for OER.[176] Similarly, the most active catalysts for OER such as RuO_2 and IrO_2,[62-72] are also much less effective for ORR.[177] For all these reasons, it is highly challenging to develop efficient bi-functional catalysts for both ORR and OER. It is worth noting that these two reactions have attracted a great deal of attention in the field for their implications in unitized regenerative fuel cells that are promising systems in energy storage, working as a fuel cell and in reverse as a water electrolyzer producing H_2 and O_2 to feed the fuel cell.

Non-noble metal oxides with a spinel structure have aroused considerable attention as ORR/OER catalysts in alkaline solution. Cobalt- and manganese-based spinel-type oxides, including binary oxides (Co_3O_4) and ternary oxides ($NiCo_2O_4$, $CoMn_2O_4$, $LiCo_2O_4$, etc.), are the most studied.[175, 178] However, the disadvantages of spinel oxides for ORR/OER catalysis are their poor electronic conductivity and weak oxygen sorption on the surface of spinel oxides, which in turn leads to poor catalytic activity.[179, 180] Different synthetic strategies including mixing or supporting on conducting materials have been developed to overcome these problems. Thus, carbon and its derivatives, with large surface area, superior electronic conductivity, good mechanical properties, and excellent chemical stability, are identified as the superior conductive support for ORR/OER catalysts.[181]

In 2011, Dai et al.[43] reported a general two-step method to synthesize Co_3O_4/N-doped reduced graphene oxide (naming it Co_3O_4/N-rGO) nanomaterials as bifunctional catalyst for ORR and OER (**Figure 3-1**). They demonstrated that their ORR and OER performance can be enhanced dramatically by integrating Co_3O_4 and N-doped graphene. They explained that the synergetic chemical coupling effects between Co_3O_4 and graphene can enhance the catalytic activity of ORR and OER. Along the same lines, a variety of hybrid catalysts, such as Co_3O_4/N-doped carbon nanoweb,[182] $MnCoO_4$/ graphene,[181] $FeCo_2O_4$/hollow graphene spheres,[180] etc., have been fabricated for high efficiency bifunctional catalysts.

Within non-noble metal oxides with a spinel structure mixed valence manganese oxides like Mn_3O_4 have attracted attention due to the fact that they are low-cost, environment friendly, and highly active.[183] Although these oxide nanostructures have been well-exploited for supercapacitor and battery applications, only a handful papers describes their performance towards ORR when they are hybridised with carbon to improve their low electrical conductivity.[184, 185] For instance, Dai et al. synthesised the ORR activity of electrically interconnected hybrid material based on graphene oxide-carbon nanotubes-Mn_3O_4.[186] And Qiao et al. reported the synthesis of mesoporous Mn_3O_4-nitrogen doped graphene by a solvothermal route.[187] Recently, Raj et al. demonstrated the single-step synthesis of nitrogen-doped reduced graphene oxide-Mn_3O_4 hybrid for the ORR from graphene oxide (GO) and Mn(VII) using hydrazine.[188]

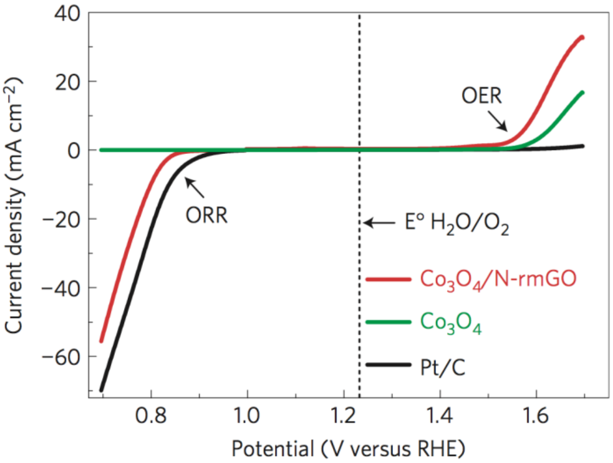

Figure 3-1. Polarisation curves of ORR and OER for Co_3O_4/NrmGO hybrid, Co_3O_4 nanocrystals and Pt/C catalysts in O_2-saturated 0.1M KOH.[43]

3.2. Aim, objectives and scope of experiments

In this chapter we will study the bifunctional behaviour towards ORR and OER of new hybrid carbon nanomaterials (developed in my group by Dr. Maria Gimenez-Lopez and Carlos Herreros-Lucas) based on (**i**) preformed and (**ii**) in-situ synthesised Mn_3O_4 nanoparticles (NP) supported or encapsulated within graphitised carbon nanofibers (GNF).

Mn_3O_4 nanoparticles (NP) with a unique mixed- valence state has been already performed as an active electrocatalyst in redox reactions.[189] The coexistence of Mn^{2+} and Mn^{3+} can facilitate the creation of defects, which would affect the electronic properties between Mn_3O_4 and the carbon material. As in the case of other NP, nanostructured supports are much desired to stop Mn_3O_4 nanoparticles from dissolving and sintering during catalytic processes to improve their performance.[190] In this work, we proposed to use the stabilizing effects of the corrugated interiors of GNF composed of rolled-up graphene sheets (nanocones) (**Figure 3-3d**) to improve stability of Mn_3O_4 NP, which are known to be highly labile in ORR and OER conditions.[185]

In this chapter we will pursue:

1- To test confinement effects on the electrocatalyst behaviour of preformed Mn_3O_4 NP when are confined within GNF (Mn_3O_4@GNF). To this end, Mn_3O_4NP supported on surface of GNF will be also studied (Mn_3O_4/GNF). Here, we will prove whether the corrugated interiors of GNF (**Figure 3-3d**) can serve as anchoring points to stabilise the electrocatalytic Mn_3O_4 NP to avoid ripening and aggregation.

2- To evaluate whether the graphitisation of the carbon support has an influence on the performance of the Mn_3O_4 NP towards ORR and OER, preformed Mn_3O_4NP will be supported in carbon nanotubes and graphite flakes.

3- To study whether the synthetic procedure chosen for the hybrid preparation has an effect on the electrochemical activity and durability, in-situ synthesised Mn_3O_4NP were encapsulated inside and also supported on GNF.

4- To prove whether the length of the chosen GNF has an effect of the transport resistance of reactants/products on the electrocatalytic performance of the hybrid.

5- To test the suitability of GNF and S-GNF as supports for electrocatalytic nanoparticles.

The electrocatalytic activity for the ORR and the OER of these new hybrid electrocatalysts were evaluated and compared with Pt/C for the ORR and Ir/C commercial electrocatalyst for OER.

3.3. Experimental Section

3.3.1. General

XRD patterns were obtained on a Bruker AXS D8-Advanced diffractometer with Cu Kα radiation (λ=1.5418 Å). TGA analyses were performed in a TA/TGA Q500 instrument. Samples for TEM analysis were prepared dispersing the material either in hexane or HPLC grade iso-propanol by ultasonication, and then drop casting the solution onto lacey carbon film coated copper grid. The samples were dried under nitrogen gas flow for 3 minutes to remove any residual solvent. HRTEM image was obtained on a JEOL 2010F TEM using accelerating voltage of 200 kV. To maximise the active surface area of these electrocatalyst, a thermal procedure for the removal the organic surfactant surrounding Mn_3O_4NP was applied by Carlos Herreros-Lucas before structural characterisation and electrochemical analysis for all electrocatalysts.

3.3.2. Electrochemical measurements

The electrochemical experiments were performed on an electrochemical work station Autolab potentiostat PGSTAT204 using a glassy carbon electrode (GCE) as working electrode in a commercial (Pine Instruments) GCE disk electrode, a HydroFlex reversible hydrogen electrode (RHE) electrodes as reference electrodes, respectively. The GCE was cleaned with 0.05µm principal particle size alumina powder solution (Agar Scientific Ltd.) on a polishing paper to remove any impurity which may affect electrochemical measurements. The investigated samples were dropped onto the GCE as ink with an optimised constant metal loading of 100 µg/cm^2 and then dried in air[156, 157]. The potential was cycled at fast scan rates (500 or 200 mV/s) for up to 100 cycles before readings were taken in order to remove any impurities and unwanted species from the surface of the platinum electrodes. Impedance measurements, the cell resistance was measured immediately after OER and ORR measurements taking the ac impedance spectra from 32 to 0.1 kHz and a voltage perturbation of 10 mV. The real part of the resistance at 1 kHz was taken as the cell resistance and was used to obtain the IR-free potential of the working electrode.

All measurements for OER and ORR were conducted at 10 mVs^{-1} under O_2 (99.994%, Airgas) saturation at room temperature in 0.1M KOH from 1 to 1.9 V vs RHE for OER and from 1 to 0.2 V vs RHE at 1600 rpm for ORR. For the rotating disk electrode (RDE) measurements[158] for ORR the working electrode was scanned cathodically at a rate of 5 mVs^{-1} with varying rotating speed from 400 rpm to 2500 rpm. Electrochemical durability test was carried out by continuously applying linear potential sweeps up to 5000 cycles from 1.4 to 1.75 V vs RHE at 50 mV/s in KOH which caused surface oxidation/reduction cycles of catalysts. For comparison, Ir/C commercial catalysts with metal loading of 14 $\mu g/cm^2$ as that in the electrocatalysts were subjected to the same potential cycling conditions.

3.4. Results and discussion

3.4.1. Preformed approach synthesised bifunctional Mn_3O_4-CN electrocatalyst for ORR/OER

3.4.1.1. Structural characterisation of Mn_3O_4 -CN electrocatalysts

High-resolution transmission electron microscopy (HRTEM) images show oleylamine-stabilized manganese oxide (Mn_3O_4) nanobrick shaped nanoparticles to self-assemble into highly ordered (**Figure 3-2a**).[128] Energy-dispersive X-ray (EDX) spectrum of Mn_3O_4 shown in **Figure A- 12a,** confirmed the presence of manganese.

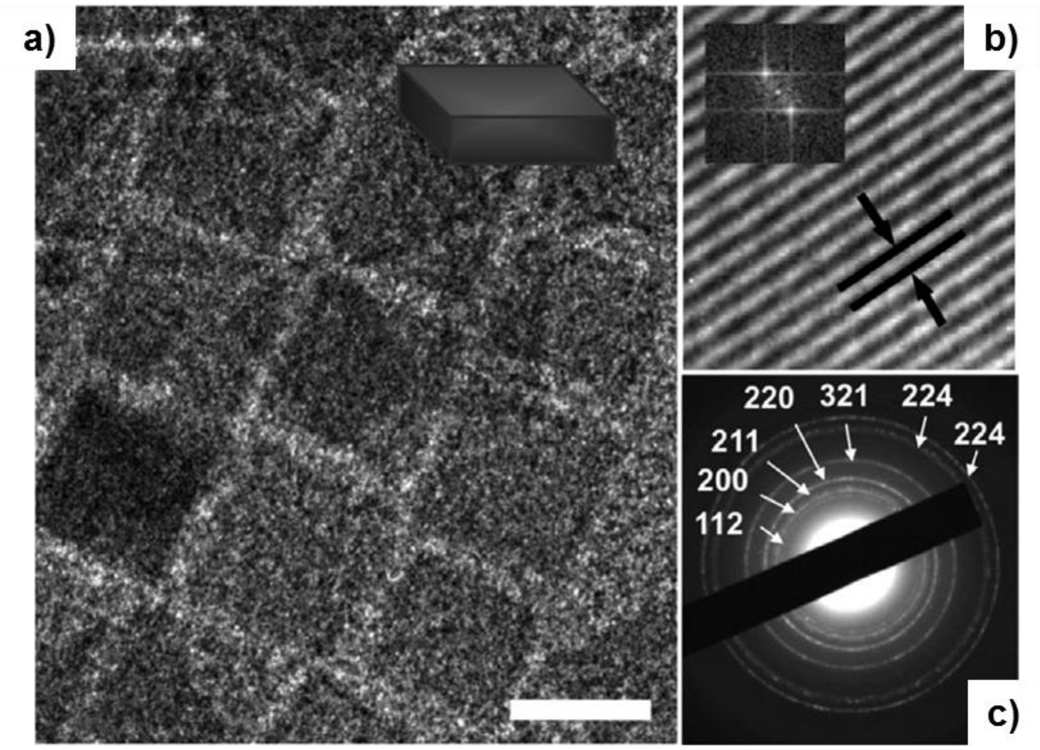

Figure 3-2. (**a**) HRTEM image of oleylamine-stabilized Mn_3O_4 nanobricks (with side dimensions of 11.4 ± 1.6 and 10.1 ± 1.5 nm and thickness of 5.7 ± 0.9 nm; the scale bar is 10 nm). (**b**) Lattice planes imaged parallel to the edge of a Mn_3O_4 NP correlating with a (200) d-spacing value of 0.288 nm (Inset: optical diffractogram). (**c**) Selected area electron diffraction (SAED) pattern showing clear diffraction rings indexed to the Mn_3O_4 spinel structure.[128]

Furthermore, HRTEM imaging investigation of Mn_3O_4@GNF, Mn_3O_4/GNF, Mn_3O_4/C, Mn_3O_4/GMWNT, Mn_3O_4@G1 and Mn_3O_4/G2 hybrid electrocatalysts were performed. The HRTEM observations show the large facets of the NP aligned with the GNF step-edge surfaces with an average diameter of 10.6 ± 0.8 nm (**Figure 3-3**). Mn_3O_4NP (**Figure 3-2**) were located at the internal step-edges (shown with white arrows in **Figure 3-3c**), encapsulated throughout the GNF. It is considered that this favoured orientation of Mn_3O_4@GNF is driven by a requirement to maximize NP-GNF interactions combined with a reduction of the Mn_3O_4NP surface area exposed to the environment (shown with black arrows in **Figure 3-3d**). Energy-dispersive X-ray (EDX) spectrum of Mn_3O_4@GNF shown in **Figure A- 12b**, confirmed the presence of manganese.

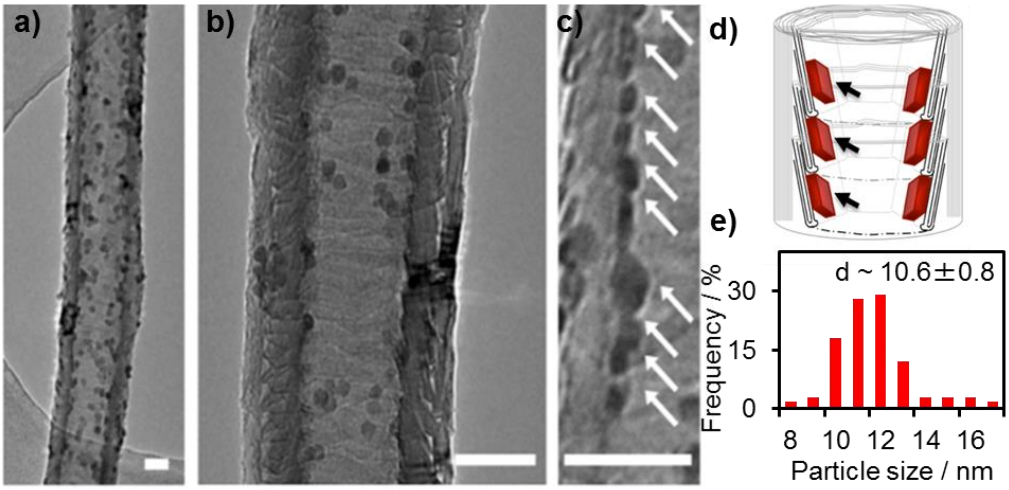

Figure 3-3. (**a-c**) HRTEM images of Mn_3O_4@GNF illustrating Mn_3O_4 encapsulated within a GNF through attaching to the graphitic step-edges. Scale bar are 100nm for a, 50nm for b and 20nm for c. (**d)** Schematic diagrams illustrating Mn_3O_4NP sparsely distributed within a GNF through anchoring to the graphitic step-edges, (**e**) particle size distributions and average size of Mn_3O_4 NP.[128]

In contrast for Mn_3O_4/GNF electrocatalyst, the nanoparticles are largely located on the smooth external surfaces of nanofibres shown in **Figure 3-4**. The external surfaces of GNF are smooth and have fewer defects in comparison to internal surface of GNF. Therefore, the NP can freely move on external smooth surface of GNF and then agglomerate to bigger nanoparticles. The particle size of nanoparticles of Mn_3O_4/GNF electrocatalyst was increased to 15.2 ± 1.7 nm after the thermal treatment for the removal of the organic surfactant surrounding Mn_3O_4 NP.

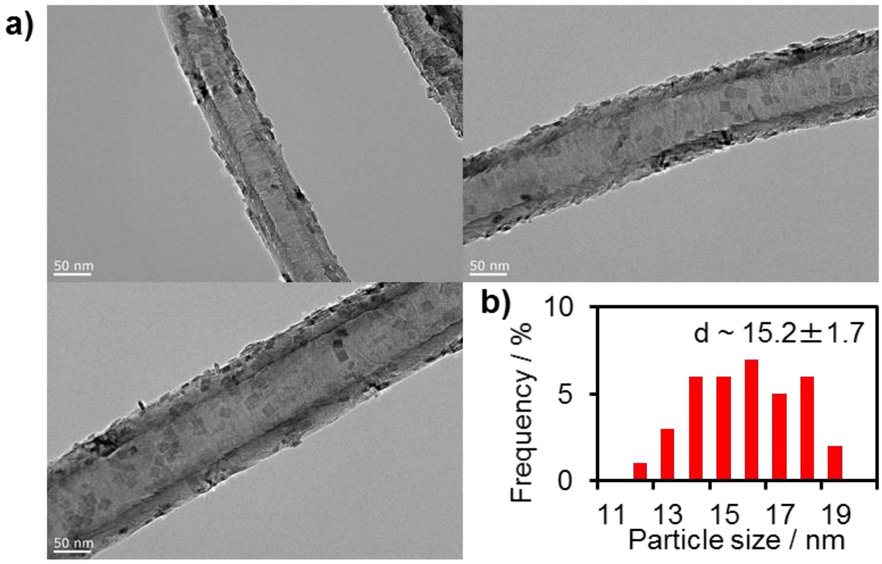

Figure 3-4. (**a**) HRTEM image of Mn_3O_4/GNF, (**b**) particle size distributions and average size of Mn_3O_4 NP.

Similarly, in **Figure 3-5** HRTEM imaging of Mn_3O_4/GMWNT electrocatalyst with an average diameter of 12.4 ± 4 nm and most of the Mn_3O_4 NP are located on the smooth external surface of GMWNT, but not well dispersed.

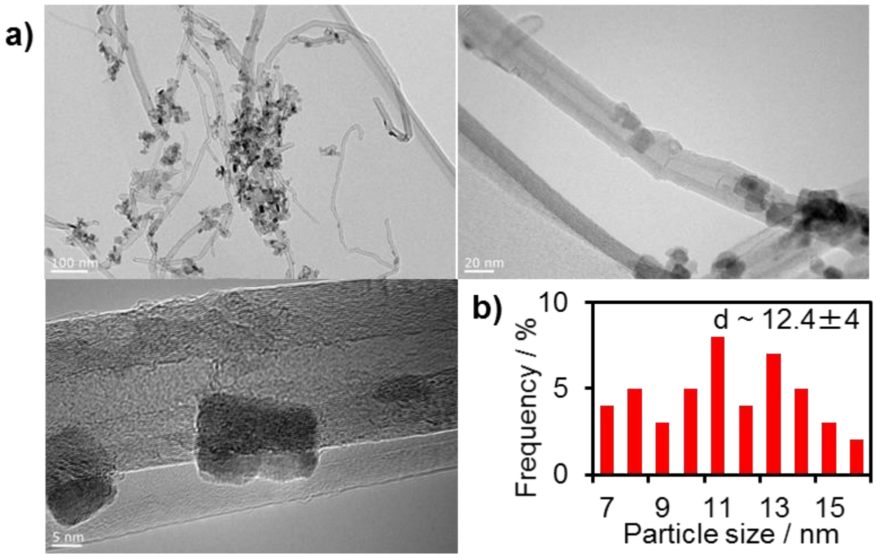

Figure 3-5. (**a**) HRTEM image of Mn_3O_4/GMWNT, (**b**) particle size distributions and average size of Mn_3O_4 NP.

The HRTEM imaging of the Mn_3O_4/C electrocatalyst illustrated in **Figure 3-6** shows that; the nanoparticles are not uniformly dispersed on carbon black (Vulcan XC-72R) with an average diameter of 18.1 ± 5 nm. The NP on carbon black agglomerated to bigger clusters.

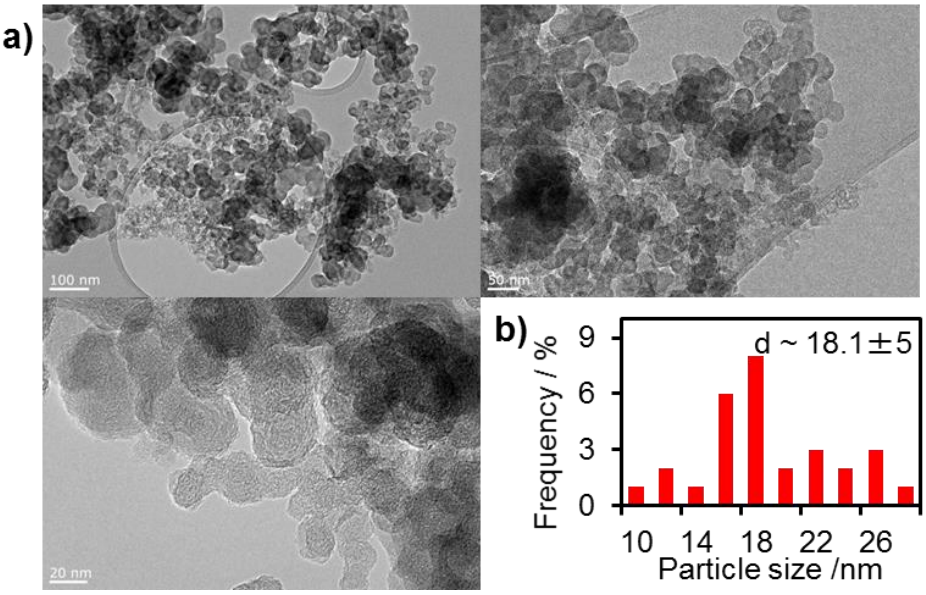

Figure 3-6. (**a**) HRTEM image of Mn_3O_4/C, (**b**) particle size distributions and average sizes of Mn_3O_4 NP.

In **Figure 3-7,** HRTEM imaging of the synthesised Mn_3O_4NP shows not uniformly dispersed on graphene-1 (G1) with an average diameter of 10.9 ± 2.7 nm. In contrast, apart from HRTEM images of the synthesised preformed Mn_3O_4NP shows uniformly dispersed on the ball milled graphene stacked graphite (G2) with an average diameter of 13 ± 2.6 nm (**Figure 3-8)**. The ball milling process provides carboxylic groups on G2. It is worth mentioning that the introduction of carboxylic groups that act as anchoring points for the PtNP in PtNP/Ox-S-GNF provides more uniform dispersion of the NP on the ball milled G2 when compared that of G1.

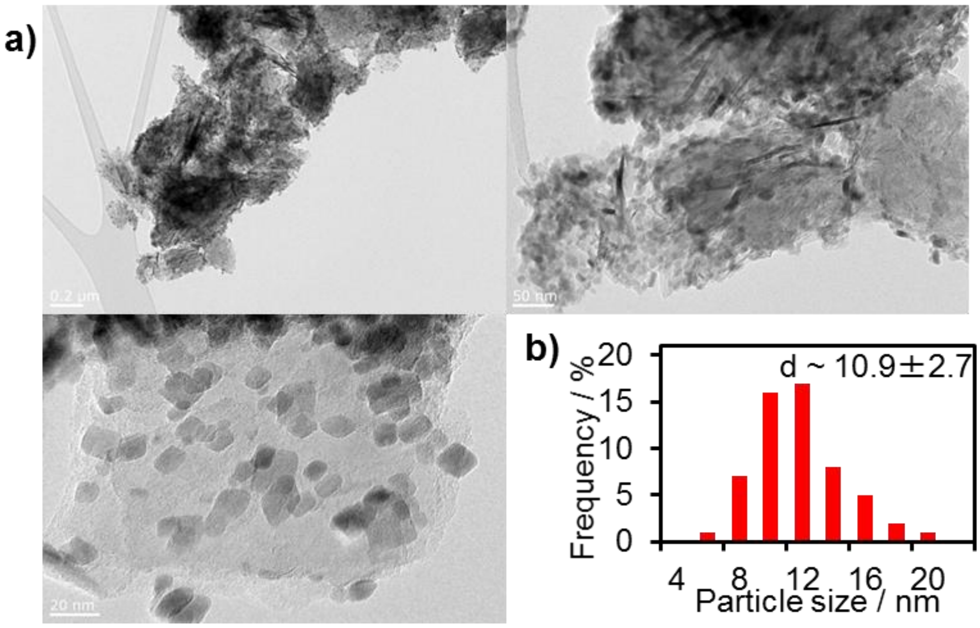

Figure 3-7. (**a**) HRTEM image of Mn_3O_4/G1, (**b**) particle size distributions and average sizes of Mn_3O_4 NP.

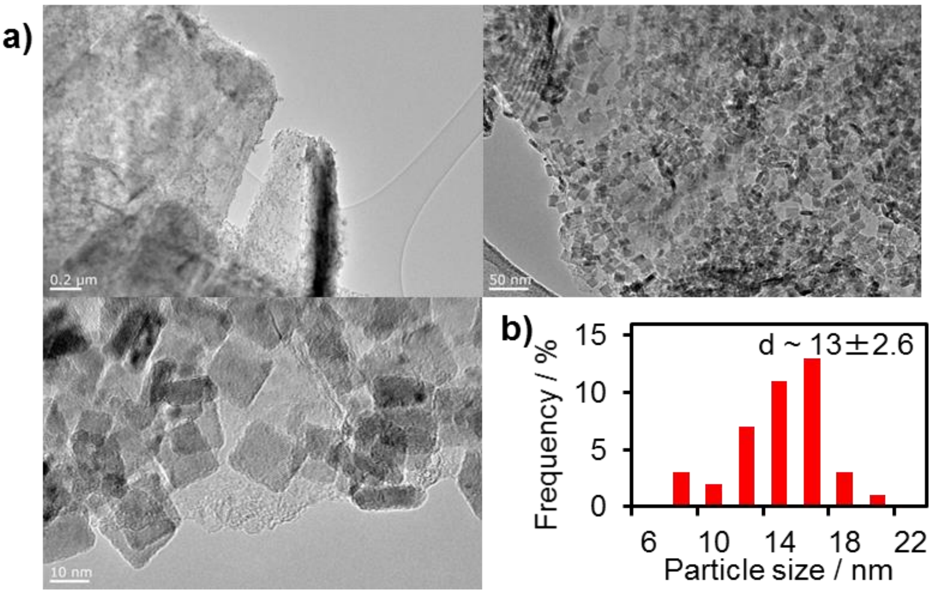

Figure 3-8. (**a**) HRTEM image of Mn_3O_4/G2, (**b**) particle size distributions and average sizes of Mn_3O_4 NP.

Thermogravimetric analysis (TGA) performed by Carlos Herreros-Lucas indicates ~12 % for Mn_3O_4/C, 26 % for Mn_3O_4/GMWNT, 26 % for Mn_3O_4/G1, 6 % for Mn_3O_4/G2, 12 % for Mn_3O_4/GNF, 11 % for Mn_3O_4@GNF of Mn by weight (**Figure A- 7**). To maximise the active surface area of these electrocatalyst, a thermal procedure (heated in air at 300 °C for 10 minutes) for the removal the organic surfactant surrounding Mn_3O_4 NP was applied by Carlos before structural characterisation and electrochemical analysis for all electrocatalysts.

3.4.1.2. Electrocatalysis of ORR/OER by Mn_4O_3-CN hybrid nanostructures

The ORR and OER catalytic performances of Mn_4O_3-CN bifunctional electrocatalyst were measured using rotating disk electrode (RDE) measurements. After the electrolyte was saturated with pure oxygen, the polarization curves were recorded between 1.0 and 0.4 V vs RHE for ORR and between 1.2 and 1.9V vs RHE for OER at a sweep rate of 10 mV/s in 0.1M KOH at room temperature. A freshly prepared 0.1 M KOH electrolyte was used for each measurement, as described above. The currents have been normalized to the geometric area of the glassy carbon electrode, and the potentials corrected by taking the ohmic drop ($\Delta E_{\Omega} = I \cdot R_s$) in the solution ($E$ *is* electrode potential, I current and R_s solution resistivity) into consideration.

The electrocatalytic activities for Mn_4O_3-CN bifunctional electrocatalyst were investigated by depositing on a glassy carbon electrode using a typical three-electrode setup in two different categories; (**i**) one-dimension carbon supported Mn_3O_4/GMWNT, Mn_3O_4/GNF, Mn_3O_4@GNF, (**ii**) two and three-dimension carbon supported Mn_3O_4/C, Mn_3O_4/G1, Mn_3O_4/G2. As a benchmark electrocatalyst, Pt/C (20 wt. % Pt on Vulcan carbon black) for ORR and IR/C (20 wt. % IR on Vulcan carbon black) for OER also were tested exhibiting high electrocatalytic performance.

- Electrocatalysis Mn_4O_3 nanoparticles supported on one-dimensional carbon

Bifunctional electrocatalyst activities Mn_3O_4/GMWNT, Mn_3O_4/GNF, Mn_3O_4@GNF, for the ORR and the OER are shown in **Figure 3-9** and compared with commercial Ir/C and Pt/C.

Polarisation curves for the ORR/OER obtained for these electrocatalyst on a rotating disk electrode in O_2-saturated 0.1 M KOH solution.

The potential corresponding to one-half of the diffusion current (half-wave potential, $E_{1/2}$ shown in **Figure 3-9**) for ORR can be used to qualitatively determine the catalyst activity; the higher the potential indicates the better the ORR activity.[158] An insight of the ORR and OER mechanism can be obtained by fitting the polarisation curve or plotting the potential (E) *vs.* log(J_k) (Tafel plot) shown in **Figure 3-12**, as the number of electrons transferred in the rate-limiting step. The $E_{1/2}$ and Tafel slope (**Table 3-1**) for commercial Pt/C catalyst is 0.811 V and 85/115 mV/dec while for Mn_3O_4@GNF and Mn_3O_4/GMWNT are marginally lower which were 0.664 V and 121/139 mV/dec and 0.651 V and 147/211 mV/dec respectively, whereas for Mn_3O_4/GNF the $E_{1/2}$ values were 0.581 V and 95/217 mV/dec which are significantly lower. Comparison of half wave potential and Tafel slope of Mn_3O_4@GNF with Mn_3O_4/GNF indicates that the activity of Mn_3O_4 is not reduced by the confinement in nanocontainers, which is remarkable considering the high aspect ratio of GNF.

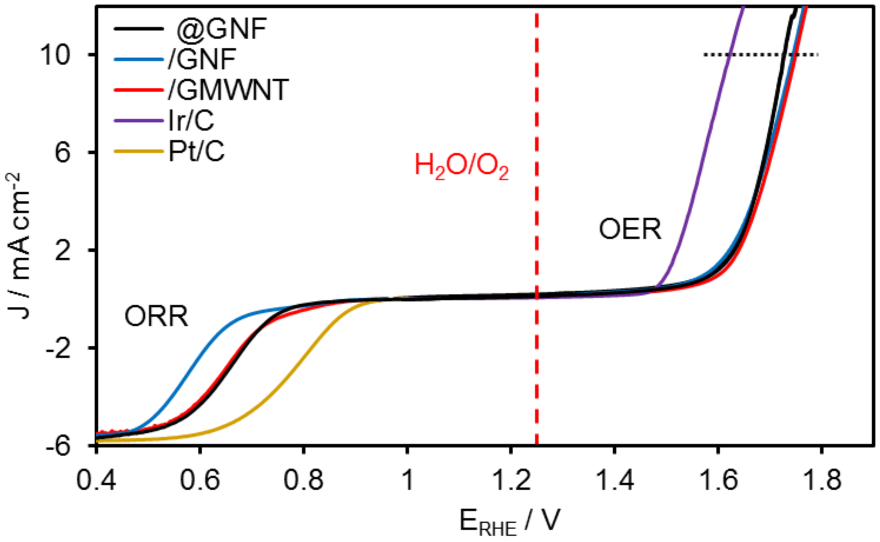

Figure 3-9. Disk currents obtained during the ORR in the anodic sweep by RRDE method and OER in the cathodic sweep on Mn_3O_4/GMWNT, Mn_3O_4/GNF, Mn_3O_4@GNF, Ir/C and Pt/C at room temperature at the scan rate of 10 mV/s; current densities (J) normalized to the geometric electrode area.

As a result, Mn_3O_4@GNF is to be active for ORR and indicates close catalytic activity to commercial Pt/C. This indicates that Mn_3O_4 nanoparticles in GNF show high electrocatalytic performance by the confinement in the nanocontainer. More surprisingly, Mn_3O_4 NP on surface of GNF exhibits the lowest activity among the materials. which is unexpected since NPs in Mn_3O_4/GNF should be more accessible for O_2 than in Mn_3O_4@GNF, but this can be explained by a higher surface of interaction of Mn_3O_4 NP with the step-edge inside GNF (**Figure 3-3d**) than with the convex surface of the outside of GNF, hence a better connectivity of catalytic centers in Mn_3O_4@GNF leading to a higher $E_{1/2}$ potential as compared to Mn_3O_4/GNF (**Figure 3-9**).

For a quantitative comparison, the kinetic current for the selected electrocatalysts that show a negligible film resistance can be obtained from the ORR polarisation curve according to the Koutecký-Levich equation:[158] $1/J = 1/J_k + 1/J_d$, where J is the current density obtained experimentally, J_k is the mass-transport corrected kinetic current density and J_d is the diffusion-limited current density. The specific activity (J_k) was determined by normalising the I_k to the electrode geometric surface area value of 0.196 cm^2, while the catalyst mass activity was obtained by normalising to the catalyst loading on the electrode (100 $\mu g/cm^2$).

Moreover, Levich-Koutecky plots for the highest performance electrocatalysts (Mn_3O_4@GNF) indicate that the reaction proceeds through a 4 electrons pathway. The RRDE measurement revealed an electron transfer number of ~3.9 at 0.65, 0.7 and 0.75 V (**Figure 3-10b**).

The overall 4-electron ORR in alkaline solution, O_2 can be reduced by a $4e^-$ process to form hydroxide, OH^-: $O_2 + 2H_2O + 4e^- \rightarrow 4OH^-$ ($E^0 = 0.401$ V), or by $2e^-$ processes to form HO_2^- and then OH^- (**Equation 3-1, 2**):[185]

$O_2 + H_2O + 2e^- \rightarrow HO_2^- + OH^-$ E° = -0.065 V **Equation 3-1**

$HO_2^- + H_2O + 2e^- \rightarrow 3OH^-$ E° = 0.867 V **Equation 3-2**

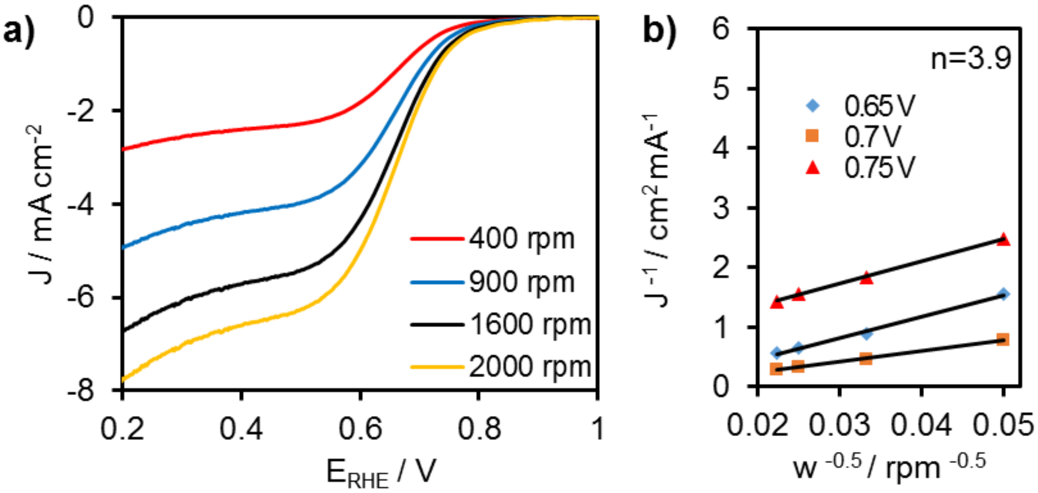

Figure 3-10. For Mn_3O_4@GNF (**a**) disk currents obtained during the ORR by RRDE at 400, 900, 1600 and 2000 rpm and (**b**) Koutecky-Levich plots of J^{-1} (current density) *versus* $\omega^{-0.5}$ (rotating speed), current densities (J) normalized to the geometric electrode area.

On the other hand, we extended the potential of our electrocatalyst coated electrode to 1.9V versus RHE to the water oxidation windows and assessed electrocatalytic oxygen evolution reaction (OER) in 0.1M KOH (**Figure 3-9**). A Tafel analysis of OER polarization curves (E *vs.* log(J_k)) for these electrocatalyst and the commercial catalyst is shown in **Figure 3-13**. Regarding OER activity, Mn_3O_4@GNF has similar activity with Ir/C commercial catalyst and is by far more active than Mn_3O_4/GMWNT, Mn_3O_4/GNF. Mn_3O_4 in GNF electrocatalyst reaches a current density of 10 mA/cm^2 at a very small overpotential of 0.499 V and a small Tafel slope down to 126 mV/decade; for the loading of 0.1 mg/cm^2 on glassy carbon electrode. Mn_3O_4/GMWNT and Mn_3O_4/GNF electrocatalyst reaches a current density of 10 mA/cm^2 at a marginally larger overpotential of 0.521 V and 0.514 V, and a small Tafel slope down to 132 mV/decade and 159 mV/decade (**Table 3-1**). As a result of this the confinement of Mn_3O_4 NP in GNF affect OER activity, as it showed only slightly higher OER activity than

Mn_3O_4/GMWNT and Mn_3O_4/GNF electrocatalyst. This indicates that Mn_3O_4 nanobricks in GNF shows high electrocatalytic performance by the confinement in the nanocontainer. This can be explained by a higher surface of interaction of Mn_3O_4 NP with the step-edge inside GNF (**Figure 3-3d**) than with the convex surface of the outside of GNF and GMWNT.

The most generally accepted OER mechanisms (**Equation 3-3-5**) on different electrodes surface in alkaline media involve steps below,

$$\mathrm{OH^-_{ads}} \rightleftarrows \mathrm{OH_{ads}} + \mathrm{e^-}$$ **Equation 3-3**

$$\mathrm{OH^-} + \mathrm{OH_{ads}} \rightleftarrows \mathrm{O_{ads}} + \mathrm{H_2O} + \mathrm{e^-}$$ **Equation 3-4**

$$\mathrm{O_{ads}} + \mathrm{O_{ads}} \rightleftarrows \mathrm{O_2}$$ **Equation 3-5**

where the rate determining step is the electron-transfer steps.[75-77]

The difference between onset point of the ORR and the OER was recorded to measure the oxygen electrode activity (**Table 3-1**). The smaller difference indicates an ideal reversible oxygen electrode. As a result, Mn_3O_4@GNF and Mn_3O_4/G1 have the best oxygen electrode activity of 1.072 and 1.064 V, which can be compared that of Mn_3O_4/C, Mn_3O_4/GMWNT, Mn_3O_4/G2, and Mn_3O_4/GNF (1.167, 1.100, 1.176 and 1.163 V vs RHE).

These results make Mn_3O_4@GNF a powerful bifunctional catalyst for both oxygen reduction and water oxidation and indicates marginally less active than commercial Pt/C for ORR and Ir/C for OER. This indicates that Mn_3O_4 nanoparticles in GNF shows high electrocatalytic performance by the confinement in the nanocontainer and this can be explained by a higher surface of interaction of Mn_3O_4 NP with the step-edge inside GNF (**Figure 3-3d**). Previously, manganese oxide was shown to be a bifunctional catalyst for ORR and OER[132, 185, 191-195] Our Mn_3O_4@GNF catalyst outperforms the manganese oxide electrocatalysts that are reported in the literature with smaller overpotentials for both ORR and OER, showing high performance for non-precious bifunctional catalyst.[132, 185, 195, 196]

- Electrocatalysis Mn_4O_3 nanoparticles supported on two and three-dimensional carbon

The electrocatalytic performance of these bifunctional electrocatalyst of Mn_3O_4/GMWNT, Mn_3O_4/GNF, Mn_3O_4@GNF, for the ORR and the OER are shown in **Figure 3-11** and compared with commercial Ir/C for OER and Pt/C for ORR. According ORR polarization curve of these electrocatalysts, the $E_{1/2}$ and Tafel slope for commercial Pt/C catalyst is 0.811 V and 85/115 mV/dec while for Mn_3O_4/G1 is marginally lower (0.679 V and 98/180 mV/dec) and for Mn_3O_4/G2 (0.632 V and 92/149 mV/dec), Mn_3O_4/C (0.663 V and 104/135 mV/dec) are significantly lower.

Regarding OER activity of two and three dimensional carbon supported Mn_4O_3 bifunctional electrocatalyst (**Figure 3-11**), Mn_3O_4@G1 has similar activity with Ir/C commercial catalyst and is by far more active than Mn_3O_4/G2, Mn_3O_4/C. Mn_3O_4 on G1 electrocatalyst reaches a current density of 10 mA/cm^2 at a small overpotential of 0.51V and a large Tafel slope 149 mV/decade (**Figure 3-13**); with loading of 0.1 mg/cm^2 on glassy carbon electrode. Mn_3O_4/G2 and Mn_3O_4/C electrocatalyst reaches a current density of 10 mA/cm^2 at a marginally larger overpotential of 0.57 V and 0.61 V and a large Tafel slope down to 130 mV/decade and 240 mV/decade. This indicate, confinement of Mn_3O_4 NP in GNF affects OER activity, as it showed higher OER activity than Mn_3O_4/G1, Mn_3O_4/G2 and Mn_3O_4/C electrocatalyst.

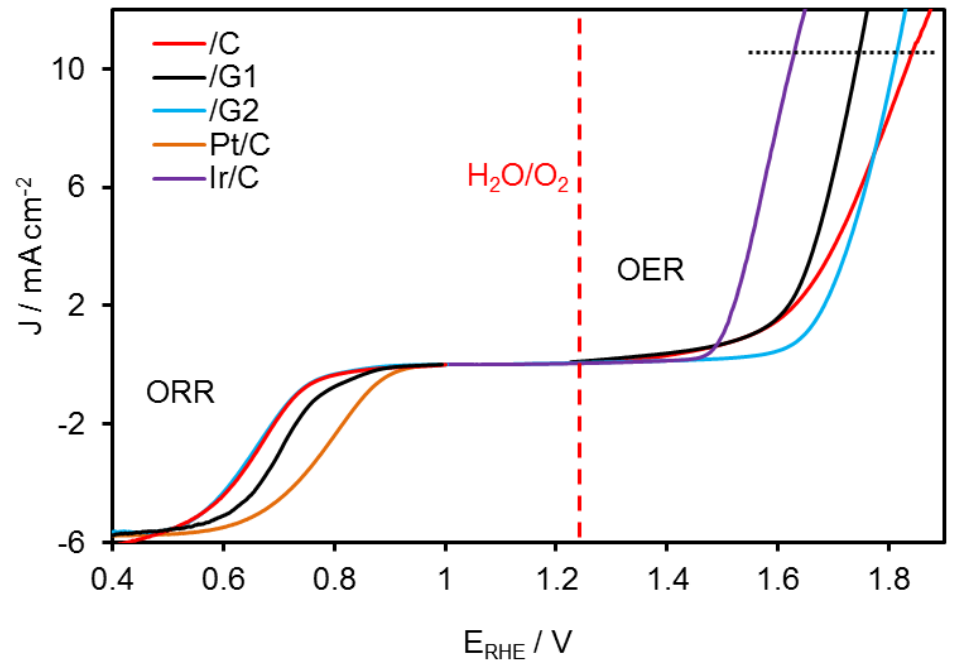

Figure 3-11. Disk currents obtained during the ORR by RRDE method and OER on Mn_3O_4/C, Mn_3O_4/G1, Mn_3O_4/G2, Ir/C and Pt/C at room temperature at the scan rate of 10 mV/s; current densities (J) normalized to the geometric electrode area.

These results make Mn_3O_4/G1 to be active for both oxygen reduction and water oxidation. This indicates that Mn_3O_4 nanobricks on G1 shows high electrocatalytic performance, nevertheless Mn_3O_4@GNF showed better OER activity then Mn_3O_4/G1.

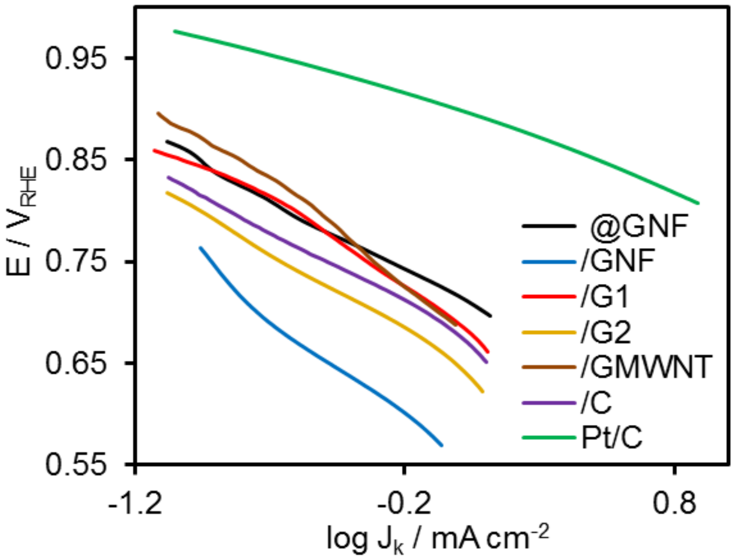

Figure 3-12. Comparison of ORR Tafel plots for Mn_3O_4/GMWNT, Mn_3O_4/GNF, Mn_3O_4@GNF, Mn_3O_4/C, Mn_3O_4/G1, Mn_3O_4/G2 electrocatalyst and Pt/C commercial benchmark electrocatalyst.

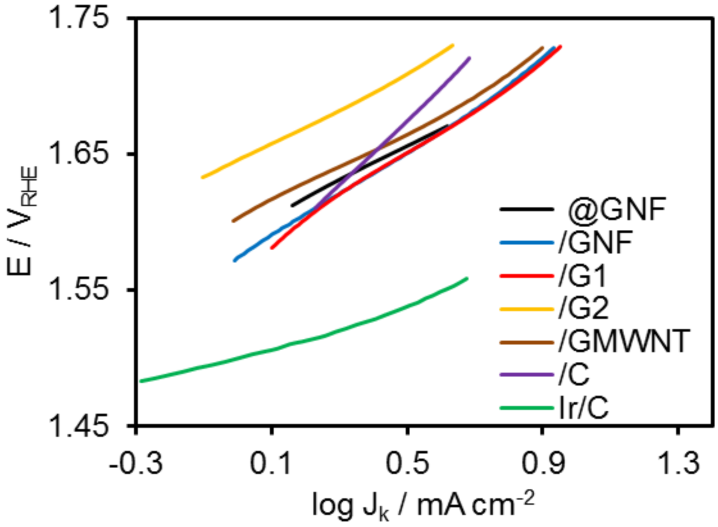

Figure 3-13. Comparison of OER Tafel plots for Mn_3O_4/GMWNT, Mn_3O_4/GNF, Mn_3O_4@GNF, Mn_3O_4/C, Mn_3O_4/G1, Mn_3O_4/G2 electrocatalyst and Ir/C commercial benchmark electrocatalyst.

Some important electrochemical parameters for the ORR and OER of Mn_3O_4/C, Mn_3O_4/GMWNT, Mn_3O_4/G1, Mn_3O_4/G2, Mn_3O_4/GNF, Mn_3O_4@GNF, Ir/C and Pt/C.are summarised in **Table 3-1** below.

Table 3-1. Summary of electrochemical parameters for Mn_3O_4/C, Mn_3O_4/GMWNT, Mn_3O_4/G1, Mn_3O_4/G2, Mn_3O_4/GNF, Mn_3O_4@GNF, Ir/C and Pt/C.

	Oxygen Electrode Δ(OER-ORR) / V	**ORR**				**OER**	
		Half-wave potential at 1600 rpm / V	**Specific activity at 0.7 V / mA/cm^2**	**Mass Activity at 0.7 V / A/mg**	**Tafel slope lcd/hcd / mV/dec**	**Tafel slope / mV/dec**	**Potential at 10 mAcm^{-2} / V**
`Mn_3O_4/C	1.167	0.663	0.753	0.0075	104/135	240	1.830
Mn_3O_4/GMWNT	1.100	0.651	0.842	0.0084	147/211	132	1.751
Mn_3O_4/G1	1.064	0.679	0.875	0.087	117/180	149	1.743
Mn_3O_4/G2	1.176	0.632	0.496	0.0049	92/149	130	1.808
Mn_3O_4/GNF	1.163	0.581	0.179	0.0018	95/217	159	1.744
Mn_3O_4@GNF	1.072	0.657	1.2	0.012	121/139	126	1.729
Ir/C	-	-	-	-	-	60	1.604
Pt/C	-	0.811	9.26	0.096	85/115	-	-

3.4.1.3. Durability test

Additional significant criterion for an ideal electrocatalyst is its high durability. Therefore, durability studies of the selected Mn_3O_4/GNF, Mn_3O_4@GNF were carried out to determine whether the corrugated interiors of GNF can serve as anchoring points to stabilise the electrocatalytic Mn_3O_4 NP to avoid ripening and aggregation. Durability test were performed on both electrocatalysts by continuously applying linear potential sweeps up to 5000 cycles from 1.4 to 1.75 V vs RHE at the sweep rate of 50 mV/s in 0.1M KOH and compared with Ir/C as benchmark electrocatalyst. At the end of the durability test, the polarisation curves were compared, the overpotential at a current density of 10 mA/cm^2 for these electrocatalyst in **Table 3-2** which show that there is no significant change for Mn_3O_4@GNF (44 mV) and larger change for Ir/C (63 mV), Mn_3O_4/GNF (99 mV) shown in **Figure 3-14a**. Comparison of the catalitic performance for Mn_3O_4@GNF before and after durability test highligths by far the durability of our electrocatalyst that can allow a sustainable use of Mn.

The lack of stability of Ir on carbon black may be related to the absence of long-range order in in this support material leading to electrochemical corrosion that aggravates the Ir nanoparticle sintering and leads to a reduced durability of Ir/C in comparison to Mn_3O_4@GNF. This provides further evidence of the stabilising effects of step-edges in GNF cavities and Mn_3O_4NP confinement within the GNF. The poorer electrical connectivity of carbon black with the Ir gives rise to a higher electron transfer resistance and undesired decrease in HER activity as compared to the graphitic structures of GNF.

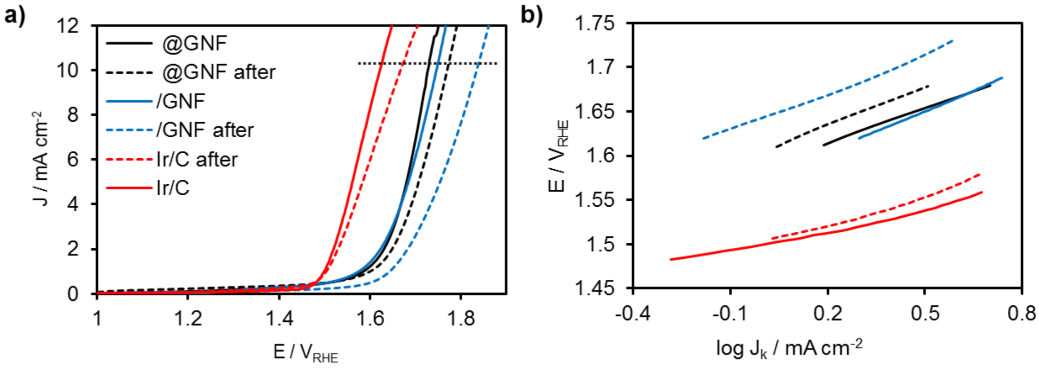

Figure 3-14. (**a**) Comparison of OER polarisation curves and (**b**) Tafel plots for Mn_3O_4/GNF, Mn_3O_4@GNF and Ir/C initial and after 5000 potential cycles, between 1.4 and 1.75 V vs RHE in an oxygen saturated 0.1 M KOH electrolyte at room temperature with a sweep rate of 50 mV/s.

Interestingly, after cycling there was no significant change for Tafel slope of Mn_3O_4@GNF from 126 mV/dec to 144 mV/dec while it changed for Ir/C commercial catalyst from 60 to 81 mV for Mn_3O_4/GNF form 159 mV/dec to 140 mV/dec shown in **Figure 3-14b**.

Table 3-2. Summary of electrochemical parameters for Mn_3O_4/GNF, Mn_3O_4@GNF and Ir/C before and after 5000 cycles durability test.

	Tafel slope / mV/Dec	**Potential at 10 mAcm^{-2} / V**
Mn_3O_4/GNF	159	1.744
Mn_3O_4/GNF after	140	1.843
Mn_3O_4@GNF	126	1.729
Mn_3O_4@GNF after	144	1.773
Ir/C	60	1.604
Ir/C after	81	1.667

3.4.2. In-situ approach synthesised bifunctional $Mn_3O_{4(in\text{-}situ)}$-CN electrocatalysts for ORR/OER

3.4.2.1. Structural characterisation of $Mn_3O_{4(in\text{-}situ)}$ -CN electrocatalysts

High-resolution transmission electron microscopy (HRTEM) investigation of $Mn_3O_{4(in\text{-}situ)}$/GNF, $Mn_3O_{4(in\text{-}situ)}$/Ox-GNF, $Mn_3O_{4(in\text{-}situ)}$@GNF and $Mn_3O_{4(in\text{-}situ)}$@S-GNF hybrid electrocatalysts were performed. In **Figure 3-15** the HRTEM imaging of the synthesised $Mn_3O_{4(in\text{-}situ)}$ shows that nanobricks nanoparticles are located mostly on the smooth external surface of GNF, with an average diameter of 14.7 ± 3.8 nm.

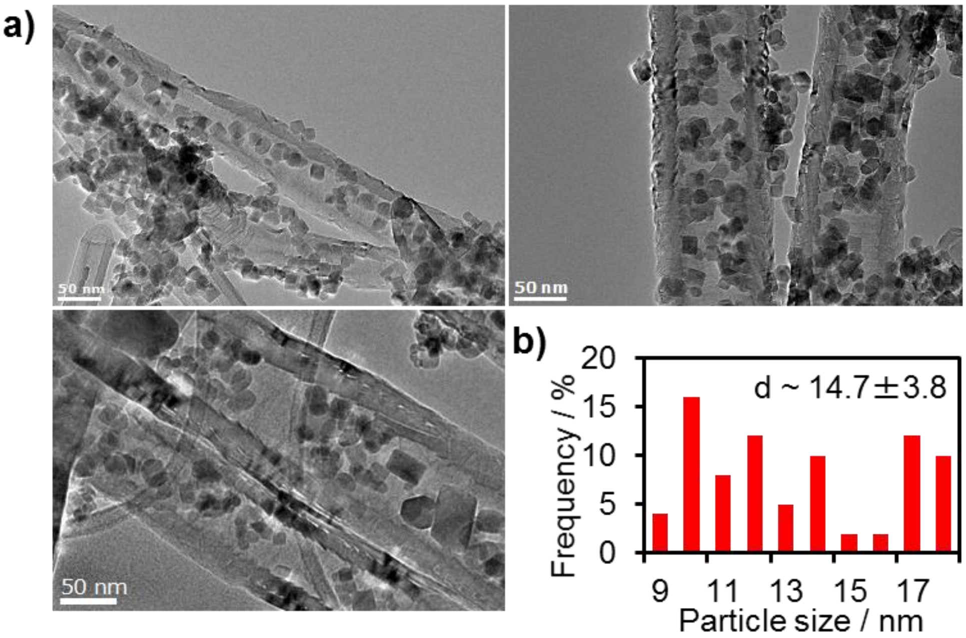

Figure 3-15. (**a**) HRTEM image of $Mn_3O_{4(in\text{-}situ)}$/GNF, (**b**) particle size distributions and average sizes of Mn_3O_4 NP.

In **Figure 3-16** HRTEM imaging of the synthesised $Mn_3O_{4(in\text{-}situ)}$NP are located mostly on the smooth external surface of Ox-GNF, with an average diameter of 10.8 ± 2.5 nm.

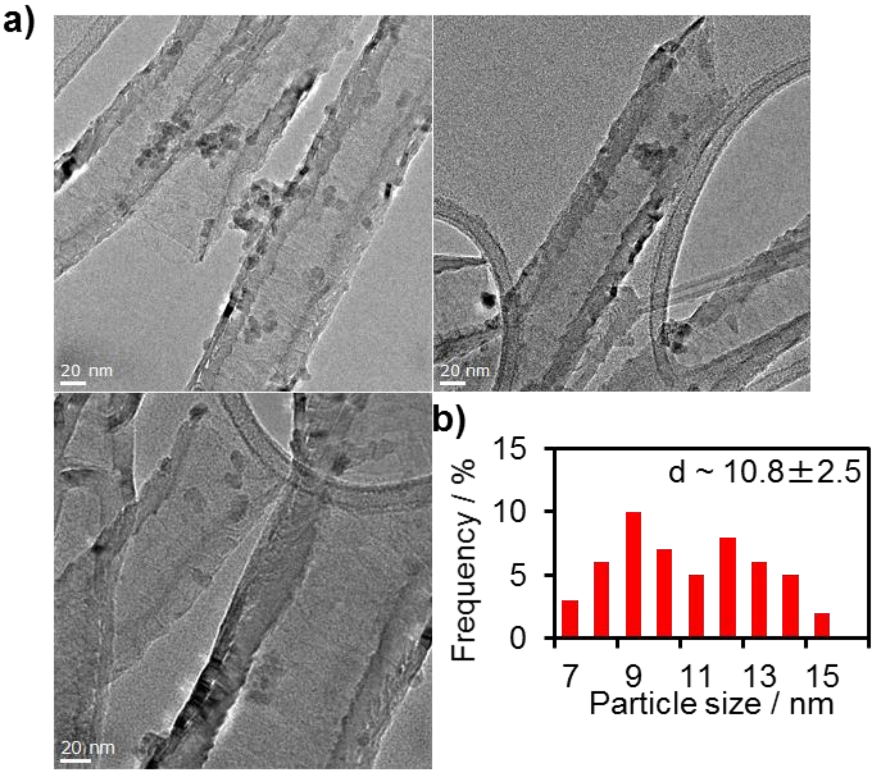

Figure 3-16. (**a**) HRTEM image of $Mn_3O_{4(in\text{-}situ)}$/Ox-GNF, (**b**) particle size distributions and average sizes of Mn_3O_4 NP.

The HRTEM observations are exhibiting the large facets of the NP aligned with the GNF step-edge surfaces (**Figure 3-17**), with an average diameter of 9.3 ± 1.6 nm.

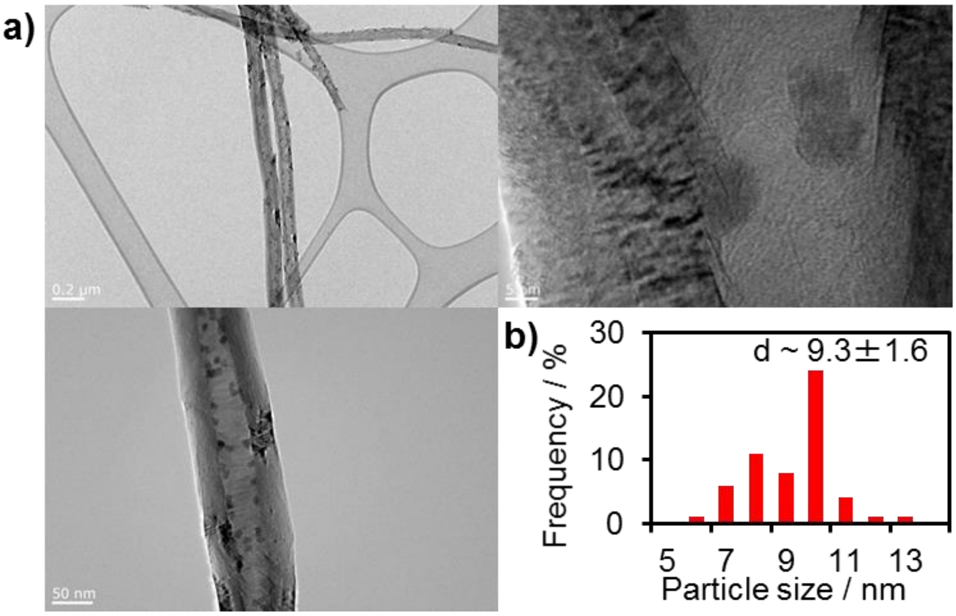

Figure 3-17. (**a**) HRTEM image of $Mn_3O_{4(in\text{-}situ)}$@GNF, (**b**) particle size distributions and average sizes of Mn_3O_4 NP.

The HRTEM observations is exhibiting the large facets of the NP aligned with the GNF step-edge surfaces (**Figure 3-18**), with an average diameter of 12.2 ± 3.9 nm. Mn_3O_4 NP were located at the internal step-edges, well dispersed into the GNF. It is considered that this favoured orientation of Mn_3O_4NP in GNF is driven by a requirement to maximize NP-GNF interactions combined with a reduction of the nanoparticles surface area exposed to the environment.

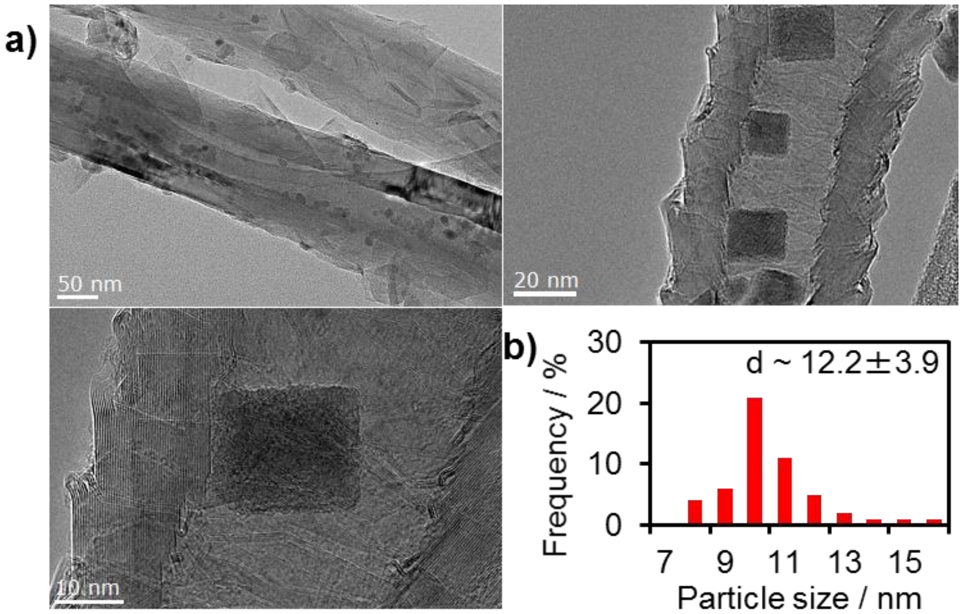

Figure 3-18. (**a**) HRTEM image of $Mn_3O_{4(in\text{-}situ)}$@S-GNF, (**b**) particle size distributions and average sizes of Mn_3O_4 NP.

3.4.2.2. Electrochemical properties towards ORR and OER of $Mn_3O_{4(in\text{-}situ)}$-CN electrocatalyst

The ORR and OER catalytic performances of $Mn_4O_{3(in\text{-}situ)}$-CN bifunctional electrocatalyst were measured using three electrode measurements. After the electrolyte was saturated with pure oxygen, the polarization curves were recorded between 1.0 and 0.2 V vs RHE at 1600 rpm for ORR and from 1 to 1.9V vs RHE for OER at a sweep rate of 10 mV/s in 0.1M KOH at room temperature. A freshly prepared 0.1 M KOH electrolyte was used for each measurement, as described above. The currents have been normalized to the geometric area of the glassy carbon electrode, and the potentials corrected in accordance with by the ohmic drop ($\Delta E_\Omega = I{\cdot}R_s$) in the solution (*E is* electrode potential, *I* current and R_s solution resistivity).

The electrocatalytic activities for $Mn_3O_{4(in\text{-}situ)}$-CN bifunctional electrocatalyst were investigated by depositing on a glassy carbon electrode using a typical three-electrode setup for $Mn_3O_{4(in\text{-}situ)}$/GNF, $Mn_3O_{4(in\text{-}situ)}$/Ox-GNF, $Mn_3O_{4(in\text{-}situ)}$@GNF, $Mn_3O_{4(in\text{-}situ)}$@S-GNF. As a benchmark electrocatalyst, Pt/C (20 wt. % Pt on Vulcan carbon black) for ORR and IR/C (20 wt. % IR on Vulcan carbon black) for OER also were tested exhibiting high electrocatalytic performance.

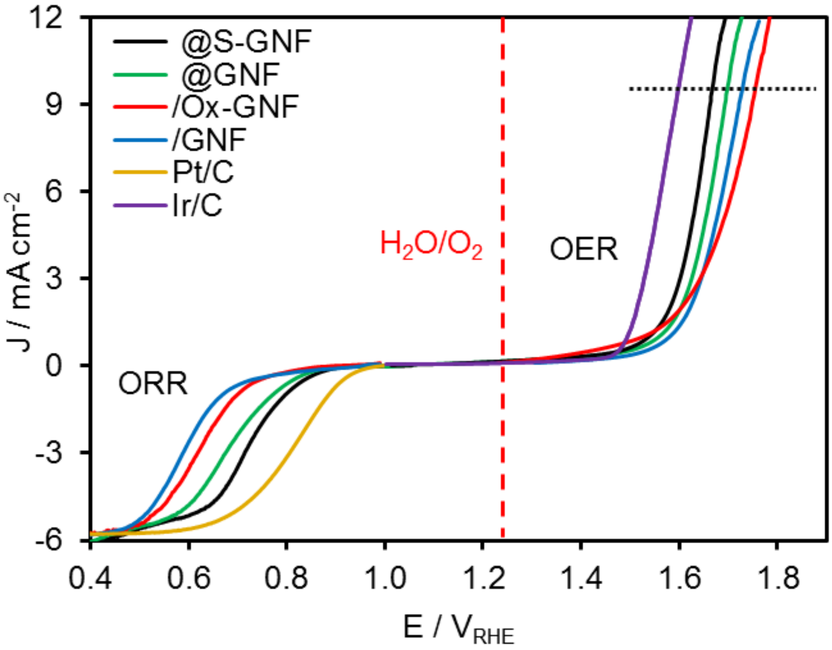

Figure 3-19. Disk currents obtained during the ORR by RRDE method and OER in the cathodic sweep on $Mn_3O_{4(in\text{-}situ)}$/GNF, $Mn_3O_{4(in\text{-}situ)}$/Ox-GNF, $Mn_3O_{4(in\text{-}situ)}$@GNF, $Mn_3O_{4(in\text{-}situ)}$@S-GNF, Ir/C and Pt/C at room temperature at scan rate of 10 mV/s; current densities (J) normalized to the geometric electrode area.

Bifunctional electrocatalyst activities $Mn_3O_{4(in\text{-}situ)}$/GNF, $Mn_3O_{4(in\text{-}situ)}$/Ox-GNF, $Mn_3O_{4(in\text{-}situ)}$@GNF, $Mn_3O_{4(in\text{-}situ)}$@S-GNF for the ORR and the OER are shown in **Figure 3-19** and compared with commercial Ir/C and Pt/C. Polarisation curves for the ORR/OER obtained for these electrocatalyst on a rotating disk electrode in O_2-saturated 0.1 M KOH solution.

The $E_{1/2}$ and Tafel slope for commercial Pt/C catalyst is 0.811 V and 85/115 mV/dec while for $Mn_3O_{4(in\text{-}situ)}$@S-GNF is similar (0.660 V and 80/165 mV/dec) and for $Mn_3O_{4(in\text{-}situ)}$@GNF (0.645 V and 91/195 mV/dec) is marginally lower, and $Mn_3O_{4(in\text{-}situ)}$/Ox-GNF (0.612 V and 90/143 mV/dec), $Mn_3O_{4(in\text{-}situ)}$/GNF (0.588 V and 273/471 mV/dec) are significantly lower.

Shortening GNF length makes the NP more accessible for oxygen as products get out more effortlessly, largely minimising the diffusion problems as compared to longer GNF. An increase on the performance of $Mn_3O_{4(in\text{-}situ)}$@S-GNF comparison with $Mn_3O_{4(in\text{-}situ)}$@GNF is observed after decreasing the length of the nanocontainer.

$Mn_3O_{4(in\text{-}situ)}$@S-GNF is to be active for both ORR and OER, and indicates less active than commercial Pt/C for ORR and Ir/C for OER. Nevertheless, this indicates that *in-situ* synthesized Mn_3O_4 nanobricks in GNF shows high electrocatalytic performance by the confinement in GNF nanocontainers. More surprisingly, $Mn_3O_{4(in\text{-}situ)}$ NP on surface of GNF exhibit the lowest activity among the materials which is unexpected since NPs in $Mn_3O_{4(in\text{-}situ)}$/GNF should be more accessible for O_2 than in $Mn_3O_{4(in\text{-}situ)}$@S-GNF, but this can be explained by a higher surface of interaction of $Mn_3O_{4\ (in\text{-}situ)}$NP with the step-edge inside GNF than with the convex surface of the outside of GNF, hence a better connectivity of catalytic centres in $Mn_3O_{4(in\text{-}situ)}$@S-GNF leading to a higher $E_{1/2}$ potential as compared to $Mn_3O_{4(in\text{-}situ)}$/GNF (**Figure 3-18**).

For a quantitative comparison for ORR activity of these electrocatalyst, the kinetic current for the selected electrocatalysts that shows a negligible film resistance can be obtained from the ORR polarisation curve according to the Koutecký-Levich equation:[158] $1/J = 1/J_k + 1/J_d$, where J is the current density obtained experimentally, J_k is the mass-transport corrected kinetic current density and J_d is the diffusion-limited current density. A Tafel analysis of the rotating ring-disk electrode (RRDE) data (E *vs.* log(J_k)) for the selected electrocatalyst and the commercial catalyst is shown in Figure 3-20. The specific activity (J_k) was determined by normalising the I_k to the electrode geometric surface area value (0.196 cm^2), while the catalyst mass activity was obtained by normalising to the catalyst loading on the electrode (100 $\mu g/cm^2$).

We extended the potential of our electrocatalyst coated electrode to 1.9V vs RHE to the water oxidation windows and assessed electrocatalytic oxygen evolution reaction (OER) 0.1M KOH. Regarding OER activity, $Mn_3O_{4(in\text{-}situ)}$@S-GNF has similar activity with Ir/C commercial catalyst and is by far more active than on $Mn_3O_{4(in\text{-}situ)}$/GNF, $Mn_3O_{4(in\text{-}situ)}$/Ox-GNF, $Mn_3O_{4(in\text{-}situ)}$@GNF. Mn_3O_4 in S-GNF electrocatalyst reaches a current density of 10 mA/cm^2 at a very small overpotential of 0.442 V shown in **Figure 3-19** and a small Tafel slope down to 129 mV/decade (**Figure 3-21**) with the loading of 0.1 mg/cm^2 on glassy carbon electrode. These values are comparable with the best bifunctional hybrid electrocatalyst reported (Co_3O_4/N-rmGO; overpotential: 0.310 V; Tafel slope: 67 mV/decade; loading: 1 mg/cm^2 on Ni foam.[43] $Mn_3O_{4(in\text{-}situ)}$@GNF, $Mn_3O_{4(in\text{-}situ)}$/GNF and $Mn_3O_{4(in\text{-}situ)}$/Ox-GNF, electrocatalyst reaches a current density of 10 mA/cm^2 at a marginally larger overpotential of 0.472 V, 0.502 V and 0.535 V shown in **Figure 3-19**, and a small Tafel slope down to 140 mV/dec, 147 mV/dec and 215 mV/dec (**Figure 3-21**). This indicate, confinement of Mn_3O4 NP in S-GNF affect OER activity, as it showed only slightly higher OER activity than $Mn_3O_{4(in\text{-}situ)}$/GNF, $Mn_3O_{4(in\text{-}situ)}$/Ox-GNF, $Mn_3O_{4(in\text{-}situ)}$@GNF electrocatalyst.

These results make $Mn_3O_{4(in\text{-}situ)}$@S-GNF a powerful bifunctional catalyst for both ORR and OER. Previously, Mn_xO_y was shown to be a bifunctional catalyst for ORR and OER.[132, 185, 191-195] Our $Mn_3O_{4(in\text{-}siu)}$@S-GNF catalyst outperforms Mn_3O_4NP with smaller overpotentials for both ORR and OER, showing high performance non-precious bifunctional catalyst.[132, 185, 195, 196]

The difference between onset point of the ORR and the OER was recorded to measure the oxygen electrode activity (**Table 3-1**). The smaller the difference indicates the more ideal reversible oxygen electrode. As a results, $Mn_3O_{4(in\text{-}situ)}$@S-GNF has the best oxygen electrode activity of 0.953 V which compares with $Mn_3O_{4(in\text{-}situ)}$@GNF, $Mn_3O_{4(in\text{-}situ)}$/GNF and $Mn_3O_{4(in\text{-}situ)}$/Ox-GNF (1.021, 1.137 and 1.139 V vs RHE). The oxygen electrode activity of $Mn_3O_{4(in\text{-}}$

situ)@S-GNF is in excellent agreement with the value calculated by Jaramillo et al.[132] (0.92 V for Ir/C and 1.04 V for Mn oxide) for ORR/OER under similar conditions.

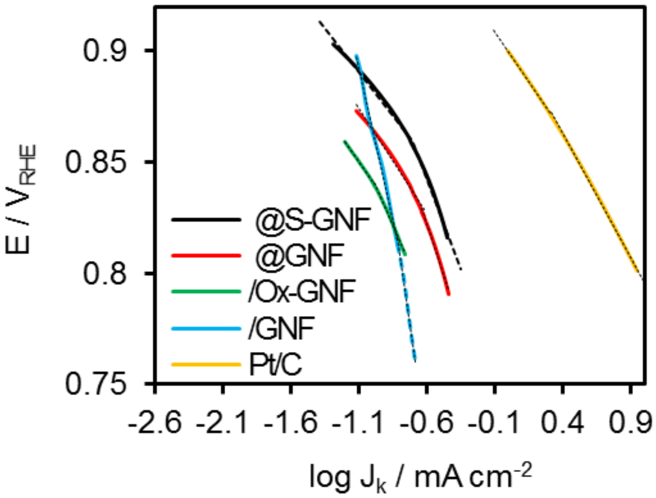

Figure 3-20. Comparison of ORR Tafel plots for $Mn_3O_{4(in\text{-}situ)}$/GNF, $Mn_3O_{4(in\text{-}situ)}$/Ox-GNF, $Mn_3O_{4(in\text{-}situ)}$@GNF, $Mn_3O_{4(in\text{-}situ)}$@S-GNF and Pt/C commercial benchmark electrocatalyst.

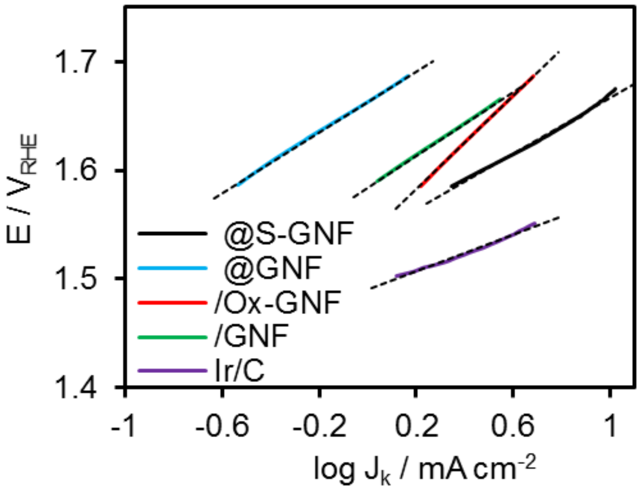

Figure 3-21. Comparison of OER Tafel plots for $Mn_3O_{4(in\text{-}situ)}$/GNF, $Mn_3O_{4(in\text{-}situ)}$/Ox-GNF, $Mn_3O_{4(in\text{-}situ)}$@GNF, $Mn_3O_{4(in\text{-}situ)}$@S-GNF and Ir/C commercial benchmark electrocatalyst.

Some important electrochemical parameters for the ORR and OER of Mn_3O_4/C, Mn_3O_4/GMWNT, Mn_3O_4/G1, Mn_3O_4/G2, Mn_3O_4/GNF, Mn_3O_4@GNF, Ir/C and Pt/C are summarised in **Table 3-3**.

Table 3-3. Summary of electrochemical parameters for $Mn_3O_{4(in\text{-}situ)}$/GNF, $Mn_3O_{4(in\text{-}situ)}$/Ox-GNF, $Mn_3O_{4(in\text{-}situ)}$@GNF, $Mn_3O_{4(in\text{-}situ)}$@S-GNF, Ir/C and Pt/C.

	Oxygen Electrode Δ(OER-ORR) / V	**ORR**				**OER**	
		Half-wave potential at 1600 rpm / V	**Specific activity at 0.7 V / mA/cm^2**	**Mass Activity at 0.7 V / A/mg**	**Tafel slope lcd/hcd / mV/dec**	**Tafel slope / mV/dec**	**Potential at 10 mAcm^{-2} / V**
$Mn_3O_{4(In\text{-}situ)}$/GNF	1.137	0.595	0.276	0.028	273/471	147	1.732
$Mn_3O_{4(In\text{-}situ)}$/Ox-GNF	1.139	0.626	0.426	0.043	90/143	215	1.765
$Mn_3O_{4(In\text{-}situ)}$@GNF	1.021	0.681	0.519	0.052	95/191	140	1.702
$Mn_3O_{4(In\text{-}situ)}$@S-GNF	0.953	0.719	0.538	0.054	80/165	129	1.672
Ir/C		-	-	-	-	60	1.604
Pt/C		0.811	9.26	0.096	85/115	-	-

3.4.2.3. Durability test

Additional significant criterion for an ideal electrocatalyst is high durability. Therefore, durability studies of the selected $Mn_3O_{4(in\text{-}situ)}$@S-GNF, electrocatalyst were performed in an accelerated durability test by continuously applying linear potential sweeps up to 5000 cycles from 1.4 to 1.75 V vs RHE at 50 mV/s in 0.1M KOH and compared with Ir/C as benchmark electrocatalyst. At the end of the durability test, the polarisation curves were compared, the overpotential at a current density of 10 mA/cm^2 for these electrocatalyst in **Table 3-4** which show that there is no significant change for $Mn_3O_{4(in\text{-}situ)}$@S-GNF (38 mV) and larger change for Ir/C (63 mV). Moreover, after cycling there was no significant change for Tafel slope of $Mn_3O_{4(in\text{-}situ)}$@GNF, from 129 mV/dec to 136 mV/dec while it changed for Ir/C commercial catalyst from 60 to 81 mV (**Figure 3-22**). The lack of stability of Ir on carbon black may be related to the absence of long-range order in in this support material leading to electrochemical corrosion that aggravates the Ir nanoparticle sintering and leads to a reduced durability of Ir/C in comparison to $Mn_3O_{4(in\text{-}situ)}$@S-GNF. This provides further evidence of the stabilising effects of step-edges in GNF cavities and Mn_3O_4NP confinement within the GNF. The poorer electrical connectivity of carbon black with the Ir gives rise to a higher electron transfer resistance and undesired decrease in HER activity as compared to the graphitic structures of GNF.

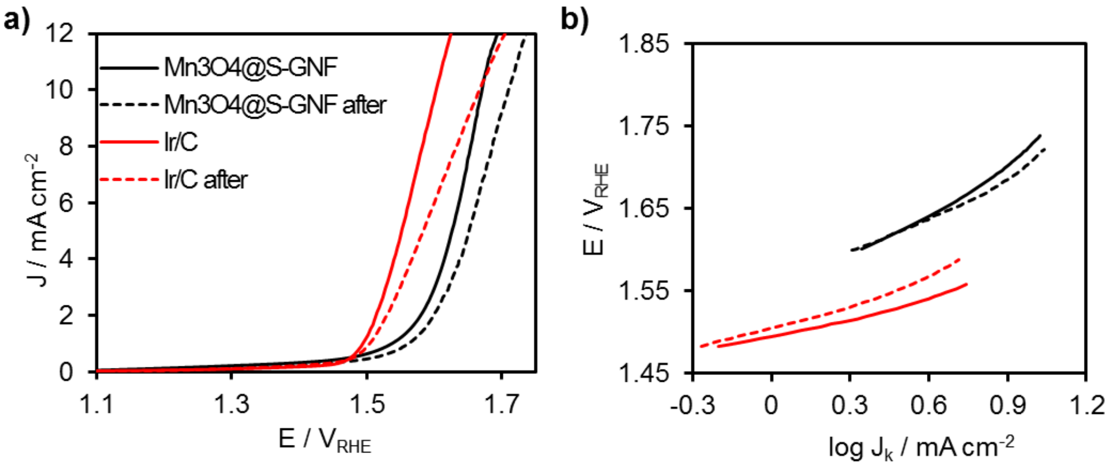

Figure 3-22. (a) Comparison of OER polarisation curves and (**b**) tafel plots for the ORR normalised to the geometric surface area for $Mn_3O_{4(in\text{-}situ)}$@S-GNF and Ir/C initial and after 5000 potential cycles, between 1.3 and 1.7 V vs RHE in an oxygen saturated 0.1 M KOH electrolyte at room temperature with a sweep rate of 50 mV/s.

Table 3-4. Summary of electrochemical parameters for $Mn_3O_{4(in\text{-}situ)}$@S-GNF and Ir/C before and after 5000 cycles durability test.

	Tafel slope / mV/dec	**Potential at 10 mAcm^{-2} / V**
Mn3O4($_{In\text{-}situ}$)@S-GNF	129	1.672
Mn3O4($_{In\text{-}situ}$)@S-GNF after	136	1.710
Ir/C	60	1.604
Ir/C after	81	1.667

3.4.2.4. Comparison both synthesis approaches

Preform nanoparticles approach synthesised Mn_3O_4@GNF is to be less active for both ORR and OER than *in-situ* nanoparticles approach synthesised $Mn_3O_{4(in\text{-}situ)}$@GNF. It is considered that this favoured orientation of $Mn_3O_{4(in\text{-}situ)}$NP@GNF is driven by a requirement to maximize NP-GNF interactions combined with a reduction of the nanoparticles surface area exposed to the environment shown in **Figure 3-23**.

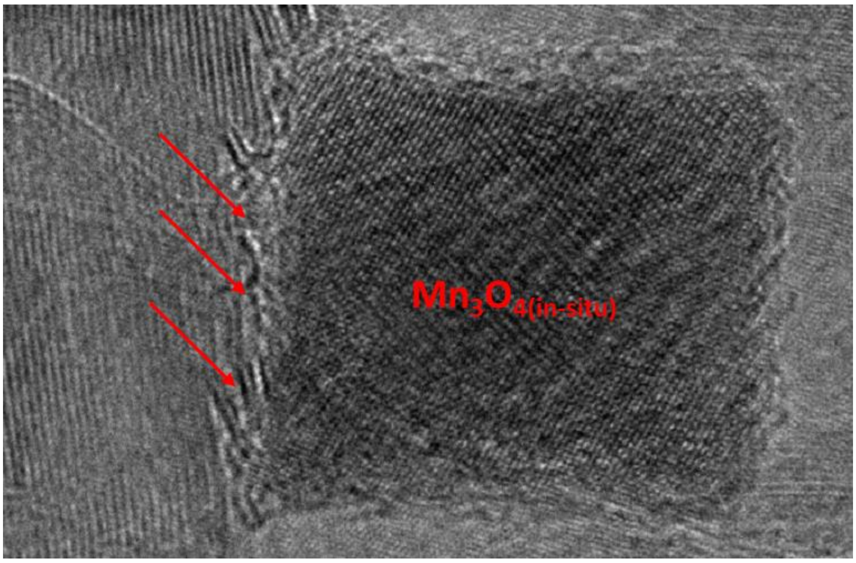

Figure 3-23. HRTEM image of $Mn_3O_{4(in\text{-}situ)}$@GNF indicates maximizing host–guest interactions in GNF nanocontainers by using the *in-situ* approach.

Comparison ORR/OER polarisation curves of Mn_3O_4@GNF and $Mn_3O_{4(in\text{-}situ)}$@GNF in O_2 saturated 0.1 M $HClO_4$ at room temperature are shown in **Figure 3-24**. This indicates that $Mn_3O_{4(in\text{-}situ)}$ nanoparticles in GNF shows high electrocatalytic performance by maximizing NP-GNF interactions in GNF nanocontainers.

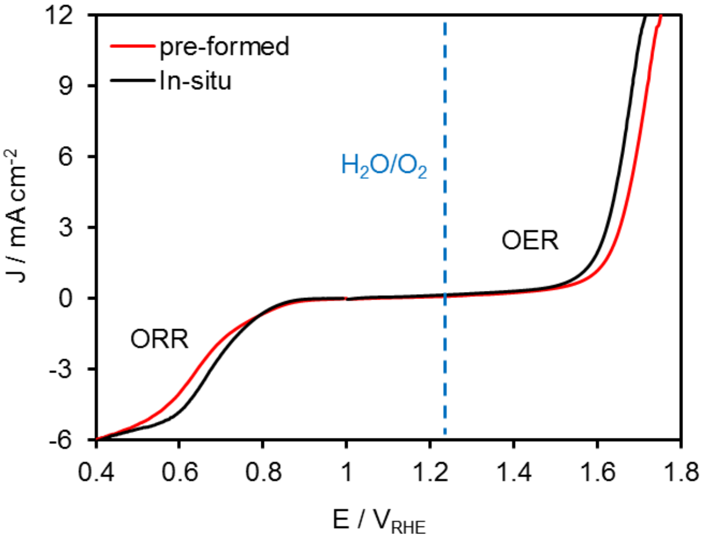

Figure 3-24. Disk currents obtained during the ORR by RRDE method and OER in the cathodic sweep on Mn_3O_4@GNF (red) and $Mn_3O_{4(in\text{-}situ)}$@GNF (black) at room temperature at scan rate of 10 mV/s; current densities (J) normalized to the geometric electrode area.

3.4.3. Investigation of carbon nanostructures in OER potential windows

The electrochemical oxidation of G1, G2, S-GNF, GNF, GMWNT and carbon black (C, XC-72R) were investigated by applying 5000 potential cycles from 1.4 to 1.75 V vs RHE at the sweep rate of 50mV/s in O_2 saturated 0.1M KOH at room temperature. Cyclic voltammogram and Nyquist plots were recorded before and after durability test for each carbon nanostructure support material in **Figure 3-25**. Observations show that there is a noticeable current peak at about 0.6 V vs RHE in all carbon support materials **Figure 3-25**, which concludes from the formation of surface oxide due to the hydroquinone–quinone (HQ–Q) redox couple on the surface of carbon materials.[197-199] This reaction related to the current peaks in the HQ–Q redox reaction can be expressed as the below (**Equation 3-6**):

$$CO + e^{-} + H^{+} \rightleftarrows C\text{–}OH \qquad \textbf{Equation 3-6}$$

Furthermore, the amount of HQ/Q redox couple there is no change for S-GNF from 6.58 to 7.90 µC cm^{-2} and for GNF from 8.62 to 8.67 µC cm^{-2}, while the amount on the G1 from 2.67 to 3.98 µC cm^{-2}, G2 from 1.37 to 24.6 µC cm^{-2}, C from 4.53 to 5.61 µC cm^{-2}, GMWNT from 1.6 to 2.1 µC cm^{-2} **Table 3-5**.

In **Figure 3-25**, Nyquist plots recorded in the frequency range from 100 KHz to 0.1 Hz and an amplitude of 10 mV on CN support material on GCE disk electrode at room temperature. These plots indicate the solution impedance of CN on GCE in the electrode/electrolyte interface. The solution resistance is decreased for S-GNF from 50 to 39 Ω, for GNF from 63 to 27 Ω, G1 from 63 to 55 Ω, G2 from 38 to 31 Ω, and for GMWNT from 63 to 27 Ω, while the amount increased only on the C from 79 to 86 Ω **Table 3-5**. These results indicate that GNF and S-GNF show better durability behaviour than rest of carbon nanostructures because of stronger graphitic atomic structure. As a result of this, we can safely say that GNF is an ideal carbon support when compared alternative carbon nanostructures.

Table 3-5. Summary of electrochemical parameters for G1, G2, S-GNF, GNF, GMWNT and carbon black(C, XC-72R) before and after 5000 cycles durability test.

	HQ/Q μC/cm-2 **Initial/After**	**Impedance / Ω** **Initial/After**
S-GNF	6.58/7.90	50/39
GNF	8.62/8.67	63/27
GMWNT	1.6/2.1	79/86
C (XC-72R)	1.38/24.7	63/55
G1	2.67/3.98	88/62
G2	1.38/24.7	38/31

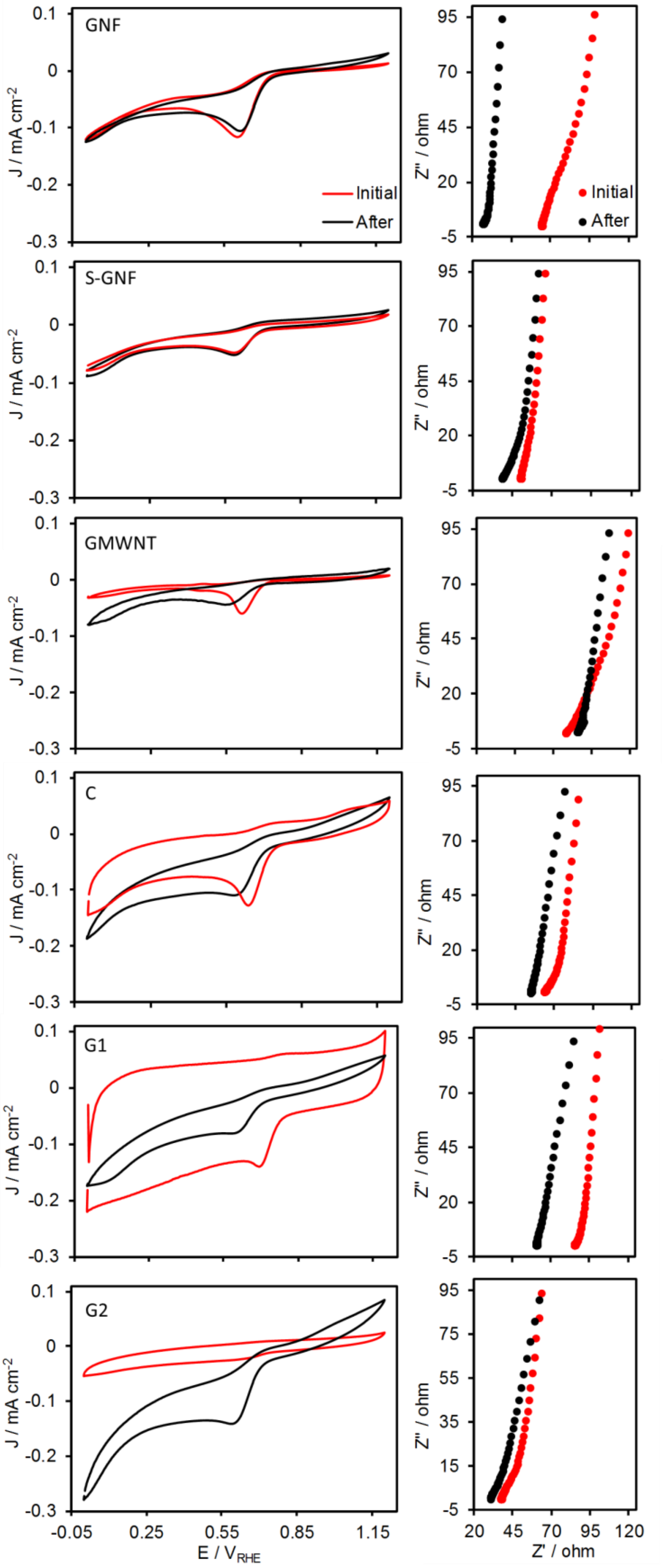

Figure 3-25. Cyclic voltammograms and Nyquist plot of GNF, S- GNF, GMWNT, C, G1, G2 before and after 5000 cycles durability test.

3.5. Conclusion

In this chapter, the ORR and OER catalytic performances of (**i**) preform nanoparticles approach synthesised Mn_4O_3-CN bifunctional electrocatalyst were measured using rotating disk electrode (RDE) measurements. Durability studies of the selected Mn_3O_4/GNF, Mn_3O_4@GNF, electrocatalyst were performed in an accelerated durability test by continuously applying linear potential sweeps up to 5000 cycles from 1.4 to 1.75 V. Interestingly, after cycling there was no significant change for the OER onset point of Mn_3O_4@GNF.

Furthermore, the ORR and OER catalytic performances of (**ii**) *in-situ* nanoparticles approach synthesised $Mn_4O_{3(in\text{-}situ)}$-CN bifunctional electrocatalyst were investigated. In conclusion, $Mn_3O_{4(in\text{-}situ)}$@GNF can be considered to be a powerful bifunctional catalyst for both the ORR and the OER and outperforms high performing electrocatalyst with smaller overpotentials for both oxygen reduction and water oxidation on non-precious bifunctional catalyst.[18, 25, 27, 28] $Mn_3O_{4\ (in\text{-}situ)}$NP on surface of GNF exhibit the lowest activity among the materials which is unexpected since NPs in $Mn_3O_{4(in\text{-}situ)}$/GNF should be more accessible for O_2 than in $Mn_3O_{4(in\text{-}situ)}$@S-GNF, but this can be explained by a higher surface of interaction of $Mn_3O_{4\ (in\text{-}situ)}$NP with the step-edge inside GNF than with the convex surface of the outside of GNF, hence a better connectivity of catalytic centers in $Mn_3O_{4(in\text{-}situ)}$@S-GNF leading to a higher $E_{1/2}$ potential as compared to $Mn_3O_{4(in\text{-}situ)}$/GNF. Considering all aspects, preform nanoparticles approach synthesised Mn_3O_4@GNF is to be less active for both ORR and OER than in-situ nanoparticles approach synthesised $Mn_3O_{4(in\text{-}situ)}$@GNF.

Finally, the electrochemical oxidation of G1, G2, S-GNF, GNF, GMWNT and carbon black (XC-72R) were investigated by applying 5000 potential cycles from 1.4 to 1.75 V vs RHE. It found that GNF and S-GNF show better durability behaviour than rest of carbon nanostructures because of stronger graphitic atomic structure. As a result of this, GNF is an ideal carbon support in comparison with alternative carbon nanostructures.

Chapter 4. Bifunctional PdS_2- carbon nanostructure electrocatalysts

4.1. Introduction

The hydrogen evolution reaction (HER) is an electrochemical reaction to harvest H_2 from water, and hence store electrical energy in the form of H_2, which is a half reaction of water splitting on the cathode. Hydrogen oxidation reaction (HOR), the reverse reaction to convert H_2 into electricity, is the anode reaction in $H_2{-}O_2$ fuel cell. The HER and HOR compared to oxygen reduction reaction (ORR), only take place two electron transfers and perform faster reaction kinetics.[200] Many studies in the field have been dedicated to improving the activity of Pd by surface modification and alloying.[95, 97-100, 104, 109] This study builds on the recent progress of electrocatalysts containing Pd for both HOR and ORR, as a good electrocatalyst for HOR is usually also a good catalyst for HER.

Sulphide edge of metal nanoparticles has been extensively studied as a promising electrocatalyst for the HER.[201-207] In order to take advantage of the recent finding, showing that sulphide edges result in enhanced catalytic activity, we extend this idea to PdS_2NP supported on carbon nanostructure (CN) to test the activity of the hybrid nanostructures in HER and HOR. It is expected that our novel PdS_2/CN hybrid nanostructures may enhance catalytic activity to the levels of Pt/C for HER and Pd/C for HOR.

4.2. Aim, objectives and scope of experiments

The main aim of the study is to prepare and test the PdS_2/CN nanostructures (developed in my group by Dr. Maria Gimenez-Lopez and Carlos Herreros-Lucas) as active electrocatalyst for

HER in the electrolysis reaction and also HOR in the fuel cell anode reaction. The PdS_2/CN nanostructures were tested for HER/HOR activity for use as a bifunctional electrocatalyst. In addition, our finding that GNF step-edges play an important role in stabilising catalytic centres (as described in Chapter 2) gives an opportunity to improve the electrocatalyst durability in HER using the same principles as described for the ORR.

Three different types of CN support materials were explored in this study: quasi one-dimensional hollow graphitised nanofibres (PR24-GNF and PR19GNF), two-dimensional sheets of multi-layered graphene (Graphene1 (G1) is untreated, and Graphene2 (G2) is ball-milled) (**Figure A- 14**), and three-dimensional amorphous carbon (carbon black). Both PR24-GNF and PR19-GNF exhibit the same corrugated interior surfaces defined by internal stacked-nanocone structures, with a typical step-edge comprising of several rolled-up graphene sheets (as described in Chapter 1), they have different external diameter and length (PR24-GNF average external diameter is 96 ± 32 nm, and PR19-GNF average external diameter and length 115 ± 37 nm).[130] Furthermore, shortened graphitised nanofibre (S-GNF) prepared by ball-milling (as described in Chapter 2) were used as carbon support materials in PdS_2@S-PR24-GNF and PdS_2@S-PR19-GNF structures.

One of objective of this study is to investigate the properties of PdS_2NP in GNF and to evaluate the effects of nanoscale confinement by comparing catalytic activity of PdS_2@GNF with PdS_2 on carbon black and graphene. Another objective of this work is to assess durability of the selected electrocatalysts (PdS_2@S-PR19, Pd/C and Pt/C) in a durability test by continuously applying linear potential sweeps up to 5000 cycles. Pd/C (20wt %, Alfa easer) and Pt/C (20wt % Pt on vulcan carbon black was supplied by Johson Matthey, HiSPECTM 3000) were utilized as benchmark electrocatalysts. This chapter is focused on electrochemical properties rather than structural properties and characterisation of PdS_2-CN as electrocatalyts.

Table 4-1. Different types of CN-supported PdS_2NP used as electrocatalysts for HER/HOR in this study.

One dimensional (1D)	**Two dimensional (2D)**	**Three dimensional (3D)**
PdS_2@PR24	PdS_2/G1	PdS_2/C
PdS_2@S-PR24	PdS_2/G2	
PdS_2@S-PR19		

4.4. Experimental Section

4.4.1. General

XRD patterns were obtained on a Bruker AXS D8-Advanced diffractometer with Cu Kα radiation (λ=1.5418 Å). TGA analyses were performed in a TA/TGA Q500 instrument. Samples for TEM analysis were prepared dispersing the material either in hexane or HPLC grade iso-propanol by ultasonication, and then drop casting the solution onto lacey carbon film coated copper grid. The samples were dried under nitrogen gas flow for 3 minutes to remove any residual solvent. HRTEM images were obtained on a JEOL 2010F TEM using accelerating voltage of 200 kV.

4.4.2. Electrochemical measurements

The electrochemical experiments were performed on an electrochemical work station Autolab potentiostat PGSTAT204 using a glassy carbon electrode (GCE) as working electrode in a commercial (Pine Instruments) GCE disk electrode, a HydroFlex reversible hydrogen electrode (RHE) electrodes as reference electrodes, respectively. The GCE was cleaned with 0.05µm principal particle size alumina powder solution (Agar Scientific Ltd.) on a polishing paper to remove any impurity which may affect electrochemical measurements. The investigated samples were dropped onto the GCE as ink with an optimised constant metal loading of 100 µg/cm^2 and then dried in air[156, 157]. The potential was cycled at fast scan rates (500 or 200 mV/s) for up to 100 cycles before readings were taken in order to remove any impurities and unwanted species from the surface of the platinum electrodes. Impedance measurements, the cell resistance was measured immediately after OER and ORR measurements taking the ac impedance spectra from 32 to 0.1 kHz and a voltage perturbation of 10 mV. The real part of the resistance at 1 kHz was taken as the cell resistance and was used to obtain the IR-free potential of the working electrode.

All the polarization curves were recorded between 0.2V and -0.5 V vs RHE for HER and between 0 V and 1 V vs RHE at 1600 rpm for HOR at a sweep rate of 10 mV/s in hydrogen saturated 0.1M $HClO_4$ at room temperature. Exchange current densities J_0 of the HOR/HER were obtained by fitting the experimental data to the Butler–Volmer equation. Electrochemical durability test was carried out by continuously applying linear potential sweeps up to 5000 cycles from -0.2 to 0.4 V vs RHE at 50 mV in $HClO_4$ which caused surface oxidation/reduction cycles of catalysts, and then compared with Pd/C and Pt/C as benchmark electrocatalysts with metal loading of 14 µg/cm^2.

4.3. Results and discussion

4.3.1. Structural characterisation of PdS_2-CN hybrid nanostructures

High-resolution transmission electron microscopy (HRTEM) investigation of PdS_2-CN hybrid electrocatalyst materials have been performed to assess the size and location of PdS_2NP on carbon nanostructures. HRTEM imaging (**Figure 4-1a)** of the synthesised PdS_2NP showed polyhedral nanoparticles uniformly dispersed on/into PR24-GNF with an average diameter of 6 ± 2.6 nm. Most of the PdS_2NP are attached to the step-edges, some of large NP are located on the smooth external surface of nanofibres. In contrast, in **Figure 4-2a** HRTEM imaging of PdS_2@S-PR24 showed that the vast majority of nanoparticles are randomly dispersed on the inner surface of the shortened graphitised nanofibres S-PR24 and attached to the step-edges as tilted HRTEM measurements confirmed (**Figure A- 9**), similar to platinum nanoparticles encapsulated into S-PR24 reported in our previous studies[208] (as described in Chapter 2). The PdS_2NP in this study have an average diameter of 2.6 ± 1 nm which matches well with the size of graphitic step-edges in S-PR24.

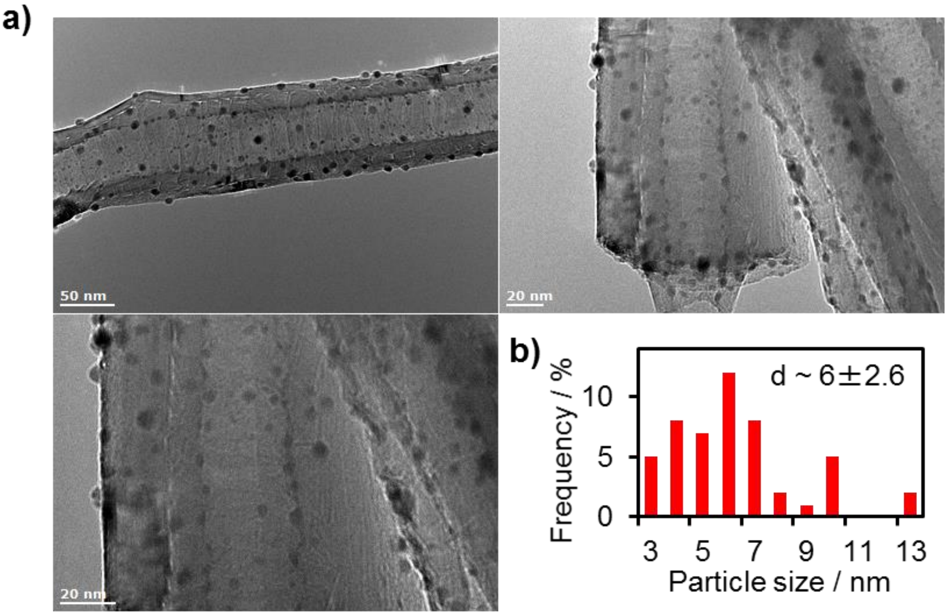

Figure 4-1. (**a**) HRTEM images of PdS_2@PR24, (**b**) particle size distributions and average sizes of PdS_2NP.

It is interesting that the introduction of surface defects on GNF by mechanical milling (S-GNF) has a noticeable influence on the final size of PdS_2NP during the preparation process with the trend PdS_2@PR24> PdS_2@S-PR24 confirming that greater concentration of surface defects suppresses the ripening and coalescence of nanoparticles.

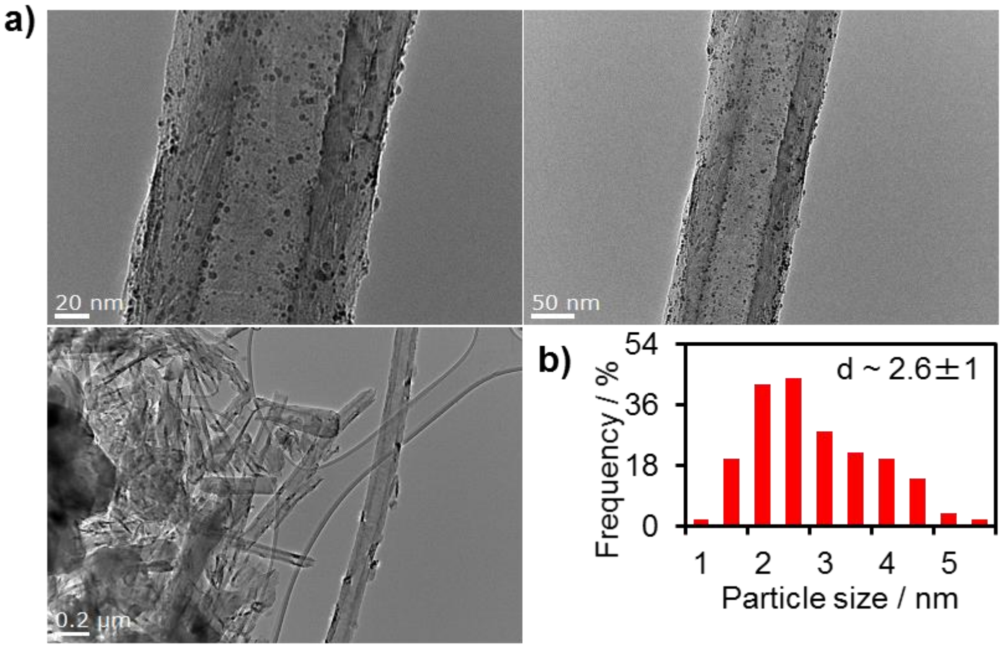

Figure 4-2. (**a**) HRTEM images of PdS_2@S-PR24, (**b**) particle size distributions and average sizes of PdS_2NP.

HRTEM imaging of PdS_2@S-PR19 prepared from ball-milled graphitised nanofibres PR19 showed PdS_2NP with the average diameter of 7.3 ± 4.3 nm in **Figure 4-3**. In contrast, nanoparticles in PdS_2@S-PR19 are elongated shape and have larger particles size than PdS_2@PR24 and PdS_2@S-PR24. This can be explained that S-PR19 GNF obtained with ball milling method and used for the encapsulation experiments, they are clearly observed in the HRTEM images in **Figure 4-3a.** However, a significant number of defects and damages after the ball milling can be clearly observed in HRTEM not only on surface of PdS_2@S-PR19 nanostructures but also in the internal structure and step edges of the GNF. As a result, the PdS_2NP in PdS_2@S-PR19 agglomerated to elongated shape and have larger cluster. Seriously damaging of PdS_2@S-PR19 after the ball milling may let to reduce the durability of PdS_2@S-PR19 and may enhanced electrocatalytic performance of PdS_2@S-PR19 due to active carbon sites[209] which have oxygen-containing groups (*i.e.* carboxylic, quinonic, lactonic, phenolic and others groups)[151] on seriously damaged S-PR19 surface. Energy-dispersive X-ray (EDX) spectrum of this sample shown in **Figure 4-3c**, confirmed palladium and sulfur in the electrocatalyts. S-PR19 GNF obtained with ball milling method and used for the encapsulation experiments, they are clearly observed in the HRTEM images in **Figure 4-3a.** For PdS_2@S-PR19 X-ray diffraction (XRD) pattern is consistent with PdS_2 (**Figure A- 11)**, exhibiting a strong 2θ peak at around 30°.

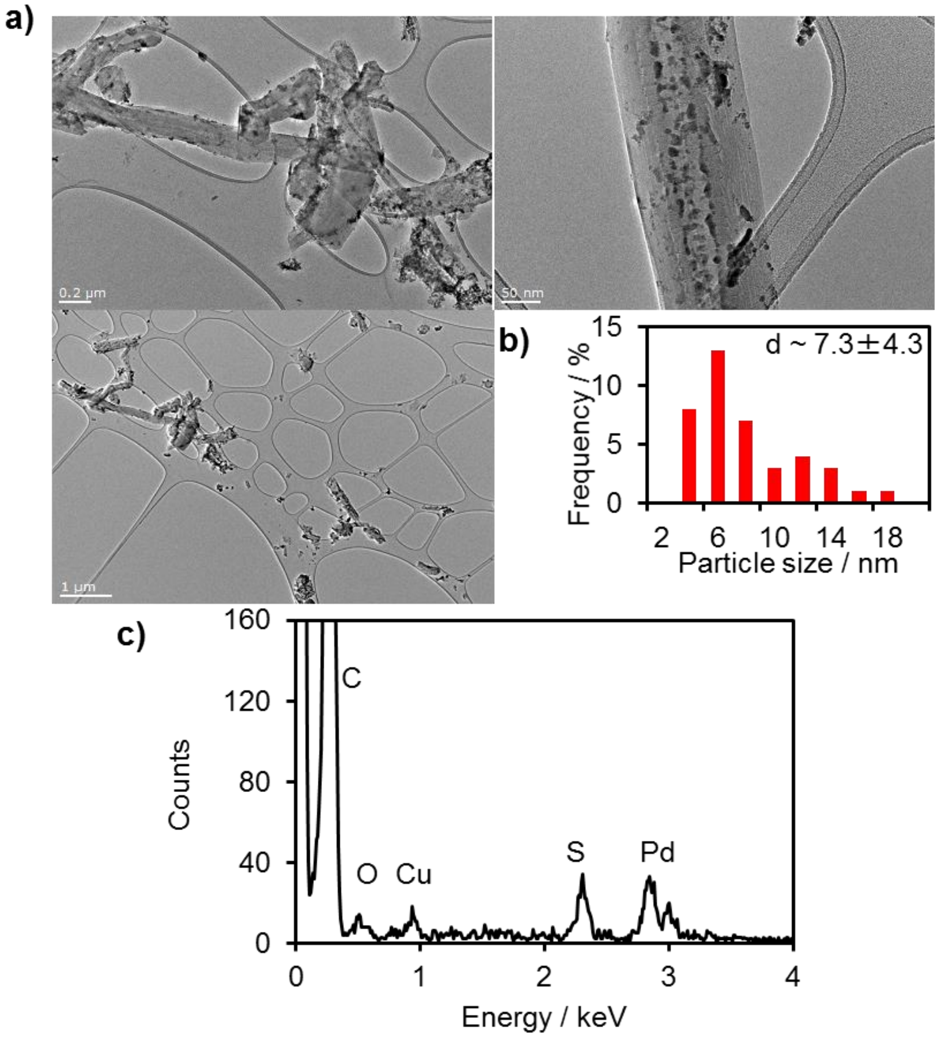

Figure 4-3. (**a**) HRTEM images of PdS_2@S-PR19, (**b**) particle size distributions and average sizes of PdS_2NP and (**c**) EDX spectrum of PtS_2@S-PR19 mounted onto a copper TEM grid coated with“lacey” carbon film.

HRTEM imaging of PdS_2/G1 and PdS_2/G2 exhibited that PdS_2 polyhedral NP uniformly dispersed on the G1 with an average diameter of 3.4 ± 1.7 nm (**Figure 4-4a)** and the size NP on G2 are smaller (2.8 ± 1.6 nm) and more uniformly dispersed than the NP on G1 (**Figure 4-4b)**. Similarly, it is observed that the introduction of surface defects on G2 by mechanical milling has a noticeable influence on the final size of PdS_2NP during the preparation process with the trend PdS_2/G1> PdS_2/G2 confirming that greater concentration of surface defects suppresses the ripening and coalescence of the nanoparticles. Surprisingly, under the same conditions PdS_2NP deposited on G1 exhibited smaller NP size (3.4 ± 1.7 nm) than NP in PdS_2@PR24 (6 ± 2.6 nm) (**Table 4-2**). This may indicate strong interactions between the PdS_2NP and G1 surface due to the higher degree of functionalisation and defects on G1 than on the GNF surface. However, the high degree of functionalisation and defect may have a detrimental effect on the catalytic performance of nanoparticles because of a potentially high electron transfer resistance and greater tendency to corrosion[120, 145] than GNF.

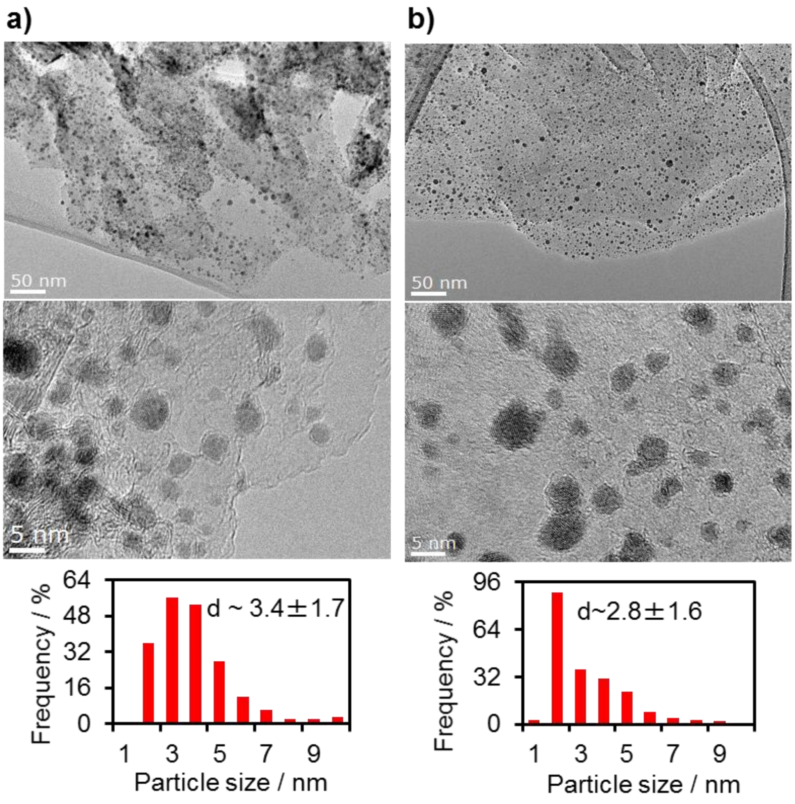

Figure 4-4. HRTEM images, particle size distributions and average size of PdS_2NP for (**a**) PdS_2/G1 (**b**) PdS_2/G2.

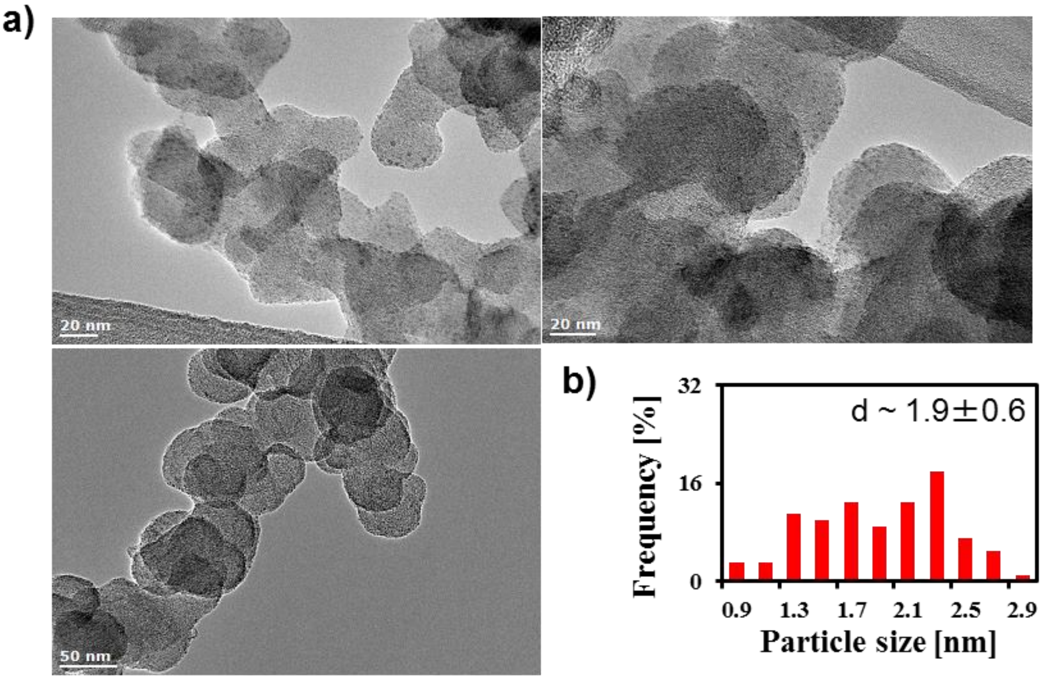

Figure 4-5. (**a**) HRTEM images of PdS_2/C, (**b**) particle size distributions and average size of PdS_2NP.

More Surprisingly, under the same conditions PdS_2NP deposited on carbon black exhibited the smallest particle size distribution (1.9 ± 0.6 nm), smaller than exhibited in commercial Pd/C (4.5 ± 1.3 nm). This may indicate very strong interactions between the PdS_2NP and the carbon black surface due to the high degree of functionalisation of carbon black surface with oxygen-containing groups (*i.e.* carboxylic, quinonic, lactonic, phenolic and others groups)[151] which effectively inhibit PdS_2migration and coalescence to an even greater extent than the graphitic step-edges of S-GNF. However, the high degree of functionalisation and the significant disorder of carbon black may have a detrimental effect on the catalytic performance of nanoparticles.

Thermogravimetric analysis (TGA) were performed by Carlos Herreros-Lucas and indicated ~20 % for Pd/C, 10 % for PdS_2/C, 20 % for PdS_2/G1, 24 % for PdS_2/G2, 5 % for PdS_2@PR24, 9 % for PdS_2@S-PR24 and 25 % for PdS_2@S-PR19 of Pd by weight (**Figure A- 10**).

Table 4-2. Summary of particles size for PdS_2-CN hybrid nanostructures, Pd/C and Pt/C.

	Particle size / nm
PdS_2@PR24	6 ± 2.6
PdS_2@S-PR24	2.6 ± 1
PdS_2@S-PR19	7.3 ± 4.3
PdS_2/G1	3.4 ± 1.7
PdS_2/G2	2.8 ± 1.6
PdS_2/C	1.9 ± 0.6
Pd/C	4.5 ± 1.3
Pt/C	3.3 ± 0.7

4.3.2. Electrocatalysis of HER by PdS_2-CN hybrid nanostructures

The HER catalytic performances of these PdS_2-CN electrocatalyst hybrid materials were investigated using rotating disk electrode (RDE) measurements by depositing on a glassy carbon electrode using a typical three-electrode setup. After the electrolyte was saturated with pure hydrogen, HER polarization curves were recorded between 0.2 and -0.5 V vs RHE at a sweep rate of 10 mV/s in $HClO_4$ at room temperature. A freshly prepared 0.1 M $HClO_4$ electrolyte was used for each measurement, as described above. The currents have been normalized to the geometric surface area of the glassy carbon electrode, and the potentials corrected by the ohmic drop ($\Delta E_\Omega = I \cdot R_s$) in the solution ($E$ *is* electrode potential, I current and R_s solution resistivity). Exchange current densities (J_0), is the current density at zero overpotential of the HER. These values were obtained by fitting the experimental data to the Butler–Volmer equation (**Equation 4-1**):

$$i = i_0 \times \left(e^{\frac{\alpha_a F \eta}{RT}} - e^{\frac{\alpha_c F \eta}{RT}} \right)$$ **Equation 4-1**

α_a and α_c represent the anodic (HOR) and cathodic (HER) transfer coefficients respectively, F is Faraday’s constant (96485 As/mol) and R is the universal gas constant (8.314 J/mol K), T is temperature (298 K). Anodic and cathodic Tafel slopes (b in V/decade) can be calculated via **Equation 4-2**, using the respective anodic and cathodic transfer coefficients:

$$b_{a/c} = \frac{2.303RT}{F\alpha_{a/c}} \qquad \textbf{Equation 4-2}$$

The HER in acid medium proceed via a combination of several of the following elementary reaction steps: first is a primary discharge step of adsorbed hydrogen (H_{ads}) (Volmer reaction, **Equation 4-3**) which is then a recombination step, the dissociative adsorption of molecular hydrogen on surface without electron transfer (Tafel reaction, **Equation 4-4**), or a desorption step with simultaneous electron transfer (Heyrovský reaction, **Equation 4-5**). [84-87, 210]

Volmer: $H_3O^+ + e^- \leftrightarrow H_{ads} + H_2O$ b ≈ 120 mV **Equation 4-3**
Tafel: $2H_{ads} \leftrightarrow H_2$ b ≈ 30 mV **Equation 4-4**
Heyrovský: $H_{ads} + H_3O^+ + e^- \leftrightarrow H_2 + H_2O$ b ≈ 40 mV **Equation 4-5**

The possible HER/HOR mechanisms based on these three elementary reactions are thus the Tafel–Volmer (**Equation 4-3, 4**) or the Heyrovský -Volmer (**Equation 4-3, 5**) reaction sequences. It is hypothesized that one of the elementary reactions in each of the two reaction sequences is the rate-determining step (rds) for the simplest kinetic HER/ HOR mechanism. The Tafel slope shows a characteristic mechanism of the electrocatalyst by determining the rate-determining step of the HER.

4.3.3. Electrocatalysis PdS_2 nanoparticles supported on one-dimensional carbon

As a reference point, a commercial Pt/C and Pd/C exhibited 0 mV[205] and 51 mV overpotential during HER (**Figure 4-6**). It was observed that the shortened GNF supported PdS_2@S-PR19 exhibited high HER catalytic performance with a small overpotential (39 mV), beyond which the cathodic current decrease sharply under more negative potentials. The onset potential was read from Tafel plot as shown in **Figure 4-7**. The same approach was used to determine the overpotential for all electrocatalysts.

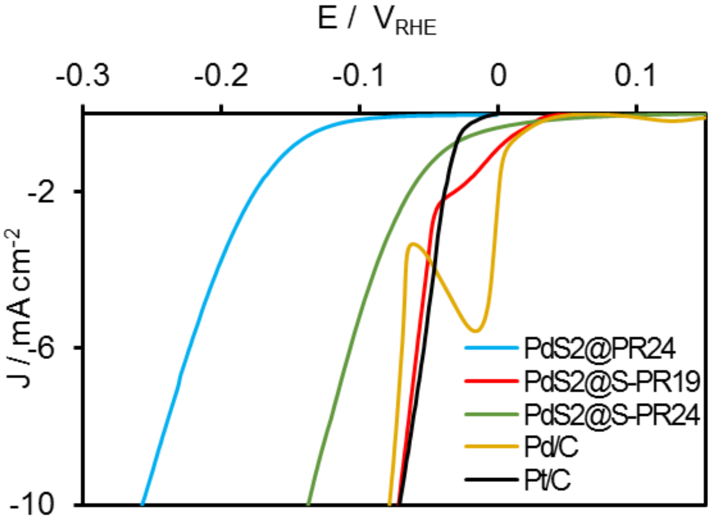

Figure 4-6. Comparison of HER polarisation curves for PdS2 nanoparticles supported on quasi one-dimensional nanocarbons PdS_2@PR24, PdS_2@S-PR24, PdS_2@S-PR19 electrocatalyst and commercial benchmark electrocatalyst of carbon black.

Furthermore, PdS_2@S-PR19 shows the largest exchange current density of 0.75 mAcm^{-2} which is shown to have the highest activity superior to that of the commercial electrocatalyst 0.652 mAcm^{-2} for Pt/C (this compares well with literature data)[105, 211] and 0.331 mAcm^{-2} for Pd/C (**Table 4-3)**. Our PdS_2@S-PR19 indicated excellent activity with 39 mV overpotential for the HER, the activity that may correlate with catalytically active sulfur edge sites[109, 212] and active carbon edge sites[209] which appeared after billing of PdS_2@S-PR19. Moreover, this may indicate that GNF are shortened to enhance the mass transport of solvent, reactants and products during HER.[208]

The linear portions of the Tafel plots below onset potential of these electrocatalyts in the region of low current density (**Figure 4-7**) were fitted to the Tafel equation:

$$\eta = b \log J + a \qquad \textbf{Equation 4-6}$$

where *J* is the current density and *b* is the Tafel slope), calculating Tafel slopes of 73.9, 67.3, 30.4, 31.3 and 30.3 mVdec^{-1} for PdS_2@PR24, PdS_2@S-PR24, Pd/C and Pt/C respectively (**Table 4-3**). For PdS_2@S-PR19 nanostructures, this is in excellent agreement with the value calculated for the Pt/C commercial catalyst (~ 30 mVdec^{-1}) and also with literature data[205, 213] for HER in similar condition. Having a very high H_{ads} coverage, the HER on a Pt/C (30.3 mVdec^{-1}) surface is known to go through the Volmer-Tafel mechanism[210] (**Equation 4-3, 4**), and the recombination step is the rds at low overpotentials, as shown by measured Tafel slope of 30.4 mVdec^{-1} for PdS_2@S-PR19.

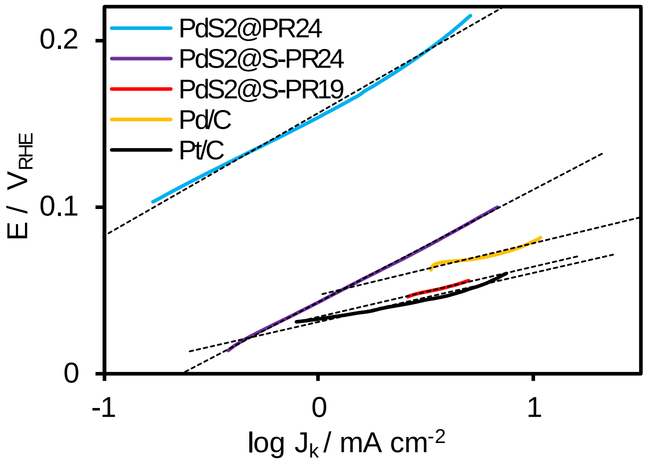

Figure 4-7. Comparison of HER Tafel plots for PdS_2 supported on quasi one-dimensional carbons PdS_2@PR24, PdS_2@S-PR24, PdS_2@S-PR19 and commercial benchmark electrocatalyst of carbon black.

The polarization curve of PdS_2@PR24 and PdS_2@S-PR24 on glassy carbon electrode showed 101 mV and 41 mV overpotential vs. RHE for HER. PdS_2@S-PR24 exhibited higher HER activity and higher exchange curerent density (0.272 mAcm^{-2}) then PdS_2@PR24 (0.045 mAcm^{-2}). This may indicate that S-PR24 GNF has led to an advanced carbon support material with competitive performance relative to alternative carbon support materials. Our recent studies[129, 131, 150, 151] have shown that van der Waals forces play crucial role in interactions of metal nanoparticles with carbon nanotubes and nanofibers and their effectiveness is proportional to the contact surface between NP and GNF. When a nanoparticle is positioned on the smooth graphitic external surface of a GNF, the area of surface contact is minimal, but if the nanoparticle is residing at a graphitic step-edge, the surface of interaction increases significantly. HRTEM imaging of PdS_2@S-PR24 proved that most of the NP were attached to the step-edges, some of large NP located on the smooth external surface of nanofibres (**Figure 4-2**). This can be explained by a higher surface of interaction of PdS_2NP with the step-edge inside PR24-GNF, hence a better connectivity of catalytic centres in PdS_2@S-PR24 leading to a close electrocatalytic performance as compared to Pd/C Pt/C commercial catalysts. Moreover, GNF are shortened to enhance the mass transport of solvent, reactants and products during HER.[208] The Tafel slope for PdS_2@PR24 and PdS_2@S-PR24 exhibited that the HER took place through a Volmer-Heyrovský mechanism[210] which is the electrochemical desorption of H_{ads} and H_3O^+ to form hydrogen gas. The desorption step is the rate-determining step at low overpotentials.

4.3.4. Electrocatalysis PdS_2 nanoparticles supported on two-dimensional carbon

The polarization curve of PdS_2/G1 and PdS_2/G2 in **Figure 4-8** indicated a close and very small overpotential of 18 mV versus RHE for HER, beyond which the cathodic current decreases sharply under more negative potentials to produce hydrogen gas.

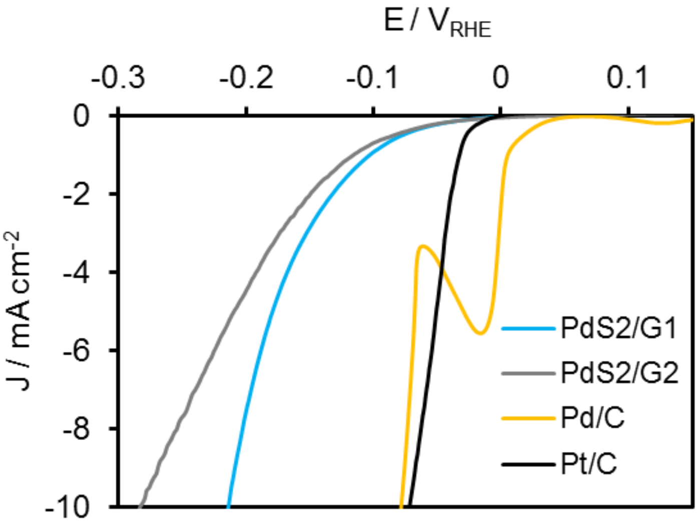

Figure 4-8. Comparison of HER polarisation curves for PdS_2 nanoparticles supported on quasi two-dimensional nanocarbons PdS_2/G1, PdS_2/G2 electrocatalyst and commercial benchmark electrocatalyst of carbon black.

As listed **Table 4-3**, PdS_2/G1 and PdS_2/G2 showed lower exchange current density of 0.058 and 0.061 $mAcm^{-2}$ which determined lower electrocatalytic performance in comparison to the PdS_2 encapsulated S-GNF such as PdS_2@S-24 (0.072 $mAcm^{-2}$), PdS_2@S-PR19 (0.75 $mAcm^{-2}$) and also to the Pt/C (0.652 $mAcm^{-2}$) and Pd/C (0.331 $mAcm^{-2}$) commercial catalysts. The cross section of GNF is polygonal (not circular) the surface area of contact between the PdS_2NP and GNF in PdS_2@S-24 are PdS_2@S-PR19 are further maximized when the PdS_2NP are located at the apexes of the graphitic facets of step-edges, which leads to a drastic enhancement in van der Waals interactions between the PdS_2NP and the carbon support. This increased interaction greatly may enhance the electrocatalytic performance of the PdS_2NP.

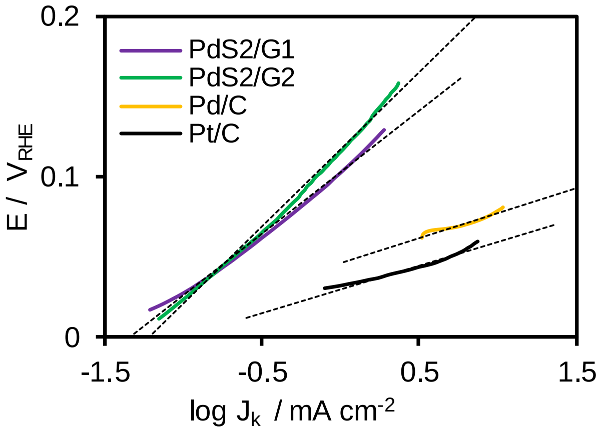

Figure 4-9. Comparison of HER Tafel plots for PdS_2 supported on quasi two-dimensional carbons PdS_2/G1, PdS_2/G2 and commercial benchmark electrocatalyst of carbon black.

The linear portions of the Tafel plots (**Figure 4-9**) were fitted to **Equation 4-6** to calculate the Tafel slopes of 76.8 and 96.1 mV/dec for PdS_2/G1 and PdS_2/G2 respectively. The Tafel slopes in **Figure 4-9** exhibited that the HER on PdS_2/G1 and PdS_2/G2 take place through a Volmer-Heyrovský mechanism[210] which is the electrochemical desorption of H_{ads} and H_3O^+ to form hydrogen. In contrast Pt/C and Pd/C proceed through the Volmer-Tafel mechanism[210] as mentioned above.

4.3.5. Electrocatalysis PdS_2 nanoparticles supported on three-dimensional carbon

HER polarization curves of PdS_2/C in **Figure 4-10** displayed a small overpotential 64 mV vs RHE, beyond which cathodic current decreased sharply under more negative potential. The calculated exchanged current density of 0.286 $mAcm^{-2}$ for PdS_2/C showed a similar activity to Pd/C (0.331 $mAcm^{-2}$) and a lower activity than Pt/C (0.652 $mAcm^{-2}$) commercial electrocatalysts (**Table 4-3**). This indicates very strong interactions between PdS_2NP and carbon black surface due to the high degree of functionalisation of carbon black surface with oxygen-containing groups (*i.e.* carboxylic, quinonic, lactonic, phenolic and others groups).[151]

However, the high degree of functionalisation and the significant disorder of carbon black may have a detrimental effect on the catalytic performance of nanoparticles because of a potentially high electron transfer resistance and undesired increase in HER overpotential, and greater tendency to corrosion[18, 19] than S-GNF.

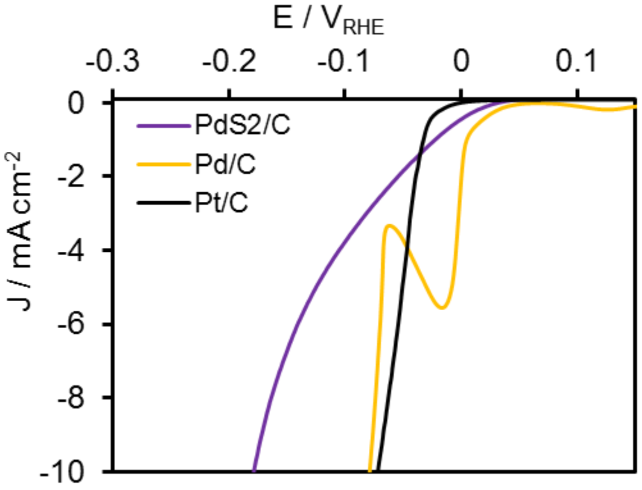

Figure 4-10. Comparison of HER polarisation curves for PdS_2 nanoparticles supported on quasi one-dimensional nanocarbons PdS_2/C electrocatalyst and commercial benchmark electrocatalyst of carbon black.

The Tafel plots of these electrocatalysts showed classic Tafel behaviour in **Figure 4-11**. The Tafel slopes were observed in low current density 68.1, 30.3 and 31.3 $mVdec^{-1}$ for PdS_2/C, Pd/C and Pt/C. The Tafel slope for PdS_2/C was exhibited that the HER take place through a Volmer-Heyrovský mechanism[210] which is the electrochemical desorption of H_{ads} and H_3O^+ to form hydrogen while Pt/C and Pd/C proceed through the Volmer-Tafel mechanism[210] as mentioned above.

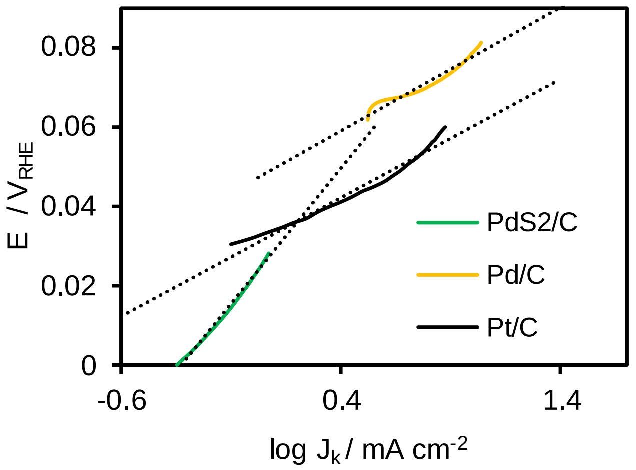

Figure 4-11. Comparison of HER Tafel plots for PdS_2 supported on quasi three-dimensional carbons PdS_2/C and commercial benchmark electrocatalyst of carbon black.

Table 4-3. Summary of electrochemical parameters for PdS_2@PR24, PdS_2@S-PR24, PdS_2@S-PR19, PdS_2/G1 and PdS_2/G2, PdS_2/C, Pd/C and Pt/C.

	Overpotential / mV	**Tafel Slope / mV dec^{-1}**	**J_0 / mAcm^{-2}**
PdS_2@PR24	101	73.9	0.045
PdS_2@S-PR24	41	67.3	0.272
PdS_2@S-PR19	39	30.4	0.75
PdS_2/G1	18	76.8	0.058
PdS_2/G2	18	96.1	0.061
PdS_2/C	64	68.1	0.286
Pt/C	0	30.3	0.652
Pd/C	51	31.3	0.331

4.3.6. Durability test

Additional significant criterion for an ideal electrocatalyst is high durability. Therefore, durability studies of the selected PdS_2@S-PR24 and PdS_2@S-PR19 electrocatalyst were performed by continuously applying linear potential from -0.2 to 0.4 V vs RHE at 50 mV in $HClO_4$ for 5000 cycles. The data produced was compared with commercial Pd/C and Pt/C as benchmark electrocatalysts. At the end of the durability test, the polarisation curves were compared, negligible loss of exchange current density from 0.272 to 0.236 mAcm^{-2} for PdS$_2$@S-PR24 and from 0.331 to 0.27 mAcm^{-2} were observed for Pd/C (**Figure 4-11**). These values are in contrast to the larger decrease of the exchange current density from 0.652 to 0.403 mAcm^{-2} observed for Pt/C and from 0.75 to 0.331 mAcm^{-2} were observed for PdS$_2$@S-PR19 (**Figure 4-11**).

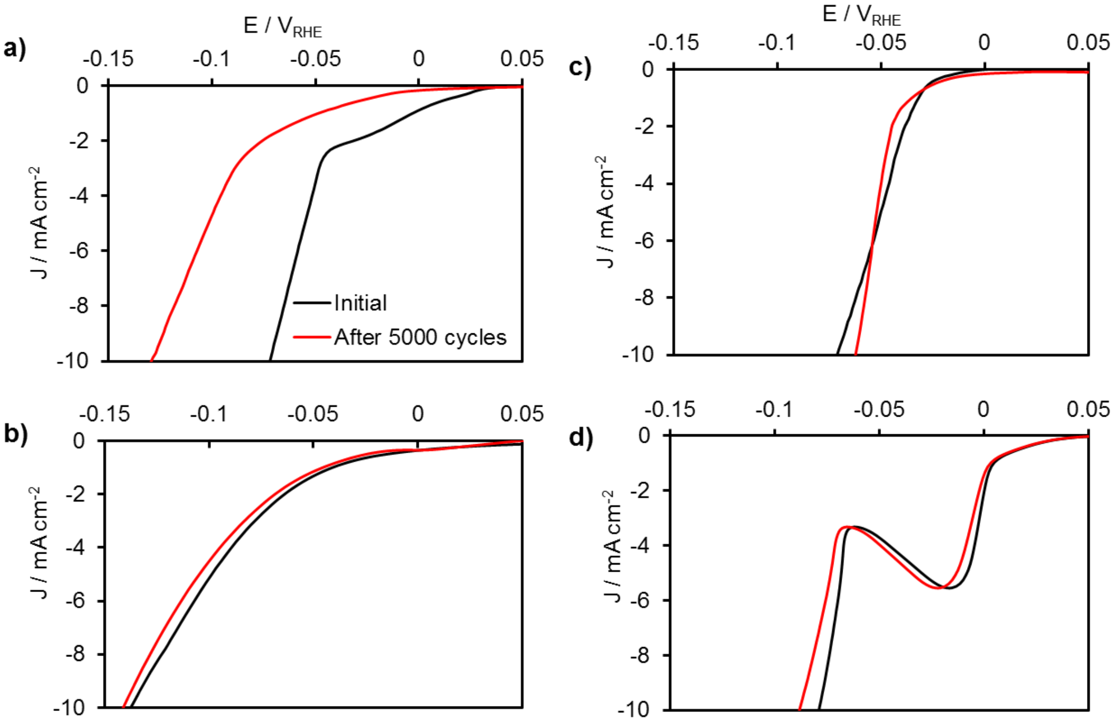

Figure 4-12. Comparison of (**a**) PdS$_2$@S-PR19, (**b**) PdS$_2$@S-PR24, (**c**) Pt/C and (**d**) Pd/C electrocatalysts before and after the durability test over 5000 cycles from -0.2 to 0.4 V vs RHE at 50 mV.

The lack of stability of Pt on carbon black may be related to the absence of long-range order in in this support material leading to electrochemical corrosion that aggravates the Pt nanoparticle sintering (**Figure A- 15d**) and leads to a reduced durability of Pt/C in comparison to PdS$_2$@S-PR24. This provides further evidence of the stabilising effects of step-edges in GNF cavities and PtNP confinement within the GNF. The poorer electrical connectivity of carbon black with the Pt gives rise to a higher electron transfer resistance and undesired decrease in HER activity as compared to the graphitic structures of GNF. This may indicate that S-PR24 GNF has led to an advanced carbon support material with competitive durability relative to alternative carbon materials. Our recent studies[129, 131, 150, 151] have shown that van der Waals forces play crucial role in interactions of metal nanoparticles with carbon nanotubes and nanofibers and their effectiveness is proportional to the contact surface between NP and GNF. When a nanoparticle is positioned on the smooth graphitic external surface of a GNF, the area of surface contact is minimal, but if the nanoparticle is residing at a graphitic step-edge, the surface of interaction increases significantly. This can be explained by a higher surface of interaction of PdS_2NP with the step-edge inside PR24-GNF, hence a better connectivity of catalytic centres in PdS_2@S-PR24 leading to higher durability as compared to Pd/C Pt/C commercial catalysts.

Comparison of the overpotentials of these electrocatalysts in **Table 4-4** showed that there is no change for Pt/C, 3 mV increase for PdS_2@S-PR24, 9 mV for Pd/C and 35 mV for PdS_2@S-PR19. A significant change of the overpotential for was observed for PdS_2@S-PR19. This can be explained that a significant number of defects and damages after the ball milling can be clearly observed in HRTEM not only on surface of PdS_2@S-PR19 nanostructures but also in the internal structure and step edges of the GNF. As a result, seriously damaging of PdS_2@S-PR19 after the ball milling may let to reduce the durability of PdS_2@S-PR19. A significant change in particle size and morphology was also found for PdS_2@S-PR19, Pt/C and Pd/C after 5000 cycles durability test shown in **Figure A- 15.**

Table 4-4. Summary of electrochemical parameters for PdS_2@S-PR24, PdS_2@S-PR19, Pd/C and Pt/C before and after the potential cycling from -0.2 to 0.4 V vs RHE at 50 mV in $HClO_4$ for 5000 cycles.

	Overpotential / mV	**J_0 / mA cm^{-2}**
PdS_2@S-PR19-Initial	39	0.75
PdS_2@S-PR19-After	74	0.331
PdS_2@S-PR24	41	0.272
PdS_2@S-PR24-After	44	0.236
Pd/C-Initial	51	0.331
Pd/C-After	60	0.27
Pt/C- Initial	0	0.652
Pt/C -After	0	0.403

4.3.7. Electrocatalysis of HOR by PdS_2-CN hybrid nanostructures

The HOR voltammograms were recorded via the RDE technique in acid media. The electrolyte was saturated with pure hydrogen, the polarization curves were recorded between 0 V and 1 V vs RHE at a sweep rate of 10 mV/s at room temperature and rotation rates of 400, 900, 1600, and 2500 rpm (**Figure 4-13**). A freshly prepared 0.1 M $HClO_4$ electrolyte was used for each measurement at each temperature, as described above. The currents have been normalized to the geometric area of the glassy carbon electrode, and the potentials corrected for both the ohmic drop ($\Delta E_\Omega = I \cdot R_S$) in the solution and mass transport correction by Koutecky-Levich equation (**Equation 4-8**) for extracting the kinetic HOR current.[214] Exchange current densities J_0 of the HOR were obtained by fitting the experimental data to the Butler–Volmer equation (**Equation 4-1**).

Following the HER activity experiments, our most active electrocatalyst for HER, PdS_2@S-PR19, was investigated for hydrogen oxidation reaction (HOR) activity. As a reference electrocatalysts, Pt/C (20 wt % Pt on Vulcan carbon black) was also tested exhibiting high HOR catalytic performance.

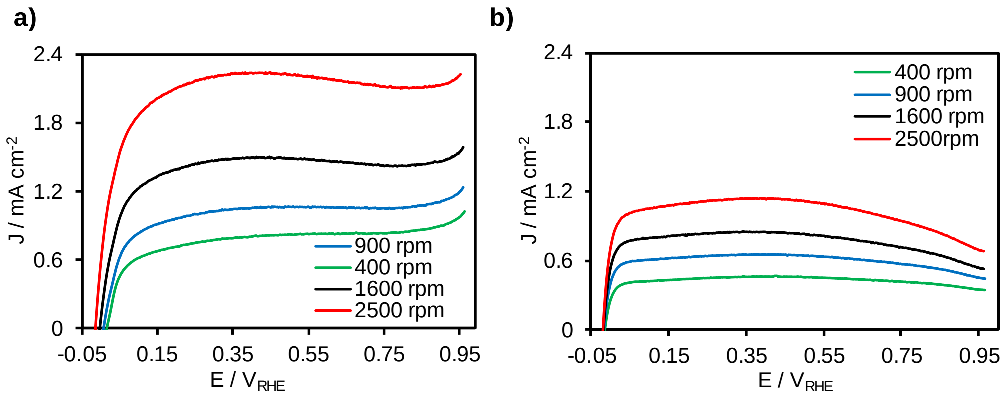

Figure 4-13. Linear-sweep voltammograms for RDEs of (**a**) PdS_2@S-PR19 and (**b**) Pt/C in 0.1 M $HClO_4$.

Diffusion limiting current of HOR determine with Levich equation (**Equation 4-7**):

$$i_d = 0.20nFD^{2/3}v^{-1/6}c_0\omega^{1/2} \quad \textbf{Equation 4-7}$$

where D the diffusion coefficient of H_2 in the electrolyte, F is the Faraday's constant, n the number of electrons in the HOR (n = 2), v the kinematic viscosity of the electrolyte, ω scan rate and c_0 the solubility of H_2 in 0.1 M $HClO_4$. The total current density obtained by activation and diffusion combined process, can be named in terms of the kinetic (J_k) and diffusional (J_d) current densities in Koutecky-Levich equation:

$$\frac{1}{J} = \frac{1}{J_d} + \frac{1}{J_k} \qquad \textbf{Equation 4-8}$$

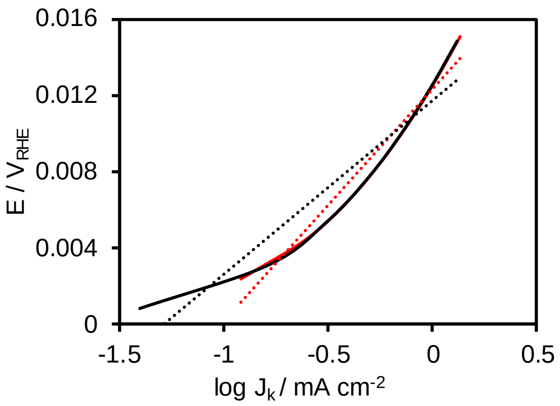

Figure 4-14. Mass-transfer corrected Tafel plots for the HOR PdS_2@S-PR19 (red) and Pt/C (black) in 0.1 M $HClO_4$.

A Tafel plot is commonly used for HOR, to obtain mechanism and kinetic data for electrode reaction.[215-217] On polycrystalline platinum in acid medium, the most commonly known mechanism is electrochemical adsorption step (Heyrovský) (**Equation 4-5**) or the adsorption step (Tafel) (**Equation 4-4**), then discharge step of the adsorbed hydrogen atom (Volmer),[215] (**Equation 4-3**).

Marković and co-workers measured a Tafel slope of 28 mV dec^{-1} on Pt (110) for the HOR in 0.05 M H_2SO_4 at 303 K.[216] In our study, mass transport corrected Tafel slope is calculated 30.2 $mVdec^{-1}$ for PdS_2@S-PR19 and 30.3 $mVdec^{-1}$ for Pt/C in similar experimental condition. Therefore, this comparison indicates that the HOR occurs on PdS_2@S-PR19 and Pt/C via the Tafel–Volmer mechanism[215] with Tafel as the rate determining step (**Table 4-5**). The exchange current density, J_0, shows the intrinsic electrochemical activity of electrocatalysts, is a significant electrochemical value for assessing catalysts as anodes for HOR. The exchange current density was found 1.086 $mAcm^{-2}$ for PdS_2@S-PR19 and 1.098 for Pt/C which is in excellent agreement with the value calculated by Marković et al. (0.98 $mAcm^{-2}$) for HOR under similar conditions.[216] Our PdS_2@S-PR19 has shown excellent activity with respect to the HOR, the activity may correlate with catalytically active sulfur edge sites[109, 212] and and active carbon edge sites[209] which appeared after billing of PdS_2@S-PR19. Moreover, this may indicate that GNF are shortened to enhance the mass transport of solvent, reactants and products during HER.[208] S-PR19 GNF has led to an advanced carbon support material with competitive performance relative to alternative carbon materials, Hovewer, it is not durable carbon support due to a significant number of defects and damages after the ball milling can be clearly observed in HRTEM not only on surface of PdS_2@S-PR19 nanostructures but also in the internal structure and step edges of the GNF.

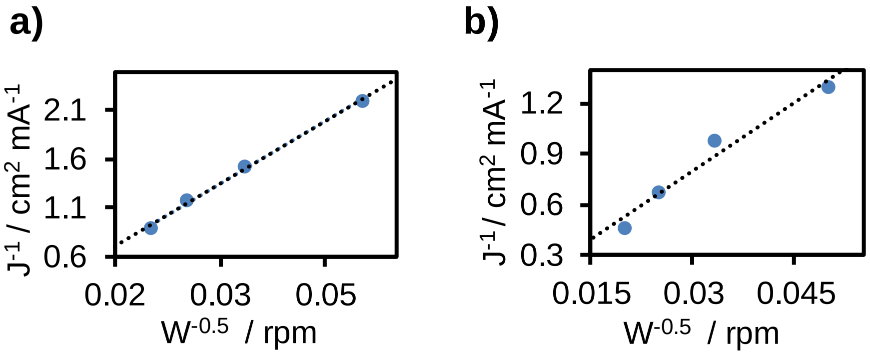

Figure 4-15. Koutecky–Levich plot (axes J^{-1} versus $\omega^{-1/2)}$ for (**a**) Pt/C and (**b**) PdS_2@S-PR19.

At fixed potential 0.3V, Koutecky–Levich plots (axes J^{-1} versus $\omega^{-1/2)}$ were plotted (**Figure 4-15)**. By applying **Equation 4-8**, the linear lines were used to predict J_k from their slope and the J^{-1}

Table 4-5. Summary of electrochemical parameters for PdS_2@S-PR19 and Pt/C in HOR.

	Tafel Slope / mVdec^{-1}	Exchange current density / mAcm^{-2}	Mechanism	Rate determining step (rds)
PdS_2@S-PR19	30.2	1.086	Tafel-Volmer	Tafel
Pt/C	30.3	1.098	Tafel-Volmer	Tafel

4.5. Conclusion

In this chapter, we tested PdS_2/CN composite materials as active electrocatalysts for the HER in electrolysis reaction and also HOR in fuel cell anode reaction. The PdS_2/CN electrocatalysts were tested as bifunctional electrocatalysts for HER and HORs, it can be concluded that our PdS_2@S-PR19 is the best bifunctional electrocatalyst for the HER, the activity that may correlate with catalytically active sulfur edge sites[109, 212] and active carbon edge sites[209] which appeared after billing of PdS_2@S-PR19. Moreover, this may indicate that GNF are shortened to enhance the mass transport of solvent, reactants and products during HER.[208] We found that PdS_2@S-PR19 was not durable electrocatalyst for HER/HEOR due to a significant number of defects and damages after the ball milling on the external and internal structure and step edges of the GNF.

In addition, the selected PdS_2@S-PR24, PdS_2@S-PR19, Pd/C and Pt/C electrocatalysts were studied in a durability test by continuously applying linear potential sweeps up to 5000 cycles. It can be concluded that our PdS_2@S-PR24 is the most durable bifunctional electrocatalyst for the HER. This can be explained by a higher surface of interaction of PdS_2NP with the step-edge inside PR24-GNF, hence a better connectivity of catalytic centres in PdS_2@S-PR24 leading to higher durability and a close electrocatalytic performance as compared to Pd/C and Pt/C commercial catalysts. This provides further evidence of the stabilising effects of step-edges in GNF cavities and PtNP confinement within the GNF. Thus, the approach of preformed nanoparticle insertion into GNFs has led to an advanced PdS_2 electrocatalyst with highly competitive performance and durability relative to commercial Pt/C and Pd/C electrocatalysts for HER/HOR. More generally, this nanoscale design for an electrocatalyst architecture can be applied to a wide range of electrocatalyst materials with for the sustainable use of Pd.

Chapter 5. Concluding remarks

During this project, new functional nanostructures based on PtNP, Mn_3O_4NP and PdS_2NP encapsulated into S-GNF hybrid nanostructures have been prepared, optimized and developed as efficient electrocatalyst materials for hydrogen fuel cell applications and water splitting devices with enhanced performance and/or durability.

The most significant outcomes of this project include establishing the insertion of preformed Pt nanoparticles into S-GNF from solution phase using self-assembly techniques as a new approach for the development of durable hybrid metal-carbon nanostructures as electrocatalysts for ORR with enhanced stability. PtNP interacts stronger with the step-edges of the GNF interior than the surface of GNF or carbon black support, while the GNF cavity creates a nanoscale environment highly beneficial for oxygen reduction reaction on PtNP.

Furthermore, we demonstrated that shortening GNF length made PtNP more accessible for oxygen and water as the reactants and products enter and exit the S-GNF more easily thus largely eliminating diffusion problems as compared to longer GNF. An increase in the performance of the electrocatalyst materials is observed after decreasing the length of the nanocontainer and/or increasing the number of acid groups on the GNF surface. An enhancement of contact of PtNP and GNF is observed after acid treatment of the nanofibers that introduces carboxylic groups on GNF.

While confinement of PtNP catalysts inside GNF slightly decreases their electrochemical activity as compared to the commercial Pt/C, the nanocontainers significantly stabilize the nanoparticles due to the enhanced interaction with internal graphitic step-edges during the electrochemical reactions as compared to traditional Pt/C catalyst. We found that performed PtNP interact stronger with the step-edges of the S-GNF than the in-situ formed Pt nanoparticles yielding to hybrid nanostructures with higher catalytic activity for ORR. This method can provide a better control over the size and shape of the Pt particles than the in-situ methods which involve chemical reduction or decomposition of volatile metal complexes. The size of the NP sitting on the step-edges tends to remain unaffected after removing the surfactant molecules by heating the composite. As a result, the electrocatalytic nanoreactors PtNP@S-GNF, where nanofibers are shortened to improve the mass transport during the reaction, have been demonstrated to possess initial ECSA comparable to best Pt/carbon electrocatalysts reported to date, and outstanding durability retaining much of their activity over the long-term (50,000 potential cycles) thus outperforming all known electrocatalysis for oxygen reduction reaction. The remarkable and unexpected properties of Pt nanoparticles within carbon nanocontainers open new avenues for improving durability of electrochemical devices and enhancing sustainable use of Pt and other elements with critically low abundance to ensure future technological progress.

The ORR and OER performances of bifunctional electrocatalysts Mn_4O_3-CN prepared by deposition of preformed nanoparticles onto CN and $Mn_4O_{3(in\text{-}situ)}$-CN synthesised by in-situ growth of nanoparticles on CN were measured and compared using rotating disk electrode (RDE). In conclusion, $Mn_3O_{4(in\text{-}situ)}$@GNF can be considered to be the most powerful bifunctional catalyst for both the ORR and the OER and outperforms high performing electrocatalyst with smaller overpotentials for both oxygen reduction and water oxidation on non-precious bifunctional catalyst. [18, 25, 27, 28] This can be explained by a higher surface of interaction of $Mn_3O_{4\ (in\text{-}situ)}$NP with the step-edge inside GNF than with the convex surface of the outside of GNF, hence a better connectivity of catalytic centres in $Mn_3O_{4(in\text{-}situ)}$@S-GNF leading to a higher $E_{1/2}$ potential as compared to $Mn_3O_{4(in\text{-}situ)}$/GNF. Considering all aspects, preform nanoparticles approach synthesised Mn_3O_4@GNF is to be less active for both ORR and OER than in-situ nanoparticles approach synthesised $Mn_3O_{4(in\text{-}situ)}$@GNF.

The PdS_2/CN electrocatalysts were tested as bifunctional electrocatalysts for HER and HORs, it can be concluded that our PdS_2@S-PR19 is the best bifunctional electrocatalyst for the HER, the activity that may correlate with catalytically active sulfur edge sites[109, 212] and active carbon edge sites[209] which appeared after billing of PdS_2@S-PR19. We found that PdS_2@S-PR19 was not durable electrocatalyst for HER/HEOR due to a significant number of defects and damages after the ball milling on the external and internal structure and step edges of the GNF. In addition, the selected PdS_2@S-PR24, PdS_2@S-PR19, Pd/C and Pt/C electrocatalysts were studied in a durability test by continuously applying linear potential sweeps up to 5000 cycles. It can be concluded that our PdS_2@S-PR24 is the most durable bifunctional electrocatalyst for the HER. This can be explained by a higher surface of interaction of PdS_2NP with the step-edge inside PR24-GNF, hence a better connectivity of catalytic centres in PdS_2@S-PR24 leading to higher durability and a close electrocatalytic performance as compared to Pd/C and Pt/C commercial catalysts. This provides further evidence of the stabilising effects of step-edges in GNF cavities and PtNP confinement within the GNF

Overall, this project contributed to the development of methodologies for the encapsulation of nanoparticles to produce high performance electrocatalysts for hydrogen fuel cell application and water splitting devices. Controlling the length distribution of GNF enabled efficient access of oxygen and water to catalytic nanoparticles, while maintaining confinement of nanoparticles inside GNF due to strong interactions with the step-edges thus providing materials with good catalytic activity for ORR/OER and HOR/HER and exceptional durability. Finally, the unique nanoscale features of GNF and S-GNF make them superior nanoparticle supports as compared to alternatives carbon nanostructures.

Consequently, the work reported in this thesis makes a significant contribution to the field of hybrid metal-carbon nanostructures for electrocatalysis, opening the door for a new strategy.

Further experimental investigation is needed to increase metal loading into GNF from 10% to 20% or 50% for large-scale fuel cell and water splitting device applications. Harnessing the confinement effects within GNF to improve the performance and durability of hybrid metal-carbon nanostructures in electrocatalysis is one of the potential directions for translating this research towards industrial applications, while the general approach to nanoscale design of electrocatalysts developed in this project may pave the way to a wide range of other systems replacing precious metals in catalysis applications.

References

1. J. Kunze and U. Stimming, *Angewandte Chemie International Edition*, 2009, **48**, 9230-9237.
2. R. Dante, F. Menzl, J. Lehmann, C. Sponholz, O. Luschtinetz and O. Solorza-Feria, *J Appl Electrochem*, 2006, **36**, 187-193.
3. J. Chen, B. Lim, E. P. Lee and Y. Xia, *Nano Today*, 2009, **4**, 81-95.
4. Y. Liang, Y. Li, H. Wang and H. Dai, *Journal of the American Chemical Society*, 2013, **135**, 2013-2036.
5. E. Antolini, *Energ Environ Sci*, 2009, **2**, 915-931.
6. H. A. Gasteiger, S. S. Kocha, B. Sompalli and F. T. Wagner, *Applied Catalysis B: Environmental*, 2005, **56**, 9-35.
7. H. A. Gasteiger and N. M. Markovic, *Science*, 2009, **324**, 48-49.
8. J. B. Wu and H. Yang, *Accounts Chem Res*, 2013, **46**, 1848-1857.
9. C. Wang, N. M. Markovic and V. R. Stamenkovic, *Acs Catal*, 2012, **2**, 891-898.
10. V. R. Stamenkovic, B. Fowler, B. S. Mun, G. Wang, P. N. Ross, C. A. Lucas and N. M. Marković, *Science*, 2007, **315**, 493-497.
11. U. A. Paulus, A. Wokaun, G. G. Scherer, T. J. Schmidt, V. Stamenkovic, V. Radmilovic, N. M. Markovic and P. N. Ross, *J Phys Chem B*, 2002, **106**, 4181-4191.
12. S. J. Guo, D. G. Li, H. Y. Zhu, S. Zhang, N. M. Markovic, V. R. Stamenkovic and S. H. Sun, *Angew Chem Int Edit*, 2013, **52**, 3465-3468.
13. K. Sasaki, L. Zhang and R. R. Adzic, *Physical Chemistry Chemical Physics*, 2008, **10**, 159-167.
14. N. M. Markovic, T. J. Schmidt, V. Stamenkovic and P. N. Ross, *Fuel Cells*, 2001, **1**, 105-116.
15. J. E. Newton, J. A. Preece, N. V. Rees and S. L. Horswell, *Physical Chemistry Chemical Physics*, 2014, **16**, 11435-11446.
16. Y. Shao, Y. Cheng, W. Duan, W. Wang, Y. Lin, Y. Wang and J. Liu, *Acs Catal*, 2015, **5**, 7288-7298.
17. B. Li, M. Gu, Z. Nie, X. Wei, C. Wang, V. Sprenkle and W. Wang, *Nano letters*, 2014, **14**, 158-165.
18. B. Li, M. Gu, Z. Nie, Y. Shao, Q. Luo, X. Wei, X. Li, J. Xiao, C. Wang, V. Sprenkle and W. Wang, *Nano letters*, 2013, **13**, 1330-1335.
19. Y. Shao, X. Wang, M. Engelhard, C. Wang, S. Dai, J. Liu, Z. Yang and Y. Lin, *J Power Sources*, 2010, **195**, 4375-4379.
20. Y. Shao, M. Engelhard and Y. Lin, *Electrochem Commun*, 2009, **11**, 2064-2067.
21. M. K. Debe, *Nature*, 2012, **486**, 43-51.
22. G. Girishkumar, B. McCloskey, A. C. Luntz, S. Swanson and W. Wilcke, *The Journal of Physical Chemistry Letters*, 2010, **1**, 2193-2203.
23. M. Armand and J. M. Tarascon, *Nature*, 2008, **451**, 652-657.
24. A. C. Luntz and B. D. McCloskey, *Chemical reviews*, 2014, **114**, 11721-11750.
25. J. Lu, L. Li, J.-B. Park, Y.-K. Sun, F. Wu and K. Amine, *Chemical reviews*, 2014, **114**, 5611-5640.
26. Y. Shao, F. Ding, J. Xiao, J. Zhang, W. Xu, S. Park, J.-G. Zhang, Y. Wang and J. Liu, *Advanced Functional Materials*, 2013, **23**, 987-1004.
27. Y.-C. Lu, B. M. Gallant, D. G. Kwabi, J. R. Harding, R. R. Mitchell, M. S. Whittingham and Y. Shao-Horn, *Energ Environ Sci*, 2013, **6**, 750-768.
28. Y. Shao, S. Park, J. Xiao, J.-G. Zhang, Y. Wang and J. Liu, *Acs Catal*, 2012, **2**, 844-857.
29. F. Cheng and J. Chen, *Chem Soc Rev*, 2012, **41**, 2172-2192.

30. J.-S. Lee, S. Tai Kim, R. Cao, N.-S. Choi, M. Liu, K. T. Lee and J. Cho, *Adv Energy Mater*, 2011, **1**, 34-50.
31. Y.-C. Lu, Z. Xu, H. A. Gasteiger, S. Chen, K. Hamad-Schifferli and Y. Shao-Horn, *Journal of the American Chemical Society*, 2010, **132**, 12170-12171.
32. D. S. Su and G. Sun, *Angewandte Chemie International Edition*, 2011, **50**, 11570-11572.
33. Y. Bing, H. Liu, L. Zhang, D. Ghosh and J. Zhang, *Chem Soc Rev*, 2010, **39**, 2184-2202.
34. J. K. Norskov, T. Bligaard, J. Rossmeisl and C. H. Christensen, *Nat Chem*, 2009, **1**, 37-46.
35. J. K. Nørskov, J. Rossmeisl, A. Logadottir, L. Lindqvist, J. R. Kitchin, T. Bligaard and H. Jónsson, *The Journal of Physical Chemistry B*, 2004, **108**, 17886-17892.
36. J. A. Keith and T. Jacob, *Angew Chem Int Edit*, 2010, **49**, 9521-9525.
37. E. J. E. Stuart, N. V. Rees and R. G. Compton, *Chem Phys Lett*, 2012, **531**, 94-97.
38. Y. Zheng, Y. Jiao, M. Jaroniec, Y. Jin and S. Z. Qiao, *Small*, 2012, **8**, 3550-3566.
39. J. Perez, E. R. Gonzalez and E. A. Ticianelli, *Electrochim Acta*, 1998, **44**, 1329-1339.
40. B. Lim, M. Jiang, P. H. C. Camargo, E. C. Cho, J. Tao, X. Lu, Y. Zhu and Y. Xia, *Science*, 2009, **324**, 1302-1305.
41. A. R. Kucernak and G. J. Offer, *Physical chemistry chemical physics : PCCP*, 2008, **10**, 3699-3711.
42. S. Guo, S. Zhang and S. Sun, *Angewandte Chemie International Edition*, 2013, **52**, 8526-8544.
43. Y. Y. Liang, Y. G. Li, H. L. Wang, J. G. Zhou, J. Wang, T. Regier and H. J. Dai, *Nature materials*, 2011, **10**, 780-786.
44. A. J. Bard, L. R. Faulkner, C. G. Zoski and J. Leddy, *Electrochemical methods : fundamentals and applications*, John Wiley, New York, 2001.
45. V. G. e. Levich, *Physiochemical hydrodynamics*, Prentice-Hall, Englewood Cliffs, N.J., 1962.
46. A. J. Bard and M. A. Fox, *Accounts Chem Res*, 1995, **28**, 141-145.
47. D. G. Nocera, *Inorganic Chemistry*, 2009, **48**, 10001-10017.
48. A. Kudo and Y. Miseki, *Chem Soc Rev*, 2009, **38**, 253-278.
49. H. B. Gray, *Nat Chem*, 2009, **1**, 112-112.
50. M. G. Walter, E. L. Warren, J. R. McKone, S. W. Boettcher, Q. Mi, E. A. Santori and N. S. Lewis, *Chemical reviews*, 2010, **110**, 6446-6473.
51. M. W. Kanan and D. G. Nocera, *Science*, 2008, **321**, 1072-1075.
52. R. Subbaraman, D. Tripkovic, K. C. Chang, D. Strmcnik, A. P. Paulikas, P. Hirunsit, M. Chan, J. Greeley, V. Stamenkovic and N. M. Markovic, *Nature materials*, 2012, **11**, 550-557.
53. S. Pintado, S. Goberna-Ferron, E. C. Escudero-Adan and J. R. Galan-Mascaros, *Journal of the American Chemical Society*, 2013, **135**, 13270-13273.
54. A. Marshall, B. Børresen, G. Hagen, M. Tsypkin and R. Tunold, *Energy*, 2007, **32**, 431-436.
55. Y. Zhao, K. Kamiya, K. Hashimoto and S. Nakanishi, *The Journal of Physical Chemistry C*, 2015, **119**, 2583-2588.
56. Y. Gorlin and T. F. Jaramillo, *Journal of the American Chemical Society*, 2010, **132**, 13612-13614.
57. N. S. Lewis and D. G. Nocera, *Proceedings of the National Academy of Sciences*, 2006, **103**, 15729-15735.
58. G. Chen, S. R. Bare and T. E. Mallouk, *J Electrochem Soc*, 2002, **149**, A1092-A1099.
59. T. Ioroi, N. Kitazawa, K. Yasuda, Y. Yamamoto and H. Takenaka, *J Appl Electrochem*, 2001, **31**, 1179-1183.
60. L. L. Swette, A. B. LaConti and S. A. McCatty, *J Power Sources*, 1994, **47**, 343-351.

61. H. Liu, B. Yi, M. Hou, J. Wu, Z. Hou and H. Zhang *Electrochemical and Solid-State Letters*, 2004, **7**, A56-A59.
62. R. S. Yeo, J. Orehotsky, W. Visscher and S. Srinivasan, *J Electrochem Soc*, 1981, **128**, 1900-1904.
63. M. Carmo, D. L. Fritz, J. Mergel and D. Stolten, *Int J Hydrogen Energ*, 2013, **38**, 4901-4934.
64. C. C. L. McCrory, S. Jung, J. C. Peters and T. F. Jaramillo, *Journal of the American Chemical Society*, 2013, **135**, 16977-16987.
65. T. Reier, M. Oezaslan and P. Strasser, *Acs Catal*, 2012, **2**, 1765-1772.
66. M. Yagi, E. Tomita and T. Kuwabara, *Journal of Electroanalytical Chemistry*, 2005, **579**, 83-88.
67. Y. Lee, J. Suntivich, K. J. May, E. E. Perry and Y. Shao-Horn, *The Journal of Physical Chemistry Letters*, 2012, **3**, 399-404.
68. M. E. G. Lyons and S. Floquet, *Physical Chemistry Chemical Physics*, 2011, **13**, 5314-5335.
69. S. Trasatti, *Electrochim Acta*, 1984, **29**, 1503-1512.
70. S. Trasatti, *Journal of Electroanalytical Chemistry*, 1980, **111**, 125-131.
71. M. E. G. Lyons and L. D. Burke, *Journal of the Chemical Society-Faraday Transactions I*, 1987, **83**, 299-321.
72. S. Ardizzone, G. Fregonara and S. Trasatti, *Electrochim Acta*, 1990, **35**, 263-267.
73. Y. Li, P. Hasin and Y. Wu, *Advanced Materials*, 2010, **22**, 1926-1929.
74. F. Cheng, J. Shen, B. Peng, Y. Pan, Z. Tao and J. Chen, *Nature Chemistry*, 2011, **3**, 79-84.
75. J. W. Schultze and K. J. Vetter, *Electrochim Acta*, 1973, **18**, 889-896.
76. M. H. Miles, G. Kissel, P. W. T. Lu and S. Srinivasan, *J Electrochem Soc*, 1976, **123**, 332-336.
77. A. J. Appleby and C. J. Van Drunen, *Journal of Electroanalytical Chemistry and Interfacial Electrochemistry*, 1975, **60**, 101-108.
78. K. N. Ferreira, T. M. Iverson, K. Maghlaoui, J. Barber and S. Iwata, *Science*, 2004, **303**, 1831-1838.
79. S. Chrétien and H. Metiu, *The Journal of Chemical Physics*, 2008, **129**, 074705.
80. D. S. Gnanamuthu and J. V. Petrocelli, *J Electrochem Soc*, 1967, **114**, 1036-1041.
81. M. Pourbaix, *Atlas of electrochemical equilibria in aqueous solutions*, Pergamon Press, Oxford; New York, 1966.
82. M. S. Dresselhaus and I. L. Thomas, *Nature*, 2001, **414**, 332-337.
83. S. Chen and A. Kucernak, *The Journal of Physical Chemistry B*, 2004, **108**, 13984-13994.
84. E. Skulason, G. S. Karlberg, J. Rossmeisl, T. Bligaard, J. Greeley, H. Jonsson and J. K. Norskov, *Physical Chemistry Chemical Physics*, 2007, **9**, 3241-3250.
85. W. C. Sheng, H. A. Gasteiger and Y. Shao-Horn, *J Electrochem Soc*, 2010, **157**, B1529-B1536.
86. K. Krischer and E. Savinova, in *Handbook of Heterogeneous Catalysis*, ed. H. K. G. Ertl, F. Schüth, and J. Weitkamp, Wiley-VCH, Chichester, 2009, p. 1873.
87. K. J. Vetter, *Electrochemical kinetics : theoretical and experimental aspects*, Academic Press, New York, N.Y, 1967.
88. G. Jerkiewicz, *Electrocatalysis*, 2010, **1**, 179-199.
89. N. M. Markovic, B. N. Grgur and P. N. Ross, *J Phys Chem B*, 1997, **101**, 5405-5413.
90. H. J. Dai, *Abstr Pap Am Chem S*, 2013, **245**.
91. B. E. Conway and B. V. Tilak, *Electrochim Acta*, 2002, **47**, 3571-3594.
92. M. Shao, *J Power Sources*, 2011, **196**, 2433-2444.
93. A. J. Bard and M. A. Fox, *Accounts Chem Res*, 1995, **28**, 141-145.

94. Y. Okamoto, S. Ida, J. Hyodo, H. Hagiwara and T. Ishihara, *Journal of the American Chemical Society*, 2011, **133**, 18034-18037.

95. D. Merki and X. Hu, *Energ Environ Sci*, 2011, **4**, 3878-3888.

96. C. Lupi, A. Dell'Era and M. Pasquali, *Int J Hydrogen Energ*, 2009, **34**, 2101-2106.

97. H. I. Karunadasa, C. J. Chang and J. R. Long, *Nature*, 2010, **464**, 1329-1333.

98. T. F. Jaramillo, K. P. Jørgensen, J. Bonde, J. H. Nielsen, S. Horch and I. Chorkendorff, *Science*, 2007, **317**, 100-102.

99. B. Hinnemann, P. G. Moses, J. Bonde, K. P. Jorgensen, J. H. Nielsen, S. Horch, I. Chorkendorff and J. K. Norskov, *Journal of the American Chemical Society*, 2005, **127**, 5308-5309.

100. M. L. Helm, M. P. Stewart, R. M. Bullock, M. R. DuBois and D. L. DuBois, *Science*, 2011, **333**, 863-866.

101. J. Greeley, T. F. Jaramillo, J. Bonde, I. Chorkendorff and J. K. Norskov, *Nature materials*, 2006, **5**, 909-913.

102. D. J. Evans and C. J. Pickett, *Chem Soc Rev*, 2003, **32**, 268-275.

103. S. Cobo, J. Heidkamp, P.-A. Jacques, J. Fize, V. Fourmond, L. Guetaz, B. Jousselme, V. Ivanova, H. Dau, S. Palacin, M. Fontecave and V. Artero, *Nature materials*, 2012, **11**, 802-807.

104. E. S. Andreiadis, P.-A. Jacques, P. D. Tran, A. Leyris, M. Chavarot-Kerlidou, B. Jousselme, M. Matheron, J. Pécaut, S. Palacin, M. Fontecave and V. Artero, *Nat Chem*, 2013, **5**, 48-53.

105. W. Sheng, H. A. Gasteiger and Y. Shao-Horn, *J Electrochem Soc*, 2010, **157**, B1529-B1536.

106. J. Greeley, J. K. Nørskov, L. A. Kibler, A. M. El-Aziz and D. M. Kolb, *ChemPhysChem*, 2006, **7**, 1032-1035.

107. S. Schuldiner, *J Electrochem Soc*, 1959, **106**, 891-895.

108. A. Le Goff, V. Artero, B. Jousselme, P. D. Tran, N. Guillet, R. Métayé, A. Fihri, S. Palacin and M. Fontecave, *Science*, 2009, **326**, 1384-1387.

109. A. B. Laursen, S. Kegnaes, S. Dahl and I. Chorkendorff, *Energ Environ Sci*, 2012, **5**, 5577-5591.

110. T. J. Schmidt, H. A. Gasteiger, G. D. Stab, P. M. Urban, D. M. Kolb and R. J. Behm, *J Electrochem Soc*, 1998, **145**, 2354-2358.

111. J. Hou, Y. Shao, M. W. Ellis, R. B. Moore and B. Yi, *Physical Chemistry Chemical Physics*, 2011, **13**, 15384-15402.

112. Z. Chen, M. Waje, W. Li and Y. Yan, *Angewandte Chemie*, 2007, **119**, 4138-4141.

113. Z. Chen, M. Waje, W. Li and Y. Yan, *Angewandte Chemie International Edition*, 2007, **46**, 4060-4063.

114. R. Kou, Y. Shao, D. Wang, M. H. Engelhard, J. H. Kwak, J. Wang, V. V. Viswanathan, C. Wang, Y. Lin, Y. Wang, I. A. Aksay and J. Liu, *Electrochem Commun*, 2009, **11**, 954-957.

115. C. V. Rao, A. L. M. Reddy, Y. Ishikawa and P. M. Ajayan, *Carbon*, 2011, **49**, 931-936.

116. Li and W., *Carbon*, 2004, **42**, 436-439.

117. R. Q. Yu, L. W. Chen, Q. P. Liu, J. Y. Lin, K. L. Tan, S. C. Ng, H. S. O. Chan, G. Q. Xu and T. S. A. Hor, *Chem Mater*, 1998, **10**, 718-722.

118. B. Beden, F. Largeaud, K. B. Kokoh and C. Lamy, *Electrochim Acta*, 1996, **41**, 701-709.

119. P. M. Ajayan, T. W. Ebbesen, T. Ichihashi, S. Iijima, K. Tanigaki and H. Hiura, *Nature*, 1993, **362**, 522-525.

120. Y. Zhao, C. Li, K. Yao and J. Liang, *Journal of Materials Science*, 2007, **42**, 4240-4244.

121. E. Castillejos, R. Chico, R. Bacsa, S. Coco, P. Espinet, M. Perez-Cadenas, A. Guerrero-Ruiz, I. Rodriguez-Ramos and P. Serp, *European Journal of Inorganic Chemistry*, 2010, DOI: 10.1002/ejic.201000643, 5096-5102.
122. N. M. Rodriguez, M. S. Kim and R. T. K. Baker, *Journal of Physical Chemistry*, 1994, **98**, 13108-13111.
123. C. A. Bessel, K. Laubernds, N. M. Rodriguez and R. T. K. Baker, *J Phys Chem B*, 2001, **105**, 1115-1118.
124. H. Bonnemann, W. Brijoux, R. Brinkmann, E. Dinjus, T. Joussen and B. Korall, *Angewandte Chemie-International Edition in English*, 1991, **30**, 1312-1314.
125. E. Castillejos, P.-J. Debouttiere, L. Roiban, A. Solhy, V. Martinez, Y. Kihn, O. Ersen, K. Philippot, B. Chaudret and P. Serp, *Angew Chem Int Edit*, 2009, **48**, 2529-2533.
126. A. C. U. Ugarte, W. A. De Heer, *Science*, 1996, **274**, 1897.
127. Z. S. L. Guan, M. Li, Z. Gu,, *Carbon*, 2005, **43**, 2780.
128. M. d. C. Gimenez-Lopez, A. La Torre, M. W. Fay, P. D. Brown and A. N. Khlobystov, *Angewandte Chemie (International ed. in English)*, 2013, **52**, 2051-2054.
129. A. La Torre, M. D. Gimenez-Lopez, M. W. Fay, G. A. Rance, W. A. Solomonsz, T. W. Chamberlain, P. D. Brown and A. N. Khlobystov, *Acs Nano*, 2012, **6**, 2000-2007.
130. S. A. Miners, G. A. Rance, A. La Torre, S. M. Kenny and A. N. Khlobystov, *Journal of Materials Chemistry C*, 2014, **2**, 8357-8363.
131. M. d. C. Gimenez-Lopez, A. La Torre, M. W. Fay, P. D. Brown and A. N. Khlobystov, *Angew Chem Int Edit*, 2013, **52**, 2051-2054.
132. Y. Gorlin and T. F. Jaramillo, *Journal of the American Chemical Society*, 2010, **132**, 13612-13614.
133. D. Wang, C. V. Subban, H. Wang, E. Rus, F. J. DiSalvo and H. D. Abruña, *Journal of the American Chemical Society*, 2010, **132**, 10218-10220.
134. J. N. Tiwari, K. Nath, S. Kumar, R. N. Tiwari, K. C. Kemp, N. H. Le, D. H. Youn, J. S. Lee and K. S. Kim, *Nat Commun*, 2013, **4**.
135. Y. Shao, G. Yin and Y. Gao, *J Power Sources*, 2007, **171**, 558-566.
136. T. Fujigaya and N. Nakashima, *Advanced Materials*, 2013, **25**, 1666-1681.
137. N. V. Rees and R. G. Compton, *Energ Environ Sci*, 2011, **4**, 1255-1260.
138. Y. J. Wang, D. P. Wilkinson and J. J. Zhang, *Chemical reviews*, 2011, **111**, 7625-7651.
139. Y. Shao-Horn, W. C. Sheng, S. Chen, P. J. Ferreira, E. F. Holby and D. Morgan, *Topics in Catalysis*, 2007, **46**, 285-305.
140. X. J. Zhou, J. L. Qiao, L. Yang and J. J. Zhang, *Adv Energy Mater*, 2014, **4**.
141. X. Wang, W. Li, Z. Chen, M. Waje and Y. Yan, *J Power Sources*, 2006, **158**, 154-159.
142. Y. Shao, G. Yin, J. Zhang and Y. Gao, *Electrochim Acta*, 2006, **51**, 5853-5857.
143. Y. Wang, Y. P. Wu, Y. Huang, F. Zhang, X. Yang, Y. F. Ma and Y. S. Chen, *J Phys Chem C*, 2011, **115**, 23192-23197.
144. S. Iijima, *Nature*, 1991, **354**, 56-58.
145. R. Wu, Y. Xue, X. Qian, H. Liu, K. Zhou, S. H. Chan, J. N. Tey, J. Wei, B. Zhu and Y. Huang, *Int J Hydrogen Energ*, 2013, **38**, 16677-16684.
146. B. Singh and E. Dempsey, *Rsc Advances*, 2013, **3**, 2279-2287.
147. M. Endo, Y. A. Kim, M. Ezaka, K. Osada, T. Yanagisawa, T. Hayashi, M. Terrones and M. S. Dresselhaus, *Nano letters*, 2003, **3**, 723-726.
148. P. Serp and E. Castillejos, *ChemCatChem*, 2010, **2**, 41-47.
149. J. P. Tessonnier, O. Ersen, G. Weinberg, C. Pham-Huu, D. S. Su and R. Schlogl, *Acs Nano*, 2009, **3**, 2081-2089.
150. A. La Torre, M. W. Fay, G. A. Rance, M. D. Gimenez-Lopez, W. A. Solomonsz, P. D. Brown and A. N. Khlobystov, *Small*, 2012, **8**, 1222-1228.

151. A. La Torre, M. D. Gimenez-Lopez, M. W. Fay, C. H. Lucas, P. D. Brown and A. N. Khlobystov, *Small*, 2015, **11**, 2756-2761.
152. B. Singh, E. Dempsey, C. Dickinson and F. Laffir, *The Analyst*, 2012, **137**, 1639-1648.
153. C. Wang, H. Daimon, Y. Lee, J. Kim and S. Sun, *Journal of the American Chemical Society*, 2007, **129**, 6974-6975.
154. T. W. Chamberlain, A. M. Popov, A. A. Knizhnik, G. E. Samoilov and A. N. Khlobystov, *Acs Nano*, 2010, **4**, 5203-5210.
155. C. Wang, H. Daimon and S. Sun, *Nano letters*, 2009, **9**, 1493-1496.
156. D. E. Ramaker, A. Korovina, V. Croze, J. Melke and C. Roth, *Physical Chemistry Chemical Physics*, 2014, **16**, 13645-13653.
157. M. T. M. Koper, S. C. S. Lai and E. Herrero, in *Fuel Cell Catalysis*, John Wiley & Sons, Inc., 2008, DOI: 10.1002/9780470463772.ch6, pp. 159-207.
158. K. J. J. Mayrhofer, D. Strmcnik, B. B. Blizanac, V. Stamenkovic, M. Arenz and N. M. Markovic, *Electrochim Acta*, 2008, **53**, 3181-3188.
159. J. Zhang, K. Sasaki, E. Sutter and R. R. Adzic, *Science*, 2007, **315**, 220-222.
160. N. Markovic, H. Gasteiger and P. N. Ross, *J Electrochem Soc*, 1997, **144**, 1591-1597.
161. J. X. Wang, N. M. Markovic and R. R. Adzic, *The Journal of Physical Chemistry B*, 2004, **108**, 4127-4133.
162. S.-A. Park, D.-S. Kim, T.-J. Kim and Y.-T. Kim, *Acs Catal*, 2013, **3**, 3067-3074.
163. N. Cheng, M. N. Banis, J. Liu, A. Riese, X. Li, R. Li, S. Ye, S. Knights and X. Sun, *Advanced Materials*, 2015, **27**, 277-281.
164. Z.-Z. Jiang, Z.-B. Wang, Y.-Y. Chu, D.-M. Gu and G.-P. Yin, *Energ Environ Sci*, 2011, **4**, 728-735.
165. S. Chen, Z. Wei, X. Qi, L. Dong, Y.-G. Guo, L. Wan, Z. Shao and L. Li, *Journal of the American Chemical Society*, 2012, **134**, 13252-13255.
166. Z.-Z. Jiang, Z.-B. Wang, Y.-Y. Chu, D.-M. Gu and G.-P. Yin, *Energ Environ Sci*, 2011, **4**, 2558-2566.
167. M. Dou, M. Hou, D. Liang, W. Lu, Z. Shao and B. Yi, *Electrochim Acta*, 2013, **92**, 468-473.
168. S. Sun, G. Zhang, D. Geng, Y. Chen, R. Li, M. Cai and X. Sun, *Angewandte Chemie International Edition*, 2011, **50**, 422-426.
169. H. Duan and C. Xu, *Electrochim Acta*, 2015, **152**, 417-424.
170. B. Arumugam, B. A. Kakade, T. Tamaki, M. Arao, H. Imai and T. Yamaguchi, *RSC Advances*, 2014, **4**, 27510-27517.
171. T. J. Kim, G. Kwon and Y. T. Kim, *Chem Commun*, 2014, **50**, 596-598.
172. Y. Nie, S. Chen, W. Ding, X. Xie, Y. Zhang and Z. Wei, *Chem Commun*, 2014, **50**, 15431-15434.
173. W. Li, C. Liang, W. Zhou, J. Qiu, Zhou, G. Sun and Q. Xin, *The Journal of Physical Chemistry B*, 2003, **107**, 6292-6299.
174. A. M. Gomez-Marin and J. M. Feliu, *Chemsuschem*, 2013, **6**, 1091-1100.
175. L. L. Liu, J. Wang, Y. Y. Hou, J. Chen, H. K. Liu, J. Z. Wang and Y. P. Wu, *Small*, 2016, **12**, 602-611.
176. H. Liu, Y. Zheng, G. X. Wang and S. Z. Qiao, *Adv Energy Mater*, 2015, **5**.
177. G. Nam, J. Park, M. Choi, P. Oh, S. Park, M. G. Kim, N. Park, J. Cho and J. S. Lee, *Acs Nano*, 2015, **9**, 6493-6501.
178. T. N. Lambert, J. A. Vigil, S. E. White, D. J. Davis, S. J. Limmer, P. D. Burton, E. N. Coker, T. E. Beechem and M. T. Brumbach, *Chemical Communications*, 2015, **51**, 9511-9514.
179. H. L. Wang, Y. Yang, Y. Y. Liang, G. Y. Zheng, Y. G. Li, Y. Cui and H. J. Dai, *Energ Environ Sci*, 2012, **5**, 7931-7935.
180. W. N. Yan, Z. R. Yang, W. Y. Bian and R. Z. Yang, *Carbon*, 2015, **92**, 74-83.

181. J. Du, C. C. Chen, F. Y. Cheng and J. Chen, *Inorganic Chemistry*, 2015, **54**, 5467-5474.
182. S. Y. Liu, L. J. Li, H. S. Ahnb and A. Manthiram, *J Mater Chem A*, 2015, **3**, 11615-11623.
183. Y. G. Wang, L. Cheng, F. Li, H. M. Xiong and Y. Y. Xia, *Chem Mater*, 2007, **19**, 2095-2101.
184. L. Q. Mao, T. Sotomura, K. Nakatsu, N. Koshiba, D. Zhang and T. Ohsaka, *J Electrochem Soc*, 2002, **149**, A504-A507.
185. Y. Gorlin, C.-J. Chung, D. Nordlund, B. M. Clemens and T. F. Jaramillo, *Acs Catal*, 2012, **2**, 2687-2694.
186. J. Feng, Y. Y. Liang, H. L. Wang, Y. G. Li, B. Zhang, J. G. Zhou, J. Wang, T. Regier and H. J. Dai, *Nano Research*, 2012, **5**, 718-725.
187. J. J. Duan, Y. Zheng, S. Chen, Y. H. Tang, M. Jaroniec and S. Z. Qiao, *Chemical Communications*, 2013, **49**, 7705-7707.
188. S. Bag, K. Roy, C. S. Gopinath and C. R. Raj, *Acs Applied Materials & Interfaces*, 2014, **6**, 2692-2699.
189. Z. R. Tian, W. Tong, J. Y. Wang, N. G. Duan, V. V. Krishnan and S. L. Suib, *Science*, 1997, **276**, 926-930.
190. S. J. Guo, S. Zhang, L. H. Wu and S. H. Sun, *Angew Chem Int Edit*, 2012, **51**, 11770-11773.
191. J. J. Li, L. Li, W. Cheng, F. Wu, X. F. Lu and Z. P. Li, *Chem Eng J*, 2014, **244**, 59-67.
192. Q. W. Tang, L. H. Jiang, J. Liu, S. L. Wang and G. Q. Sun, *Acs Catal*, 2014, **4**, 457-463.
193. R. Frydendal, M. Busch, N. B. Halck, E. A. Paoli, P. Krtil, I. Chorkendorff and J. Rossmeisl, *Chemcatchem*, 2015, **7**, 149-154.
194. Y. Gao, H. Zhao, D. Chen, C. Chen and F. Ciucci, *Carbon*, 2015, **94**, 1028-1036.
195. S. Dresp, F. Luo, R. Schmack, S. Kuhl, M. Gliech and P. Strasser, *Energ Environ Sci*, 2016, **9**, 2020-2024.
196. Y. Gorlin, C. J. Chung, J. D. Benck, D. Nordlund, L. Seitz, T. C. Weng, D. Sokaras, B. M. Clemens and T. F. Jaramillo, *Journal of the American Chemical Society*, 2014, **136**, 4920-4926.
197. J. S. Ye, X. Liu, H. F. Cui, W. D. Zhang, F. S. Sheu and T. M. Lim, *Electrochem Commun*, 2005, **7**, 249-255.
198. J. H. Chen, W. Z. Li, D. Z. Wang, S. X. Yang, J. G. Wen and Z. F. Ren, *Carbon*, 2002, **40**, 1193-1197.
199. K. H. Kangasniemi, D. A. Condit and T. D. Jarvi, *J Electrochem Soc*, 2004, **151**, E125-E132.
200. N. M. Marković and P. N. Ross Jr, *Surface Science Reports*, 2002, **45**, 117-229.
201. B. Hinnemann, P. G. Moses, J. Bonde, K. P. Jørgensen, J. H. Nielsen, S. Horch, I. Chorkendorff and J. K. Nørskov, *Journal of the American Chemical Society*, 2005, **127**, 5308-5309.
202. T. F. Jaramillo, K. P. Jørgensen, J. Bonde, J. H. Nielsen, S. Horch and I. Chorkendorff, *Science*, 2007, **317**, 100-102.
203. J. Bonde, P. G. Moses, T. F. Jaramillo, J. K. Norskov and I. Chorkendorff, *Faraday Discuss*, 2009, **140**, 219-231.
204. Z. Chen, D. Cummins, B. N. Reinecke, E. Clark, M. K. Sunkara and T. F. Jaramillo, *Nano letters*, 2011, **11**, 4168-4175.
205. Y. G. Li, H. L. Wang, L. M. Xie, Y. Y. Liang, G. S. Hong and H. J. Dai, *Journal of the American Chemical Society*, 2011, **133**, 7296-7299.
206. D. Escalera-Lopez, Y. B. Niu, J. L. Yin, K. Cooke, N. V. Rees and R. E. Palmer, *Acs Catal*, 2016, **6**, 6008-6017.

207. H. A. Burch, M. Isaacs, K. Wilson, R. E. Palmer and N. V. Rees, *Rsc Advances*, 2016, **6**, 26689-26695.

208. M. del Carmen Gimenez-Lopez, A. Kurtoglu, D. A. Walsh and A. N. Khlobystov, *Advanced Materials*, 2016, **28**, 9103-9108.

209. X. J. Fan, Z. W. Peng, J. J. Wang, R. Q. Ye, H. Q. Zhou and X. Guo, *Advanced Functional Materials*, 2016, **26**, 3621-3629.

210. A. Saraby-Reintjes, *Electrochim Acta*, 1986, **31**, 251-254.

211. P. Xiao, M. A. Sk, L. Thia, X. M. Ge, R. J. Lim, J. Y. Wang, K. H. Lim and X. Wang, *Energ Environ Sci*, 2014, **7**, 2624-2629.

212. J. F. Xie, H. Zhang, S. Li, R. X. Wang, X. Sun, M. Zhou, J. F. Zhou, X. W. Lou and Y. Xie, *Advanced Materials*, 2013, **25**, 5807-+.

213. W. Liu, E. Y. Hu, H. Jiang, Y. J. Xiang, Z. Weng, M. Li, Q. Fan, X. Q. Yu, E. I. Altman and H. L. Wang, *Nat Commun*, 2016, **7**.

214. P. J. Rheinländer, J. Herranz, J. Durst and H. A. Gasteiger, *J Electrochem Soc*, 2014, **161**, F1448-F1457.

215. R. M. Q. Mello and E. A. Ticianelli, *Electrochim Acta*, 1997, **42**, 1031-1039.

216. N. M. Marković, B. N. Grgur and P. N. Ross, *The Journal of Physical Chemistry B*, 1997, **101**, 5405-5413.

217. M. R. Gennero de Chialvo and A. C. Chialvo, *Physical Chemistry Chemical Physics*, 2004, **6**, 4009-4017.

218. E. Negro, M. A. De Vries, R. Latsuzbaia and G. J. M. Koper, *Fuel Cells*, 2014, **14**, 350-356.

Appendix

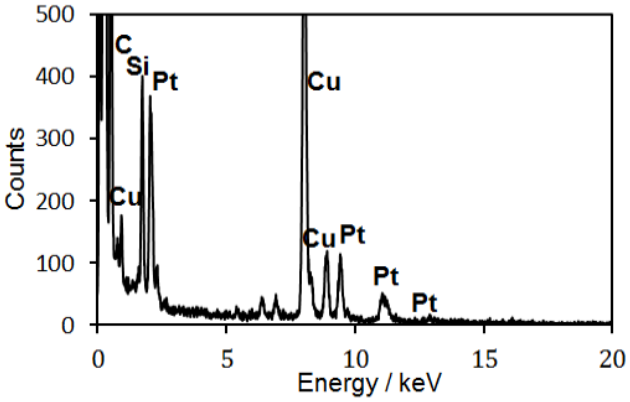

Figure A- 1. EDX spectrum of PtNP onto copper-grid mounted “lacey” carbon fim.

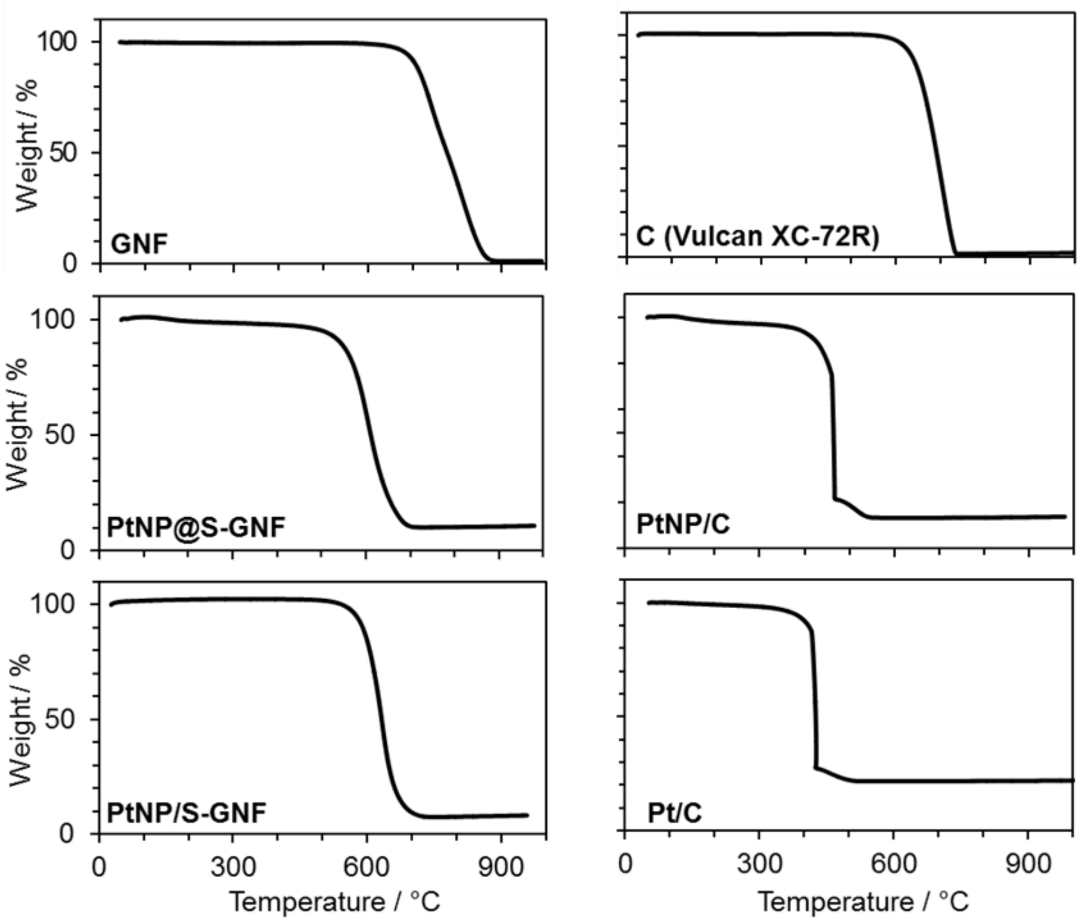

Figure A- 2. Thermal gravimetric analysis (TGA) carried out in air up to 1000 ˚C with a scan rate of 10˚C/min for PtNP@S-GNF, PtNP/C, PtNP/S-GNF and Pt/C, GNF and carbon black (Vulcan XC-72R) are shown here for comparison.

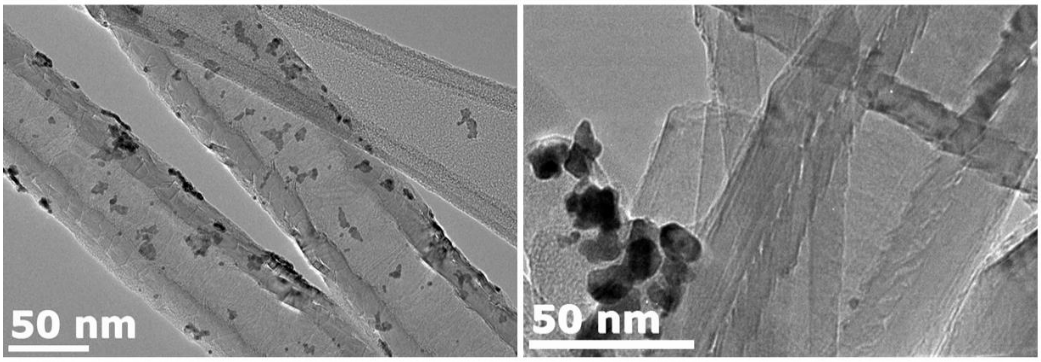

Figure A- 3. HRTEM images for PtNP/S-GNF before (left image) and after (right image) 5000 cycles.

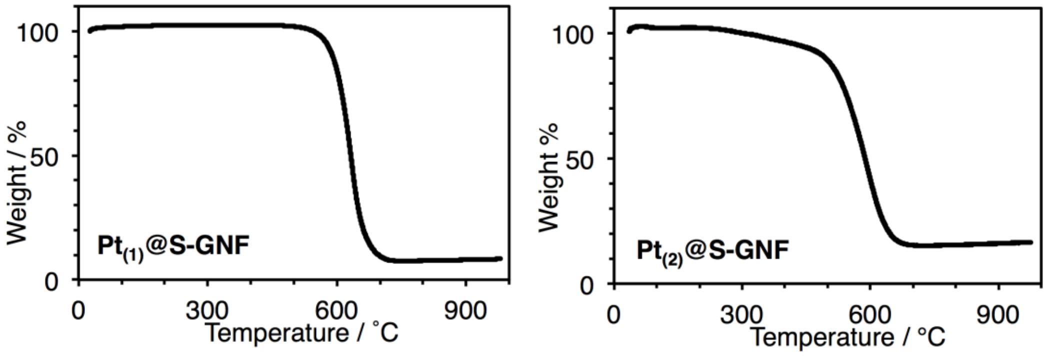

Figure A- 4. Thermal gravimetric analysis (TGA) carried out in air up to 1000 ˚C with a scan rate of 10˚C/min for Pt$_1$@S-GNF and Pt$_2$@S-GNF**.**

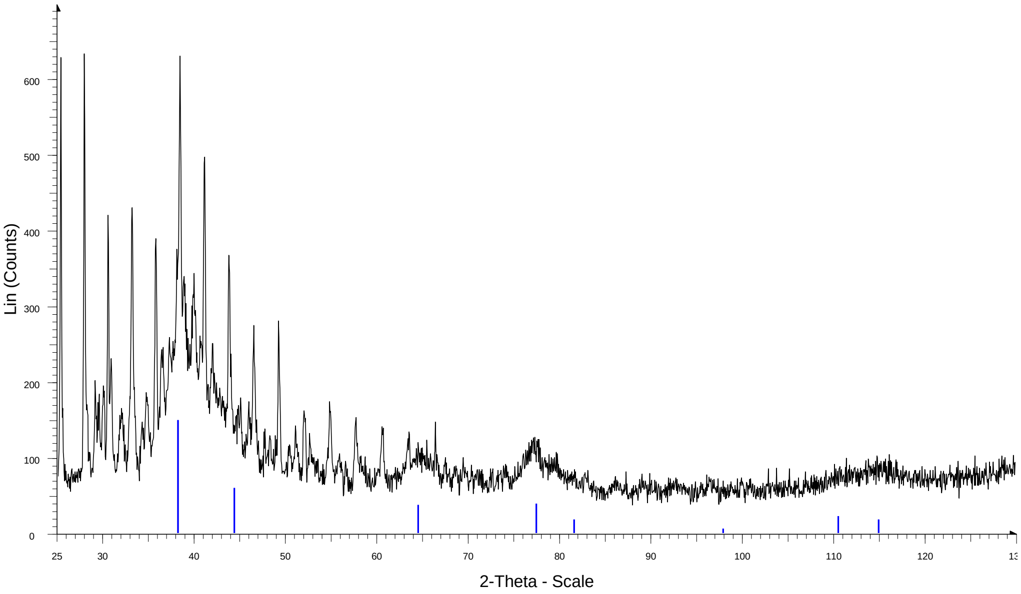

Figure A- 5. XRD diffraction pattern for the obtained AgNP.

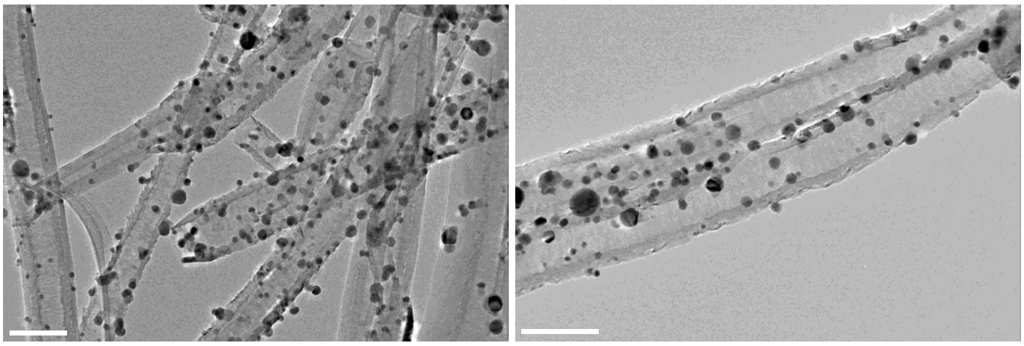

Figure A- 6. HRTEM images for AgNP after thermal heating at 250 °C in air for 2h.

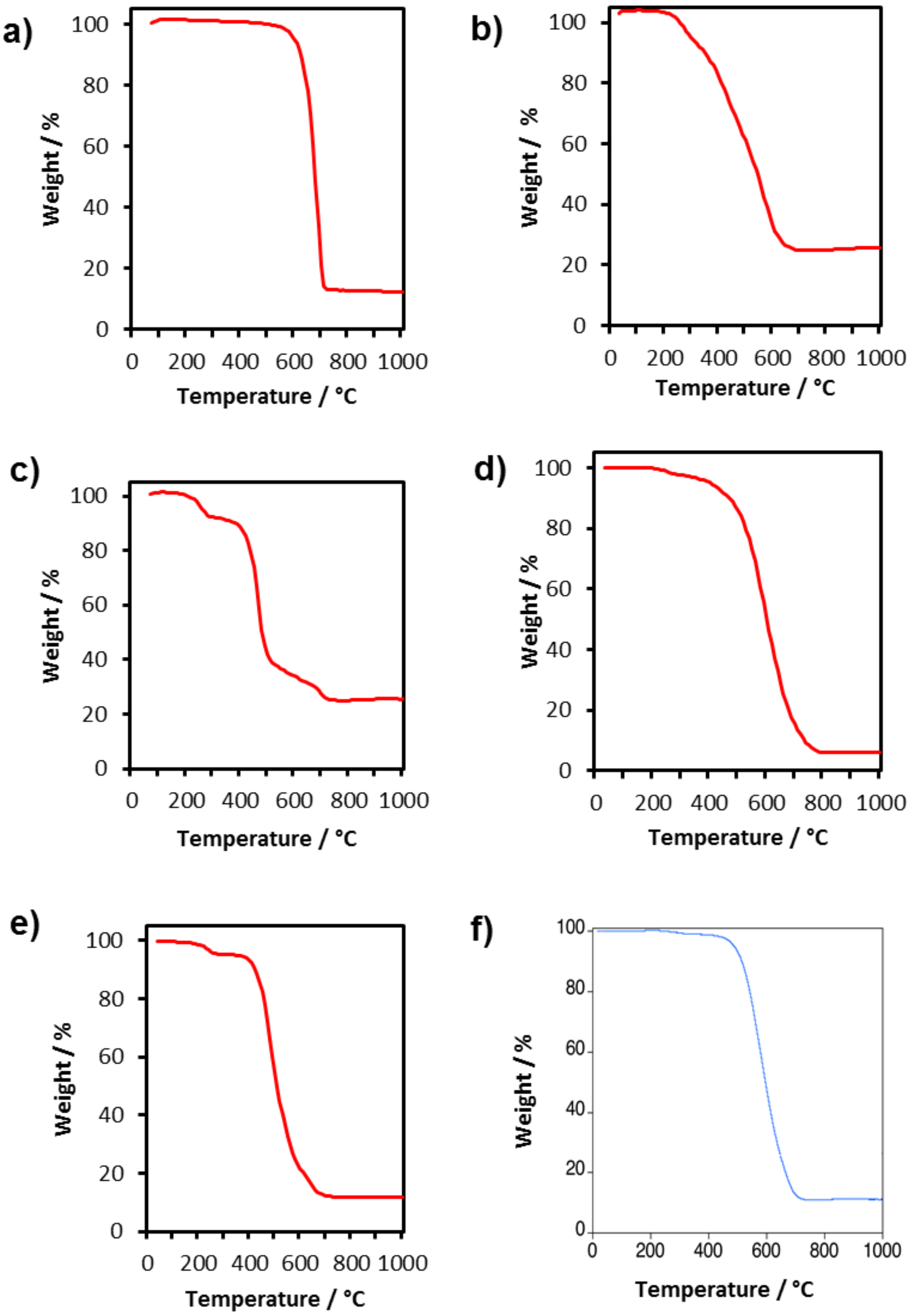

Figure A- 7. TGA for (**a**) Mn_3O_4/C, (**b**) Mn_3O_4/GMWNT, (**c**) Mn_3O_4/G1, (**d**) Mn_3O_4/G2, (**e**) Mn_3O_4/GNF, (**f**) Mn_3O_4@GNF in the range 25-1000 °C in air.[131]

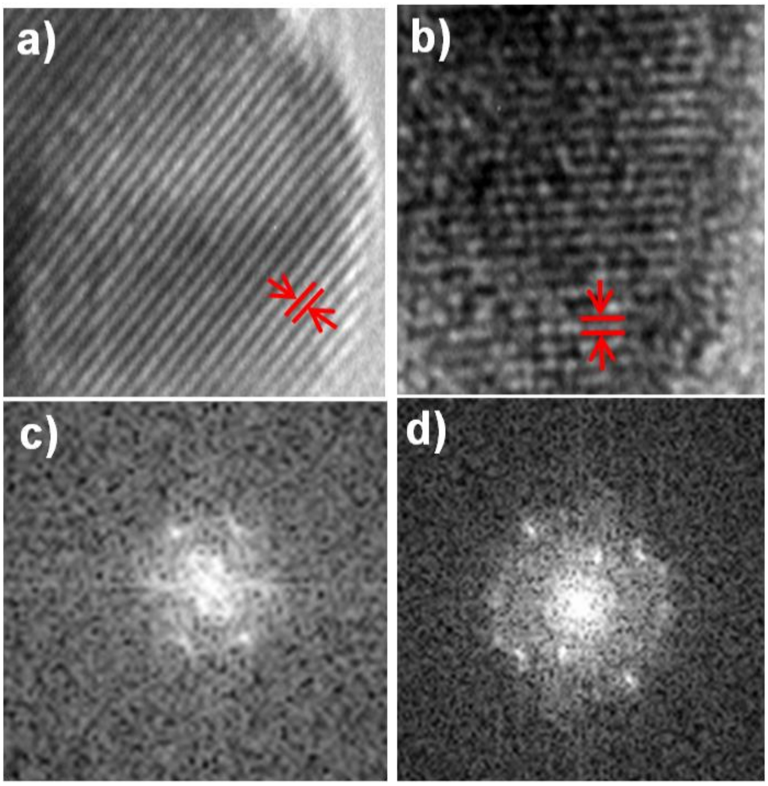

Figure A- 8. HRTEM images showing lattice planes correlating (110) d-spacing value of 0.193 nm and optical diffractograms of PtNP on step-edges before (**a, c**) and after (**b, d**) 50K potential cycling for lifetime stability experiments.

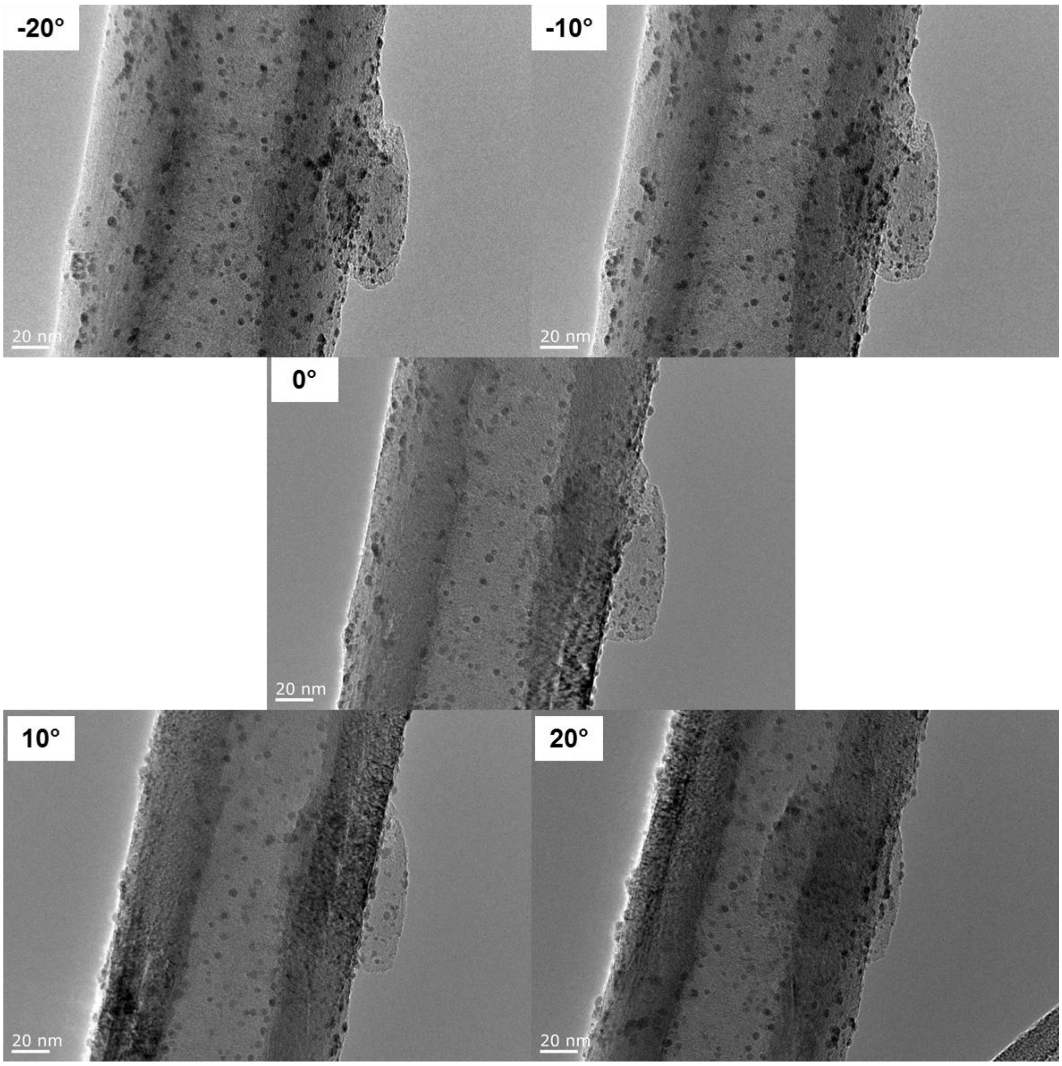

Figure A- 9. HRTEM images of PdS_2@S-PR24, at -20°, -10°, 0°, 10°, 20°

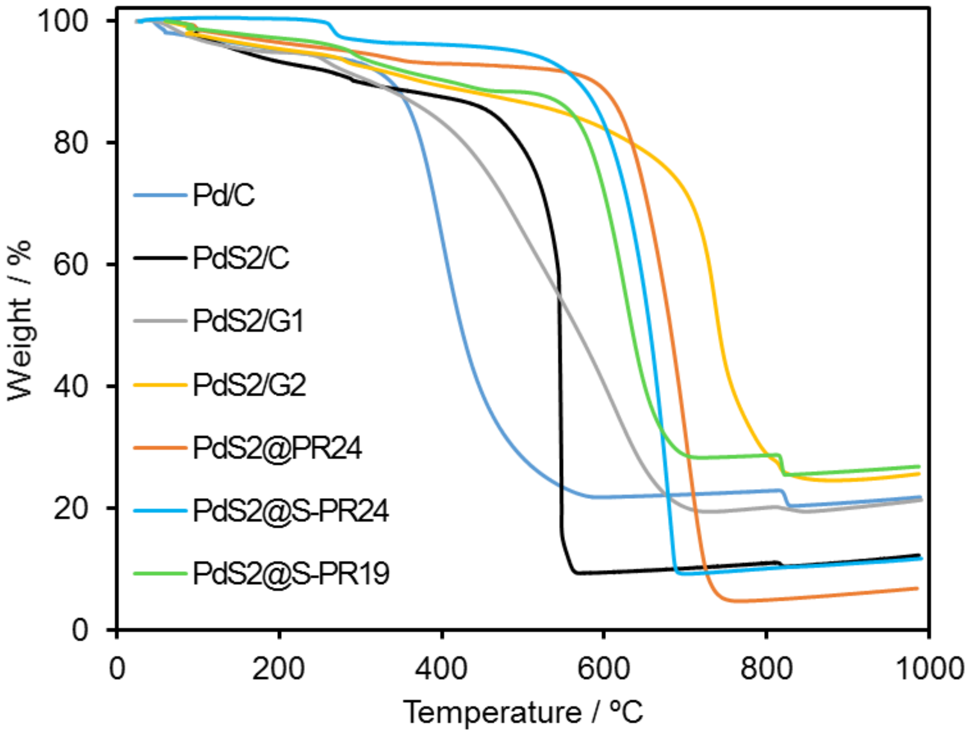

Figure A- 10. Thermal gravimetric analysis (TGA) carried out in air up to 1000 ˚C with a scan rate of 10˚C/min for Pd/C, PdS_2/C PdS_2/G1, PdS_2/G2, PdS_2@PR24, PdS_2@S-PR24 and PdS_2@S-PR19.

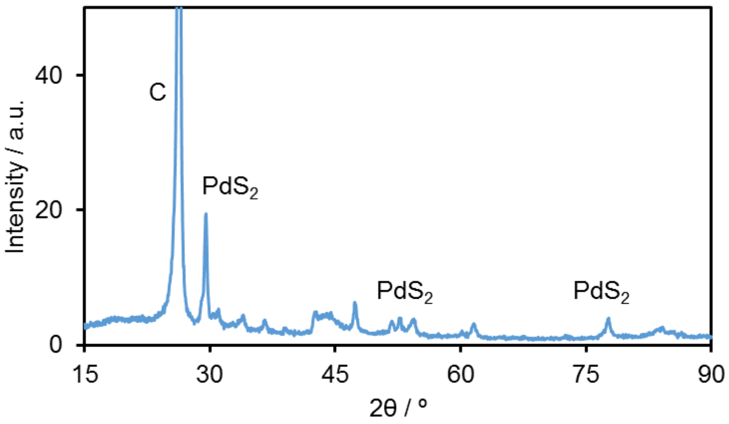

Figure A- 11. XRD diffraction pattern for the obtained PdS_2@S-PR19.

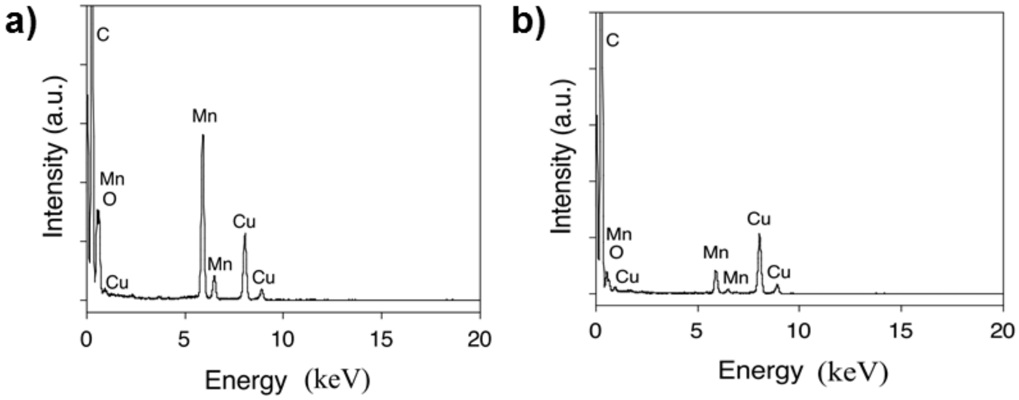

Figure A- 12. EDX spectrum of (**a**) Mn_3O_4NP and (**b**) Mn_3O_4@GNF, confirming the presence of manganese.[131]

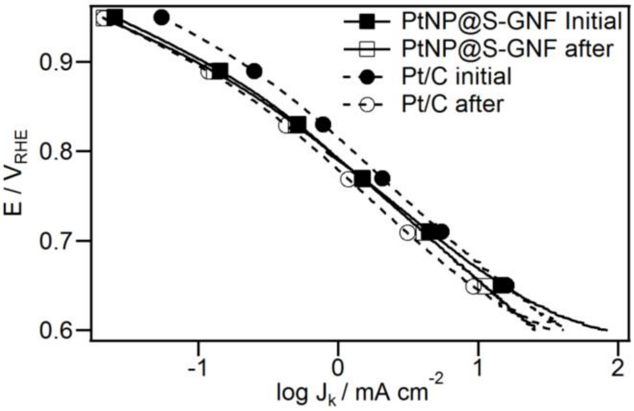

Figure A-13. Tafel plots for the ORR normalised to the real surface area at room temperature, (anodic sweep 5 mV/s, 1600 rpm) on PtNP@S-GNF and Pt/C before and after 5,000 cycles of ORR.

Table A- 1. Summary of electrochemical parameters for different platinum electrocatalyst from literature, our PtNP@S-GNF electrocatalyst and Pt/C commercial catalyst. (*this work, § I_{sa} at 0.85 V, $^{\#}$ I_{mass} at 0.9 V, $^{¥}$ I_{sa} at 0.9 V)

Sample name	Conditions	% ECSA Loss (m^2/g)	% Average NP size increase (nm)	% Half-wave potential at 1600 rpm (V)	% Activity loss	Cycling number
PtNP@S-GNF*	0.6-1.1 V vs. RHE, 0.1M $HClO_4$, 100 mV/s, O_2, RT	22	17	9	$19^{\S}$	50K
Pt/C*	0.6-1.1 V vs. RHE, 0.1M $HClO_4$, 100 mV/s, O_2, RT	72	190	48	$79^{\S}$	50K
Pt–S-MWNT[171]	0.395-0.895 V vs. Ag/AgCl, 0.1M $HClO_4$, 50 mV/s, 100 rpm, O_2	57.5	-	5	-	12K
PFSA-Pt/CNTs[218]	0.6 and 1.2 V vs. RHE, 50 mV/s, 0.1 M $HClO_4$, N_2	-	45	-	-	3K
NP-PtPd[169]	0.6 -1.0 V vs. RHE, 0.1 M $HClO_4$	12	-	9	-	5K
PtFeCo[170]	Applying square wave potential cycling, at 0.6 V for 3s and 1.0 V for 3s vs. RHE, 0.1 M $HClO_4$	15	17.5	13	$21.5^{\#}$	5K
Pt/S-MWNT[162]	0.6-1.1 V vs. RHE, 0.1 M $HClO_4$, 50 mV/s, O_2	14	-	1	$18^{¥}$	4K
N-Pt_3Fe_1/C[168]	0.6 -1.2 V vs. NHE, 0.1 M $HClO_4$, O_2	-	-	-	$7^{¥}$	20K
ZrO_2 -Pt/NCNT 600˚C[163]	0.6 -1.2 V vs. RHE, 0.5 M H_2SO_4,50 mV/s, O_2,	8	0	-	$3.5^{\#}$	4K
Pt/C@NGC[172]	0-1.2 V vs. RHE, 0.1 M HClO4,50 mV/s, N_2	8	15	16	-	1.5 K
Carbon riveted Pt/TiO_2-C[164]	-------	21.5	-	-	-	1K
Pt/C@PANI(30%)[165]	0-1.2 V vs. RHE, 0.5 M H_2SO_4, 50 mV/s, N_2 RT	30	71	-	-	1.5K
Carbon riveted microcapsule Pt/MWCNTs-TiO_2[166]	-------	12				3K
Pt/SnO_2[167]	-------	36				4K
Pt-NWs[168]	0.6-1.2 V vs. RHE, 0.5M H_2SO_4,50 mV/s, O_2	13	-	9	-	4K

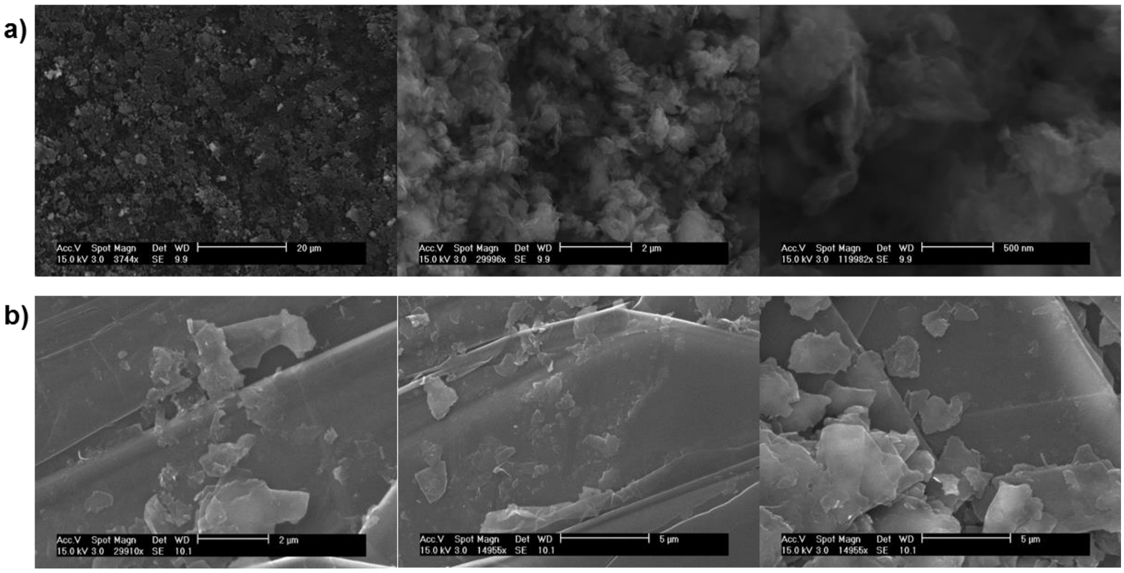

Figure A- 14. SEM images of (**a**) G1 and (**b**) G2.

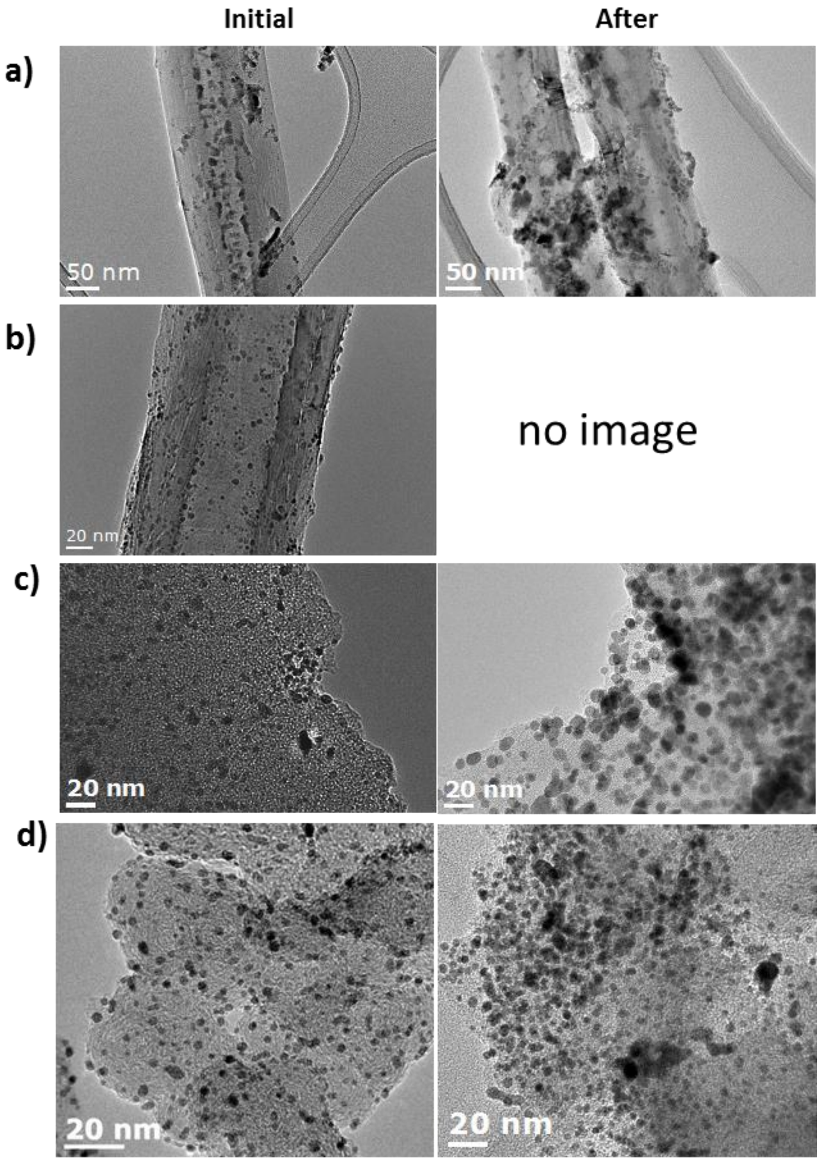

Figure A- 15. HRTEM images of (**a**) PdS_2@S-PR19, (**b**)PdS_2@S-PR24, (**c**)Pd/C and (**d**)Pt/C catalysts before and after the potential cycling from -0.2 to 0.4 V vs RHE at 50 mV in $HClO_4$ for 5000 cycles.